THE STEADY-STATE PERFORMANCE OF AN H-FORM AERODYNAMIC GYRO BEARING HAVING CONNECTED JOURNAL AND THRUST SPIRAL GROOVED SURFACES; WITH PARTICULAR REFERENCE TO ITS OPERATIONAL LIFE AND MANUFACTURING LIMITATIONS

GEOFFREY BEARDMORE

An engineering research thesis submitted for the degree of Ph. D at the University of Aston

SEPTEMBER 1974

ACKNOWLEDGEMENTS

The work described in this thesis was carried out in the Research and Engineering Laboratories of Smiths Industries Limited at Cheltenham, and the writer gratefully acknowledges the Company's permission to submit it in this form.

Special thanks are due to the following individuals.

To Dr. G.K. Lewis internal supervisor (University of Aston), Mr. J.B. Dunne external supervisor (Smiths Industries) and Mr. A.J. Edge, for their continued advice and encouragement, and for their willingness to read and criticise the proof script. To Mr. R. Taylor, Mr. P. Webster and Mr. A. Lister who at various times assisted with the experimental work, to Mr. R. Owen and Mr. J. Brown who carried out much of the laborious metrology required upon each set of bearings, to Mr. E.U. Trevorrow of the Royal Aeronautical Establishment for his advice on numerical instability and to Mr. E.C. Richards of the University Computer Centre for arranging the computer processing of the numerical programme and advising thereon.

Many of the photomicrographs were prepared in the Material Research Laboratories of Smiths Industries Limited, and in the Department of Metallurgy at Aston. The efforts of the personnel concerned are greatly appreciated.

The author would also like to offer his appreciation and thanks to Mr. D.W. Dudley and Mr. R. Joy for their valued support and to Mrs. S. Messenger, Miss. B. Wright and Mrs. L. Harris for undertaking the typing.

During the course of this research programme the author has been in frequent contact with personnel at the University of Aston; The Admiralty Compass Observatory, Slough; The Royal Aeronautical Establishment, Farnborough; and M.I.T. Draper Laboratories, Massachusetts, United States. Their advice and encouragement is gratefully acknowledged.

G. Beardmore

LIST OF CONTENTS

PREFACE

The research described in this thesis was carried out in conjunction with a seven year development programme to evolve a gas lubricated spin bearing for use in miniature rate gyroscopes.

These gyroscopes, designated the 'Series 700', are designed for use in a wide range of commercial and military applications where the prime requirements are a long operational life, high reliability and relatively low cost.

The results discussed in this report were obtained from various experimental and prototype bearing assemblies and do not necessarily represent the performance of Smiths Industries Limited products, which are published separately.

Certain manufacturing techniques and design features referred to in the text are the subject of patents held by the Company*

* Smiths Industries Limited.

NOMENCLATURE

The symbols used throughout this thesis are based upon those recommended by Grassam and Powell in reference 84. This nomenclature was originally suggested by the Franklin Institute, Philadelphia, U.S.A., which in recent years has been a major centre for gas bearing research. These symbols have been used widely, though by no means exclusively, in many of the references detailed at the end of this report. Some modification has however been necessary, due to the fact that the majority of the bearing analysis was carried out numerically on a digital computer, and it was considered very desirable to use symbols which would be directly compatible with the computer input and output facilities. This interface was achieved by the use of upper case characters only where appropriate. Those variables and integers relating directly to the numerical programme are identified in accordance with the rules governing the choice of variable names published by the manufacturer of the computing equipment (115).

Though much of the theoretical analysis has been carried out in dimensionless terms, existing manufacturing arrangements, metrology equipment and test gear have obliged most of the experimental work to be defined in imperial units. Notable exceptions are the traditional use of metric units for torque and inertia measurements throughout the gyroscope industry.

Wherever possible, S.I. equivalents have been included for the convenience of the reader, but any consistent set of units will, of course, be applicable throughout.

SYMBOL	DESCRIPTION	IMPERIAL UNITS	S.I. UNITS
β or B	Length to diameter ratio of journal, $\frac{L}{D}$	Dimensionless	
δ or DEL	Misalignment angle of journal axis.	rad.	rad.
ε or E	Eccentricity ratio, $\frac{\varepsilon}{C}$	Dimensionless	
ε'	Eccentricity ratio of spin motor air gap.	Dimensionless	
θ or TH	Angle between radial eccentricity and angular misalignment planes.	rad.	rad.
θ'	Angular reference in journal measured from position of maximum clearance in direction of rotation.	rad.	rad.
μ or MU	Dynamic Viscosity.	$lb_f sec/in^2$	Ns/m^2
ρ	Density	lb_m/in^3	kg/m^3
ϕ or PHI	Attitude Angle	rad.	rad.
ψ or PSI	Angle between axis of applied torque and axis of resulting deflection for journal.	rad.	rad.
ω or W	Angular velocity of rotor	rad/sec.	rad/s.
ω'	Angular velocity of rotor at touchdown or take-off.	rad/sec.	rad/s.
Λ or S	Compressibility number,	Dimensionless	
$\dot{\Phi}$	Input rate to gyroscope	rad/sec.	rad/s.
Ω	Angular acceleration of rotor from rest.	rad/sec^2	rad/s^2
a	Thrust bearing constant (1.93)	Dimensionless	
b	Thrust bearing constant (4.0)	Dimensionless	

SYMBOL	DESCRIPTION	IMPERIAL UNITS	S.I. UNITS
d	Distortion of thrust plate.	in.	m
e	Eccentricity of journal axis.	in.	m
f	Friction coefficient		Dimensionless
h	Local bearing clearance	in.	m
h_g	Groove depth	in.	m
k	Thermal conductivity	Btu. in/ft^{2}h $^\circ$F	W/m°C
ℓ	Characteristic length	in.	m
ℓ_g	Length of journal pumping groove.	in	m
$\frac{l}{m}$	Poisson's ratio		Dimensionless
M_R	Mass of rotor	lb_m	kg
P	Pressure	lb_f/in^2	N/m^2
Pa	Ambient or atmospheric pressure.	lb_f/in^2	N/m^2
r_o	Outer radius of thrust plate	in.	m
r_i	Inner radius of thrust plate.	in.	m
s	Shear stress	lb_f/in^2	N/m^2
t	Time	sec.	s
Δt	Incremental time	sec.	s
t_w	Wall thickness of thrust plate	in	m
u v w	Linear velocity components	in/sec	m/s
x y z	Rectangular co-ordinates	in.	m
$\bar{x}$	Dimensionless co-ordinate in x-direction $\frac{x}{R}$		Dimensionless

SYMBOL	DESCRIPTION	IMPERIAL UNITS	S.I. UNITS
$\bar{y}$	Dimensionless co-ordinate in y - direction, $\frac{Y}{L}$		Dimensionless
ALPHA	Number of grid points outside residual.		Dimensionless
B_p	Peak flux density in spin motor air gap.	-	T
C	Mean radial clearance of journal.	in.	m
D	Diameter of journal	in.	m
D'	Diameter of spin motor air gap	in.	m
DIFF	Difference between old & new grid pressures.		Dimensionless
E_m	Young's modulus	lb_f/in^2	N/m^2
EPSI	Allowable residual		Dimensionless
F	Relaxation factor		Dimensionless
$\bar{G}$	Dimensionless Groove Depth, $\frac{h}{C}_g$		Dimensionless
Go	Gravitational constant	in/sec^2	m/s^2
$\bar{H}$	Dimensionless bearing clearance over land region, $\frac{h}{C}$		Dimensionless
$\overline{HG}$	Dimensionless bearing clearance over groove region, $\frac{h+h}{C}_g$		Dimensionless
$\bar{H1}, \bar{H2}, \bar{H3}, \bar{H4}$	Dimensionless bearing clearance at surrounding points one half grid interval from the central mesh point.		Dimensionless
I	Mesh co-ordinate in x-direction		Dimensionless
IMAX	Maximum number of rows		Dimensionless
I_R	Rotor Inertia about spin axis.	$lb_m in^2$	$kg.m^2$
J	Mesh co-ordinate in y-direction		Dimensionless
JMAX	Maximum number of columns		Dimensionless

SYMBOL	DESCRIPTION	IMPERIAL UNITS	S.I. UNITS
K	Array of numbers containing information on the position of each mesh point.	Dimensionless	
L	Length of journal bearing	in.	m
L'	Length of spin motor air gap.	in.	m
$\overline{M1}$	Torque component about axis of angular deflection.	Dimensionless	
$\overline{M2}$	Torque component perpendicular to axis of angular deflection.	Dimensionless	
$\overline{MT}$	Total torque load resolved from M1 & M2, $\frac{ML}{Pa.R.L}$	Dimensionless	
ML	Dimensional torque load.	lb_fin.	Nm
N	Number of iterations completed.	Dimensionless	
NMAX	Maximum number of iterations desired.	Dimensionless	
N_R	Rotational speed.	rev/sec	rev/s
$\overline{P}$	Dimensionless bearing pressure $\frac{P}{Pa}$	Dimensionless	
$\overline{P1}, \overline{P2}, \overline{P3}, \overline{P4}$	Dimensionless bearing pressures at surrounding points one half grid interval from the central mesh point.	Dimensionless	
P_E	Power loss of equivalent plain journal assembly.	lb_fin/sec	W
PRESS	New value for grid pressure.	Dimensionless	
PREV	Previous pressure value at any grid point.	Dimensionless	
P_V	Viscous power dissipation	lb_fin/sec	W
Q	Integer subscript to K.	Dimensionless	
Q_F	Frictional heat input	lb_fin/sec	W
QMAX	Maximum value of Q used in calculation	Dimensionless	

SYMBOL	DESCRIPTION	IMPERIAL UNITS	S.I. UNITS
R	Journal radius.	in.	m
Rl	Outer radius of rotor	in.	m
Re	Reynold's number $\frac{\rho U \ell}{\mu G_o}$	Dimensionless	
S'	Specific loading.	lb_m/in^2	kg/m^2
T_0, T_1, T_2, etc	Isotherms	°C	°C
T_F	Friction torque	lb_fin.	Nm
T_G	Gyroscopic torque.	lb_fin.	Nm
T_m	Melting temperature	°C	°C
T_s	Starting torque	lb_fin.	Nm
U	Linear velocity of bearing surface.	in/sec	m/s
VAR	New iterated value for $\bar{Z}$ at any grid point.	Dimensionless	
V_o	Rubbing velocity due to simple overload.	in/sec	m/s
V_w	Rubbing velocity due to whirl	in/sec	m/s
$\overline{W1}$	Radial load component acting parallel to deflection	Dimensionless	
$\overline{W2}$	Radial load component acting perpendicular to deflection.	Dimensionless	
$\overline{WT}$	Total radial load resolved from $\overline{W1}$, & $\overline{W2}$, $\frac{WL}{Pa.R.L}$	Dimensionless	
W_L	Dimensional radial load.	lb_f	N
$\bar{X}$	Dimensionless grid length in x-direction.	Dimensionless	
$\bar{Y}$	Dimensionless grid length in y-direction.	Dimensionless	
$\bar{Z}$	Dependant variable on which iteration is performed.	Dimensionless	
$\bar{Z}_o$	Previous value of $\bar{Z}$ at point I, J	Dimensionless	

SYMBOL	DESCRIPTION	IMPERIAL UNITS	S.I. UNITS
$\overline{\text{Ƶ}1}, \overline{\text{Ƶ}2}, \overline{\text{Ƶ}3}, \overline{\text{Ƶ}4}$	Value of dependant variable at surrounding mesh points.		Dimensionless
$\delta\overline{\text{Ƶ}}$	Incremental increase in $\overline{\text{Ƶ}}$ after each single iteration.		Dimensionless
JMOD M KON NON IARL T PGRID KOP ALSTOR KIP KAP NAP RAT	Arbitary variables used during numerical computation.		Dimensionless
$\frac{\delta L}{2C}$	Misalignment ratio		Dimensionless

CHAPTER 1
INTRODUCTION

1.1 The Hydrodynamic Gyro Bearing

Bearings of this type generate pressure gradients on the air film as a result of relative motion between the bearing surfaces, as opposed to hydrostatic bearings where the film pressure is supplied from an external source. The latter were used in gyroscope applications in the early 1940's but the need for an external air supply, from a compressor or vacuum line ejector, has now restricted their use to a small number of specialised applications.

The reasons for choosing a hydrodynamic gas bearing in preference to the more conventional ball bearing are given by the writer in reference 16. To achieve a high level of steady and dynamic performance, hydrodynamic gyro bearings must be manufactured to exceedingly close dimensional and geometric tolerances; normally in the order of a few micro-inches (1μ in. = 0·025 μm). They are invariably 'made-to-measure' for a particular gyro design, and it is found that the majority of contemporary gas lubricated gyroscopes are adaptations of existing ball bearing instruments. Here, the designer has had to balance the advantage of proven components and layout against the inevitable limitations that this approach imposes upon the design of the gas bearing.

1.2 Historical Background

Early experiments were carried out by Kingsbury (93) on an air lubricated bearing in 1897 and by 1913, Harrison (75) had published work on the hydrodynamic theory of air lubrication. Despite these achievements, self acting gas bearings remained little more than a laboratory curiosity for the next quarter of a century. While the basic manufacturing methods* were available, the corresponding disciplines of metrology and materials science required further development before their full potential could be exploited.

* Even the erosion of materials under ion-bombardment had been observed as long ago as 1891.

1.2 Historical Background (Continued)

In summer 1942, Judson Swearingen, a Texan Chemical Engineer and Professor of Chemical Engineering at the University of Texas, was asked to assist in the secret American programme to develop an atomic bomb. This programme had by that time reached a critical stage, due to the inability to produce suitable bearings and seals for the Oak Ridge diffusion plant (35). Perfectly leak-proof seals and bearings were required to operate continuously in a highly corrosive UF_6 atmosphere*, and in the absence of any additional lubricant.

Swearingen solved the problem in December 1942 by using grooved hydrodynamic seals and bearings and by New Years Day 1943, a hand lapped model was ready for testing. Much of the theoretical work was developed at Columbia University and many tens of thousands of electroless nickel plated bearings and seals were later manufactured by Allis-Chalmers at their Hawley plant.

Throughout this period, the theory and practice of self-acting bearings received uprecidented attention and most of the bearing designs known today were developed to an operational stage. However, this work was given a 'Secret' classification which prevented, and still prevents, its publication. Many years elapsed before the ideas generated during this relatively short period were re-invented, and this situation probably delayed the wider application of hydrodynamic bearings and seals by at least fifteen years.

Hydrodynamic gas bearings were first used in the U.S.A. for military inertial guidance gyros in the mid-1950's, and for similar applications in the U.K. towards the end of the decade. Design data on the spiral groove and herringbone groove bearings were first published openly by the United Kingdom Atomic Energy Authority (8) and this was followed by an enormous increase in published work that has continued to the present day, with commercial gyro applications being actively considered by the mid-1960's (See CHAPTER 2).

* Uranium Hexafluoride

1.3 Omissions In Prior Work

The published data referred to in Section 1.2 contains very few serious conflicts and the understanding of hydrodynamic bearings appears to have progressed in an orderly manner up to the present day, though much of it remains incomplete as far as the gyro bearing designer is concerned.

Available design charts (23)(3)(28)(20) refer to optimised bearing configurations which are not necessarily representative of practical designs. Those analyses dealing with grooved journals (19)(9)(91) consider the case of infinite grooving only and thus the effect of manufacturing defects cannot easily be gauged. Some work has been done which allows the infinite grooving solutions to be corrected for finite numbers of grooves (67)(31) but the problem of how to deal with a local manufacturing defect remains. Bearing performance under angular misalignment conditions has received little attention (3)(29) and few papers consider bearing power loss (1). Both these areas are of particular interest in gyro spin bearing applications.

Published work has tended to concentrate on the theoretical aspects of bearing development and very few papers contain experimental data; especially data from small gyro bearings. This has in turn made it difficult to fully verify much of the corresponding theoretical work (80). Previous papers (78) relating to operational life merely list the design features believed to be desirable, and include little explanation for their choice. Since, in gyro applications at least, the case for gas lubrication is based almost entirely upon improved life and reliability (4)(16), it is surprising that a broad-based survey of these features has not previously been attempted. Similarly, statistical information on bearing geometry and behaviour is practically unobtainable and only one publication (89) includes statistical data from actual gyro bearings.

The above references are discussed more fully in CHAPTER 2, but from the observations already made, it is now possible to outline the scope of the investigation presented here.

1.4 The Objectives Of This Investigation

The aims of the work fall into four categories, which may be summarised as follows:-

1.4.1 The development of a numerical programme for the solution of Reynold's equation around a grooved journal bearing containing finite numbers of pumping grooves. This programme shall be suitable for investigating steady-state performance under both radial and angular misalignment conditions, and shall also allow the effect of manufacturing defects to be studied at a later date. Information of this nature cannot readily be obtained from previously published design curves (CHAPTER 2, Section 2.1.).

1.4.2 The experimental measurement of bearing behaviour, particularly pressure distributions, power dissipation, contact characteristics and misalignment, when used as a gyroscope spin bearing. Many of these measurements have not previously been published and the notable lack of experimental data from scale bearings should make the results of particular value for assessing new analytic techniques. (CHAPTER 2, Section 2.2).

1.4 3 A broadly-based survey of factors influencing the operational life and reliability of a gas lubricated gyro bearing, with a view to establishing a set of design goals for an "ideal" bearing which would have a maximum operational life and reliability. Prior work has not considered these aspects of performance in a sufficiently comprehensive manner. (CHAPTER 2, Section 2.3 and 2.4).

1.4 4 A statistical investigation into the correlation between geometric tolerances, test performance and operational life on a representative sample of gyro bearings. A statistical survey of this nature has not previously been attempted. (CHAPTER 2, Section 2.2 and 2.4).

CHAPTER 2

INITIAL LITERATURE SURVEY

An initial literature survey was carried out in order to ascertain the scope of previously published work and its relevance to self-generating bearings of small dimensions. It soon became clear that little of this work dealt specifically with the problems associated with gyroscope bearings. In particular, the subject of operational life had received little direct attention, and the influence of material properties and manufacturing techniques had not been considered in an academic and formal manner. The analysis of both grooved and plain bearings was found to be extensively covered, but invariably assumed perfect geometry, infinite numbers of grooves and optimisation for either load capacity or stiffness; all features unknown to the practising gyro designer. The practical restraints and manufacturing limitations were rarely acknowledged and the resulting design charts unlikely to be appropriate to a fully developed commercial bearing, where hydrodynamic optimisation may not be the dominant design feature.

Since the commencement of this investigation, the overall situation regarding papers on manufacturing aspects has improved somewhat, and more recent publications now acknowledge the specific problems of hydrodynamic gyro bearings. Particularly notable in this respect are a number of papers recently published by the M.I.T. Draper Laboratories (57), (62), (77), (4), (58), (59), (87), where both theoretical and practical aspects of modern bearing manufacture are considered.

2.1 Gas Bearing Theory and Analysis

With regards to the theory of gyro bearings, and with the exception of a few simple bearings such as the plain slider, no exact analytic solutions are available for self-generating gas bearing configurations. Two methods of solution are known; approximate analytic and numerical. Occasionally these may be combined in a hybrid solution, where numerical methods are employed to solve the resulting analytic equations.

2.1 Gas Bearing Theory and Analysis (Continued)

Solutions for the plain ungrooved self-acting journal have been presented by Harrison (75), Raimondi (23), Ausman (3),(28) and (20),(24). Early restrictions of infinite length and incompressible lubricant have been removed and design charts are available (23) covering a wide range of eccentricity ratio and compressibility number. Harrison's original numerical method assumed isothermal expansion and compression around the circumference of the bearing but Ausman removed this restriction by introducing a heat transfer relation and developed a pertubation method valid for small eccentricities. Good agreement is obtained between these numerical and analytic solutions for eccentricity ratios of up to 0·4 if only three pertubation terms are used. While this approximate analytic method can be made more and more accurate by the inclusion of more terms from the series expansion (the theory assumes that the bearing pressure can be expressed in terms of a power series in ε), in practice the analytic expressions soon become very unwieldy. In a later paper (3), the same author notes that other values of the polytropic gas constant yield the most accurate values of load capacity and attitude angle. This treatment effectively uses the gas constant as an empirical correction constant, and though an ingeneous method of obtaining accurate design data, it does imply a basic limitation to the small pertubation method. Ausman suggests that for $\varepsilon > \frac{1}{2}$, alternative methods of analysis will be necessary to confirm the bearing design, but that pertubation analysis will lead to a conservative value for load capacity in these cases. (In the case of infinitly - long journals, Eirod (26), has introduced further refinements to the series method of solution by noting that the mass content of a continuous film around the bearing centre will be conserved under certain operating conditions, and presents a useful comparison of this improved solution with an 'exact' numerical solution).

2.1 Gas Bearing Theory and Analysis (Continued)

Though radial load capacity and attitude angle have been extensively investigated in published work, the equally important aspects of slew capacity (the resistance of the bearing to angular misalignment as the journal resists the gyroscopic torque of the rotor) have received little attention. Slew capacity is of considerable importance in a rate gyroscope, which may be called upon to measure or, more generally to withstand, high angular input rates, and historically, its attainment has proved to be a limiting feature of self-generating gas bearing design. Ausman (29) (3) includes the effect of angular misalignment upon a plain journal and the small pertubation approach is in fact the only analytic one available for predicting the slew characteristics of this type of bearing.

Analytic investigation of grooved bearings was first applied to thrust elements and Whipple (8) is credited with the first published analysis of such a bearing. Whipple's work is of interest because, despite the fact that end leakage from the grooves is neglected and the overall approach is comparatively simple, the analysis yielded acceptable design data for bearings operating in a low compressibility region. Whitley and Williams (30) later extended Whipple's original work to optimise the geometric parameters for incompressible operation. Optimised parameters for a compressible lubricant have been obtained by Wildman (109). Perhaps one of the most comprehensive treatments available is that by Muijderman (67) where the effects of varying radius are considered with an incompressible lubricant. The treatment is analytic, but is supported by some excellent analogue modelling to determine the effect of finite numbers of grooves and end leakages. Muijderman is unduly critical of Whipple's original paper on spiral groove thrust bearings, criticising its over simplified approach, but overlooking the fact that it was adequate enough for the manufacturing techniques of the day. The major limitation of Whipple's analysis is that it does not predict the degradation in load capacity for bearings operating at high local compressibility numbers. In most contemporary bearing designs, and especially in those intended for miniature gyro rotor support, the trend to higher average values

2.1 Gas Bearing Theory and Analysis (Continued)

of Λ is marked, and under load conditions, the local value of Λ will increase further as the local clearance is reduced. By increasing the number of grooves, it has been shown (67) (96) that the corresponding reduction in groove width can suppress this compressibility effect, but the manufacturing limitations of this approach are discussed in APPENDIX IV . Wildmann (110) has considered the effect of compressibility and, by assuming a sinusoidal gap shape, was able to obtain some approximate analytic results. Pan (96) later developed a universally valid compressible theory for narrow-groove bearings operating at any chosen value of compressibility number.

The analysis of spiral grooved thrust surfaces has more recently been extended to cover the case of a helically grooved journal bearing. Vohr and Chow (19) have obtained design curves for a fully grooved 360° journal bearing by numerical solution of the approximate analytic equations obtained from a pertubation expansion of film pressure in terms of ε . Based upon Ausman's small pertubation approach (22), the results are only valid for the small eccentricity condition, and in order to overcome local discontinuities in pressure gradient in the region of the groove boundaries, the solution assumed an infinite number of grooves. This assumption of infinite grooving is characteristic of all analytic investigations of grooved journal bearings and is necessary in order to reduce the amplitude of the saw-toothed pressure ripple over the land-groove region to negligible proportions, when a solution for the 'smoothed' or average circumferential pressure profile can be more readily obtained. Some experimental verification of this form of analysis has been obtained by Malanoski (17). For incompressible lubricants, Hirs (9) has produced a similar solution in the form of a series expansion in ε , but again, the restriction of low eccentricity operation still applies. Hamrock and Fleming (13) have developed a computer programme which uses the analytic equations presented by Vohr and Chow (19) to optimise numerically the groove parameters for maximum radial load capacity. For design purposes, the analysis of Castelli and Vohr (91) is perhaps the most

2.1 Gas Bearing Theory and Analysis (Continued)

useful, for it overcomes the restriction of low eccentricity ratio and also considers angular misalignment about the bearing axis. This is basically a numerical solution of the form of Reynold's equation developed in reference 19, and optimised groove parameters are presented for a partially grooved journal. The restriction of infinite grooving still applies but Pan (31) has since extended Muijderman's conclusions on the effect of finite numbers of thrust grooves to cover the case of limited partial grooving on a journal.

While the previous references outline the major areas of progress in self-generating bearing analysis, numerous other investigations have been carried out into particular aspects of bearing operation. Faddy (33) has applied the small pertubation analysis of Hirs (9) to pairs of helically grooved conical bearings with boundary conditions corresponding to vented and unvented configurations, and shown that vented bearings have a greater axial stiffness and a lower attitude angle than connected pairs. Reference 31, conveniently summarises a large number of design charts from various sources, and many of these are applicable to grooved thrust and journal bearings.

Analytic or quasi analytic solutions are particularly instructive because the qualitative effects of various governing parameters can be expressed explicitely, and optimised parameters readily obtained for any chosen condition of operation. Their major drawback lies in the difficulty of applying these forms of solution to 'imperfect' bearings, where manufacturing or cost limitations may dictate the geometry and tolerances. The accuracy of most current analytic solutions has been shown (17) to be moderately good under limited operating conditions, but to decrease significantly at high deflections and bearing numbers. For these reasons, analytic methods are best utilised during the early stages of design, and exact numerical solutions later devised to check or to modify the performance of the prototype production bearings.

2.1 Gas Bearing Theory and Analysis (Continued)

The search for relevant papers on numerical/iterative techniques proved to be less satisfactory. Though many numerical solutions of Reynold's equation have been accomplished, the authors appear to assume a detailed knowledge of the methods used, and invariably present the final results only. In particular, little numerical work appears to have been done upon bearings containing pumping grooves, and the treatment of groove and other boundaries is described in rather general terms. Those references dealing with the general solution of differential equations by numerical methods (85) (111) are of very limited use, and do not cover the rather specialised case of Reynold's equation for compressible films. The situation is unlikely to improve in the immediate future because in latter years, straight numerical/iterative techniques have become less fashionable in comparison with more mathematically orientated methods.

A useful review of available numerical methods for gas film analysis is presented by Castelli and Pirvics (97), Comparison is made between alternative methods of solution but detailed information on the application of individual techniques is not provided. More practical details, especially on the treatment of boundary conditions, are discussed by Castelli in reference 31, and this includes a brief description of the application of finite difference methods to groove and other boundaries. Gross (22) has also discussed the solution of Reynold's equation by approximate numerical methods, with particular reference to the finite-difference approach. This paper is particularly useful, including as it does a number of practical observations and recommendations compiled from other sources. Unfortunately, the solution of spiral or helically grooved surfaces is not considered directly, and the attendant problems of numerical instability are not fully discussed. Raimondi and Boyd (24) have presented a series of numerical solutions for plain journals and partial arc bearings under incompressible conditions, and have included quantitative investigations into the effects of mesh size and convergence criteria in general. Tabulated comparisons are made to show the effect of the parameters concerned upon iteration time, for mesh dimensions up to 60 x 16. These mesh dimensions appear

2.1 Gas Bearing Theory and Analysis (Continued)

to be considerably larger than those used by prior workers but the conclusions will not necessarily apply to compressible problems involving grooved surfaces. In comparing this work with more recent publications, it should be noted that the iterative times quoted by Raimondi and others are directly related to the computational hardware employed, and only relative increases or decreases in cycle time are therefore comparable. Pinkus (25) has solved the partial arc bearing for incompressible conditions using a mesh of some 200 points and Sternlicht (21) has solved the compressible form of Reynold's equation for a plain finite width journal. This latter solution employed mesh dimensions of 12 x 12 and a variable relaxation factor was used throughout the iterative period to optimise convergence of the pressure solution. Angular misalignment was not considered but comparison of radial load characteristics was made with results obtained from an experimental test rig. Raimondi (23) also presents a numerical finite difference solution for a finite length gas lubricated journal, using mesh dimensions up to 40 x 16. Numerical instabilities were encountered in the solution and some of the methods employed to stabilise the iteration are discussed. Once again, the condition of angular misalignment is omitted.

Gynanadoss and Osborne (20) have considered the numerical solution on a mathematical basis, with a view to accelerating the convergence of the form of solution adopted by Raimondi and Boyd (24). The work contributes little to available knowledge, since the proposed modification of successive over-relaxation (S.O.R.) was clearly known and used by workers already engaged in gas bearing analysis (21), (22), (23). Nevertheless, the advantages of S.O.R. over a systemised Liebmann iteration are convincingly demonstrated for a typical incompressible solution, and a fivefold improvement was noted by the authors. Castelli and Pirvacs (11) present a numerical solution for an axial-groove journal, applicable to both compressible and incompressible operation. The paper is important because it presents a new and general method for overcoming numerical stability problems and for

increasing the speed of convergence. In this method, the appropriate form of Reynold's equation is written and solved in terms of a new dependent variable, chosen for its constant or linear characteristics in the region of interest. The results obtained by applying this method to grid dimensions up to 24 x 5 are impressive, and the general method well suited to high ε or Λ conditions. Numerical techniques have also been adopted by Trevorrow (15) in investigating the effect of groove edge sharpness in Rayleigh step bearings under compressible flow. The technique is of interest because in order to simulate step degeneration, the step corners were replaced by two intersecting parabolic arcs. In this way, the clearance and first derivative of clearance were continuous over the step and Reynold's equation was immediately applicable across the entire solution field. Since the performance degradation compared with a rectangular step is found to be small, and the need for groove boundary conditions eliminated, the technique could well be applied to the full analysis of bearings containing small numbers of grooves, and where the parabolic boundaries could be adequately defined by an acceptable number of mesh points.

Direct iterative solutions are seen to have been applied to most plain bearing configurations, but far less frequently to spiral or helically grooved members. As for the analytic solutions previously discussed, little attention has been given to the angular misalignment case so frequently encountered in gyro bearing design, but reasonable agreement between corresponding numerical and analytic solutions has generally been obtained under radial loading conditions.

Clearly there remains to be presented a numerical solution which will be suitable for a practical bearing containing finite numbers of grooves and manufacturing defects, and a numerical method of this form is discussed in CHAPTER 4.

2.2 Experimental Procedures and Results

While much published experimental work relates to externally pressurised bearings, comparatively little is available from self-acting assemblies, especially from grooved bearings of small dimensions. The data is often incomplete and is recorded for nominal operating conditions only. This difficulty in obtaining experimental data has also been reported by previous workers (80). University research has tended to concentrate on externally pressurised configurations, where experimental verification is comparatively easy and experimental bearings can be fabricated by conventional manufacturing techniques. Experimental measurements quoted for large scale bearings (21) may not be representative of those on smaller bearings, where surface roughness, contamination and mean free path effects are all likely to influence the final pressure profile, especially under high deflection conditions. Even where results from smaller bearings are available they are generally limited by cost considerations to a small number of samples, and any form of statistical analysis is severely restricted on this account. Industrial research results from commercially unsuccessful bearings may not always be published and even where the bearing is produced in substantial quantities, accurate pressure and load measurements may only be available from a small number of early models.

Experimental techniques for very small bearings are more exacting than those suitable for larger models, and few papers describe these techniques in any worthwhile detail. References 31, and 84, outline experimental methods which have been used on gyro bearings and Fleming (1), Cunningham (2) and Malanoski (17) each describe experimental work on grooved journal bearings.

The problem of obtaining sufficient experimental data to confirm and compare the validity of the various analytic and numerical solutions available is highlighted by Pink (112), who is attempting to obtain previously unpublished performance data from industrial and other sources, and to then collate these results with previously published design data. Unfortunately, Pink appears to have overlooked the fact that experimental data from industrial sources

invariably relates to bearings which, for various practical and theoretical reasons, do not conform to the optimised configurations upon which the individual theoretical analyses are based. Consequently, any attempt at correlating such data will not be meaningful. Pink's work concerns externally pressurised bearings, but the same dilemma would also apply if a similar exercise were attempted for self-acting configurations.

Denhard (57) presents numerical test data from a number of gyro bearings in the form of axial and radial bearing stiffness. These compliance values are compared with the corresponding theoretical predictions and discrepancies of 3 : 1 are quoted. The only statistical performance data published for self-generating gyro bearings is that due to Butler (89). This data was recorded from fifty five H-form bearings during vibration testing, and includes graphs of clearance versus resonant frequency, compliance versus frequency and a resonant frequency histogram. Faddy and Trevorrow (80) include experimental stiffness measurements obtained from one typical H-form gyro bearing and Patterson (74), (84) presents experimental pressure profiles from both thrust and journal elements of an H-form gyro. Pressure measurements on misaligned bearings do not appear to have been published and experimental values of power dissipation under slew loads are also absent from those papers surveyed. Several references are made to the use of electrical continuity measurements to detect bearing contact (84), (31), (21) but detailed investigations of touch-down and take-off characteristics on self-acting bearings are not recorded.

The principles of electrical continuity measurements as a means of investigating contact between opposing bearing surfaces have been considered by a number of prior workers (54) (53) (52) (43). Cameron's voltage discharge technique (54) has been used to measure clearances across hydrodynamic oil films for many years and in 1961, Furey (53) proposed the concept of 'percent metallic contact' after experiments in which the voltage drop across a lubricating oil film was displayed on an oscilloscope. Film resistance was found to be either low or high and no intermediate state could be

2.2 Experimental Procedures and Results (Continued)

found. The period of time during which low resistance was recorded was expressed as a percentage of the total observation period, and was defined as 'percent metallic contact'. Some controversy has arisen over the interpretation of these measurements and it is clear that the basic premise of contact resistance being proportional to contact area may not hold in all circumstances. Wilson (52) has examined various phenomena relating to the contact resistance of boundary layers on metals and found that oxide and other films play a significant part in determining contact resistance. Both metal and oxide and work-hardened Beilby layers were found to demonstrate semi-conducting properties and to result in contact resistances very much higher than found in true metallic contact. Semi-conducting properties were still retained by the Beilby layers after annealing. The observed effects are most probably due to absorbed oxygen at the contact surface, in addition to the presence of an actual chemical oxide. Boundary lubricants were also found to produce the same effect as an oxide layer. From Wilson's work it may be concluded that true ohmic contact is unlikely to occur within a gas lubricated bearing and that precise measurement of contact area by this method will not be possible. From the observations of semi-conducting effects due to boundary lubricants it can also be deduced that contaminant films may also result in non-ohmic contact and this latter effect could be of particular significance when examining actual gyro bearings by this technique. Fiennes (43) has recently completed a survey of the electrical conductivity mechanisms across oil films and confirms that the mechanisms of conduction and breakdown are exceedingly complex, though he concludes that continuity measurements are still reasonably valid if precautions are taken to minimise both voltage and current.

2.3 Manufacturing Techniques

Information on the practical aspects of bearing manufacture is, at first sight, more readily available (31), (84), (68), (67), (92), (65), but much of this information is now out of date and does not deal with materials and manufacturing equipment that have become

2.3 Manufacturing Techniques (Continued)

available over the last four or five years. More recent publications (87), (72), (64) have outlined current progress in the manufacture of high precision bearings, but the practical aspects of bearing manufacture are now changing more rapidly than in previous years and must be constantly reviewed. This state of change is due to renewed commercial interest in self-acting bearings, where progress in manufacturing techniques and materials is primarily a function of financial investment. This is in contrast to the analytic aspects of bearing design, where progress is less closely related to the degree of financial investment.

Schiesser (87) describes in detail the manufacturing techniques for an opposed hemispherical ceramic/metal configuration. The great practical difficulties which this design presents are made very clear, but the techniques evolved to overcome them are equally impressive. Schiesser concludes that ion-machining methods are superior to all prior groove forming systems, and this opinion is supported here in later chapters. Hall (58) describes the application of beryllia to an H-form bearing assembly. The machining methods are only described in general terms and the health hazards associated with the use of beryllia are not considered. A unique feature of the construction is the use of the inner gimbal walls to form the non-rotating thrust surface, but it is considered here that the additional manufacturing complexity that this imposes could not be justified on a commercial bearing assembly. Nelson (59) considers the fabrication of a small H-form assembly from boron carbide and this paper clearly demonstrates that the severe manufacturing problems associated with boron carbide have been considered in depth at M.I T. Nelson highlights the importance of eliminating surface debris by the use of ion-machining and special polishing techniques, and this theme is continued by Taylor (64) who discusses ionic machining and coating methods in greater detail. Taylor quotes a machining rate of only 150 angstroms/minute and the production rate of three components/week compares very unfavourably with contemporary development (72). Unfortunately, this paper does not disclose which electrical parameters are used

2.3 Manufacturing Techniques (Continued)

to control the machining rate, and a true comparison cannot therefore be made with similar machining techniques. Patterson (65) presents a useful appraisal of manufacturing methods for spiral grooved thrust bearings and suggests the comparison of speed-pressure curves against manufacturing cost as a method of selection. This thesis will question these criteria (Section 7.3) and will show that greater emphasis should be placed upon the elimination of surface damage and debris. Faddy and Ellis (68) give a detailed account of the manufacture of conical gyro bearings. A major criticism of this paper is its conclusion that conical bearings present fewer and less severe manufacturing problems than alternative configurations; including the H-form. This is not found to be the case in practice (see CHAPTER 3 and reference 5).

Detailed criticism of previously published work on manufacturing methods is less appropriate than critical comment on the relative merits of the techniques themselves. This comment will be elaborated in APPENDIX IV where a review is presented of those manufacturing methods currently available. However, a general criticism of all published manufacturing information is that little, if any, consideration is given to the influence of the manufacturing techniques upon the life and performance of the bearing. The surface finish and texture obtainable from various machining methods has not been documented and the influence of surface texture on wear life has not been discussed in detail.

2.4 Operational Life and Reliability

Very few published papers could be found which dealt specifically with these aspects of bearing behaviour. Freeman (4) presents an excellent review of test methods and diagnostic information, concluding that early introduction of reliability testing can substantially improve bearing reliability in service. Though Freeman suggests that a feedback of reliability test data could be used to improve the basic design, he does not elaborate, and his paper leaves many of the reader's questions unanswered in this respect. Publicover (62) considers failure mechanisms in ceramic gyro bearings and describes the different types of equipment used

2.4 Operational Life and Reliability (Continued)

for contaminant and debris analysis. Again, the use of the data obtained for improving the bearing design or predicting reliability is not discussed. While indirect references to reliability and life are made in a number of prior publications (98), (79), (86), (92), the papers of Freeman and Publicover appear to be the only two which are directly relevant to the gyro designer, and as such, are considered to be of considerable importance.

From the above survey, it is clear that much work remains to be done on the production and improvement of operational life and reliability in gas lubricated gyro bearings, and this thesis will therefore consider these aspects in some depth (See CHAPTER 7).

CHAPTER 3

BEARING CONFIGURATION AND DESIGN

The basic bearing configuration was, of necessity, fixed prior to the start of these investigations. A detailed study (116) had shown that, contrary to some opinions (68), the H-form bearing offered the best combination of performance, ease of fabrication and convenience of measurement. The study showed that while both conical and hemispherical configurations require fewer close-tolerance dimensions than an H-form assembly, their working surfaces are appreciably more difficult to prepare and inspect. In this sense, the H-form bearing, with its comparatively simple cylindrical/planar geometry was found to be better suited to large scale commercial production.

Initial design was based upon existing design information (84), (30), (19), and upon previous experimental work by the writer (116). Several different experimental bearings were constructed and tested (Plates 1 and 2) and a number of alternative manufacturing techniques were also evaluated (72), (88), As a result of this experimental work, the design illustrated in Plate 3 emerged as the most suitable arrangement in practice, and the resulting bearing dimensions were verified by extensive laboratory testing on prototype instruments(APPENDIX I). In particular, the use of a grooved journal bearing was shown to be essential in order to ensure stable operation under applied vibration conditions. The selection of bearing materials is discussed in CHAPTER 7.

The H-form bearing (Fig. 1) consists of a fixed cylindrical journal shaft which is mounted between two flat inward pumping thrust plates. Helical pumping grooves are cut into each end of the shafts outer surface, and logarithmic spiral grooves into the inward facing thrust surfaces. These latter grooves extend inwards to the journal shaft. A cylindrical rotor fits around the journal shaft and between the fixed thrust plates; to forming the gas bearing clearance. The journal is approximately 0·9 inches (23 mm) in length and 0·4 inches (10 mm) in diameter and the outer diameter of each thrust plate is almost 0·8 inches (20 mm).

This wheel assembly is contained within a gimbal structure, which also supports the spin motor stator. The stator winding generates hysteresis torque on an alloy driving ring which is let into the outside of the rotor assembly.

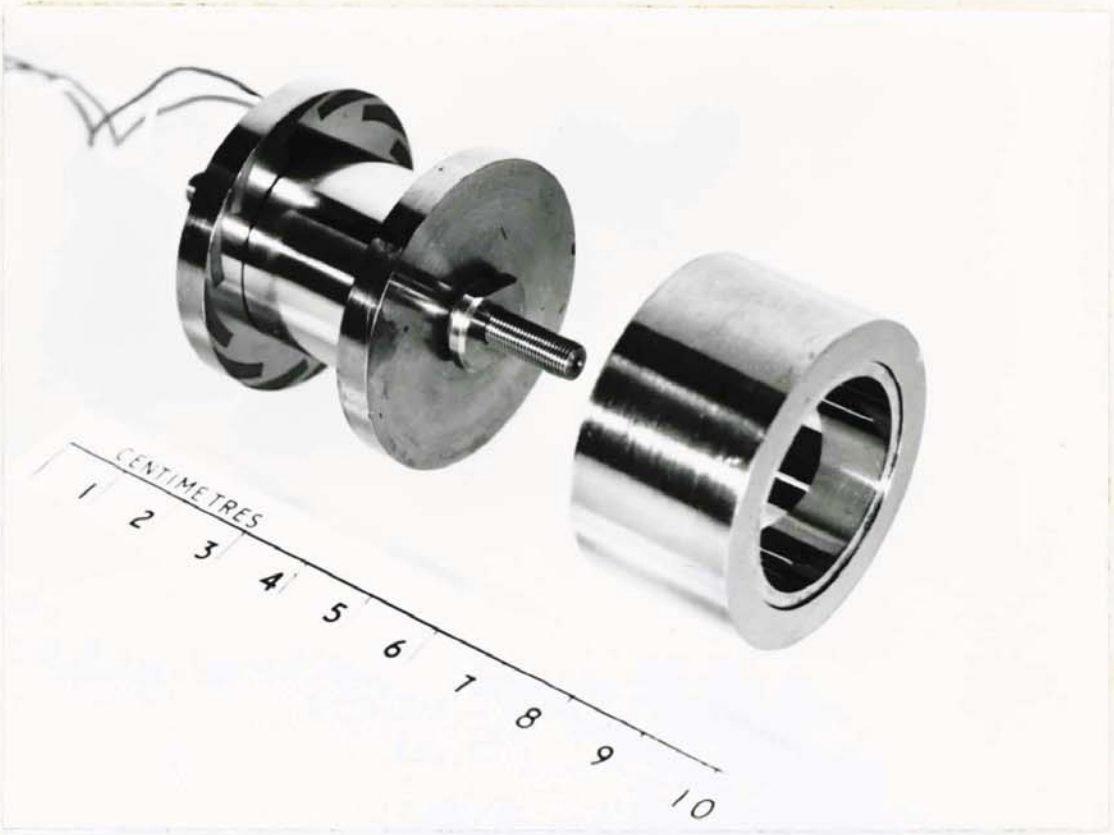

PLATE 1
EXPERIMENTAL HIGH INERTIA ROTOR AND BEARING ASSEMBLY.

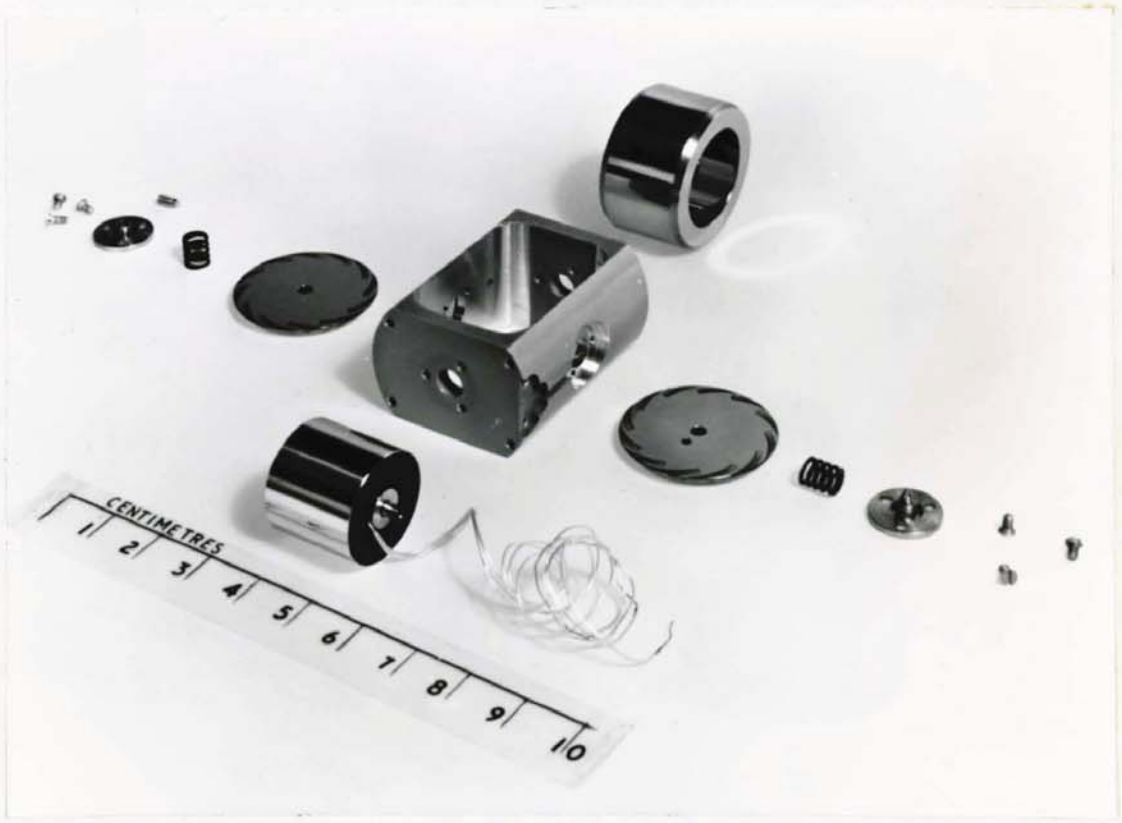

PLATE 2
EARLY EXPERIMENTAL BEARING AND GIMBAL ASSEMBLY.

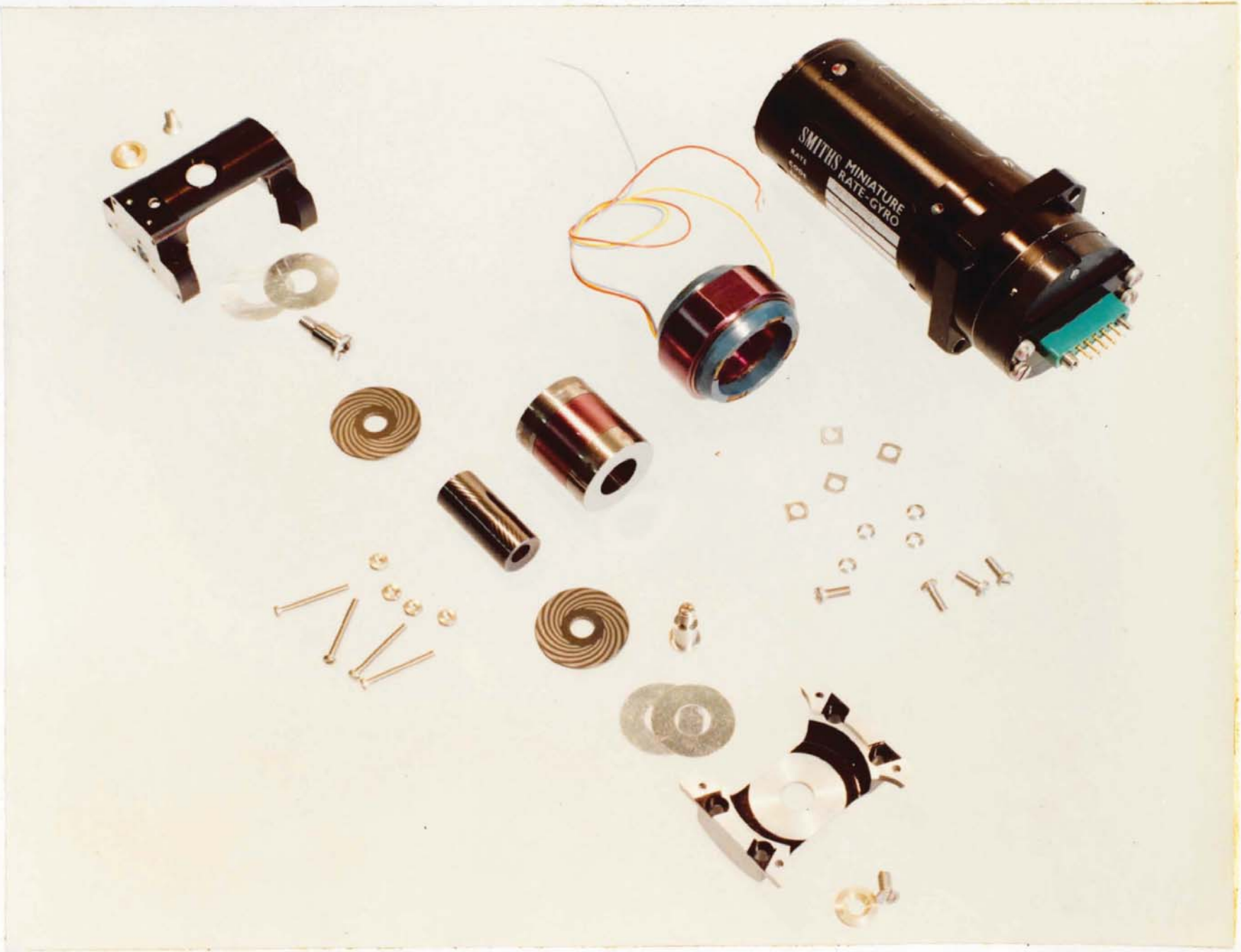

PLATE 3
EXPLODED VIEW
OF AN EXPERIMENTAL
GAS BEARING
GIMBAL UNIT,
PLUS A COMPLETED
RATE GYROSCOPE.

NOT TO SCALE

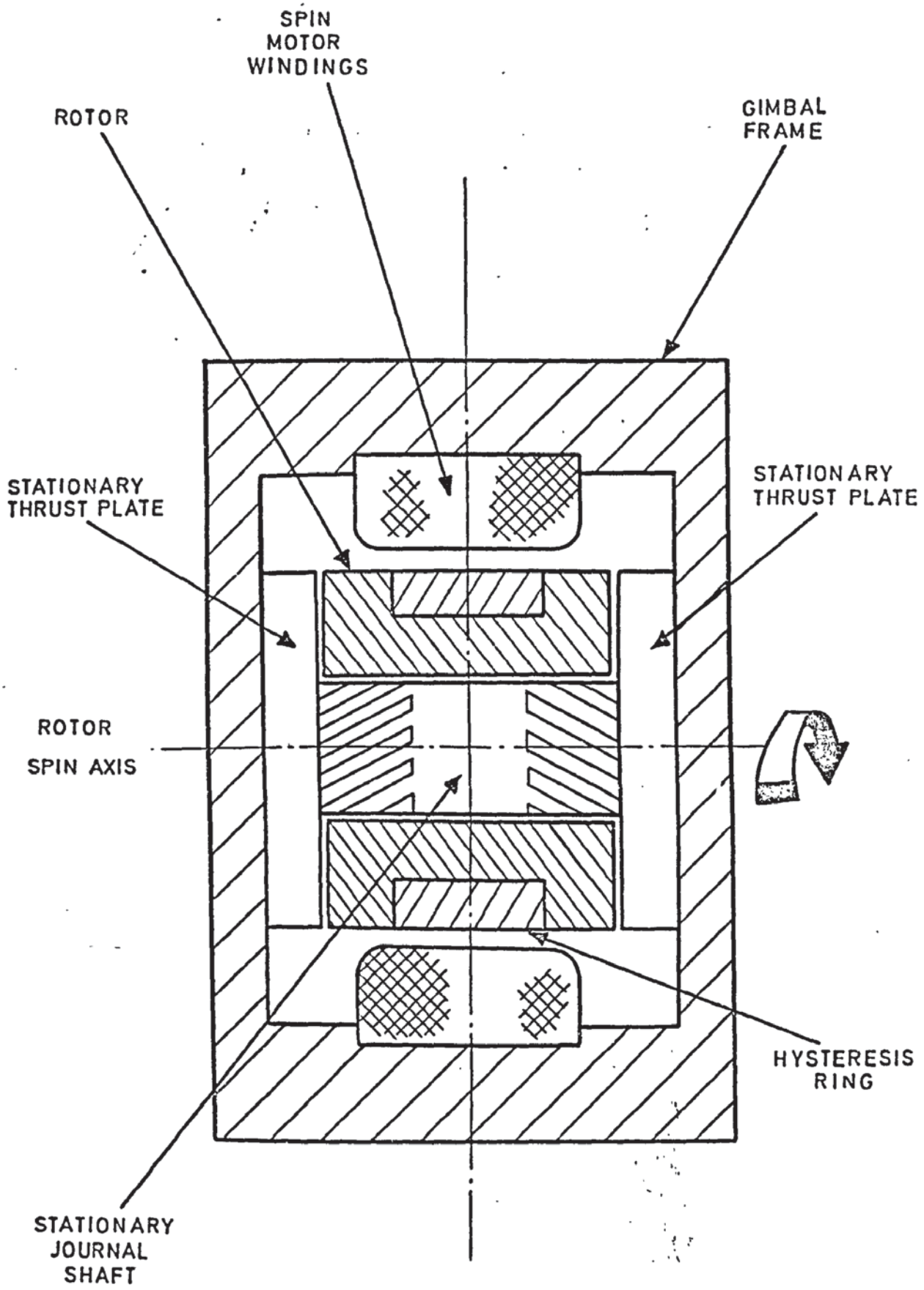

FIG. 1
SCHEMATIC LAYOUT
OF A TYPICAL H-FORM
GYRO BEARING

The following are not necessarily realistic production limits, but illustrate the order of geometric variations that can now be obtained from modern manufacturing techniques (See also Figures 63 to 68).

PARAMETER	VARIATION	
Roundness	3 micro inches	(0·07 micro metres)
Flatness	5 micro inches	(0·12 micro metres)
Straightness	7 micro inches	(0·17 micro metres)
Parallelism	7 micro inches	(0·17 micro metres)
Squareness	3 seconds of arc	-
Surface Finish	0·3 micro inches C.L.A.	(0·007 micro metres C.L.A.)
Groove Depth	±10 micro inches	(±0·24 micro metres)
Mean Radial or Axial Clearance	±5 micro inches	(±0·12 micro metres)

CHAPTER 4

THEORETICAL WORK

In this chapter, the theoretical work leading to a numerical solution of Reynold's equation around a grooved journal bearing is described.

4.1 Reynold's Equation

Reynold's equation is the accepted starting point for the analysis of most fluid lubricating films, and the particular form of equation used will depend very much upon the initial assumptions and simplifications that can be made in formulating the problem.

For the general case of compressible gas lubrication, Reynold's equation may be derived by considering the action of pressure and viscous forces on an incremental element of fluid within a bearing wedge. By resolving for dynamic equilibrium of the fluid element and imposing a condition for continuity of mass flow within the bearing, the following relation can be shown to hold:-

$$\frac{\partial}{\partial x}\left\{Ph^3 \frac{\partial P}{\partial x}\right\} + \frac{\partial}{\partial y}\left\{Ph^3 \frac{\partial P}{\partial y}\right\} = 6\mu U \frac{\partial}{\partial x}(Ph) \qquad \text{——— (1)}$$

The complete derivation of Reynold's equation from first principles is presented elsewhere (32) and will not be repeated here. It is, however, valuable to summarise the assumptions upon which equation 1 is based, and these are as follows:-

(a) Fluid velocities normal to the bearing surfaces will be very much smaller than velocities parallel to the surfaces, i.e. $w \ll u$ and v (See Figure 4).
Hence to a first approximation,

$$\frac{\partial P}{\partial z} = 0 \qquad \text{——— (2)}$$

(b) Velocities u and v will vary much more rapidly in the z - direction than in the x and y - directions, so that:-

$$\frac{\partial^2 u}{\partial x^2} << \frac{\partial^2 u}{\partial z^2} \quad \text{——— (3)} \qquad \frac{\partial^2 v}{\partial x^2} << \frac{\partial^2 v}{\partial z^2} \quad \text{——— (4)}$$

$$\frac{\partial^2 u}{\partial y^2} << \frac{\partial^2 u}{\partial z^2} \quad \text{——— (5)} \qquad \frac{\partial^2 v}{\partial y^2} << \frac{\partial^2 v}{\partial z^2} \quad \text{——— (6)}$$

(c) Elrod (26) has suggested that it is quite in order to consider only isothermal conditions within the lubricating film, with the consequent simplification of subsequent calculations. The assumption is considered valid because the gas film is thin and the thermal conductivity of the film boundary is usually high, allowing rapid dissipation of the heat generated by shearing action. This allows the following density relation to be assumed:-

$$\rho = \rho_o \frac{P}{P_o} \quad \text{——— (7)}$$

(d) The fluid viscosity is assumed to remain uniform throughout the film volume, though viscosity variations with the mean film temperature are important and must be taken into account in any numeric solutions.

(e) Unlike the liquid lubricant, cavitation or rupture of the gas film cannot occur and in practice, pressure variations around the bearing are small and do not enter the negative pressure region. This is especially true of grooved bearings, where pumping groove action normally maintains the entire fluid film above ambient pressure, regardless of any lateral excursions of the rotating member. This is analogous to the use of very high supply pressures to supress cavitation in externally pressurised oil bearings.

(f) Because the lubricating film is assumed to be very thin, inertia and gravity forces are neglected and viscous forces are presumed to be dominant.

Equation 1 is only valid if true laminar flow is maintained throughout the bearing clearance. True turbulent flow would not be expected until Reynold's numbers of around 2000 are reached, and gyro bearings of this type normally operate at $Re < 100$. (Actual values of Reynold's number for the test bearings are discussed in section 6.3). Similarly, the Taylor number, $\sqrt{Re}$, will normally be considerably smaller than the critical value, and the possibility of Taylor-vortices within the journal bearing can safely be ignored. Where pumping grooves or similar discontinuities are present in the bearing surface, laminar eddies may be generated under certain operating conditions and this will be discussed more fully in section 6.4. The assumption of true laminar flow is seen to be well justified for plain bearings, but may not always be true for grooved bearings. At high speeds, the formation of laminar eddies or lengthwise flow along the groove may impair the validity of equation 1 for grooved surfaces (See section 6.3 and 6.4).

(g) The fluid is assumed to be Newtonian.

(h) Slip flow between the fluid and the bearing surface is neglected.

Reynold's equation will in general be valid at any point within the lubricating film, subject to the application of any boundary conditions at both external boundaries and internal discontinuities. Though derived for a plain slider configuration, the equation is equally applicable to curved films of varying thickness where $C << R$. Even in its simplified form, it is a non-linear, second order partial differential equation in two dimensions with variable coefficients, and as such, no explicit solution for pressure is available for an H-form bearing. All known solutions of equation 1 are approximate, and where the bearing geometry or motion is complex, its evaluation by any analytic or numerical technique becomes a major undertaking.

4.2 Dimensionless Form of Reynold's Equation

It is both usual and convenient to convert the dimensional Reynold's equation into a dimensionless or normalised form before attempting a solution, In this way, confusion over units is avoided and the solution is obtained in its most general form; being equally applicable to all similar bearing configurations.

Normalisation is achieved by introducing the following relations, where each dimensional parameter is described as a dimensionless ratio of its current value to some chosen reference value.

$$\bar{P} = \frac{P}{P_a} \qquad (8) \qquad\qquad \bar{H} = \frac{h}{C} \qquad (9)$$

$$\bar{x} = \frac{x}{r} \qquad (10) \qquad\qquad \bar{y} = \frac{y}{L} \qquad (11)$$

$$\bar{G} = \frac{G}{C} \qquad (12) \qquad\qquad \beta = \frac{L}{D} \qquad (13)$$

$$\Lambda = \frac{6\mu U r}{P_a C^2} \qquad (14)$$

Substitution into equation 1 , together with some re-arranging of terms will eventually yield the dimensionless form of Reynold's equation for a journal bearing.

$$\frac{\partial}{\partial \bar{x}} \left\{ \bar{P}\, \bar{H}^3 \frac{\partial \bar{P}}{\partial \bar{x}} \right\} + \frac{1}{4\beta^2} \frac{\partial}{\partial \bar{y}} \left\{ \bar{P}\, \bar{H}^3 \frac{\partial \bar{P}}{\partial \bar{y}} \right\} = \Lambda \frac{\partial}{\partial \bar{x}} (\bar{P}\, \bar{H}) \qquad (15)$$

The dimensionless group Λ is the well known compressibility number, and indicates the degree to which bearing performance is degraded by compressibility of the lubricant.

Solution of equation 15 will now enable the pressure at any point in the bearing to be predicted. If this pressure distribution is known over the entire bearing surface, or at a sufficient number of points over the surface, then the load capacity, misalignment torque and other performance characteristics of the bearing can be assessed.

4.3 Numerical or Analytic Solution

The original intention was to adopt an analytic approach, but from the initial literature survey, it became clear that such a method would be lengthy, difficult, and a successful conclusion could not be guaranteed. Using numerical techniques however, the experience of others had shown that some worthwhile results could generally be obtained within a reasonable period of time, and it was concluded that a straight iterative finite-difference method would probably give the greatest chance of successful solution in the limited time available.

A further factor was the inherent flexibility of a straightforward numerical approach when considering finite numbers of pumping grooves, manufacturing defects and complex radial and angular loading conditions, where no exact analytic solutions exist. Consequently, a numerical programme of this form would be of more practical use to the subsequent manufacturing project, and may also be capable of further development at a later date to investigate new problems as they arise.

One major disadvantage of finite-difference methods has been that relatively large amounts of computer storage and process time are often necessary when elaborate bearing configurations are to be examined in detail. In recent years, the availability of large computing systems has improved considerably and this makes iterative methods worthy of re-appraisal; especially for industrially manufactured bearings where analitically optimised designs are not always feasible. In this latter respect, the cost of a computer solution has been quoted (97) as being proportional to the $-\frac{1}{2}$ power of the computer speed.

4.4 Boundary Conditions

4.4.1 Constant Pressure Boundaries

This form of boundary will arise at either end of a journal bearing where the bearing pressure falls to a constant value, corresponding to the ambient pressure Pa. Such a restraint is easily imposed on a numerical solution by specifying $\overline{P} = 1 \cdot 000$ along each boundary.

4.4.1 Constant Pressure Boundaries (Continued)

These boundary values remain unchanged throughout the iteration and are used to influence the solution of adjacent points.

4.4.2 Cyclic Boundary

In many bearing problems, it is convenient to carry out the computer solution over a rectangular field. For a 360° journal bearing, this involves cutting the bearing surface along a line parallel to the journal axis and then opening out the surface to form a rectangular plane. This domain now contains two additional boundaries; vis:- the cyclic boundary and the cyclic junction (Figure 2). In order to solve Reynold's equation for a point lying on this boundary by using finite difference techniques, it will later be shown that the pressure and clearance values of at least four surrounding points will need to be employed. One of these points will be found to be outside the rectangular domain. The restriction is lifted by noting that this point does not really lie outside the region of computation, but is identical to a corresponding point within the rectangular field and adjacent to the opposite boundary. Computation of points lying along the cyclic boundary is thus accomplished by using pressure and clearance information from corresponding points on the opposite side of the solution field as desired. Mathematically, this satisfies the condition that both $\bar{P}$ and $\bar{H}$ are continuous around the circumference of a plain 360° journal.

4.4.3 Cyclic Junction

The journal boundary opposite the cyclic boundary is defined as the Cyclic Junction. When the rectangular field is re-formed into a cylindrical shape, it can be seen that this boundary becomes coincident with the cyclic junction and the solution of Reynold's equation along its length becomes unnecessary. The solution for points adjacent to the cyclic junction will, however, involve values on the junction itself. Since these values must be equal to those for corresponding points along the cyclic boundary, the solution is arranged to select the appropriate cyclic boundary point as required

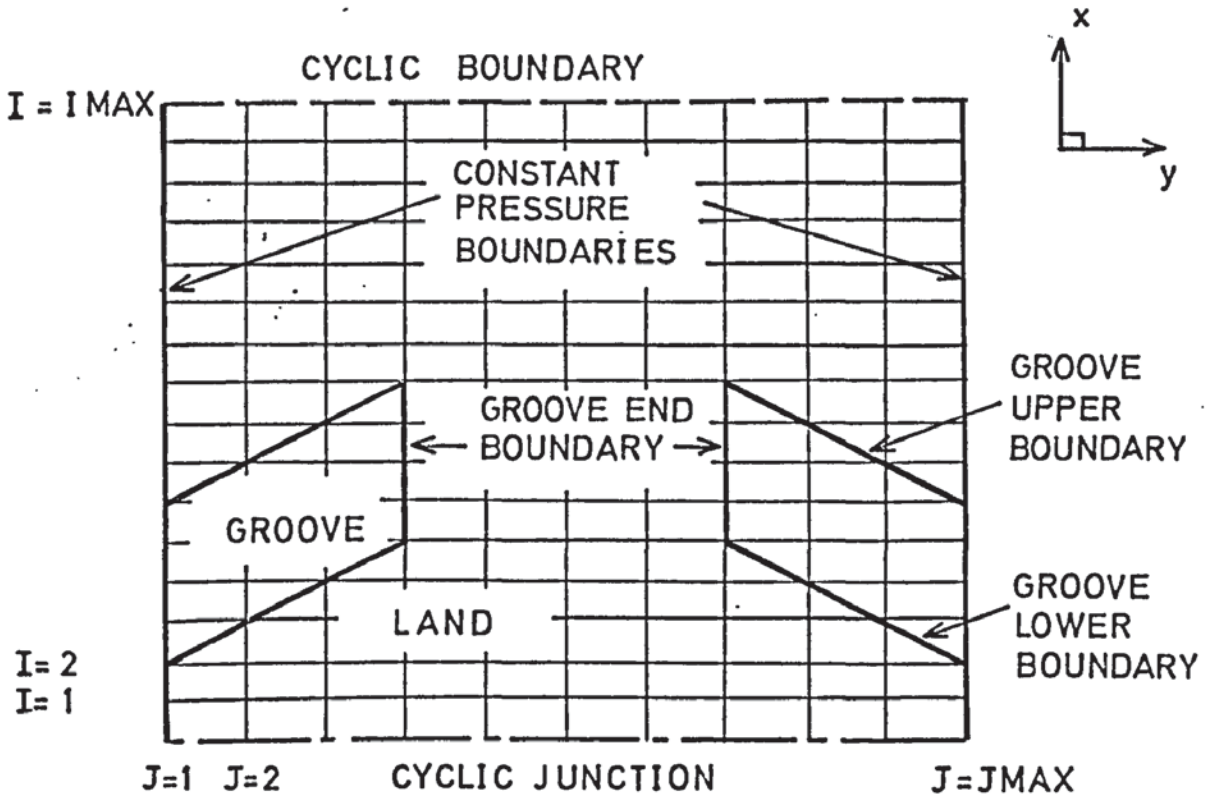

FIG. 2
SOLUTION FIELD FOR GROOVED JOURNAL.

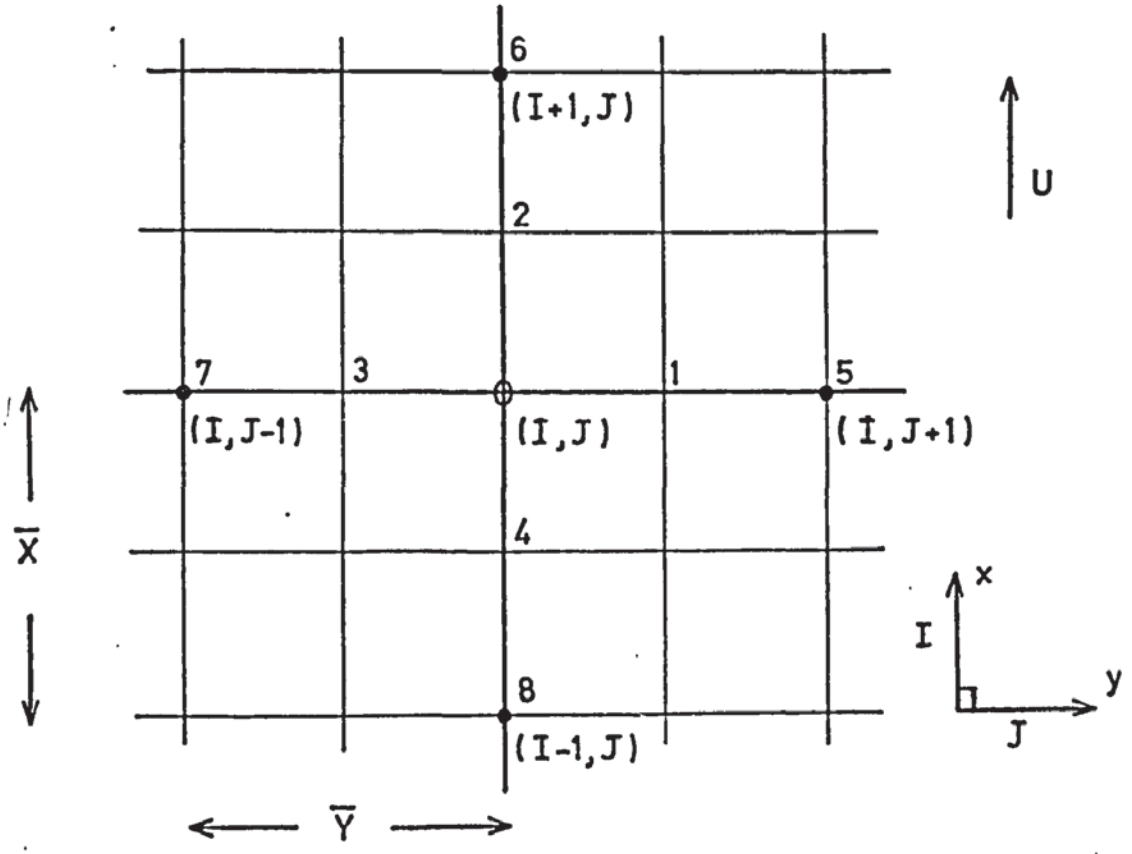

FIG. 3
MESH PATTERN AROUND A TYPICAL GRID POINT.

4.4.3 Cyclic Junction (Continued)

when solving for any point adjacent to the cyclic junction. This also satisfies the condition that $\overline{P}$ and $\overline{H}$ are continuous around the circumference.

4.4.4 Groove Boundaries

Where pumping grooves are cut into the bearing surface, the bearing clearance is no longer continuous and additional conditions must be specified for points lying on or adjacent to these boundaries. These conditions are as follows:-

(a) The pressure $\overline{P}$ must be continuous across the boundary. This is satisfied by using $\overline{P}$ or any of its powers as the dependent variable over the entire solution field, and by stating that -

$$\overline{P}_{(Land)} = \overline{P}_{(Groove)} \qquad (16)$$

at any point along the groove boundary.

(b) The pressure gradient normal to the boundary will be discontinuous across the boundary.

(c) The pressure gradients parallel to the boundary and on either side of it must approach a common limit at the boundary.

(d) Mass flow over the boundary must be continuous.

The nett mass flow over the land region in the x - direction will be due to both pressure and shear forces. Pressure flow is given by the relation,

$$\frac{\rho h^3}{12\mu} \frac{\partial P}{\partial x} \delta y \qquad (17)$$

while the shear flow component is found to be:-

$$\frac{\rho h U}{2} \delta y \qquad (18)$$

Similar expressions can be derived for land flow in the y - direction and a corresponding set may also be obtained for x and y flow components over the adjacent groove region. Because there is no velocity component in the y - direction, shear flow terms will be absent in this case. To satisfy the mass flow conditions, the total mass flow over the land region is now equated

4.4.3 Cyclic Junction (Continued)

when solving for any point adjacent to the cyclic junction. This also satisfies the condition that $\overline{P}$ and $\overline{H}$ are continuous around the circumference.

4.4.4 Groove Boundaries

Where pumping grooves are cut into the bearing surface, the bearing clearance is no longer continuous and additional conditions must be specified for points lying on or adjacent to these boundaries. These conditions are as follows:-

(a) The pressure $\overline{P}$ must be continuous across the boundary. This is satisfied by using $\overline{P}$ or any of its powers as the dependent variable over the entire solution field, and by stating that -

$$\overline{P}_{(Land)} = \overline{P}_{(Groove)} \qquad (16)$$

at any point along the groove boundary.

(b) The pressure gradient normal to the boundary will be discontinuous across the boundary.

(c) The pressure gradients parallel to the boundary and on either side of it must approach a common limit at the boundary.

(d) Mass flow over the boundary must be continuous.

The nett mass flow over the land region in the x - direction will be due to both pressure and shear forces. Pressure flow is given by the relation,

$$\frac{\rho h^3}{12\mu} \frac{\partial P}{\partial x} \delta y \qquad (17)$$

while the shear flow component is found to be:-

$$\frac{\rho h U}{2} \delta y \qquad (18)$$

Similar expressions can be derived for land flow in the y - direction and a corresponding set may also be obtained for x and y flow components over the adjacent groove region. Because there is no velocity component in the y - direction, shear flow terms will be absent in this case. To satisfy the mass flow conditions, the total mass flow over the land region is now equated

4.4.4 Groove Boundaries (Continued)

algebraically to the total mass flow over the groove region. After substituting from equation 16 and reducing to dimensionless form, the following relation is obtained.

$$\underset{[\text{LAND}]}{\frac{\bar{P}\,\bar{H}^3}{4\beta^2\Lambda}\frac{\partial\bar{P}}{\partial\bar{y}}\,\bar{X} + \bar{P}\,\bar{H}\,\bar{Y} + \frac{\bar{P}\,\bar{H}^3}{\Lambda}\frac{\partial\bar{P}}{\partial\bar{x}}\,\bar{Y}} = \underset{[\text{GROOVE}]}{\frac{\bar{P}\,\bar{H}^3}{4\beta^2\Lambda}\frac{\partial\bar{P}}{\partial\bar{y}}\,\bar{X} + \bar{P}\,\bar{H}\,\bar{Y} + \frac{\bar{P}\,\bar{H}^3}{\Lambda}\frac{\partial\bar{P}}{\partial\bar{x}}\,\bar{Y}} \qquad (19)$$

This equation expresses the condition that mass flow over the boundary is continuous and is valid along all groove boundaries. For the special case of the boundary at the inner end of any groove and where this boundary is parallel to the x - co-ordinate, some simplification is possible because only continuity of flow in the y - direction need be considered. The corresponding expression is found to be:-

$$\underset{[\text{LAND}]}{\bar{P}\,\bar{H}^3\frac{\partial\bar{P}}{\partial\bar{y}}} = \underset{[\text{GROOVE}]}{\bar{P}\,\bar{H}^3\frac{\partial\bar{P}}{\partial\bar{y}}} \qquad (20)$$

and is a particular form of equation 19 ; being valid across the end of any groove.

While the above relations allow solutions to be obtained for points which are actually on the groove boundary, special consideration is required for those land or groove points which are adjacent to this boundary. The condition that pressure is continuous across the boundary allows the normal form of Reynold's equation to be used in each case, but where this involves clearance values at the boundary, some care is required. For the solution of adjacent groove points, the clearance at the boundary is taken to be equal to that over the land region, while for the solution of adjacent land points, boundary clearances are taken to be equal to those over the groove region at that point.

4.5 The Form of Numerical Solution Employed

This takes the form of a systematic Gauss-Seidel iteration (85) over a predetermined number of points around the bearing surface. A rectangular mesh pattern is formed over the solution field and the numerical form of Reynold's equation is satisfied at the intersections of the lines forming this pattern. In practice, an initial guess is made for the pressure at each mesh point and a new value for this pressure derived by reference to the pressure and clearance values of surrounding points. This iteration proceeds row by row and as soon as an 'improved' value for the pressure is available at any point, this new value is used for subsequent iterations of surrounding points to increase the convergence rate. When a new value is obtained for all mesh points on the grid, the complete iterative cycle is repeated until the change in pressure between successive cycles is numerically less than EPSI, referred to as the residual, for all the mesh points concerned.

The optimum value of EPSI to ensure adequate accuracy and maximum economy of computer time was found to be 0·001. This value was chosen after some preliminary runs in which the corresponding values of $\overline{P}$ and $\overline{N}$ were compared for several values of EPSI. The value of EPSI was also found to be limited by numerical instability problems and this aspect is discussed further in Section 4.12.

In this way, the initial pressure distribution, whatever it might be, is progressively modified until both Reynold's equation and any additional boundary conditions are satisfied for the particular set of bearing parameters employed. Though Reynold's conditions are only satisfied at discrete points around the bearing surface, a sufficient number of these points will define any practical bearing configuration and allow a complete pressure profile to be established.

Rigorous proof of the validity of this form of solution is very difficult. Certain mathematical conditions relating to the solution matrix must be satisfied before a solution is possible (85), and only a passing reference is made to them in this work. It is sufficient to say that for all hydrodynamic lubrication problems investigated

4.5 The Form of Numerical Solution Employed

to date, the required conditions appear to hold, and have led to a wide range of successful solutions of Reynold's equation (11), (18), (20), (22), (23), (24), (25), (97), (31). These established precedents will therefore be used to justify the form of solution adopted in this thesis.

4.6 Selection of the Mesh Pattern

Any mesh pattern may, in principle, be used to segment the bearing surface, but in practice, a square pattern is more usual and much prior experience has been gained on meshes of this form by Allen (120) and others. Where plain bearings are considered, the selection of an appropriate mesh pattern usually presents few problems, but additional difficulties are involved on grooved bearings. The problem is to accommodate the various groove boundaries within the pattern in a simple and straightforward manner, and this can only be accomplished if the boundaries and mesh points intersect at each grid interval. Certainly methods are available for the treatment of boundaries which do not pass through individual mesh points, but these techniques are better suited to manual relaxation and are cumbersome and difficult to incorporate into a systematic computer solution.

The method adopted in the first place was to superimpose an inclined square mesh pattern over the rectangular journal field, with the angle of the mesh corresponding to the angle at which the pumping grooves are included to the journal axis. In this way, the mesh lines and groove boundaries may be arranged to be coincident, and the groove edges are defined by a series of mesh points. Computation around the groove boundaries is greatly simplified, but at the expense of accuracy along the constant pressure boundaries, which no longer coincide with the mesh. These outer boundaries may be approximated by a stepped boundary which follows the straight sides of each mesh square, but this approximation is quite inaccurate unless a very fine mesh pattern is employed and the steps blend into a reasonably straight line. Unlike external boundaries, the internal cyclic boundary need not be

4.6 Selection of the Mesh Pattern (Continued)

stepped because the longitudinal join on the clyindrical journal surface may take the form of a helix if desired. Quite apart from the introduction of stepped boundaries, this form of skewed mesh pattern requires a staggered co-ordinate system in order to direct the computer to the appropriate grid point. In view of these added complications, and the doubtful accuracy of the external boundary solution, this scheme was eventually abandoned in favour of a rectangular pattern, which will now be described.

A rectangular mesh pattern (Figure 2) was chosen as opposed to a more usual square mesh (Figure 3) with the mesh lines aligned with the outer boundaries of the rectangular journal field. The longest side of each mesh rectangle is parallel to the journal axis and the aspect ratio of the mesh rectangle chosen to allow a straight groove boundary to pass diagonally through the mesh. In this way, the groove side boundaries only intersect the pattern at the individual mesh points, and the mesh pattern may also be arranged to coincide exactly with both the constant pressure and cyclic boundaries. Provided the closed ends of the grooves are perpendicular to the shaft axis, the end boundaries of the grooves will also be defined by a series of mesh points. In practice, and in the absence of any conflicting requirements, the groove ends were machined in this manner in order to be fully compatible with the proposed computer solution.

With this arrangement, the groove angle can be varied by adjusting the aspect ratio of the mesh pattern and an aspect ratio of approximately 2 : 1 was found to correspond to the optimised (91) groove angle of 27° used on the test bearings. The mesh aspect ratio allows a finer resolution in the circumferential direction than in the axial direction. Since it was known from previous work (9) (19), (8) that the circumferential pressure profile was likely to follow a saw-tooth pattern over the groove/land regions, it seemed reasonable to suppose that a finer mesh pattern might be required in this direction.

4.6 Selection of the Mesh Pattern (Continued)

The use of a rectangular mesh of variable aspect ratio to accommodate helical journal grooves has not been described in previous literature.

For the bearing in question, groove width and land width are equal and a minimum of eight circumferential meshes were considered necessary to define each groove/land pair. With a fixed L/D ratio, the number of grooves will therefore dictate the total number of mesh points in the solution, and even for a modest number of grooves, a considerable number of mesh points will be involved. By way of an example, a 360° journal bearing containing a total of only twelve grooves (six at each end) requires 865 mesh points, of which 96 define the constant pressure boundaries, leaving Reynold's equation to be solved at the remaining 769 points.

On many bearing problems, the computational labour can often be reduced by the introduction of one or more symmetry boundaries across the bearing surface; iteration then being performed on only a portion of the original solution field. For a journal bearing with radial eccentricity only, the pressure distribution can be considered to be symmetric about a line bisecting the spin axis and parallel to the x - co-ordinate. More generally, a practical bearing will be operating under conditions of both radial and angular misalignment, and manufacturing defects are unlikely to be conveniently disposed about the bearing surface. In this case, symmetry will not be present, and iteration must be performed across the complete solution field. This procedure has been adopted here as it was considered important that the final computer programme should eventually be suitable for investigating these particular aspects of bearing operation.

4.7 Finite Difference Approximations

In order to carry out a computer solution at each mesh point, it is necessary to reduce the partial differential equations referred to in sections 4.2 and 4.4 to an approximate difference form. This is achieved by noting that the differential terms refer to the gradient and change in gradient of the pressure profile about the point

4.7 Finite Difference Approximations (Continued)

concerned. For a sufficiently fine mesh pattern, the gradient between adjacent points can be assumed to be approximately linear in both the x and y directions, and may thus be expressed in simple algebraic terms. A number of forms of finite difference approximation are available. They are well known, and are fully described in the appropriate references (22) (85) (31).

Simple substitution of the corresponding finite difference approximations into the dimensionless form of Reynold's equation (equation 15) will now reduce this rather complex partial differential equation into a relatively simple difference expression, which may then be re-arranged to give an expression for the pressure at any mesh point in terms of the pressures and clearances of the four surrounding points. Using the First Central Difference approximations,

$$\overline{P}_{(I,J)} = \frac{\Lambda\,\overline{P2}\,\overline{H2}}{\overline{X}} - \frac{\Lambda\,\overline{P4}\,\overline{H4}}{\overline{X}} - \frac{\overline{P2}\,\overline{P}_{(I+1,J)}\overline{H2}^{3}}{\overline{X}^{2}} - \frac{\overline{P4}\,\overline{P}_{(I-1,J)}\overline{H4}^{3}}{\overline{X}^{2}} - \frac{\overline{P1}\,\overline{P}_{(I,J+1)}\overline{H1}^{3}}{4\beta^{2}\overline{Y}^{2}} - \frac{\overline{P3}\,\overline{P}_{(I,J-1)}\overline{H3}^{3}}{4\beta^{2}\overline{Y}^{2}}$$

$$\div \left(- \frac{\overline{P2}\,\overline{H2}^{3}}{\overline{X}^{2}} - \frac{\overline{P4}\,\overline{H4}^{3}}{\overline{X}^{2}} - \frac{\overline{P1}\,\overline{H1}}{4\beta^{2}\overline{Y}^{2}} - \frac{\overline{P3}\,\overline{H3}^{3}}{4\beta^{2}\overline{Y}^{2}} \right) \qquad (21)$$

Where,

$$\overline{P1} = \frac{\overline{P}_{(I,J+1)} + \overline{P}_{(I,J)}}{2} \qquad (22)$$

$$\overline{P2} = \frac{\overline{P}_{(I+1,J)} + \overline{P}_{(I,J)}}{2} \qquad (23)$$

$$\overline{P3} = \frac{\overline{P}_{(I,J-1)} + \overline{P}_{(I,J)}}{2} \qquad (24)$$

$$\overline{P4} = \frac{\overline{P}_{(I-1,J)} + \overline{P}_{(I,J)}}{2} \qquad (25)$$

$$\overline{H1} = \frac{\overline{H}_{(I,J+1)} + \overline{H}_{(I,J)}}{2} \qquad (26)$$

$$\overline{H2} = \frac{\overline{H}_{(I+1,J)} + \overline{H}_{(I,J)}}{2} \qquad (27)$$

$$\overline{H3} = \frac{\overline{H}_{(I,J-1)} + \overline{H}_{(I,J)}}{2} \qquad (28)$$

$$\overline{H4} = \frac{\overline{H}_{(I-1,J)} + \overline{H}_{(I,J)}}{2} \qquad (29)$$

4.7 Finite Difference Approximations (Continued)

The mathematics involved in reaching this stage is long and tedious, but fairly straightforward. Expression 21 is valid for any point within either a land or groove region, providing the point does not lie on a boundary or discontinuity.

Similarly, equations 19 and 20 reduce to finite difference form, using the Second Forward and Backward Difference approximations. For the lower boundary of a groove at the left hand side of the solution field, i.e. over its leading edge with respect to the principal component of fluid motion, the pressure at any boundary point is given by the relation:-

$$\bar{P}_{(I,J)} = \frac{\bar{P}_{(I,J-1)}\overline{HG}^3}{8\beta^2\Lambda\bar{Y}^2} - \frac{\overline{P3}\,\overline{HG}^3}{2\beta^2\Lambda\bar{Y}^2} + \frac{\overline{HG}}{\bar{X}} + \frac{2\overline{P2}\,\overline{HG}^3}{\Lambda\bar{X}^2} - \frac{\bar{P}_{(I+1,J)}\overline{HG}^3}{2\Lambda\bar{X}^2} - \frac{\overline{P1}\,\bar{H}^3_{(I,J)}}{2\beta^2\Lambda\bar{Y}^2} + \frac{\bar{P}_{(I,J+1)}\bar{H}^3_{(I,J)}}{8\beta^2\Lambda\bar{Y}^2} - \frac{\bar{H}_{(I,J)}}{\bar{X}^2} + \frac{2\,\overline{P4}\,\bar{H}^3_{(I,J)}}{\Lambda\bar{X}^2} - \frac{\bar{P}_{(I-1,J)}\bar{H}^3_{(I,J)}}{2\Lambda\bar{X}^2}}{\frac{3\,\overline{HG}^3}{2\Lambda\bar{X}^2} - \frac{3\,\bar{H}^3_{(I,J)}}{8\beta^2\Lambda\bar{Y}^2} + \frac{3\,\bar{H}^3_{(I,J)}}{2\Lambda\bar{X}^2} - \frac{3\,\overline{HG}^3}{8\beta^2\Lambda\bar{Y}^2}} \qquad (30)$$

Where as before,

$$\overline{P1} = \frac{\bar{P}_{(I,J+1)} + \bar{P}_{(I,J)}}{2}$$

$$\overline{P2} = \frac{\bar{P}_{(I+1,J)} + \bar{P}_{(I,J)}}{2}$$

$$\overline{P3} = \frac{\bar{P}_{(I,J-1)} + \bar{P}_{(I,J)}}{2}$$

$$\overline{P4} = \frac{\bar{P}_{(I-1,J)} + \bar{P}_{(I,J)}}{2}$$

and $$\overline{HG} = \bar{H}_{(I,J)} + \bar{G} \qquad (31)$$

4.7 Finite Difference Approximations (Continued)

Equation 20 is treated in a similar manner.

From equation 20, pressure at a point on the inner end boundary of a left hand groove will be:-

$$\overline{P}_{(I,J)} = -\frac{2\,\overline{P3}\,\overline{HG}^3}{\overline{Y}} + \frac{\overline{P}_{(I,J-1)}\,\overline{HG}^3}{2\overline{Y}} - \frac{2\,\overline{P1}\,\overline{H}^3_{(I,J)}}{\overline{Y}} + \frac{\overline{P}_{(I,J+1)}\,\overline{H}^3_{(I,J)}}{2\overline{Y}} \Bigg/ \left(-\frac{3\,\overline{H}^3_{(I,J)}}{2\overline{Y}} - \frac{3\,\overline{HG}^3}{2\overline{Y}}\right) \quad (32)$$

An equation for the inner boundary of a right hand groove can also be derived.

For points on the cyclic junction, or adjacent to the cyclic boundary, slightly modified forms of equation 21 were used in order to satisfy the boundary conditions detailed in sections 4.2 and 4.3 respectively. In addition, it will be clear that a number of special points on the mesh may also exist. These points correspond to the intersection of upper or lower groove boundaries with either the cyclic junction or with points adjacent to the cyclic boundary. At these special points, two types of boundary condition must be satisfied. Only minor modifications to the groove boundary equations were necessary and a further eight finite difference equations were derived. No special points are generated at the intersection of the groove end and cyclic boundaries because equation 20 does not involve differential terms in the x - direction.

A grand total of seventeen finite difference expressions are thus developed and are ideally suited to solution on a high speed digital computer.

4.8 Identification of Mesh Points

The initial approach was to represent the geometric position of each internal and external boundary by means of an algebraic equation in terms of variables I and J. Details of each equation were to be stored in the programme and as each mesh point was selected, a logic network would decide which equations, if any, were satisfied by the (I, J) values for that point, and hence select the appropriate finite difference equation required for its solution. Progress was made, but it eventually became evident that the final computer programme would need to be exceedingly complicated, and would be wasteful of both storage and computational time. Some simplification was possible where a regular groove pattern could be represented by a family of linear equations, differing only in the constant term, but this method of identification was still considered unsuitable for the bearing configuration concerned.

The method finally chosen was to allocate a code number to each point on the mesh pattern. Each code number is stored as an integer within the programme data and selected in sequence at the same time as its corresponding mesh point. A logic network is then used to interrogate the code of each mesh point and so select the required finite difference equation. For a repeating groove pattern, only code numbers corresponding to one land/groove pair need be stored; the code information being repeated again and again as the solution proceeds around the bearing surface. For a rectangular journal field where the grooves are inclined to the bearing axis, the code array may contain information on more than one groove/land pair for points other than those close to the constant pressure boundaries.

A combination of eight code numbers and some preliminary logic was found to be sufficient to correctly identify which of the seventeen finite difference equations would be required for each point in the solution.

4.8 Identification of Mesh Points (Continued)

In addition, some special action was found to be necessary when evaluating land and groove points adjacent to the groove boundaries. These points invariably involved clearance values at the boundary itself. If, when performing iteration on a land point, the clearance at the boundary was taken to be equal to that over the land region, and a similar procedure was carried out for the corresponding groove point, a situation arose in which Reynold's equation could be satisfied before a pressure build-up due to groove pumping action could occur. In order to disturb this 'equilibrium', the boundary clearance was temporarily assumed to be equal to that over the land region when evaluating a groove point, and to be equal to that over the groove region when evaluating an adjoining land point. A further ten code values were introduced to identify these special points. No reference to this problem could be found in prior work.

4.9 Calculation of Bearing Clearance

In order to proceed with an iterative solution, it is first necessary to compute the dimensionless bearing clearance at each mesh point. For the general case of a grooved journal under both radial and angular misalignment, the overall clearance function will be somewhat involved. (See Figures 4 and 5).

The dimensionless clearance around a plain radially loaded journal is given by the well known relation:-

$$\overline{H} = (1 + \varepsilon \cos \theta') \qquad (33)$$

Where angular misalignment is also present, this relation can be shown to become:-

$$\overline{H} = 1 + \varepsilon \cos.\theta' + \frac{y\delta}{C}. \cos.(\theta' + \theta) \qquad (34)$$

In terms of the rectangular mesh pattern previously described, equation 34 may be shown to be equal to the following expression.

$$\overline{H} = 1 + \varepsilon. \cos.\left[(I-1)\ \overline{X}\right] + \frac{\delta}{C}\left[\frac{L}{2} - (J-1)\ L\ \overline{Y}\right]$$

$$\cos.\left[(I-1)\ \overline{X} + \theta\right] \qquad (35)$$

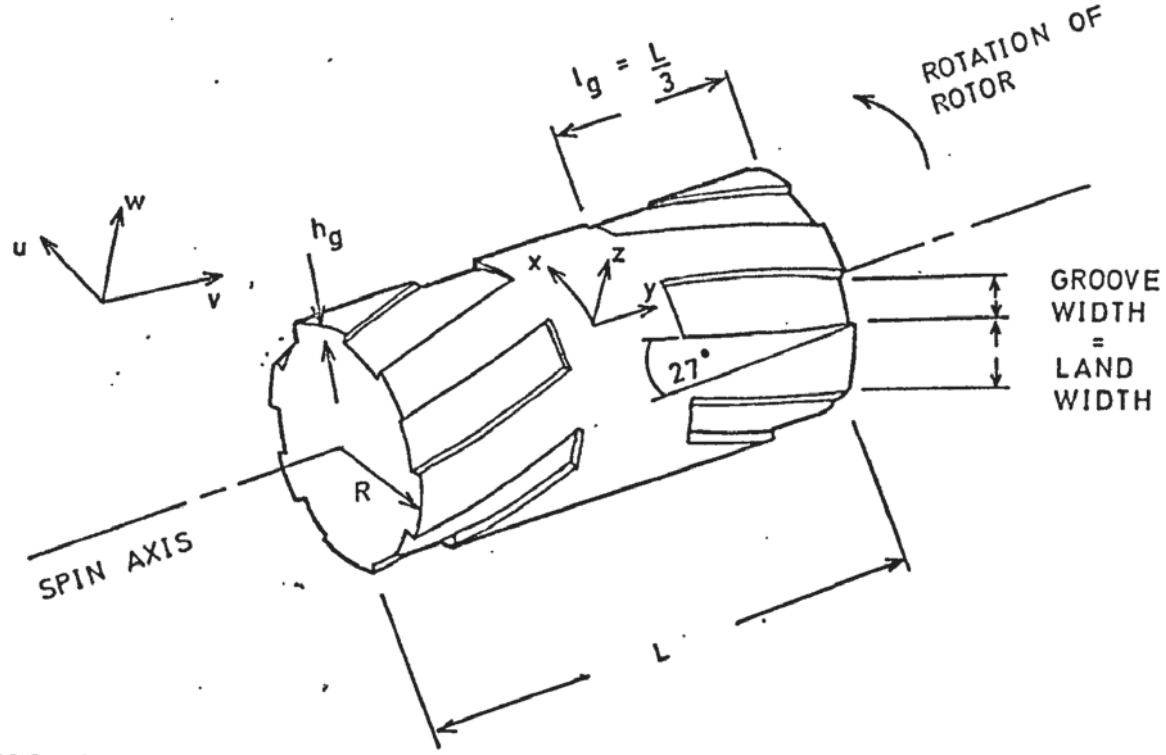

FIG. 4
HELICALLY GROOVED JOURNAL USED IN COMPUTER ANALYSIS.

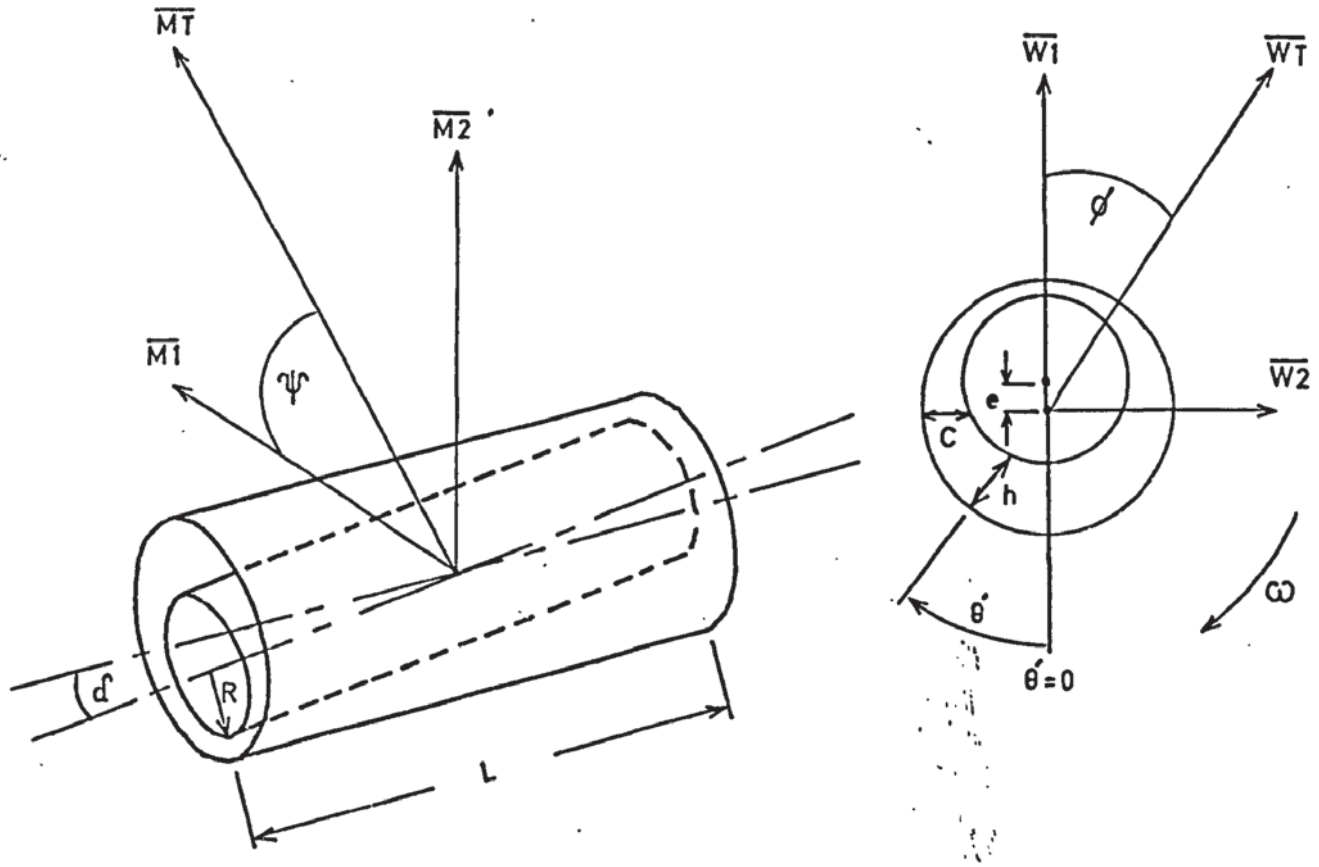

(ANGULAR MISALIGNMENT) (RADIAL MISALIGNMENT)

FIG. 5
ROTOR AND JOURNAL NOMENCLATURE.

4.9 Calculation of Bearing Clearance (Continued)

Using equation 35, the dimensionless radial clearance can be calculated for any mesh point within a plain journal, regardless of the relative displacement of the rotor and journal shaft. Where grooves are present, the code logic described in section 4.8 is first used to identify the groove regions, and the dimensionless groove depth $\overline{G}$ later added to the plain bearing clearance where appropriate, prior to each iteration.

4.10 Calculation of Load Capacities and Attitude Angles

Once an acceptable solution of Reynold's equation has been obtained at each mesh point and the radial and axial pressure profile has been established, it is a comparatively easy matter to extract the radial and angular load components from the solution. These components may then be resolved to yield the total radial load capacity or misalignment torque for the bearing geometry being considered, together with their associated attitude and deflection angles.

For the radial load condition, the force acting at any point within the bearing is equal to the pressure at that point multiplied by the incremental area over which this pressure acts. In general, this incremental force can be resolved into two components; one $\overline{W1}$, acting along the line of centres (or deflection) and the other, $\overline{W2}$ acting perpendicular to the rotor deflection. The total bearing force acting in each direction is then given by the integral of the pressure - area product over the entire bearing surface. In terms of the mesh pattern previously described, these summations may be written as:-

$$\overline{W1} = \sum_{I=1}^{I=IMAX} \sum_{J=1}^{J=JMAX} - \overline{P}\,(I,J).\ \mathrm{Cos.}(\theta').\ \overline{Y}\ \overline{X} \qquad (36)$$

$$\overline{W2} = \sum_{I=1}^{I=IMAX} \sum_{J=1}^{J=JMAX} \overline{P}\,(I,J).\ \mathrm{Sin.}(\theta').\ \overline{X}\ \overline{Y} \qquad (37)$$

4.10 Calculation of Load Capacities and Attitude Angles (Continued)

The total radial load may now be computed from the orthogonal load components.

$$\overline{WT} = \sqrt{(\overline{W1})^2 + (\overline{W2})^2} \qquad (38)$$

The angle at which this resultant radial force acts may be found from the following relation:-

$$\phi = \mathrm{Tan}^{-1} \frac{\overline{W1}}{\overline{W2}} \qquad (39)$$

A similar procedure may be used when considering the torque loads supported during angular misalignment, where the torque acting at any point within the bearing is equal to the incremental force at that point multiplied by its distance from the point about which the rotor is deflected. The two torque components, one acting about the axis of angular deflection and the other acting perpendicular to this axis, are obtained as before by summing these incremental torques over the entire bearing surface. For the mesh structure in question:-

$$\overline{M1} = \sum_{I=1}^{I=IMAX} \sum_{J=1}^{J=JMAX} -\overline{P}_{(I,J)} . \overline{X}.\overline{Y}.\overline{y}. \cos(\theta' + \theta) \qquad (40)$$

$$\overline{M2} = \sum_{I=1}^{I=IMAX} \sum_{J=1}^{J=JMAX} \overline{P}_{(I,J)} . \overline{X}.\overline{Y}.\overline{y}. \sin(\theta' + \theta) \qquad (41)$$

The additional angular term θ is required to make the expressions perfectly general for the case of combined radial and angular misalignment. As for the radial load components, the total torque moment and its axis of action may then be found.

$$\overline{MT} = \sqrt{(\overline{M1})^2 + (\overline{M2})^2} \qquad (42)$$

$$\psi = \mathrm{Tan}^{-1} \frac{\overline{M1}}{\overline{M2}} \qquad (43)$$

4.10 Calculation of Load Capacities and Attitude Angles (Continued)

Expressions 36 to 43 are readily incorporated into a digital computer programme, and since they are evaluated from dimensionless quantities, it follows that the final load and torque values obtained must also be dimensionless. By using the normalising expressions 8, 9, 10, 11, 12, 13 and 14, the relation between the dimensional and dimensionless values of radial load and torque can be shown to be as follows:-

$$W_L = \overline{WT}.\ P_a.\ R.\ L \qquad (44)$$

$$M_L = \overline{MT}.\ P_a.\ R.\ L^2 \qquad (45)$$

The actual torque and load figures can therefore be obtained if desired.

4.11 The Numerical Programme

Numerical solution of the finite difference mesh was initially carried out on an ICL 1905E digital computer at the University of Aston. The total core size of this computer is 96K words and the programme was developed in Fortran IV. The structure of this programme is summarised in Figure 6 and is presented in full in Appendix $\overline{V}$.

Programme operation commences with the input and storage of all preliminary data. Two-dimensional arrays of dimensions IMAX x JMAX, are established for the storage of pressure and clearance values, together with a single dimensional array K, used for storage of the code numbers identifying each mesh point. From the initial geometric information, the dimensionless clearance $\overline{H}(I, J)$ corresponding to each mesh point is computed from equation 35 and stored in the appropriate array. The initial pressure distribution, usually taken as $\overline{P}(I, J)=1{\cdot}000$ at all mesh points throughout the solution field, is also stored in the corresponding array, and the compressibility number Λ is likewise evaluated and retained. As the pressure array is sequentially scanned in row order along the journal axis, a code value corresponding to each mesh point is drawn from the K (Q) array. A logic network then investigates the integers I, J and K, and selects a finite difference equation appropriate to each point.

FIG. 6
SIMPLIFIED FLOW CHART FOR THE NUMERICAL COMPUTER PROGRAMME

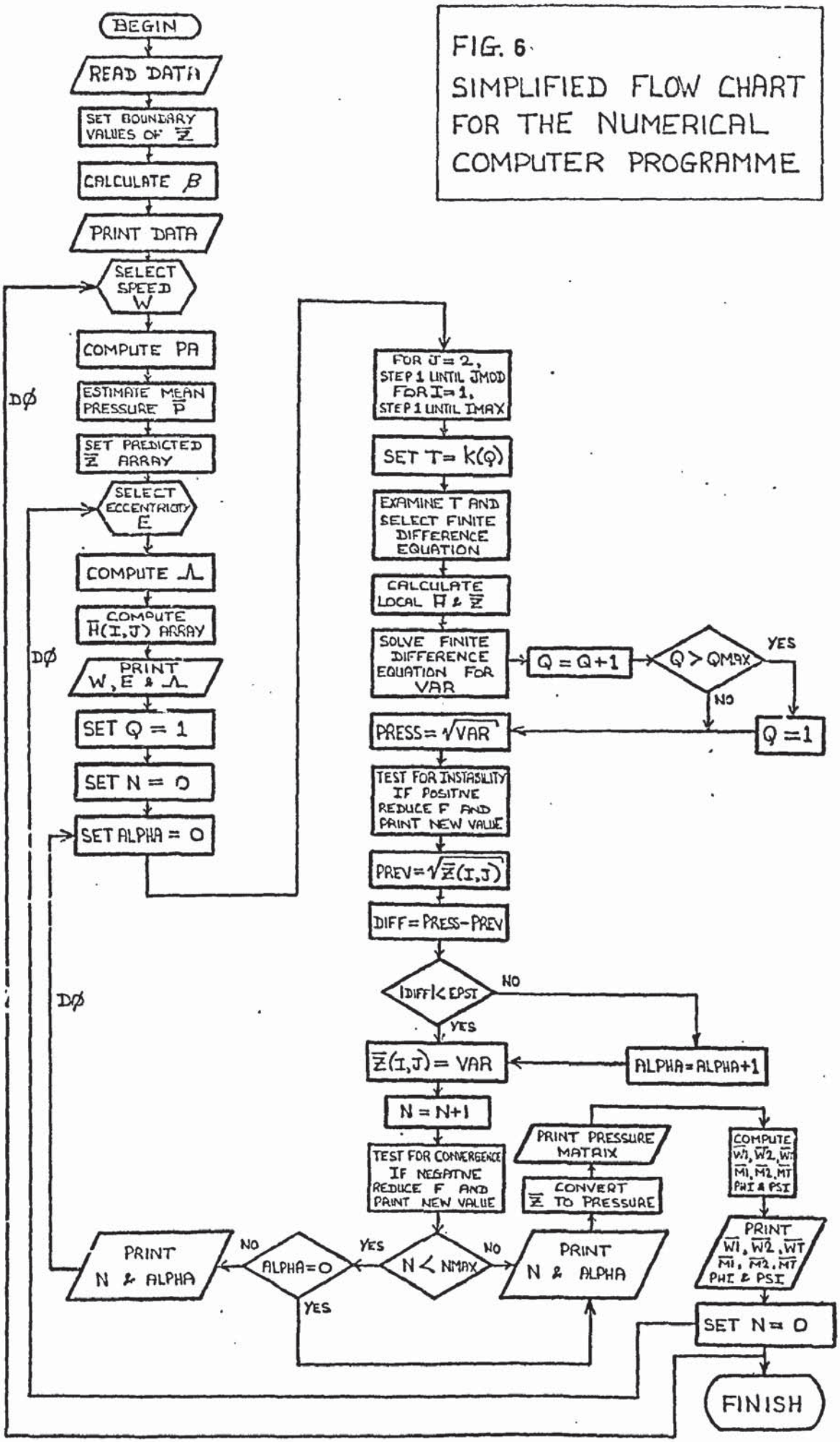

4.11 The Numerical Programme (Continued)

Using the appropriate finite difference equation and the stored values of $\bar{H}$ and $\bar{P}$ at surrounding points, a new value for the pressure at each grid point, PRESS, is obtained. Prior to evaluating the finite difference expression, it was found convenient to compute the intermediate pressure and clearance values $\overline{P1}$, $\overline{P2}$, $\overline{P3}$, $\overline{P4}$ and $\overline{H1}$, $\overline{H2}$, $\overline{H3}$, $\overline{H4}$ using separate subroutines, and to add the dimensionless groove depth $\bar{G}$ to obtain $\overline{HG}$ where required. Once a new value of pressure has been obtained for each mesh point, it is at once compared with the previous value, and the numerical difference, DIFF, then compared with the allowable residual EPSI. Where DIFF > EPSI, a counting integer ALPHA is increased by unity and the new pressure value transferred to the $\bar{P}$ array where it replaces the corresponding old value. At the same time, the code array integer Q is either increased by unity, or re-set to unity if its value exceeds QMAX. When new values have been obtained for each mesh point, the integer N is increased by unity. ALPHA is set to zero, and the iterative cycle repeated until either N exceeds NMAX or ALPHA equals zero. If ALPHA is equal to zero, the pressure values stored in the $\bar{P}$ array will hopefully satisfy Reynold's equation, and this pressure distribution may now be printed out if required.

Once a pressure distribution has been obtained where successive iterations do not change each mesh pressure by more than a given increment (EPSI), the appropriate radial load and torque components are computed by simple numerical integration of the $\bar{P}$ array. The programme then outputs both the components themselves and the total load and torque values as required, together with their corresponding attitude angles. Looping arrangements are incorporated for sequentially adjusting the eccentricity, angular misalignment and rotor speed after each solution is obtained, In this way, a set of solutions may be obtained over a range Λ, E and DEL values. The compressibility number is re-calculated after each change in rotational speed and the $\bar{H}$ array must also be revised after either DEL or E have been changed.

4.12 The Treatment of Numerical Instability and Associated Problems

Numerical instability problems previously encountered in solutions of this form (11) (31) (97), were well known both from the initial literature survey and also from discussions with contemporary workers in this field. Despite these fore warnings, the extent and magnitude of the instability problems eventually encountered were seriously underestimated, and many of the methods traditionally employed to stabilise numerical solutions were found to be either impracticable or ineffective on this particular bearing configuration.

Numerical instability of the computer solution can occur for a number of reasons. In general terms, it appears to be associated with the presence of rapidly changing pressure gradients at any point in the solution field. Such rapidly changing gradients are, in practice, encountered within bearings operating at high eccentricity ratios, or where the lubricating film is of a sharply convergent - divergent section. Stability is also influenced by the local compressibility number (Λ calculated using the local value of C) and even when comparatively stable variations of Reynold's equation are solved (97), convergence is reported to cease at local Λ values approaching 50. In particular, the presence of internal clearance discontinuities such as grooves will result in rapid fluctuations of pressure across the groove-land region, especially where small numbers of grooves are employed, and the grooved bearing becomes a major source of computational instability in comparison with the equivalent plain bearing. To a certain extent, the accuracy of the first-guess pressure distribution will also influence the convergence of the solution, Initial distribution should be as close to the anticipated pressure profile as possible if numerical problems are to be minimised. In each case, the local change in pressure is too rapid for the discretionalised iteration to follow, and Reynold's equation cannot be satisfied at the mesh points concerned. This condition will in turn be reflected across the entire solution field.

4.12 The Treatment of Numerical Instability and Associated Problems (Continued)

Two distinct forms of instability were encountered in the solution. The first was characterised by violent oscillations of the numerical pressure value at each mesh point with each successive pass of the iteration. These oscillations rapidly increased in amplitude and 'negative pressure' values were eventually generated at many points. If allowed to proceed unchecked, the increasing numerical values eventually exceed the computer storage capacity and the programme is automatically terminated. In an extreme case, this can take place before the first full iteration has been completed. The appearance of this form of instability is well documented (31), diagnosis of the phenomenon is not difficult and there is little danger of an incorrect solution being mistaken for a correct one.

The second form of instability is more insidious, and took the form of a slow divergence of the solution beyond the point at which convergence should have occurred. Because the rate of divergence can eventually become very slow, it is possible for a point to be reached where the numerical value of the allowable residual EPSI exceeds that of the difference between successive iterations DIFF at each point on the solution. If this occurs, an apparently normal exit is made from the iterative loop, and the pressure profile and subsequent load calculations are presented as if a full solution to Reynold's equation had been obtained. Unless the predicted pressure profile can be seen to be in obvious error, this second form of instability may be highly misleading, and for this reason, its presence is not immediately detected.

Slow divergence was not observed when solving Reynold's equation around a plain bearing, but the introduction of grooves appeared to increase the chances of an instability of this type. It was noted that the value at which a slowly divergent solution finally 'stabilised' depended upon the numerical value of the under or over-relaxation factor F employed, with higher pressure values being generated as this parameter was increased. Direct dependence of the pressure solution upon the speed of iteration may therefore be used as an indication that this form of instability is present.

4.12 The Treatment of Numerical Instability and Associated Problems (Continued)

This second form of instability is not documented in prior literature and may not have been recognised as such in previous solutions.

A number of methods are available for treating numerical instability, but few are entirely free from disadvantage. Some of these techniques, and their suitability for use on grooved bearing solutions, will now be considered, with particular reference to the development work carried out on the programme.

(a) Under-Relaxation

By reducing the relaxation factor F below unity, the speed of iteration is slowed down and instability can often be suppressed, Under-relaxation has the major disadvantage that it increases the number of complete iterative cycles that must be performed before an acceptable solution is achieved. A stable solution can sometimes be achieved by this method, but only at the expense of computational time, which increases dramatically as F is reduced. When this technique was applied to an oscillatory instability on a plain journal bearing, a successful solution could readily be obtained, but on an equivalent grooved journal, the result was unsatisfactory. While the first type of instability could be removed, a slowly divergent solution remained which did not respond to further reductions in relaxation factor. Castelli and Pirvics (11) have also noted the ineffectiveness of under-relaxation on the stability of an axial groove bearing solution.

In the final programme, provision was made for F to be reduced progressively during the course of the solution if either instability or non-convergence were detected.

4.12 (a) Under-Relaxation (Continued)

An additional disadvantage of reducing the pace of the iterative process is that the rate of convergence eventually becomes very small as the true solution is approached. Under certain conditions, the change in grid pressure will become smaller than that allowed by the parameter EPSI well before the desired solution has been reached, and the iterative procedure is then prematurely halted, leaving an excessive error in the computed pressure profile. Under these circumstances, the computed pressure will be an under-estimate of the true solution. An error of this form was observed where low values of W and ε coincided with a small value of F, and in an extreme case, no solution was obtained at all.

(b) Influence of the Mesh Aspect Ratio

The ratio $\frac{\bar{X}}{\bar{Y}}$ is known (22) (18) to be critical to the stability of some numerical solutions. Increasing this ratio appears to help stability. For a cylindrical journal, this will involve reducing the number of mesh points around the circumference in comparison with those along the bearing axis. This arrangement is a poor one for a journal, especially if it contains pumping grooves, where a finer resolution is required in the circumferential direction in order to follow the fluctuating pressure profile. In addition to the question of resolution, the form of solution adopted here relies upon a fixed value of aspect ratio (where $\frac{\bar{X}}{\bar{Y}} < 1$) in order to accommodate the groove boundaries, and this effectively precludes the use of this feature as a means of adjusting stability. On the contrary, the aspect ratio dictated by the groove pattern is a distinct disadvantage to computational stability, and almost certainly exacerbated the numerical problems experienced.

A similar problem arises in the numerical solution of a grooved thrust bearing, where for stability at high bearing numbers, more mesh points are needed in the radial direction (18).

4.12 The Treatment of Numerical Instability and Associated Problems (Continued)

(c) Overall Mesh Dimensions

The stability of some numerical solutions appears to be enhanced as the total number of mesh points is increased and the mesh pattern becomes finer. For a given pressure gradient, a finer mesh will reduce the pressure increment between successive mesh points and the solution is then better able to follow the changing pressure profile. This is especially true where grooved bearings are concerned.

Unfortunately, the numerical advantages gained in going to a finer mesh pattern may be outweighed by the increase in computational time required to obtain a satisfactory solution. This time will increase directly with the total number of extra mesh points to be computed, and will also increase directly with the number of additional iterations to be performed. The number of iterations can be shown to be directly proportional to the number of mesh points on the longest side of the solution field (31). Where IMAX>JMAX, the time required to converge to a steady-state solution will therefore be proportional to $(IMAX)^2$ JMAX. For a bearing containing a reasonable number of grooves, the total number of mesh points is likely to be quite large to begin with, and to increase the number further may lead in some cases to problems of computer storage capacity.

On a plain bearing, increasing the number of grid points will generally decrease the stability of the solution (31), especially at high eccentricity and misalignment ratios.

(d) Progressive Solutions

Where a set of solutions are required covering various operating conditions for the bearing in question, it is possible to arrange the computer sequence such that the computed pressure is retained after each solution, and may therefore be used as a starting point for the next set of iterations. By commencing with solutions involving low

4.12 (d) Progressive Solutions (Continued)

compressibility numbers and deflections, the more difficult cases of high compressibility number and large deflection can be approached gradually with the benefit of a better 'first-guess' solution than might otherwise have been available.

This simple and rather obvious approach will clearly result in considerable economy of computational time, and will offset some of the disadvantages of the stabilising methods previously described. It has been employed by previous workers (11) and is also used here.

(e) Advancing to a Finer Mesh

It was originally proposed to complete a preliminary solution using a reasonably coarse pattern, and then to advance to an increasingly finer mesh using the previous solution as a starting point for each successive mesh solution. In this way, it was hoped that a highly accurate solution could be arrived at, without the attendent problems of instability and lengthy computational time. This technique had previously been employed in manual relaxation problems (85), but it soon became clear that it would be of doubtful value on a grooved bearing of this form. The view is reinforced by work of Castelli and Pirvics (11), who noted small irregularities in the pressure distribution around axial groove bearings when solving differing bearing conditions with various overall mesh dimensions. They conclude that solutions for coarse grids may differ markedly from those for fine grids, and that as the pressure gradients and their derivatives become sharper, real solutions to the difference equations might not exist unless the mesh pattern is fine enough.

The technique of advancing to a progressively finer mesh also involves some programming complications where grooved bearings are involved, and for both these reasons, it was abandoned in favour of alternative devices.

4.12 The Treatment of Numerical Instability and Associated Problems (Continued)

(f) Variable Mesh Spacing

Rather than adopt a uniformly fine mesh pattern over the entire solution field, it is possible to vary the spacing at selected points in order to obtain a finer resolution of the pressure field. This will assist in reducing the basic truncation error between the differential and finite difference equations, which can itself be a source of instability. The total number of mesh points need not be excessive and computational time is therefore conserved.

An approach along these lines can be effective on a plain bearing of simple geometry, but where many clearance discontinuities are present, programming such a solution can become rather involved. As is the case here, where a regular mesh pattern is defined by the given distribution of pumping grooves, variable mesh spacing, or co-ordinate stretching as it is sometimes called, is not feasible.

(g) Initialisation Using External Data

Where computational time becomes excessive as a result of attempting to stabilise the solution, it is possible to initialise the numerical pressure distribution on the basis of the closest analytic or experimental data available. This will not in itself have much influence upon the stability of computation, nor should it influence the accuracy of the final answer, but it will reduce the total number of iterations required to achieve convergence. The approach is valid because the final answer will be essentially independent of the initial pressure distribution.

Stability may be indirectly improved because, where a solution involves a very large number of iterations, it has been observed here that there is a greater likelihood of minor irregularities growing beyond control and swamping the solution field. By examining the pressure distribution after each successive iterative cycle, it was noted that

4.12 (g) Initialisation Using External Data (Continued)

instability frequency commenced at one or two mesh points only, and rapidly spread across the remainder of the grid during further iterations. Even where no actual numerical instability is present, it is possible for a suprious character to be generated within computer system, and occasionally, this has been known to propogate across the solution field.

Any procedure which serves to limit the total number of iterative cycles required is clearly advantageous, though the form of initialisation suggested here will require either some preliminary computation or the input of a large amount of initial data. Some loss of generality is inevitable, and the method presumes that alternative data is available for the solutions in question, but where there is no alternative, it does allow a comparison to be made between experimental and theoretical results.

(h) Change of Dependent Variable

Prior discussions have assumed that $\overline{P}$ will be the dependent variable, and that the mesh pattern is solved directly in terms of pressure. As previously recalled in this section, instabilities appear to coincide with sharp variations of the pressure gradient and its derivatives. If $\overline{P}$ can be replaced by a new dependent variable $\overline{Z}$, where $\overline{Z}$ is known to vary smoothly over the regions of interest, then the iterative solution can be carried out on $\overline{Z}$ until convergence is achieved, and the corresponding value of $\overline{P}$ extracted when the iteration is complete. The new dependent variable must obviously be a function of $\overline{P}$, and may also be a function of any other property whose value is known across the solution field; for example $\overline{H}$.

4.12 (h) Change of Dependent Variable (Continued)

The selection of a suitable function to represent $\overline{Z}$ is largely a matter of experience, and a number of suitable functions have been proposed by previous workers for various types of problem. Vogelpohl, Sassenfield and Walther are reported (22) to recommend $\overline{P}\overline{H}$ as the dependent variable for incompressible journals, while the same reference quotes Elrod's choice of $\overline{P}^2\overline{H}^2$ for compressible journals. Castell and Pirvics suggest $\overline{P}\overline{H}^2$ for both compressible and incompressible journals, with the possibility of $\overline{P}^2$ at very high eccentricities. While all the above variables may be suitable for smooth bearings, the introduction of pumping grooves makes it undesirable for $\overline{Z}$ to be a function of bearing clearance, since the clearance is in itself a discontinuous function. On this basis, it was decided to choose $\overline{P}^2$ as the dependent variable as soon as it was realised that the stability problems encountered in the solution were not responding to alternative techniques.

The introduction of $\overline{Z}$ as the new dependent variable involved a great deal of additional labour, and a further seventeen finite difference equations had to be developed in terms of the new variable. In order to develop these finite difference relations, the standard form of Reynold's equation (Equation 15) must first be re-written in terms of $\overline{Z}$.

For the first term,

$$\frac{\partial}{\partial \overline{x}}\left\{\overline{P}\,\overline{H}^3\,\frac{\partial \overline{P}}{\partial \overline{x}}\right\} \qquad (46)$$

$$\overline{Z} = \overline{P}^2 \qquad (47)$$

$$\frac{\partial (\overline{Z})}{\partial \overline{x}} = \frac{d\overline{Z}}{d\overline{P}} \cdot \frac{\partial \overline{P}}{\partial \overline{x}} \qquad (48)$$

$$\therefore \frac{\partial \overline{P}}{\partial \overline{x}} = \frac{\partial \overline{Z}}{\partial \overline{x}} \Big/ \frac{\partial \overline{Z}}{\partial \overline{P}} \qquad (49)$$

$$\text{and } \frac{d\overline{Z}}{d\overline{P}} = \frac{d(\overline{P}^2)}{d\overline{P}} = 2\overline{P} \qquad (50)$$

$$\text{hence, } \frac{\partial \overline{P}}{\partial \overline{x}} = \frac{1}{2\overline{P}}\,\frac{\partial \overline{Z}}{\partial \overline{x}} \qquad (51)$$

4.12 (h) Change of Dependent Variable (Continued)

Substituting, the first term becomes:-

$$\frac{\partial}{\partial \bar{x}} \left\{ \frac{\bar{H}^3}{2} \frac{\partial \bar{p}}{\partial \bar{x}} \right\} \qquad (52)$$

The second term in equation 15 is treated in a similar manner, and becomes:-

$$\frac{1}{4\beta^2} \frac{\partial}{\partial \bar{y}} \left\{ \frac{\bar{H}^3}{2} \frac{\partial \bar{p}}{\partial \bar{y}} \right\} \qquad (53)$$

In order to convert the third term in Reynold's equation, it is necessary to introduce the values $\bar{p}_o$ and $\delta\bar{p}$, where $\bar{p}_o$ is the initial guess for parameter $\bar{p}$ and $\delta\bar{p}$ the incremental increase after each single iteration. The procedure is then as follows:-

$$\Lambda \frac{\partial}{\partial \bar{x}} (\bar{P}\ \bar{H}) \qquad (54)$$

$$\frac{\partial}{\partial \bar{x}} (\bar{P}\ \bar{H}) = \bar{H} \frac{\partial \bar{P}}{\partial \bar{x}} + \bar{P} \frac{\partial \bar{H}}{\partial \bar{x}} \qquad (55)$$

which by substitution from 47

$$= \bar{H} \frac{\partial (\bar{p}^{\frac{1}{2}})}{\partial \bar{x}} + \bar{p}^{\frac{1}{2}} \cdot \frac{\partial \bar{H}}{\partial \bar{x}} \qquad (56)$$

Now let $\bar{p}_o$ be the initial guess for parameter $\bar{p}$ and $\delta\bar{p}$ the incremental increase after each iteration.

$$\bar{p} = \bar{p}_o + \delta\bar{p} \qquad (57)$$

$$\therefore \quad (\bar{p}^{\frac{1}{2}}) = (\bar{p}_o + \delta\bar{p})^{\frac{1}{2}} \qquad (58)$$

Expanding by the Binomial Theorem and neglecting terms of order $\delta\bar{p}^2$ and higher,

$$\bar{p}^{\frac{1}{2}} = \bar{p}_o^{\frac{1}{2}} \left\{ 1 + \tfrac{1}{2} \frac{\delta\bar{p}}{\bar{p}_o} \right\} \qquad (59)$$

Substituting for $\delta\bar{p}$ from 57, it can be shown that

$$\bar{p}^{\frac{1}{2}} = \tfrac{1}{2} \left\{ \bar{p}_o^{\frac{1}{2}} + \frac{\bar{p}}{\bar{p}_o^{\frac{1}{2}}} \right\} \qquad (60)$$

4.12 (h) Change of Dependent Variable (Continued)

Further substitution of the above expression into relation 56 yields,

$$\frac{\partial(\bar{\bar{\rho}}^{\frac{1}{2}})}{\partial \bar{x}} = \frac{\partial}{\partial \bar{x}}\left[\frac{\bar{\bar{\rho}}_o^{\frac{1}{2}}}{2} + \frac{\bar{\bar{\rho}}}{2\bar{\bar{\rho}}_o^{\frac{1}{2}}}\right] \qquad (61)$$

from which the third term becomes

$$\frac{\Lambda\,\bar{H}}{4\bar{\bar{\rho}}_o^{\frac{1}{2}}} \cdot \frac{\partial \bar{\bar{\rho}}_o}{\partial \bar{x}} + \frac{\Lambda\,\bar{H}}{2\bar{\bar{\rho}}_o^{\frac{1}{2}}} \cdot \frac{\partial \bar{\bar{\rho}}}{\partial \bar{x}} - \frac{\Lambda\,\bar{H}\,\bar{\bar{\rho}}}{4\bar{\bar{\rho}}_o^{\frac{3}{2}}} \cdot \frac{\partial \bar{\bar{\rho}}_o}{\partial \bar{x}}$$

$$+ \frac{\Lambda\,\bar{\bar{\rho}}_o^{\frac{1}{2}}}{2} \frac{\partial \bar{H}}{\partial \bar{x}} + \frac{\Lambda\,\bar{\bar{\rho}}}{2\bar{\bar{\rho}}_o^{\frac{1}{2}}} \cdot \frac{\partial \bar{H}}{\partial \bar{x}} \qquad (62)$$

Reynold's equation may therefore be written as:-

$$\frac{\partial}{\partial \bar{x}}\left\{\frac{\bar{H}^3}{2} \cdot \frac{\partial \bar{\bar{\rho}}}{\partial \bar{x}}\right\} + \frac{1}{4\beta^2} \cdot \frac{\partial}{\partial \bar{y}}\left\{\frac{\bar{H}^3}{2} \cdot \frac{\partial \bar{\bar{\rho}}}{\partial \bar{y}}\right\}$$

$$= \frac{\Lambda\,\bar{H}}{4\bar{\bar{\rho}}_o^{\frac{1}{2}}} \cdot \frac{\partial \bar{\bar{\rho}}_o}{\partial \bar{x}} + \frac{\Lambda\,\bar{H}}{2\bar{\bar{\rho}}_o^{\frac{1}{2}}} \cdot \frac{\partial \bar{\bar{\rho}}}{\partial \bar{x}} - \frac{\Lambda\,\bar{H}\,\bar{\bar{\rho}}}{4\bar{\bar{\rho}}_o^{\frac{3}{2}}} \cdot \frac{\partial \bar{\bar{\rho}}_o}{\partial \bar{x}}$$

$$+ \frac{\Lambda\,\bar{\bar{\rho}}_o^{\frac{1}{2}}}{2} \cdot \frac{\partial \bar{H}}{\partial \bar{x}} + \frac{\Lambda\,\bar{\bar{\rho}}}{2\bar{\bar{\rho}}_o^{\frac{1}{2}}} \cdot \frac{\partial \bar{H}}{\partial \bar{x}} \qquad (63)$$

Finite difference approximations to this new form of Reynold's equation may now be developed in the usual manner, in terms of variable $\bar{\bar{\rho}}$. The expressions are broadly similar in form to those developed for $\bar{P}$ though each differs in detail from its original counterpart. For a normal mesh point,

4.12 (h) Change of Dependent Variable (Continued)

$$\overline{\phi}_{(I,J)} = \frac{\Lambda\,\overline{H}_{(I,J)}\overline{\phi 2}}{4\overline{\phi}_o^{\frac{1}{2}}\,\overline{X}} - \frac{\Lambda\,\overline{H}_{(I,J)}\overline{\phi 4}}{4\overline{\phi}_o^{\frac{1}{2}}\,\overline{X}} + \frac{\Lambda\,\overline{H}_{(I,J)}\overline{\phi 2}}{2\overline{\phi}_o^{\frac{1}{2}}\,\overline{X}}$$

$$- \frac{\Lambda\,\overline{H}_{(I,J)}\overline{\phi 4}}{2\overline{\phi}_o^{\frac{1}{2}}\,\overline{X}} + \frac{\Lambda\,\overline{\phi}_o^{\frac{1}{2}}\,\overline{H2}}{2\,\overline{X}} - \frac{\Lambda\,\overline{\phi}_o^{\frac{1}{2}}\,\overline{H4}}{2\,\overline{X}} - \frac{\overline{H2}^3\,\overline{\phi}_{(I+1,J)}}{2(\overline{X})^2}$$

$$- \frac{\overline{H4}^3\,\overline{\phi}_{(I-1,J)}}{2(\overline{X})^2} - \frac{\overline{H1}^3\,\overline{\phi}_{(I,J+1)}}{8\beta^2(\overline{Y})^2} - \frac{\overline{H3}^3\,\overline{\phi}_{(I,J-1)}}{8\beta^2(\overline{Y})^2}$$

$$\frac{}{}$$

$$- \frac{\overline{H2}^3}{2(\overline{X})^2} - \frac{\overline{H4}^3}{2(\overline{X})^2} - \frac{\overline{H1}^3}{8\beta^2(\overline{Y})^2} - \frac{\overline{H3}^3}{8\beta^2(\overline{Y})^2} + \frac{\Lambda\,\overline{H}_{(I,J)}\overline{\phi 2}}{4\overline{\phi}_o^{\frac{3}{2}}\,\overline{X}}$$

$$- \frac{\Lambda\,\overline{H}_{(I,J)}\overline{\phi 4}}{4\overline{\phi}_o^{\frac{3}{2}}\,\overline{X}} - \frac{\Lambda\,\overline{H2}}{2\overline{\phi}_o^{\frac{1}{2}}\,\overline{X}} + \frac{\Lambda\,\overline{H4}}{2\overline{\phi}_o^{\frac{1}{2}}\,\overline{X}} \qquad (64)$$

Where,

$$\overline{\phi 1} = \frac{\overline{\phi}_{(I,J+1)} + \overline{\phi}_{(I,J)}}{2} \qquad (65)$$

$$\overline{\phi 2} = \frac{\overline{\phi}_{(I+1,J)} + \overline{\phi}_{(I,J)}}{2} \qquad (66)$$

$$\overline{\phi 3} = \frac{\overline{\phi}_{(I,J-1)} + \overline{\phi}_{(I,J)}}{2} \qquad (67)$$

$$\overline{\phi 4} = \frac{\overline{\phi}_{(I-1,J)} + \overline{\phi}_{(I,J)}}{2} \qquad (68)$$

and as previously shown,

$$\overline{H1} = \frac{\overline{H}_{(I,J+1)} + \overline{H}_{(I,J)}}{2}$$

$$\overline{H2} = \frac{\overline{H}_{(I+1,J)} + \overline{H}_{(I,J)}}{2}$$

$$\overline{H3} = \frac{\overline{H}_{(I,J-1)} + \overline{H}_{(I,J)}}{2}$$

$$\overline{H4} = \frac{\overline{H}_{(I-1,J)} + \overline{H}_{(I,J)}}{2}$$

4.12 (h) Change of Dependent Variable (Continued)

while for the lower boundary of any left hand groove, it can be shown that:

$$\overline{\Psi}_{(I,J)} = -\frac{\overline{X}\,\overline{HG}^{3}\,\overline{\Psi 3}}{4\beta^2\,\Lambda\,\overline{Y}} + \frac{\overline{X}\,\overline{HG}^{3}\,\overline{\Psi}_{(I,J-1)}}{16\beta^2\,\Lambda\,\overline{Y}} + \frac{\overline{\Psi}_o^{\frac{1}{2}}\,\overline{HG}\,\overline{Y}}{2}$$

$$+\frac{\overline{Y}\,\overline{HG}^{3}\,\overline{\Psi 2}}{\Lambda\,\overline{X}} - \frac{\overline{Y}\,\overline{HG}^{3}\,\overline{\Psi}_{(I+1,J)}}{4\,\Lambda\,\overline{X}} - \frac{\overline{X}\,\overline{H}^{3}_{(I,J)}\,\overline{\Psi 1}}{4\beta^2\,\Lambda\,\overline{Y}}$$

$$+\frac{\overline{X}\,\overline{H}^{3}_{(I,J)}\,\overline{\Psi}_{(I,J+1)}}{16\beta^2\,\Lambda\,\overline{Y}} - \frac{\overline{\Psi}_o^{\frac{1}{2}}\,\overline{H}_{(I,J)}\,\overline{Y}}{2}$$

$$+\frac{\overline{Y}\,\overline{H}^{3}_{(I,J)}\,\overline{\Psi 4}}{\Lambda\,\overline{X}} - \frac{\overline{Y}\,\overline{H}^{3}_{(I,J)}\,\overline{\Psi}_{(I-1,J)}}{4\,\Lambda\,\overline{X}}$$

$$\frac{}{}$$

$$-\frac{3\,\overline{X}\,\overline{H}^{3}_{(I,J)}}{16\beta^2\,\Lambda\,\overline{Y}} + \frac{\overline{H}_{(I,J)}\,\overline{Y}}{2\,\overline{\Psi}_o^{\frac{1}{2}}} + \frac{3\,\overline{Y}\,\overline{H}^{3}_{(I,J)}}{4\,\Lambda\,\overline{X}}$$

$$-\frac{3\,\overline{X}\,\overline{HG}^{3}}{16\beta^2\,\Lambda\,\overline{Y}} - \frac{\overline{HG}\,\overline{Y}}{2\overline{\Psi}_o^{\frac{1}{2}}} + \frac{3\,\overline{Y}\,\overline{HG}^{3}}{4\,\Lambda\,\overline{X}} \qquad (69)$$

where $\overline{HG} = \overline{H}_{(I,J)} + \overline{G}$ as before

The remaining boundary approximations follow in a similar manner, and it is noted that all except those relating to the groove end boundaries involve the term $\overline{\Psi}_o$ raised to some fractional power. This presents no problem to the computer solution, where $\overline{\Psi}_o = \overline{\Psi}_{(I,J)}$; a value readily available from the $\overline{\Psi}$ array prior to the iteration of each point. Thus the term $\overline{\Psi}_o$ can be treated as a constant which varies both for each mesh and for successive iterations of the same point.

4.12 The Treatment of Numerical Instability and Associated Problems (Continued)

In addition to a new set of finite difference approximations, some re-organisation of the original programme was required in order to accommodate the new variable. Iteration is carried out only upon the $\overline{Z}$ array, whose initial values are preset in the same manner as for a $\overline{P}$ array. Improved values of VAR, are generated for each mesh point in turn and are used to replace the old value before proceeding to the next point on the grid. All other computations, including comparison with the allowable residual and the evaluation of load components and directions, are carried out by first extracting the corresponding value of pressure from relation 47.

While changing the dependent variable resulted in a remarkable improvement in stability, this was only achieved at the expense of a very noticeable increase in computational time, despite the fact that over-relaxation could now be employed.

Thus use of $\overline{P}^2$ as the dependent variable is not new, but its application to a helically grooved journal has not previously been described.

CHAPTER 5

EXPERIMENTAL TECHNIQUES

5.1 General Considerations

5.1.1 The Use of Scale Bearings

It has become normal practice in lubrication research to perform experimental work on large model bearings, where manufacturing tolerances are less critical and conventional measuring techniques are more readily employed. This approach was considered here, and rejected on four counts in this instance.

(1) Large model bearings could not be manufactured to the same relative geometric precision as scale size bearings, which are produced on specially developed equipment.

(2) Results were required from a large population, and the number of models would have been very limited.

(3) Previous workers had noted discrepancies between small bearings and large models (107).

(4) Existing literature contained very few experimental results from bearings of this size (See CHAPTER 2).

5.1.2 Design Criteria for Test Rigs

It was realised from the start that for measuring rotor displacements of only a few micro inches (1 micro inch = 0·025 micro metres), rigidity and stability of the test rigs would be of paramount importance. Aluminium alloy offered good thermal characteristics and was used wherever possible, with some of the more exacting measurements carried out on massive concrete plinths which extend into the foundations of the building. Alignment of the rotor spin axis to within $\pm \frac{1}{4}$ degrees of arc is necessary if gyroscopic and gravitational forces are to be distinguished during dynamic testing.

5.1.3 Practical Requirements

The major practical considerations are as follows. Assembly and testing of the bearings must be carried out in clean, dry conditions. This is to prevent contamination from influencing the bearing performance. It was also felt that testing should be carried out in a constant temperature environment, in order to minimise thermal expansion or contraction of the test structures, which could have resulted in corresponding measurement errors. Finally, due precautions are required to prevent local electrical disturbances from influencing the electronic measuring equipment (Plate 4).

The majority of the work was carried out within a clean room, incorporating air filtration, temperature and humidity control and stabilised power supplies. The test rigs were sited away from windows to avoid the influence of solar radiation, and a long warm-up period was allows prior to each set of measurements. Barometric pressure and local temperature were monitored throughout the tests and additional measurements were taken of the clean room over-pressure.

Even with the above precautions, considerable difficulty was experienced in measuring some of the smaller deflections and pressure changes, and these readings had to be taken in the evening to avoid thermal and electrical disturbances caused by other laboratory personnel.

Preliminary experiments showed that, provided ambient conditions could be maintained, pressure and deflection did not need to be recorded at the same time. This simplified the experimental work considerably.

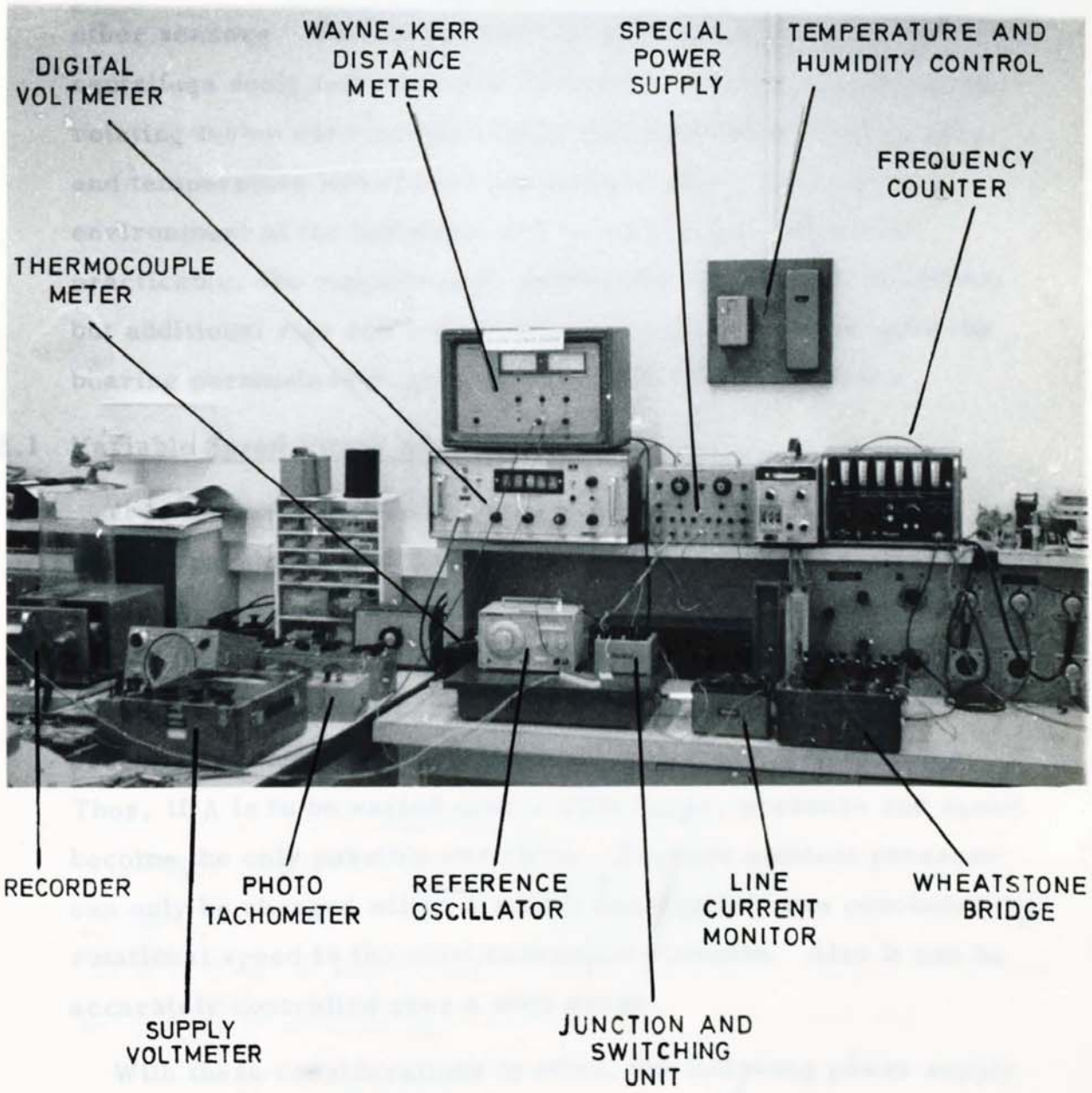

PLATE 4

INSTRUMENTATION USED FOR ROTOR DEFLECTION AND DECAY CURVE MEASUREMENTS

5.2 Test Equipment

Access was available to a wide range of very specialised equipment intended for examining conventional gyroscopes and other sensors. This equipment included precision rate tables and centrifuge equipment used for loading the bearing, elevating and rotating tables used for accurately positioning the bearing axes, and temperature and altitude cabinets in which the operating environment of the bearing could be controlled. Wherever practicable, the experimental work made use of these facilities, but additional rigs and instruments necessary to investigate the bearing parameters in greater detail are described below.

5.2.1 Variable Speed Power Supply

It is normal practice in aerodynamic bearing work to plot various parameters of interest against the principal dimensionless group Λ, the compressibility number. This group is a function of bearing geometry, viscosity, ambient pressure and rotational speed. For this bearing, geometry and mean viscosity are essentially fixed, from practical and financial considerations. Thus, if Λ is to be varied over a wide range, pressure and speed become the only possible variables. Because ambient pressure can only be changed within a sealed enclosure it was concluded that rotational speed is the most convenient variable. Also it can be accurately controlled over a wide range.

With these considerations in mind, the following power supply was designed.* Essentially, five D.C. voltage levels are created within the power supply, using potential-divider methods. These are then switched onto the output circuit at intervals and in sequence, in such a manner as to produce an approximate sine wave pattern. Switching is controlled by either a small internal oscillator, or by an external reference sine wave. Three such switching units are provided and thus a 3-phase quasi-sine wave output may be generated from a D.C. input. Voltage and frequency are variable over a wide range.

* By Mr. D. Morley of Smiths Industries Limited

5.2.1 Variable Speed Power Supply (Continued)

In use, an increase in supply frequency to the spin motor will result in a proportional decrease in current (as the effective A.C. impedance of the winding is proportional to frequency) and hence a corresponding decrease in output power. To overcome this effect, the supply voltage must be increased, hence the requirement for a variable control.

5.2.2 Photo-Tachometer

Accurate determination of the instantaneous rotor speed is essential, and is best measured by optical methods. Mechanical tachometers would be impracticable and magnetic sensors would be influenced by the spin motor field. A lamp and photocell unit is arranged to count optical pulses from a 180° band, frosted onto the rotor using an air-abrasive spray. The resultant pulse rate is converted to a voltage which may be displayed on a conventional 'Avometer'. Three speed ranges are provided, vis. 200 c/s, 400 c/s and 800 c/s.

In addition to providing an instantaneous analgoue reading of speed, digital logic circuits are incorporated which compare the photo-cell output frequency with the motor supply frequency at any instant. Any error signal will then operate one of three lamps; one to indicate a stalled rotor, one to indicate synchronous speed and a third to indicate sub-synchronous rotation. Sensitivity of the latter may be adjusted to within 1 cycle in (say) 400 i.e. ¼%

One of the major problems in measuring rotational speed is that only a small portion of the rotating surface is visible, the remainder being shielded by the spin motor. Consequently, considerable care is required in the optical design and careful optical and electrical screening is necessary in order to exclude spurious signals from fluorescent lights and other sources.

5.2.3 Capacitor Probes

Measurement of the true rotor position relative to the fixed journal is obstructed by the enveloping spin motor and gimbal structure, with only a small portion of the rotor being visible at each end of the assembly. Consequently, conventional probes are not suitable and must either be heavily modified or special miniature versions constructed. Consideration of alternative methods of measuring mechanical displacement was given, but the exceedingly small movements involved leave only capacitance methods as a reasonable choice. Inductance probes would be affected by the motor field, while optical or air gauge methods could not be readily employed on a rate table or centrifuge.

Two types of capacitor probe were successfully used. One was a modified commercial version and the other a specially constructed miniature probe, which will now be described.

The probe and guard ring (Fig.7 and Plate 5) are machined from cold working brass, and are bonded together by an insulating layer of epoxy-impregnated tape. A steel mounting tube is similarly secured over part of the probe's length. After curing, the hollow end is crushed flat in a vice and the working face lapped flat and square with the O/D. The first probe was manufactured with a curved working face to match the rotor surface, but lateral adjustment was found to be very critical and this arrangement was abandoned.

Initial calibration and linearity checks were carried out against a dummy rotor and against slip gauges, but in use, the probe is best calibrated in situ from a knowledge of the total bearing clearance.

Despite its simplicity and low cost, such a probe will resolve relative rotor movements of less than one micro-inch (0·025 micrometres) when mounted within 0·0005 inch (0·013 mm) of the rotor surface.

FINISH

ALL PARTS FINE TURNED

SCALE 4:1

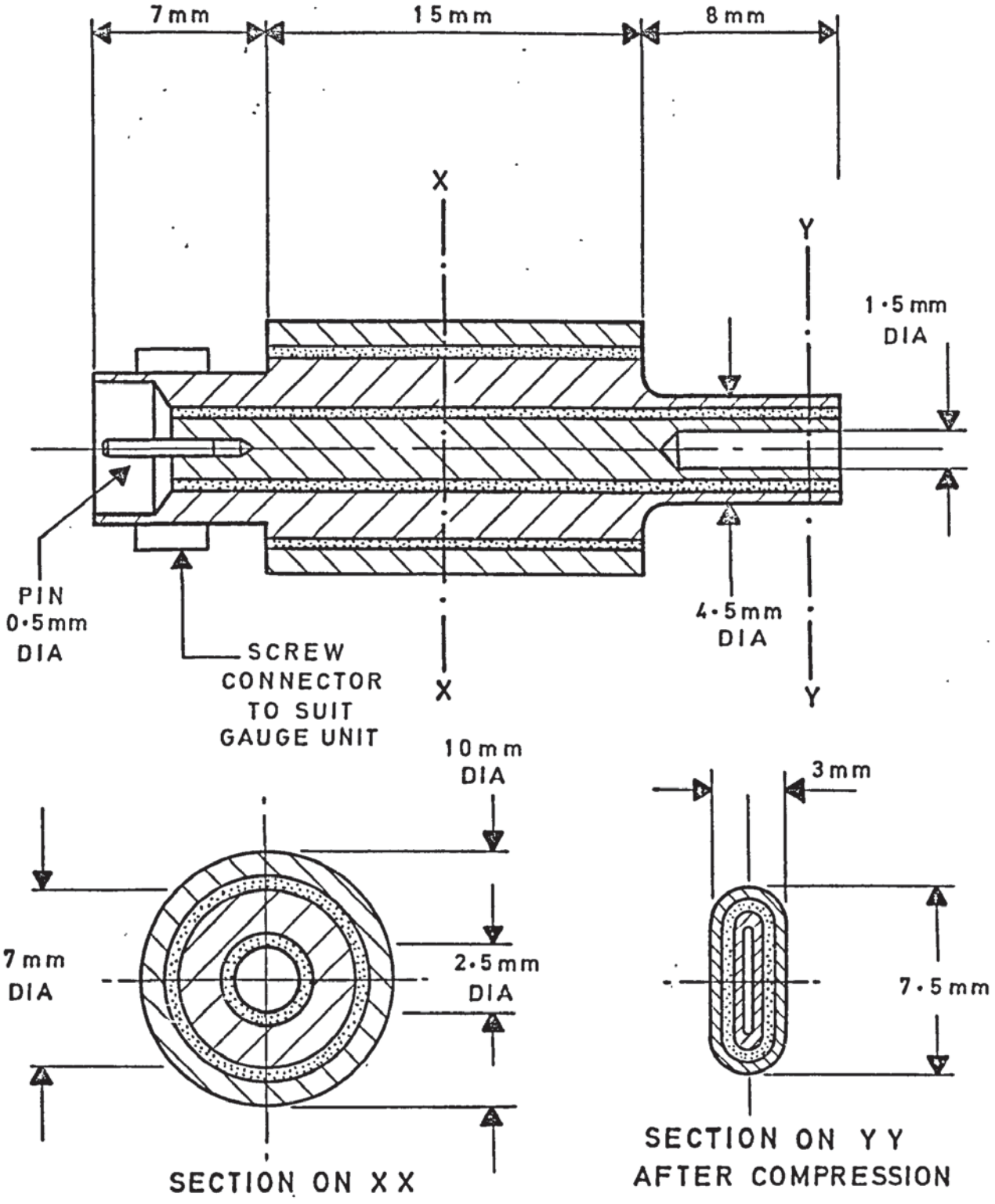

MATERIALS

CLAMPING TUBE AND PIN – SILVER STEEL

REMAINDER – COLD WORKING BRASS

FIG. 7
CONSTRUCTION OF MINIATURE CAPACITOR PROBE

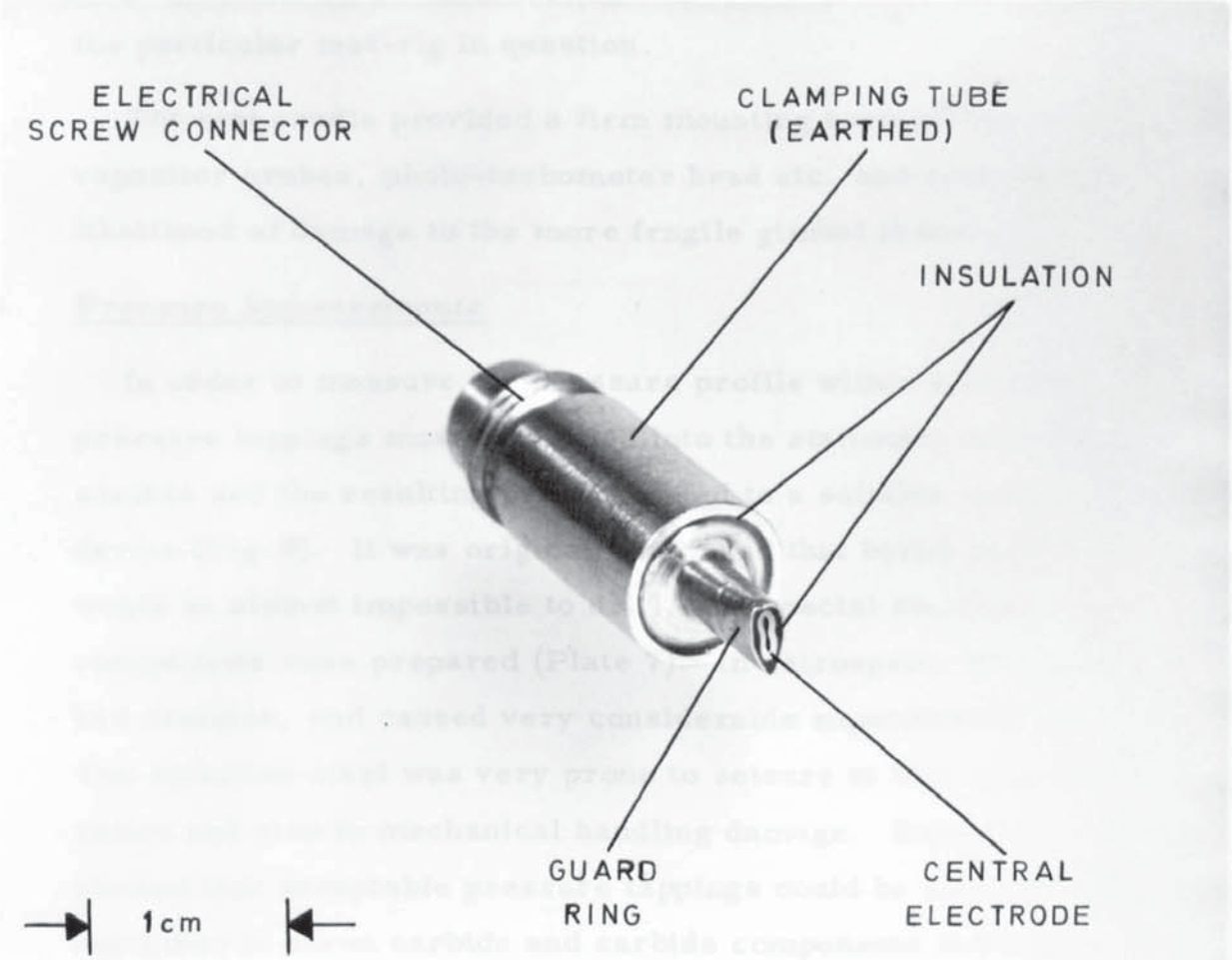

PLATE 5
MINIATURE CAPACITOR PROBE
USED TO MEASURE ROTOR
DEFLECTION

5.2.4 Test Cradles and Other Fittings

Precise location and alignment of each test bearing was achieved by clamping it within a carefully machined alloy cradle (Fig. 8 and Plate 6). Close fitting dowels were used to obtain spin axis alignment within the cradle, which could then be firmly secured to the particular test-rig in question.

The test cradle provided a firm mounting surface for the capacitor probes, photo-tachometer head etc. and reduced the likelihood of damage to the more fragile gimbal frame.

5.3 Pressure Measurements

In order to measure the pressure profile within a bearing, fine pressure tappings must be drilled into the stationary bearing surface and the resulting pressure bled to a suitable measuring device (Fig. 9). It was originally believed that boron carbide would be almost impossible to drill, and special stainless steel components were prepared (Plate 7). In retrospect, this was a bad decision, and caused very considerable experimental problems. The stainless steel was very prone to seizure at high eccentricity ratios and also to mechanical handling damage. Experience later showed that acceptable pressure tappings could be ultrasonically machined in boron carbide and carbide components were used in later tests. By using a jig borer in conjunction with an optical positioning attachment, holes down to 0·015 inch (0·39 mm) diameter were drilled in the stainless steel components, though experiments later showed that tappings as large as 0·030 inch (0·78 mm) did not significantly affect the measured pressure profile. Prior work had shown that 0·005 inch (0·13 mm) tappings were too small to allow a speedy build-up of pressure in the measuring system. Each hole was carefully de-burred by hand under a binocular microscope, as it was feared that local irregularities would disturb the flow within the bearing.

The small physical dimensions of the components tend to restrict the number of pressure tappings on a single pumping groove to one, and a high degree of groove uniformity is therefore desirable. Such an arrangement has the advantage of greater

SCALE 1:1

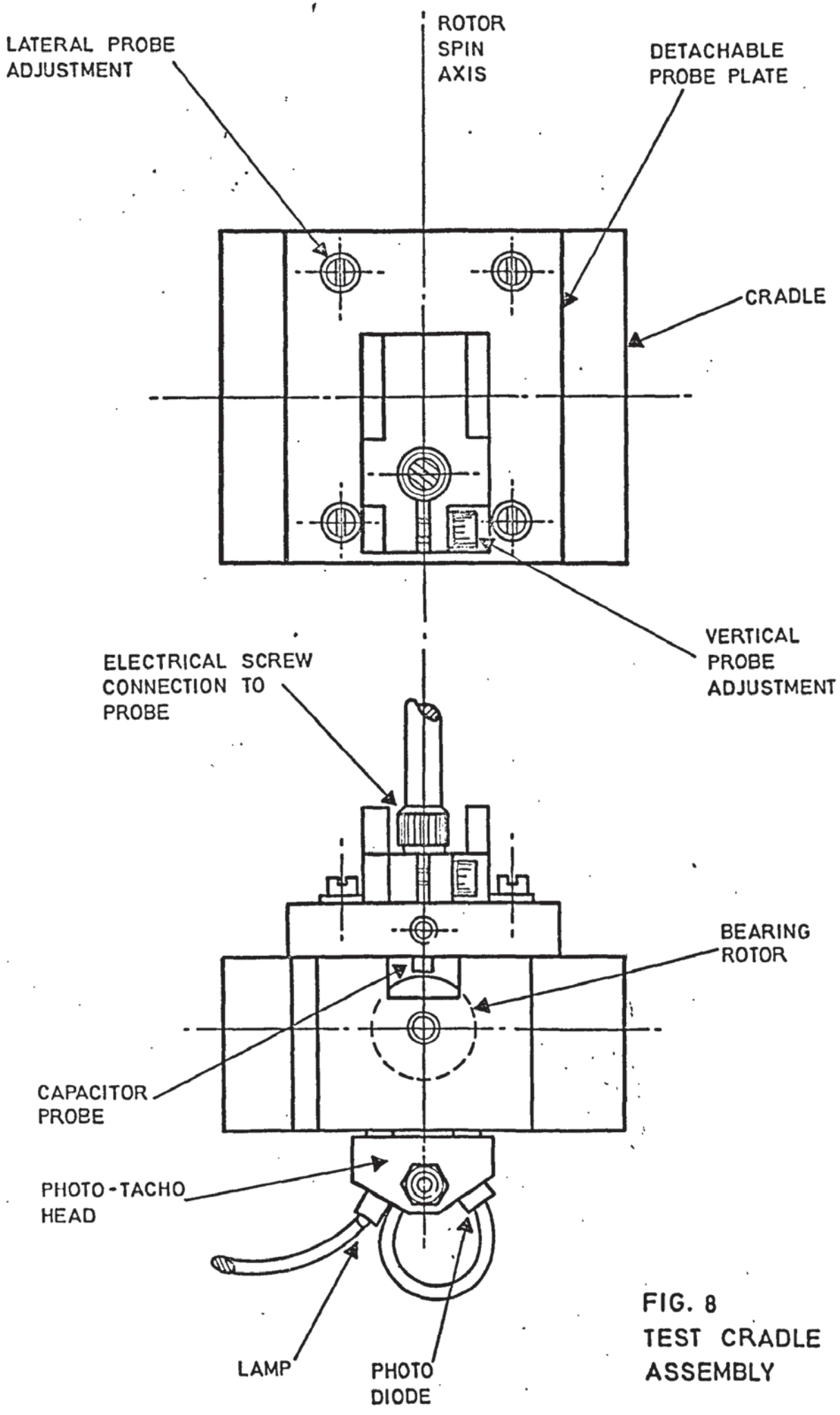

FIG. 8
TEST CRADLE ASSEMBLY

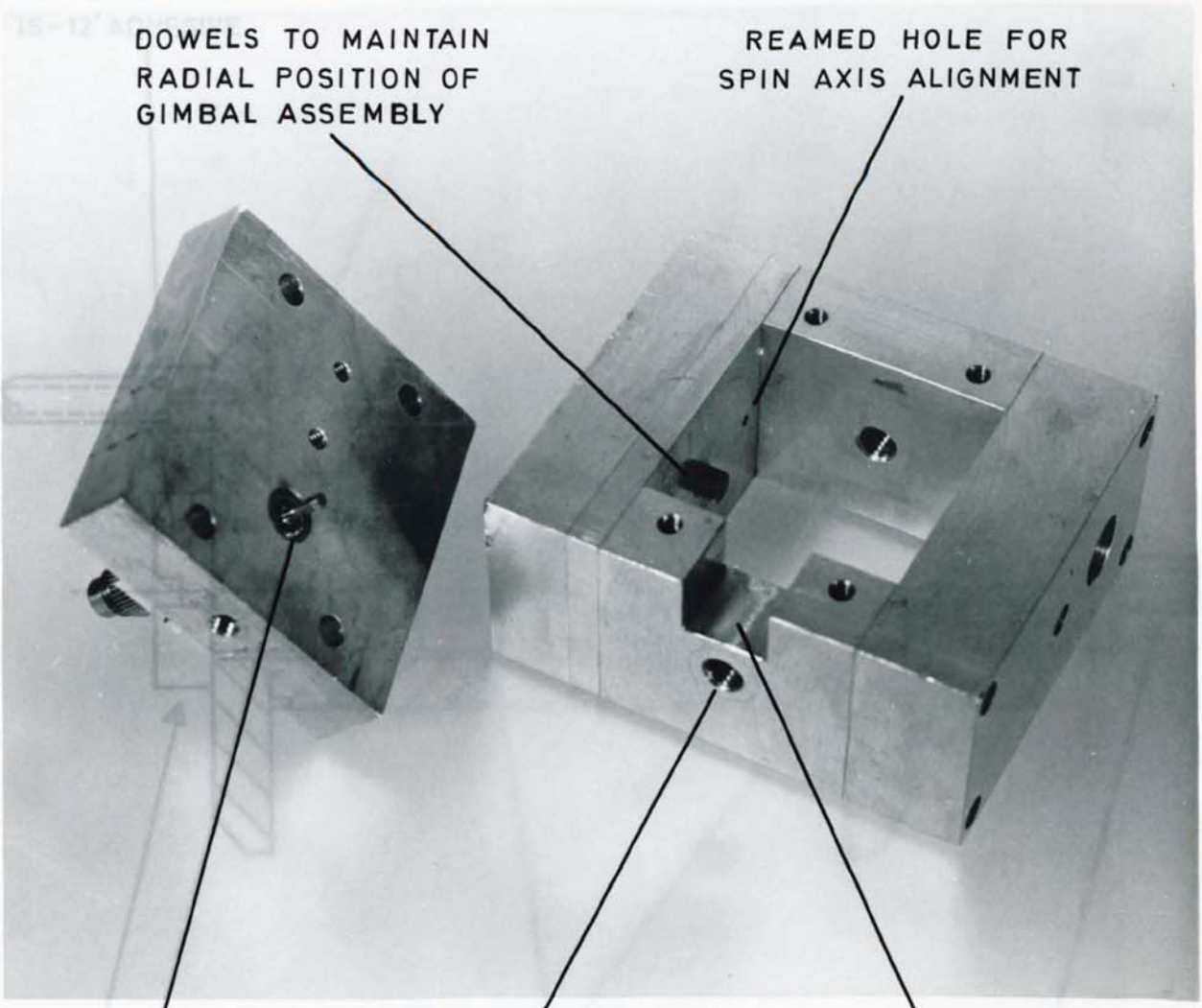

PLATE 6
TEST CRADLE AND CAPACITOR PROBE ASSEMBLY

APPROXIMATE SCALE 3:1

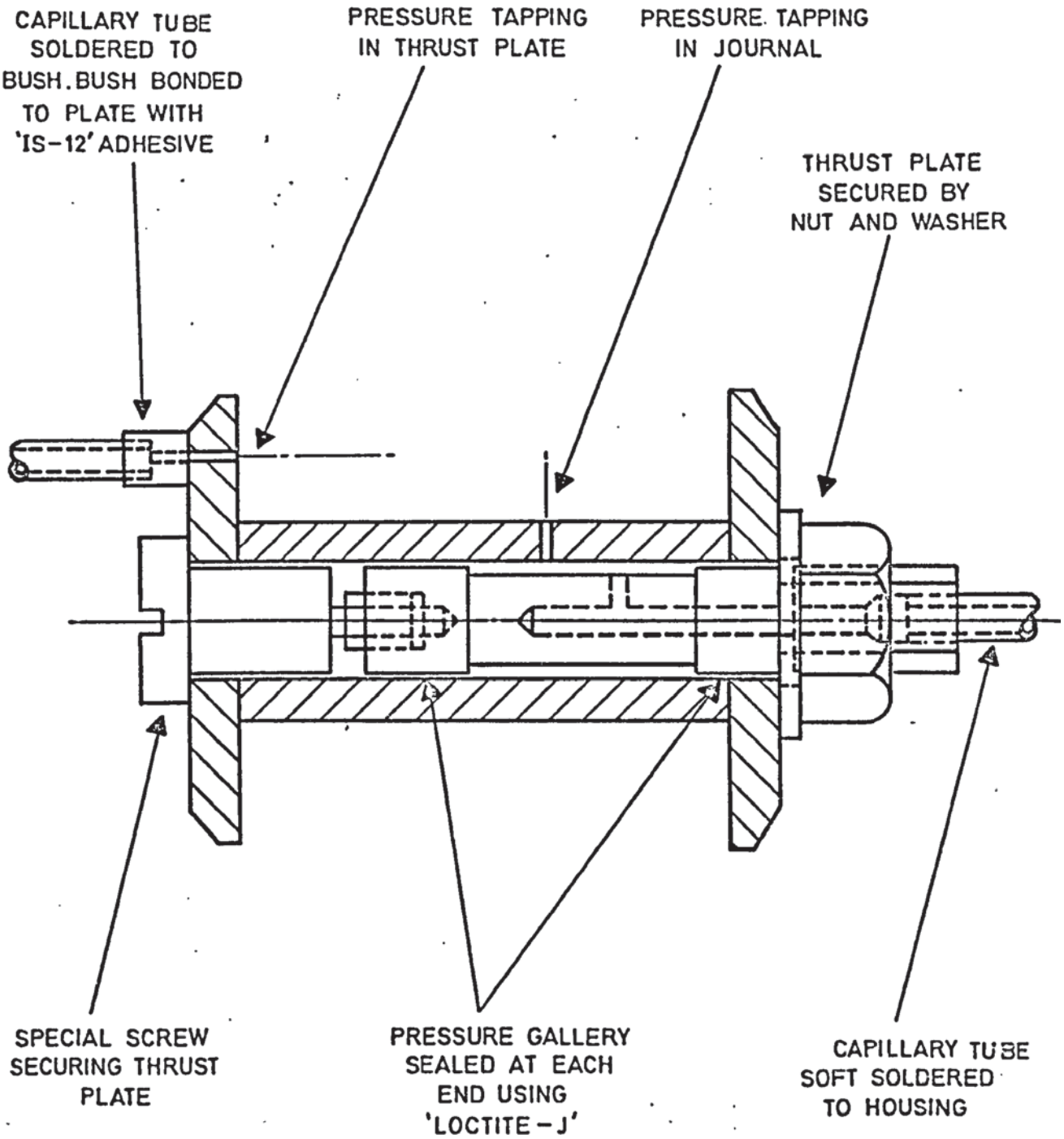

N.B.
ROTOR OMITTED
FOR CLARITY.

FIG. 9
PRESSURE TAPPING
ARRANGEMENT

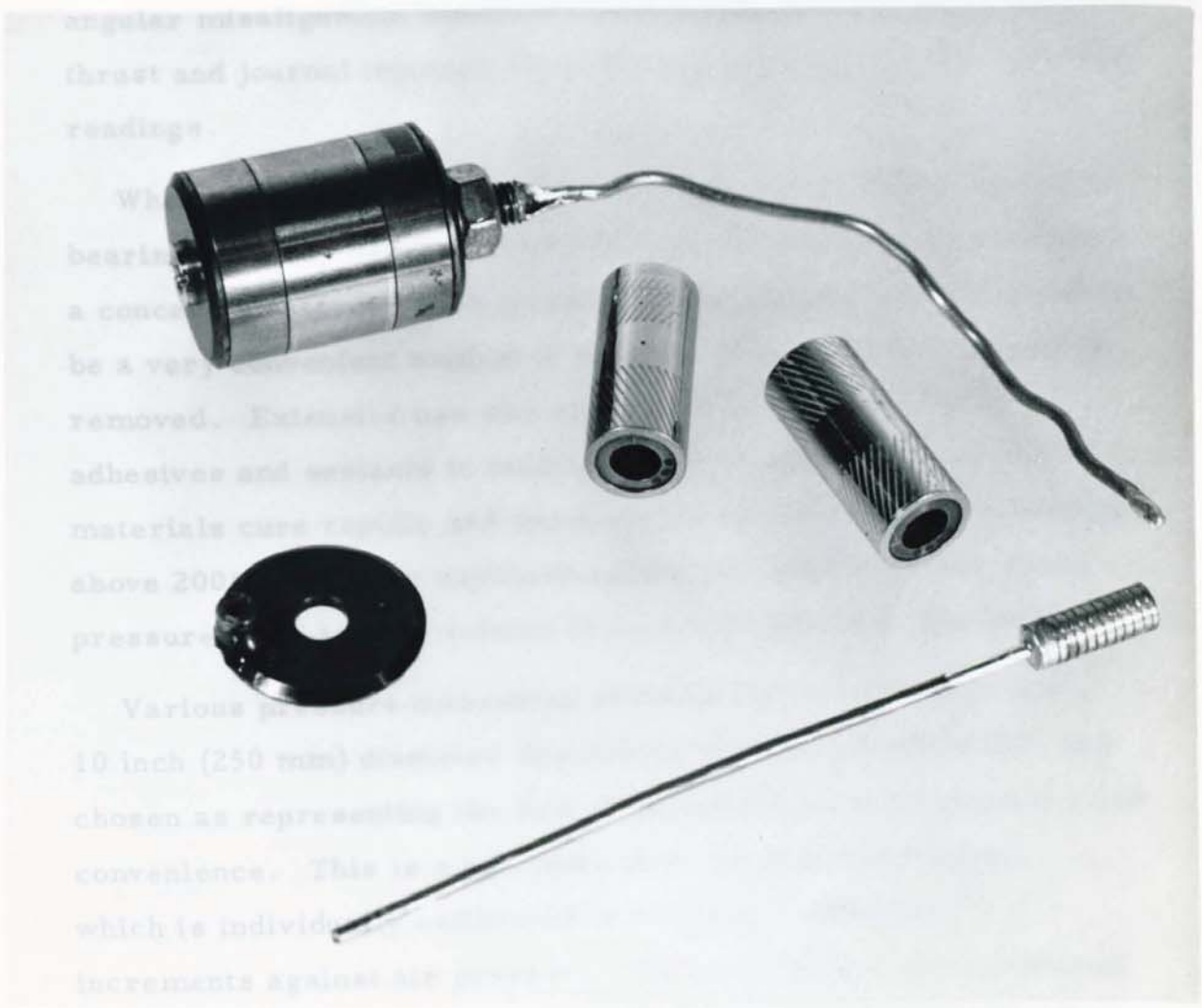

PLATE 7
SOME OF THE SPECIAL HARDWARE USED FOR BEARING PRESSURE MEASUREMENTS

5.3 Pressure Measurements (Continued)

accuracy, since adjacent tappings, being on different grooves, have a negligible effect upon the one being measured. However, in practice, there are disadvantages when measuring pressure under angular misalignment conditions, when angular rotation of both thrust and journal tappings about the spin axis is required between readings.

When not in use, the pressure tappings were blanked off at the bearing surface, using cold-curing silicone rubber. This formed a concave meniscus at the entrance of the tapping and was found to be a very convenient method of sealing; easy to apply and readily removed. Extensive use was made of anaerobic polyester adhesives and sealants in making pressure connections. These materials cure rapidly and parts can be dis-assembled by heating above 200°C. Copper capillary tubing was used for most of the pressure lines and the volume of each line kept to a minimum.

Various pressure measuring systems were considered and a 10 inch (250 mm) diameter Budenberg 'Standard Test Gauge' was chosen as representing the best compromise between accuracy and convenience. This is a precision Bourden tube instrument, which is individually calibrated in 0·1 p.s i. (689 N/m^2) increments against air pressure. Its calibration was re-checked against a U-tube manometer, and its linearity was verified when used in the horizontal plane. Initial investigations had shown that perfectly leak free connections could not easily be made though a high speed rate-table or centrifuge, and that it would be necessary to mount the pressure measuring system at the centre of the rotating platform. A simple mechanical gauge allowed this to be done.

Prior to measurements being taken, all connections were leak tested by immersing in iso-propyl-alcohol and applying internal pressure, Running checks were carried out using soap solution applied with a brush and the gauge was tested for internal leaks by sealing the line under maximum pressure; an indicated loss of less than 0·2 p.s i. (1380 N/m^2) in 15 hours being taken as generally satisfactorily.

5.3.1 Unloaded Pressure Profile

This is measured with the bearing supporting the rotor against gravitational forces only (Plate 8).

The bearing and cradle assembly was clamped to an O.M.T.* elevating and rotating table which permitted each pressure tapping to be accurately positioned within the bearing clearance. The 'datum' pressure tapping was first aligned with the table datum using a travelling microscope, and the bearing rotated in increments about its spin axis. Pressure readings were taken at each angular position to give the circumferential pressure distribution around the bearing, and a similar procedure was used to obtain the unloaded axial and thrust distributions. By plotting each reading as soon as it was available, doubtful values could be repeated. Also experience showed that, between tests, it was quicker to approach the position of maximum pressure rather than wait for the gauge pressure to drop after each test. Up to two hours was required for the gauge to pump up to nominal pressure and one hour for the pressure to stabilise between readings!

When examining the performance of a journal bearing alone, the magnetic field of the spin motor was used to support the rotor in the axial direction - no additional thrust location being necessary. It was also observed that the bearing could not be re-started with the gauge still under pressure, due to 'jacking' of the rotor by leakage from the exposed pressure tapping.

The measurements described were repeated on a number of bearing assemblies and over a range of rotor speeds.

The air film temperature, was calculated from the change in bearing clearance when 'hot' (See Appendix III) and used to evaluate the mean film viscosity.

*Optical Measuring Tools Limited

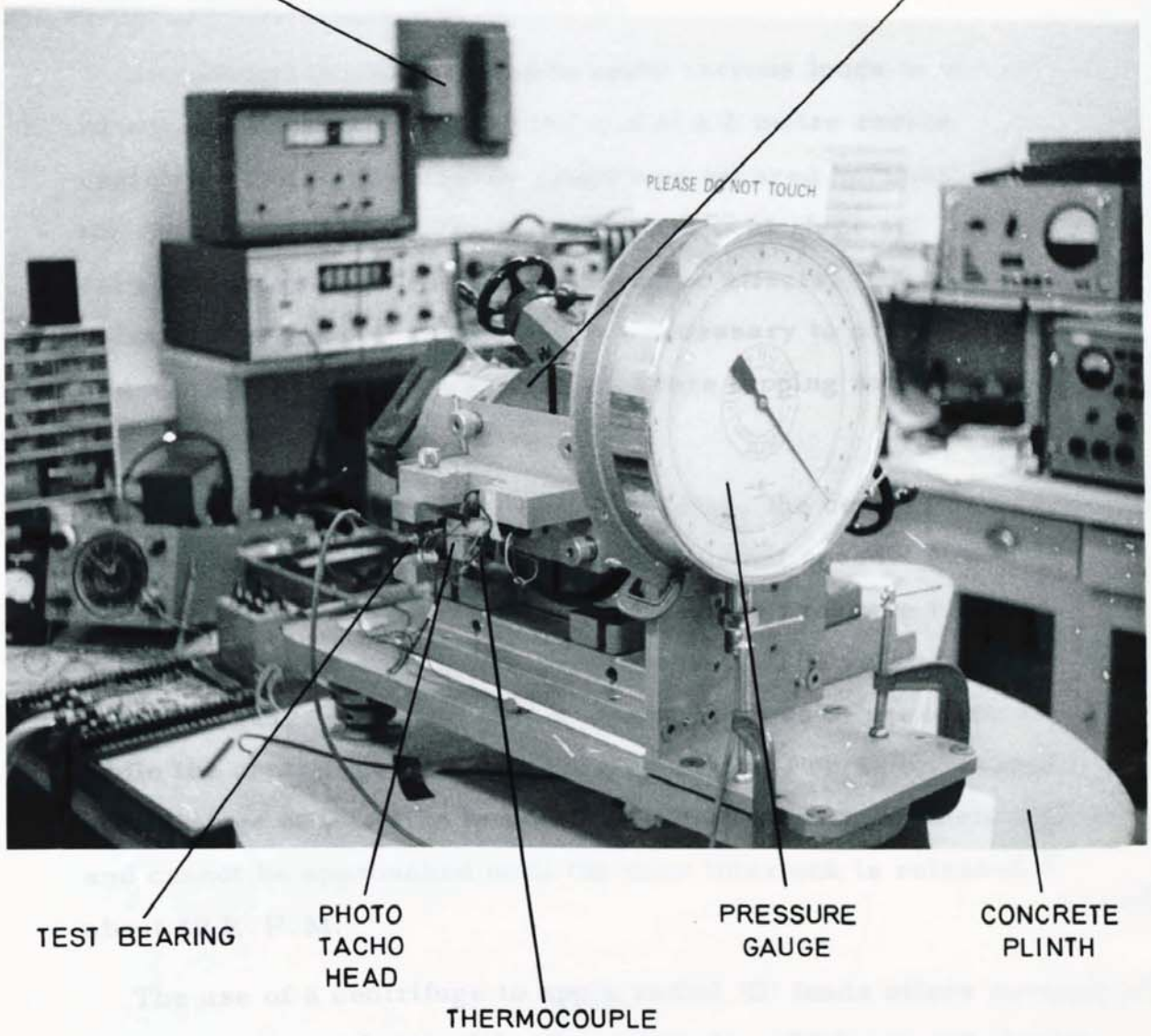

PLATE 8
TEST RIG FOR MEASUREMENT OF
UNLOADED PRESSURE PROFILES

5.3.2 Pressure Profile Due to Radial Loading

This is measured with the journal bearing supporting the rotor against radial loading only (Plate 9).

Centrifugal force was used to apply various loads to the bearing, which was securely bolted to the end of a 2 metre radius centrifuge arm. A pressure gauge was secured horizontally at the centre of the arm, and the rotor and centrifuge spin axes carefully aligned to eliminate gyroscopic effects. Counter-balancing of the centrifuge arm was necessary to prevent vibration and the angular position of each pressure tapping was set using a toolmaker's metal protractor.

After taking an initial pressure reading, the centrifuge arm was rotated for about 15 minutes at some constant speed. The centrifuge was then switched off and the new pressure reading recorded as soon as the arm came to rest. The volume of the pressure gauge was such that a negligible loss of pressure occurred while the centrifuge arm was slowing down. For safety reasons, a centrifuge of this size is operated within an armoured enclosure and cannot be approached until the door interlock is released at about 40 R.P.M.

The use of a centrifuge to apply radial 'G' loads offers several advantages over classical loading methods, which are not always possible on small gyro bearings. Steady loadings of up to 100 'G' can be applied for long periods without introducing an external friction torque. The 'G' force can be precisely controlled and acts through the mass centre of the rotor. In common with other inertial loading methods it allows the eccentricity ratio and attitude angle to be measured relatively easily, using only one capacitor probe. This is described in Section 5.4.

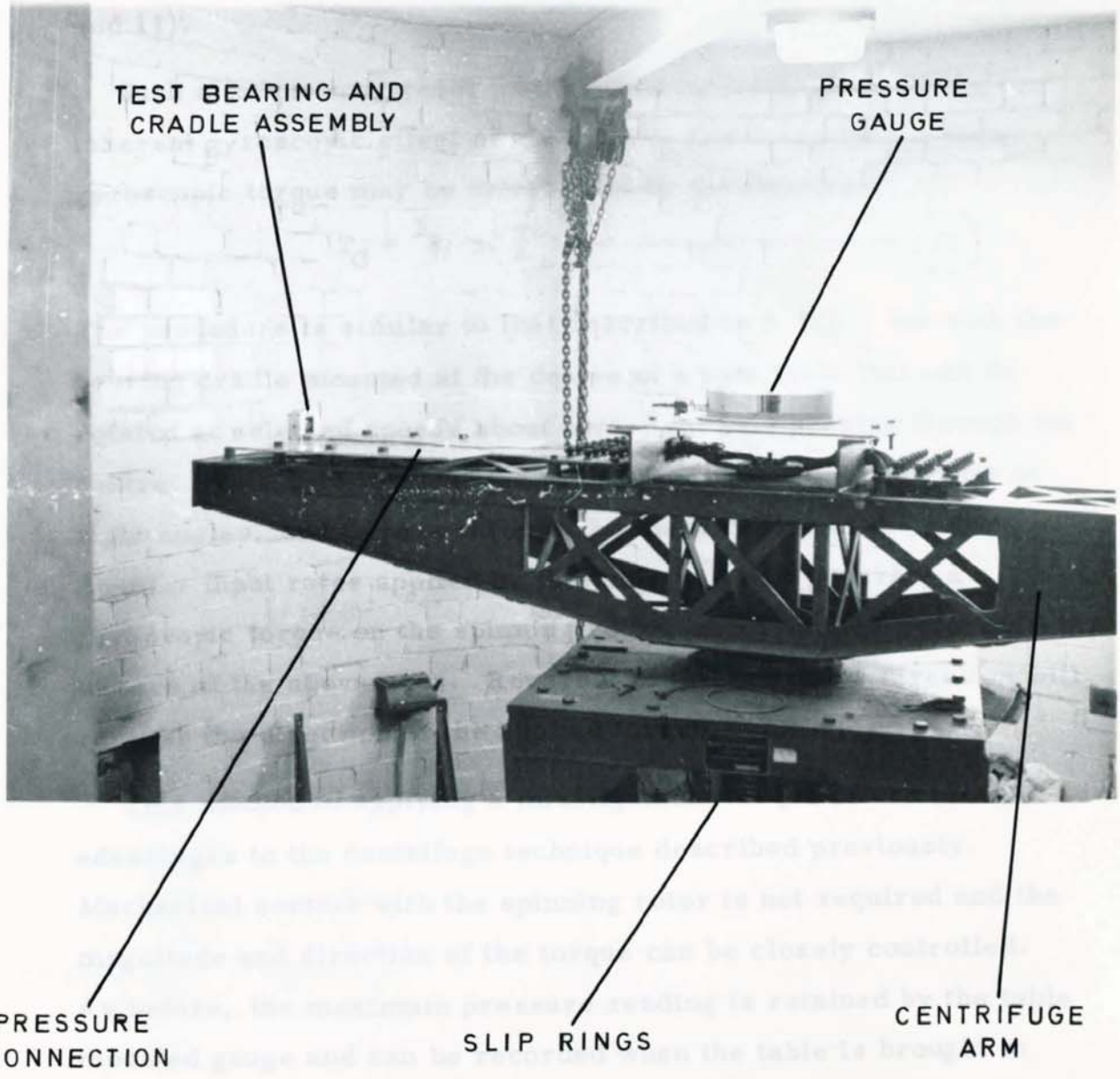

PLATE 9
THE APPLICATION OF RADIAL BEARING LOADS BY MEANS OF A CENTRIFUGE

5.3.3 Pressure Profile Due to Torque Loading

This is measured with the bearing supporting a torque load which acts about an axis perpendicular to the rotor spin axis (Plates 10 and 11).

Such a torque may readily be applied by making use of the inherent gyroscopic effect of the rotor. The magnitude of this gyroscopic torque may be determined by the relation:-

$$T_G = {}^{I}R.\ \omega.\ \overline{\dot{\phi}} \qquad \text{(69)}$$

The procedure is similar to that described in 5.3.2., but with the bearing cradle mounted at the centre of a rate table that can be rotated at selected speeds about a vertical axis passing through its centre. This axis is arranged to intersect the rotor spin axis at right angles, and to pass through the mass centre of the rotor. Angular input rates applied by the table will now generate a gyroscopic torque on the spinning rotor, about an axis perpendicular to each of the above axes. Reversal of the rate table direction will reverse the direction of the applied torque.

This method of applying a misalignment torque offers similar advantages to the centrifuge technique described previously. Mechanical contact with the spinning rotor is not required and the magnitude and direction of the torque can be closely controlled. As before, the maximum pressure reading is retained by the table mounted gauge and can be recorded when the table is brought to rest. Though not necessary in this case, a one-way valve could have been inserted in the gauge connecting line to ensure retention of the pressure reading as the torque load was removed. Provided the gauge was mounted directly over the table axis, its accuracy was not impaired by the rotational speeds involved.

Increased air cooling proved to be troublesome at high input rates, but the bearing temperature (as monitored on a thermocouple) could be maintained by raising the supply voltage, and hence the power dissipation, of the rotor spin motor.

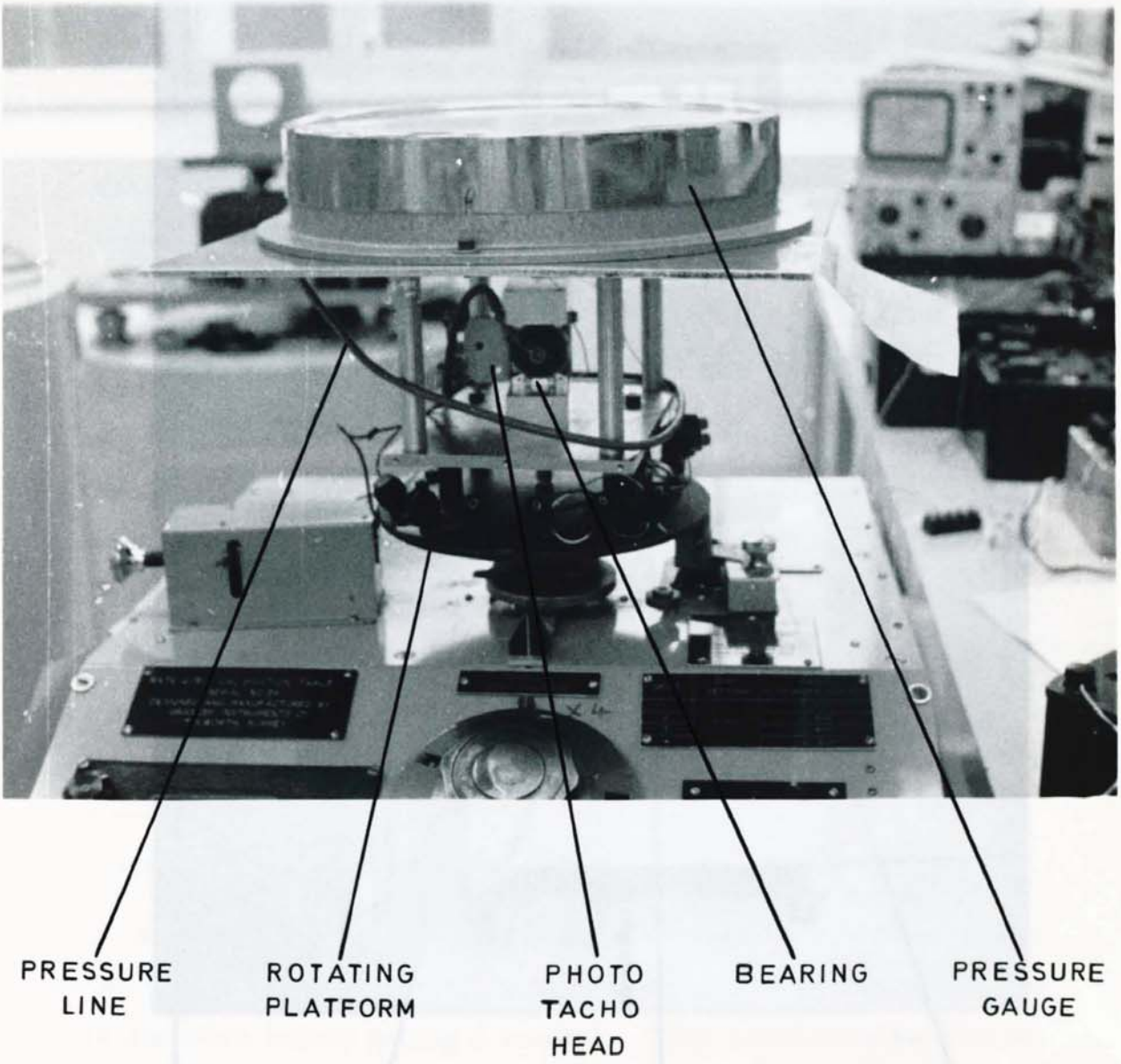

PLATE 10
EXPERIMENTAL DETERMINATION OF PRESSURE PROFILE DUE TO TORQUE LOADING

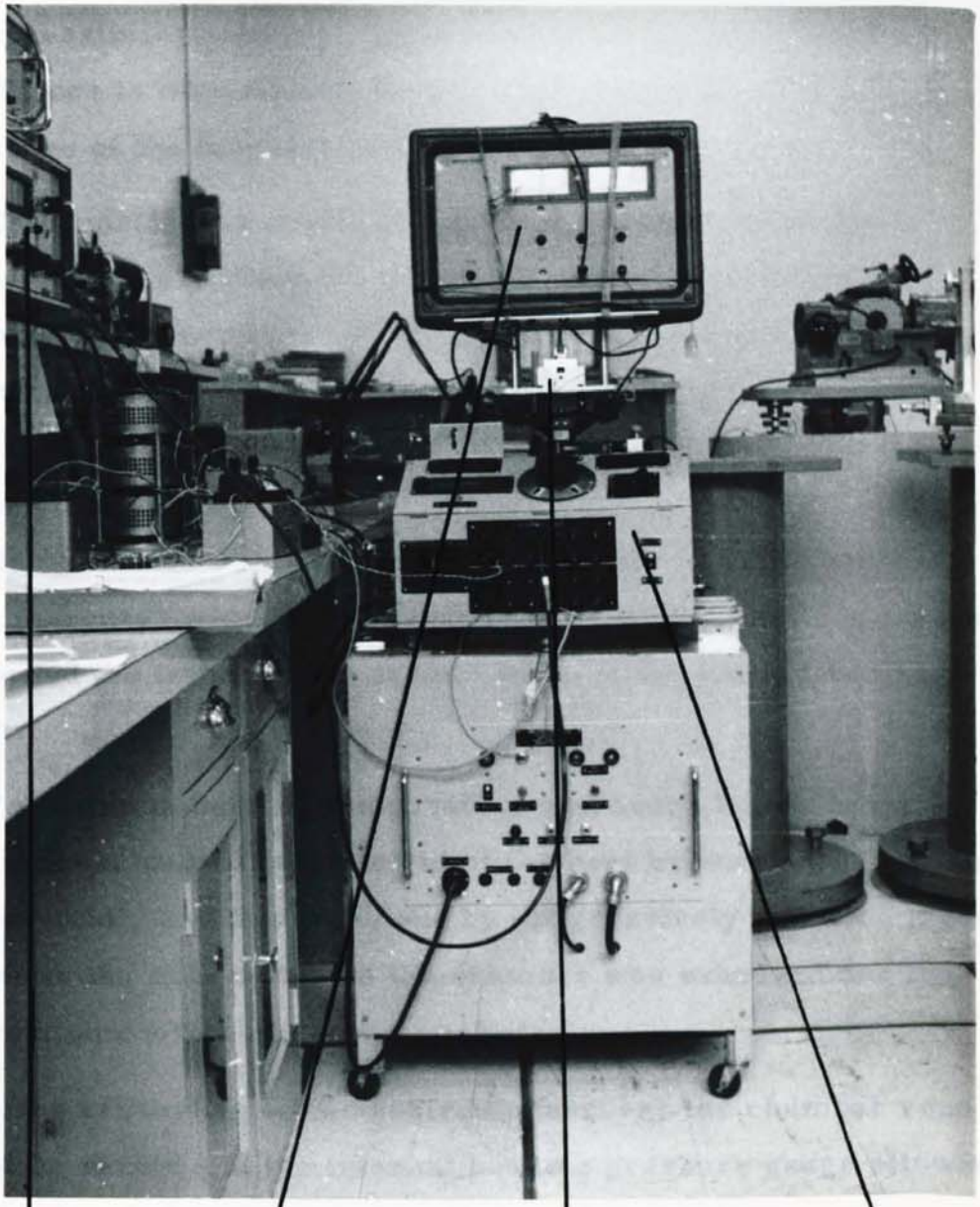

PLATE 11

TEST RIG USED TO APPLY GYROSCOPIC TORQUE LOADS

5.3.4 Pressure Profile at Reduced Ambient Pressure

Apart from providing an alternative means of adjusting the compressibility number, operation under reduced pressure conditions is important in its own right, in order to obtain a measure of the bearing's performance at high altitudes.

The bearing and cradle assembly were clamped within a sealed chamber (Plate 12) whose internal pressure could be reduced by an external vacuum pump. The pressure tapping connection was taken through a seal in the chamber wall to an external pressure gauge and all electrical connections were made via sealed terminals at the rear of the chamber. Internal air temperature was monitored through a plate glass window on a mercury-in-glass thermometer and a thermocouple instrument recorded the temperature at the centre of the journal bearing shaft.

To maintain bearing temperature and hence known bearing clearances, careful adjustment of the heat balance was found to be essential, and this was done by progressively reducing input power to the spin motor as the chamber was exhaused and the convection cooling effect diminished.

After exhausting to the desired pressure, the chamber vent could be sealed and the internal bearing pressure gauge allowed to stabilise before taking a reading. This could take as long as two hours.

It is interesting to note that if a small leak were present at the bearing pressure gague connection, the bearing acted as a viscous pump and would continue to gradually exhaust the chamber.

5.4 Rotor Deflection Measurements

Relative motion between the spinning rotor and its stationary thrust plates and journal shaft under various load conditions was sensed by a capacitor probe, which was rigidly clamped to the test cradle. The probe face was positioned within 0·0005 inch (0·013 mm) of the outer surface of the rotor. The adjustment of this air gap, the lateral position of the probe centre and its

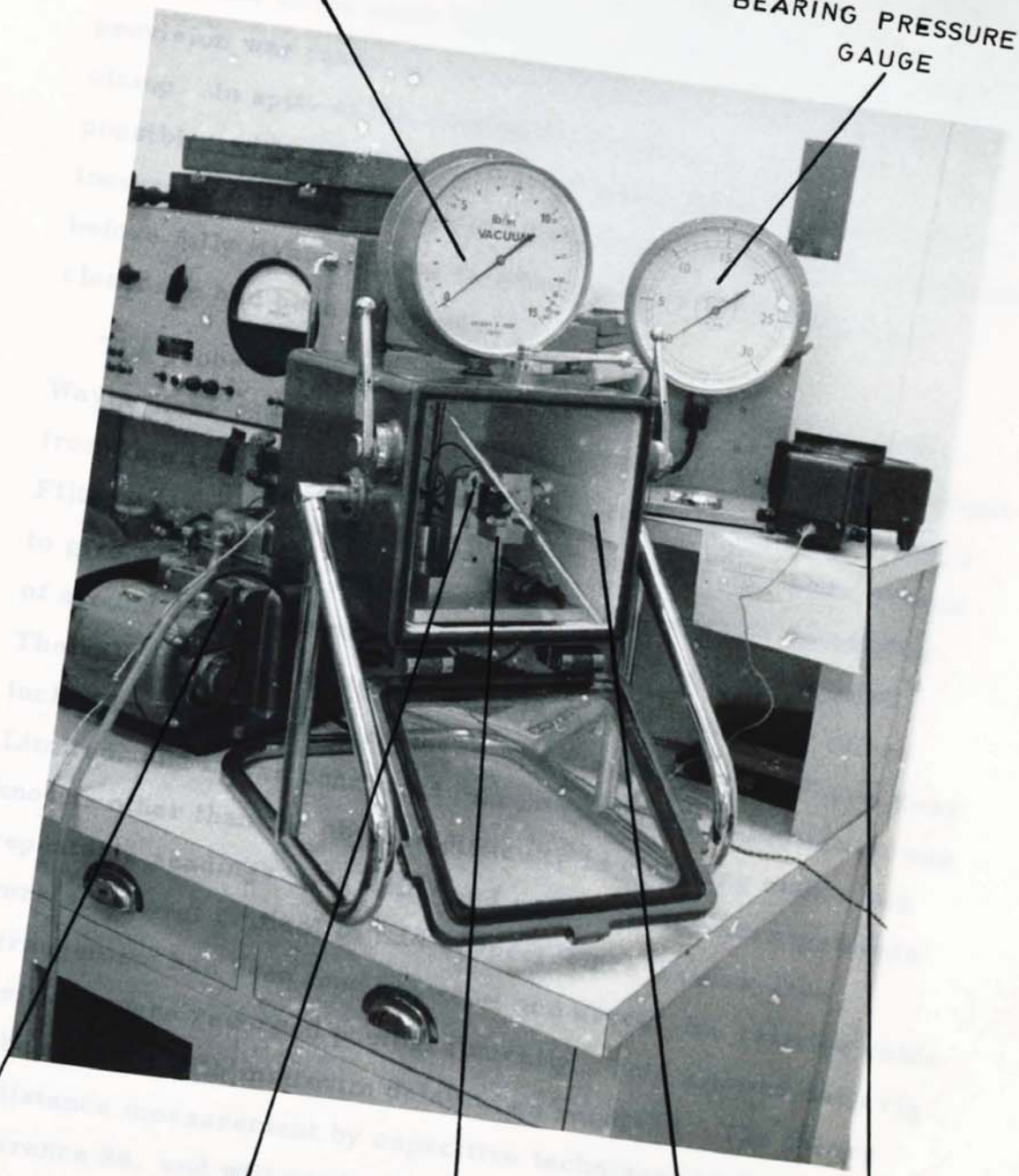

PLATE 12
TEST RIG USED TO INVESTIGATE BEARING PERFORMANCE AT REDUCED AMBIENT PRESSURE

5.4 Rotor Deflection Measurements (Continued)

squareness to the rotor surface were all found to be critical and provision was made for their adjustment by shims and a friction clamp. In spite of the crudeness of this arrangement, it was possible, with practice, to tap the probe towards the rotor in increments of approximately 10 micro inches, (0·25 micro metres) before fully tightening the friction clamp when the desired clearance had been obtained.

The probe energised from and interrogated by a standard Wayne Kerr Distance and Vibraton Meter, and the distance output from this instrument displayed on a digital voltmeter (D.V.M.). Filter, resolution and trip settings on the D.V.M. were chosen to give a reasonably stable reading, and an overall sensitivity of around 25 mV per micro inch deflection could be obtained. The validity of resolving movements of less than a few micro inches by capacitance techniques was discussed with Wayne Kerr Limited, and it was concluded that no fundamental limitation was known, other than the obvious difficulty of obtaining stable and repeatable readings. Earthing and supply wiring arrangements were somewhat critical in this respect. Once a noise-free arrangement had been found by trial and error, the relative cable positions were recorded photographically. This allowed each rig to be re-built with minimum delay when required. The theory of distance measurement by capacitive techniques is detailed in reference 84, and will not be discussed here.

To obtain both magnitude and direction of the rotor's radial displacement, measurements are required in two mutually perpendicular directions. These may then be resolved to yield the eccentricity and attitude angle. It is normal practice to use two orthogonally mounted probes, but since only steady-state readings are required, it is possible to obtain all the necessary information from a single probe by rotating the complete bearing and probe assembly through 90° about the rotor spin axis. The relative positions of the probe and journal shaft are unchanged, but provided the direction of the applied load remains fixed in relation to a reference plane, the probe will now record rotor movements at right angles to the direction of this load.

5.4 Rotor Deflection Measurements (Continued)

However well the probe mounting arrangements are designed and constructed, some mechanical deflection of the probe and test rig structure is inevitable when the assembly is subjected to high inertial loading. In order to eliminate these errors, some previous workers (1) (2) (21) (84) have inserted probes into the actual bearing surface and measured changes in the bearing clearance.

Practical difficulties prevented such an arrangement from being employed here and the following method was adopted.

The test bearing was replaced with a dummy bearing assembly in which the rotor had been firmly shimmed to prevent movement. Deflection measurements obtained from this dummy bearing were therefore a measure of the error due to movement of the capacitor probe alone, and were later used to correct the test readings proper. This error was found to account for about 10% of the actual test measurement in each case.

Prior to each series of readings, the probe was calibrated in situ by rotating the entire assembly through 180°, thus allowing the rotor assembly to fall from one side of the bearing clearance to the other under the influence of gravity. The change in probe output then corresponded to twice the mean radial or axial clearance of the bearing, and could be used to compute the eccentricity ratio and attitude angle directly. By carrying out the above calibration with the bearing at working temperature, allowance could be made for the effect of differential expansion and internal temperature gradients upon the bearing clearance. Reversal of the spin motor phase rotation applied a powerful braking torque to the rotor, and allowed it to be brought to rest rapidly as soon as the working temperature had been reached. Calibration could then be carried out before any significant cooling had taken place.

5.4.1 Unloaded Radial Deflection

Measurement of the rotor displacement due to gravity proved to be the most difficult experimental task of all. To obtain both the eccentricity ratio and attitude angle, it was necessary to resolve rotor movements of less than one micro inch (0·025 micrometres). Though wide experience in the measurement of millivolt signals was available within the Company's laboratory, thermal and electrical drift presented a formidable problem, and special procedures had to be adopted to minimise their effect.

The bearing and probe assembly were firmly clamped to an O.M.T. table which was in turn mounted on a large concrete plinth (Plate 13). With the probe at the 12 o'clock position, a reading was taken and the table quickly rotated through 180° to bring the probe to the 6 0'clock position, where a second reading was immediately recorded. The change in probe output corresponded to twice the vertical component of rotor eccentricity, and the procedure could then be repeated at 3 o'clock and 9 o'clock to yield the corresponding horizontal component. With practice, consecutive readings could be obtained at intervals of about one second, and signal drift during this period could be considered to be negligible.

Spurious electrical signals also presented a problem and to reduce their effect, over thirty sets of readings were taken for each condition and the mean difference in probe output evaluated on a desk computer. All eccentricity ratios and attitude angles were then resolved directly on a H.P.35 digital calculator.

The principle of taking a large number of difference readings very quickly to overcome the effects of drift and electrical pick-up was applied to subsequent deflection measurements wherever possible.

The measurements were repeated on several bearings, over a range of compressibility numbers.

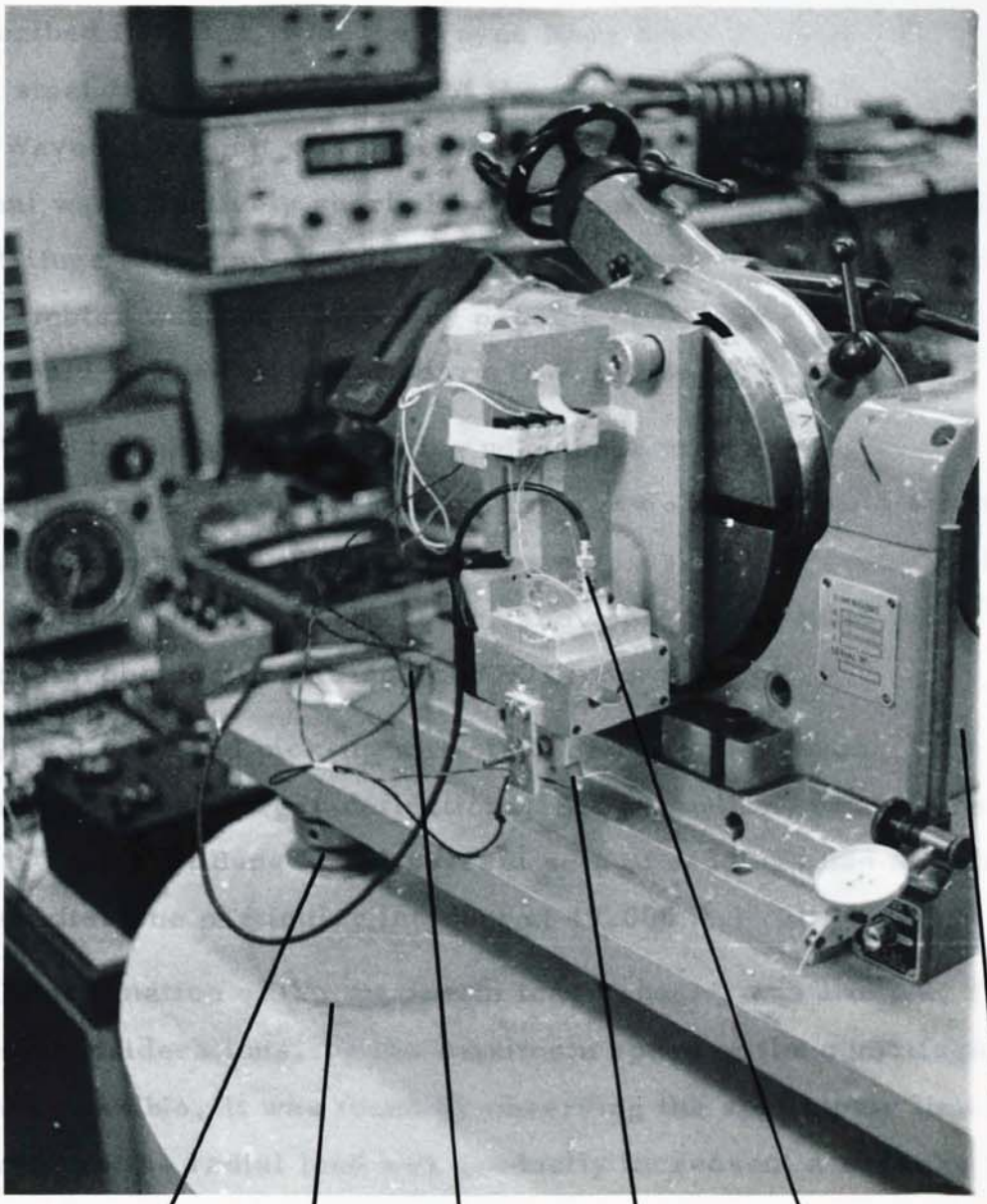

PLATE 13

MEASUREMENT OF ROTOR DEFLECTIONS DUE TO GRAVITY

5.4.2 Deflection Under Radial Loading

Radial loading was applied by the centrifuge technique described in 5.3.2, with the Wayne Kerr distance meter secured in a steel frame at the centre of the centrifuge arm. Rotation of the Wayne Kerr unit was necessary because the 20kc/s probe signal was effectively shorted by the internal capacitance of the centrifuge slip-ring system. The D.C. output from the Wayne Kerr meter was not affected by passing through the slip-rings, and could be read on a stationary D.V.M. as before.

After taking a datum reading with the arm at rest, the appropriate 'G' level was applied for a few seconds and a second reading noted. The change in probe output then corresponded to the radial movement of the rotor, and could be repeated for a second probe position, displaced 90° from the first.

Signal drift and pick-up were less of a problem when measuring these larger deflections, but grounding of the probe was a very real danger and several sets of readings had to be re-taken after one particular incident at 48,000 R.P.M.

Determination of the maximum load capacity was limited, from safety considerations, by the maximum speed of the centrifuge. Where possible, it was found by observing the spin motor line current as the radial load was gradually increased; a sudden change in reading indicating that bearing contact had occurred.

5.4.3 Deflection Under Torque Loading

Torque loading was applied by the gyroscopic method described in 5.3.3. The Wayne Kerr unit had again to be spun on the rate table, to avoid passing the high frequency probe signal through the slip-rings and brushes. This had the added advantage of increasing the inertia of the table, which in turn gave a smoother angular acceleration and a more stable input rate to the bearing (Plate 14).

The probe was mounted at the 12 o'clock and 9 o'clock positions in turn and after recording a datum reading at zero load, clockwise and anticlockwise loads were applied in quick succession and the change in probe output noted.

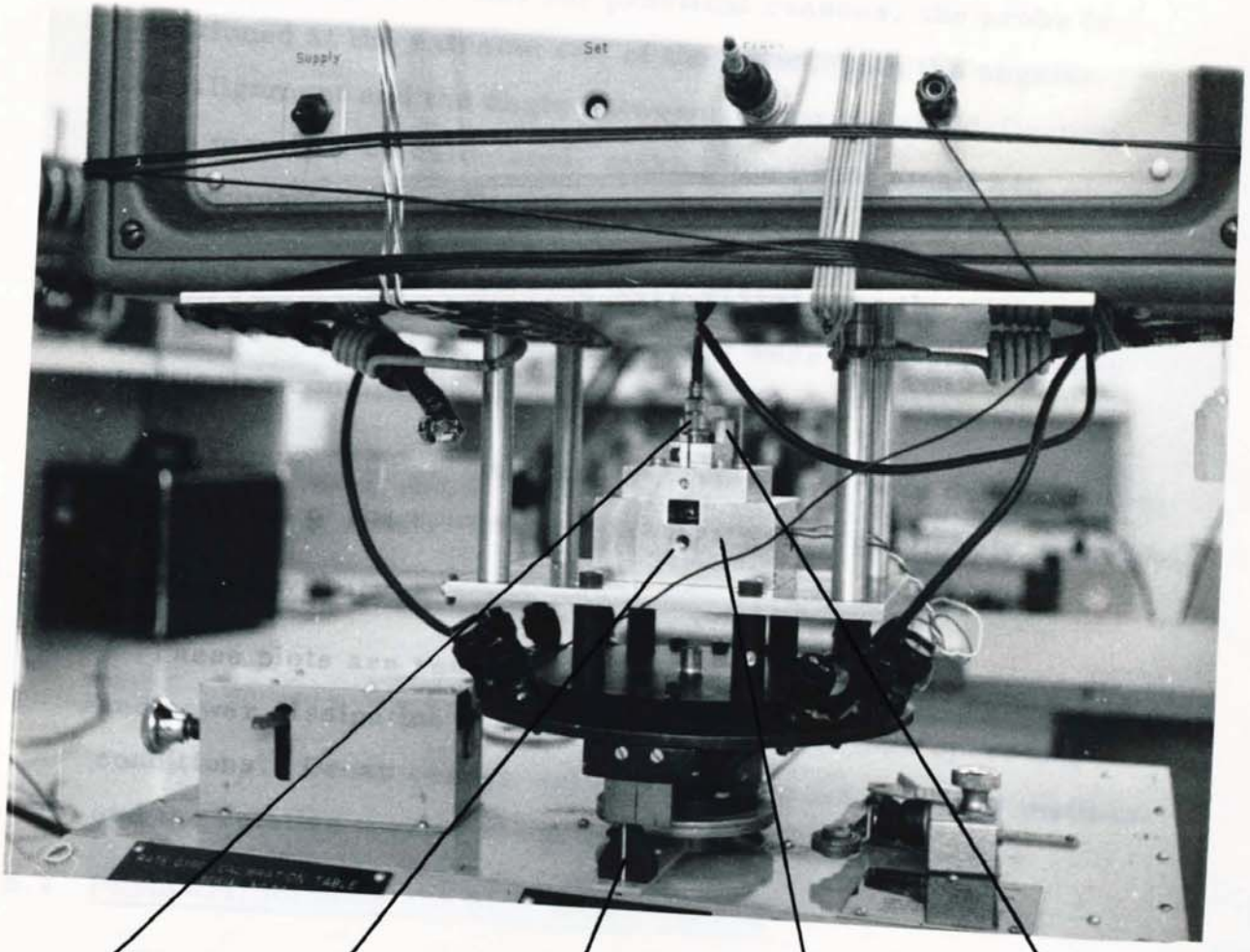

PLATE 14
MEASUREMENT OF ROTOR DEFLECTION DUE TO TORQUE LOADING

5.4.3 Deflection Under Torque Loading (Continued)

From these readings, the local eccentricity and attitude angle could be computed. As, for practical reasons, the probe is positioned at the extreme end of the rotor, both the angular misalignment and the angle between the torque and deflection axes may now be calculated, making the usual small arc approximation to a straight line.

Rotor speed and input rate were varied over the widest possible range, and large numbers of readings were averaged for each particular condition.

Maximum angular load capacity (slew rate) was determined by observation of the spin motor line current as previously described.

5.5 Speed Decay Curves

These plots are required in order to calculate the friction torque and power dissipation of the bearing under various operating conditions. Decay curves were obtained by a number of methods and the relative merits of each are discussed below.

5.5.1 Photo–tachometer and Stop Watch Method

The instantaneous rotor speed is observed on a suitable meter connected to the photo-tachometer output, and on disconnecting the rotor drive mechanism, the time required for the rotor speed to decay to various levels is measured on a stop watch. A speed-time curve may then be plotted.

This method can only be used on an open bearing assembly, but is reasonably straightforward and accurate. When used in conjunction with a rate table or centrifuge, the high impedance low voltage photo-cell output must be processed before feeding through the slip-rings. The photo-tachometer electronics must therefore be attached to the rotating platform.

5.5.2 Photo–tachometer Plus X-Y Plotter

This is essentially the same as the method just described except that the decay curve is plotted automatically as the rotor runs down by driving the X-co-ordinate from a time base and the Y-co-ordinate from the tacho. output.

In practice, accuracy was limited by the performance of the time-base, but this technique is worth considering if very large numbers of bearings are to be examined.

5.5.3 Gyro Output Method

A complete gyroscope is secured to a rate table and a steady angular input rate applied about the input axis of the instrument. The output from the gyro pick-off will now be directly proportional to rotor speed (see equation 69 page 80 and can be used to plot the decay curve directly (5.5.2) as the rotor is allowed to coast to rest.

Unlike the previous methods, it can be used on a sealed instrument, but applies a variable torque load to the bearing as its speed falls. As a method of measuring power dissipation at high angular misalignments, its most serious disadvantage is related to the limitation in gyro output signal at input rates above the design value, though for very high rate instruments this may be less of a problem.

5.5.4 'Virtual' Run-Down Current Method

This technique was devised here, to overcome some of the disadvantages that were found in the methods already described, including the difficulty of measuring the speed of an inaccessable rotor via slip-rings over a wide speed range.

With the spin motor line current displayed on an ultra-violet pen recorder, a bearing running at synchronous speed was de-energised for varying periods of time before suddenly re-applying the original supply voltage and allowing the rotor to re-synchronise. The instantaneous value of line current recorded when power is re-applied is a function of rotor speed, and the coasting time required to reach this speed can be obtained from the recorder time marker.

5.5.4 'Virtual' Run-Down Current Method (Continued)

A plot of 'virtual' run-down current against time can thus be prepared, and it can readily be shown, theoretically and practically, that this curve is identical in shape to a speed/time curve obtained by conventional methods.

The 'virtual' run-down current method offers the following advantages:-

(a) It can be used whenever access to the bearing is restricted i.e. within a sealed instrument.

(b) Speed information can be obtained through slip-rings and the method is therefore readily applied to centrifuge and rate table measurements.

(c) The method will work at any bearing speed.

(d) Accuracy is high and a permanent record of 'speed' and time values is produced.

5.5.5 Run-Down Frequency Method

A second method developed here makes use of the small A.C. voltage developed in the spin motor windings as they are cut by magnetic flux from the coasting rotor.

The frequency of this alternating voltage is directly proportional to rotor speed, and may be displayed on an oscilloscope without introducing any significant increase in electromagnetic drag. If a second trace from a variable frequency oscillator is now displayed and the time base triggered from this latter signal, relative motion between the two traces will first cease as their frequencies coincide.

By setting the reference oscillator to correspond to selected sub-synchronous speeds, a speed-time plot can quickly be prepared with the aid of a stopwatch.

The method can be used on complete instruments over any speed or load range and, due to the low impedance of the motor winding, is unaffected by brushes and slip-rings.

5.5.6 Method of Calculation

The friction torque acting on a coasting rotor is given by the relation:-

$$T_F = I_R \cdot \frac{d\omega}{dt} \qquad (70)$$

Rotor inertia is known and the decay rate term may be found for selected speeds by inspection of the speed-time curve. More accurately, the rate term may be determined by fitting a polynominal function to the speed-time curve on a digital computer, and then differentiating this function analytically.

Once the friction torque has been evaluated, the power loss may be found from:-

$$P_V = T_F \cdot \omega \qquad (71)$$

5.5.7 Correction For Electromagnetic Braking Effects and Windage Error

When driving the bearing by its own hysteresis motor, two forms of error have been found to occur due to electromagnetic braking. The first is a result of currents circulating in the motor winding, induced by residual magnetism in the spinning rotor, and may be avoided by ensuring that each motor winding is open-circuited during the rundown period. The second is due to similarly induced currents in the motor laminations, and must be determined separately before corrections can be applied to the final power figures. This is done by removing the motor stator and driving the rotor from a high pressure air blast directed tangentially across its outer surface. The difference between the two power measurements is an indication of the power loss due to electromagnetic drag.

The residual magnetism, and hence the drag, is a function of the final excitation voltage of the motor, which must be carefully controlled if repeatable results are to be obtained. Use of an air turbine to propel the rotor throughout the experimental period was neither convenient nor practical and the correction method described offered that most acceptable compromise.

Windage losses on the exposed rotor surface were shown to be negligible, by comparing the run-down period of a ballrace supported rotor of similar size in air and in a vacuum.

5.5.8 Alternative Methods of Power Measurement

Many other methods of power measurement are available, but few lend themselves to very small bearings where access to the rotating member is severely restricted.

Torque-voltage curves were prepared for a selected number of spin motors, and the limiting voltage required to maintain synchromism found by observing the 'in synchronism' light on the photo-tachometer. With a knowledge of the torque-voltage relationship, the bearing power dissipation could then be calculated, but this method was found to be less accurate than expected and was quickly abandoned in favour of the decay curve technique.

Direct observation of the increase in electrical power on a wattmeter as the bearing (and therefore spin motor) are loaded was investigated, but meaningful results could not be obtained. It is known that this technique is used successfully in the United States and it seems likely that its successful employment here was limited by the sensitivity of the available instrumentation.

5.6 Run-Up Curves

From plots of speed vs time as the bearing starts and runs into synchronous speed, it is possible to extract both the angular acceleration at the instant of starting and the rubbing velocity during the contact period.

The methods used to obtain these curves are obvious variations on those used to measure speed decay, and need not be re-iterated here.

5.7 Low Speed Contact Characteristics

Rubbing contact between the bearing surfaces as the rotor is started and stopped is of special interest because knowledge about the nature of this contact can lead to a greater understanding of the wear process within the bearing.

5.7 Low Speed Contact Characteristics (Continued)

Contact was examined by a simple electrical continuity method in which D.C. power supply, rheostat and U.V. recorder were connected in circuit with the bearing (Fig.10). A fixed electrical connection was made to the stationary part of the bearing and contact with the rotor by means of a fine wire brush. Copper, gold and silver were tried as brush materials but best results were obtained using tinned copper.

Delicate trimming of the brush angle and pressure was required if either brush bounce or excessive drag were to be avoided. Bearing damage, attributed by previous workers to excessive brush voltage and current, was not experienced; these parameters having been minimised as far as circumstances would permit.

Current flow across the bearing is monitored rather than the actual voltage drop across the clearance described elsewhere (43). In preliminary experiments the voltage drop was displayed across an oscilloscope but permanent records were more conveniently obtained by monitoring circuit current using a U.V. recorder. This current flow will be proportional to the resistance which will in turn be a function of contact area and surface electrical properties. Interpretation of the resulting traces must take into account both the finite frequency response of the recording galvonometer (2000 c/s) and its mechanical inertia. The inertia will lead to an overshoot of the galvonometer which is clearly visible on some of the traces. The mean position of the galvonometer will therefore be a function of both the contact resistance and the period of contact. Where the frequency of contact is less than the natural frequency of the galvanometer, rapid fluctuations may appear on the trace while at contact frequencies above this natural frequency the galvonometer will adopt some intermediate station. This is analogous to using the brightness of a contact light to give an approximate indication of contact areas, as discussed in reference 21. Alternative recording methods were considered, including direct photographic recording from the oscilloscope tube and the use of an oscilloscope with electronic storage facilities, but these were rejected on practical grounds.

SCALE 1:1

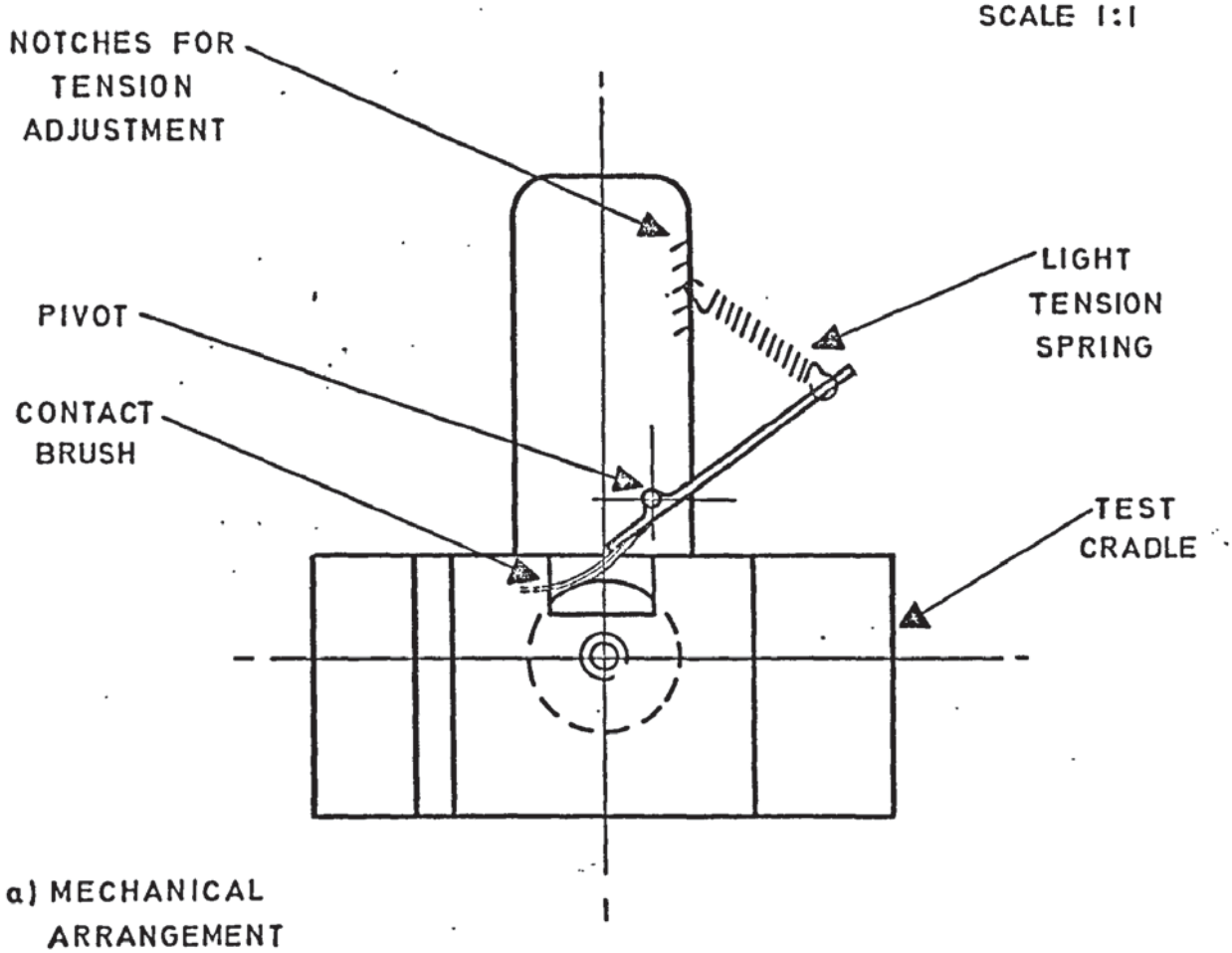

a) MECHANICAL ARRANGEMENT

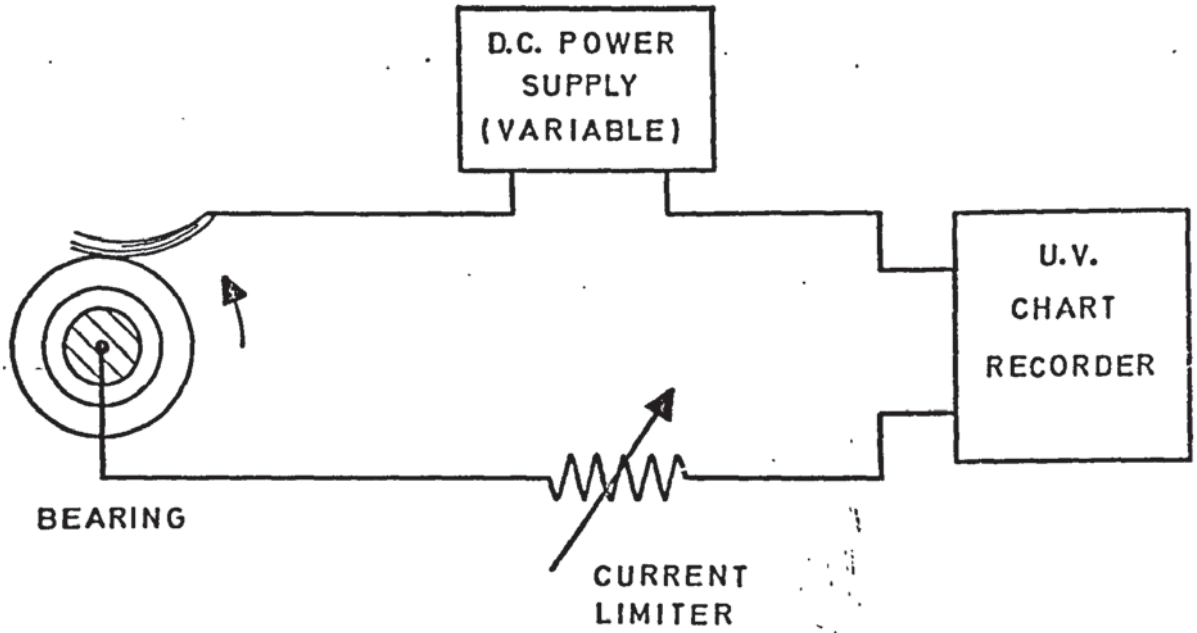

(b) ELECTRICAL CIRCUIT

FIG. 10
CONTACT INVESTIGATION RIG

5.7 Low Speed Contact Characteristics (Continued)

Starting characteristics were recorded for several accelerating torques (by adjusting the voltage to the spin motor) and touchdown contact examined as the rotor coasted to rest.

Several different combinations of rotor inertia and bearing geometry were studied, and the electrical indications of rubbing substantiated by listening to audible sounds of bearing contact on a medical stethoscope.

The duration of each phase of contact was measured with reference to the U.V. recorder's time marker.

5.8 High Speed Contact

Rubbing contact at synchronous speed was not studied in detail but a qualitative assessment has been carried out on a small number of bearings.

The most convenient method of inducing overload is by exceeding the bearing's maximum slew rate, but where this is not possible, a vibrator may be used to excite whirl-induced rubbing.

5.9 Static Friction Coefficient

Starting friction may be measured in the classical manner by attaching a light thread to the rotor, leading the free end over a pulley and attaching weights to this end until the rotor is just seen to turn. This classical method, though accurate, is too cumbersome and time consuming for general use, and it is necessary to make alternative arrangements when large numbers of bearings are to be examined.

Calibration curves of stall torque against applied voltage were obtained for each spin motor in a special test rig, prior to assembly of the bearing. When required, the minimum voltage at which the rotor will just start is determined and, knowing the rotor mass and torque-voltage relation, a value for the friction coefficient may be obtained.

5.9 Static Friction Coefficient (Continued)

In practice, close control during manufacture resulted in very little variation from motor to motor and the average torque-voltage relation could be used in each case.

This indirect method of measurement is not as precise as the direct classical method, but in work of this kind, relative changes in friction coefficient are belived to be more important than an accurate knowledge of the numerical values concerned. Neither method can provide a pure torque and in each case, a small increase in radial load will occur.

5.10 Detection of Rotor Charge

Following the discovery of unusual surface damage (Plate 22, Page 144) on a bearing that had run continuously for several months, various attempts were made to detect the formation of electrostatic charge build-up on the spinning rotor.

A quartz fibre electroscope was used to probe the moving rotor surface via a small wire brush, but problems were experienced due to contact bounce and the readings were inconclusive.

Similar experiments to measure transfer charge on the stationary bearing components, while insulated on a 'Perspex' vee-block, were also unsuccessful. This may have been due to charge leakage across the winding insulation of the motor, which had to be driven from an earthed supply to maintain the rotor speed.

In a final attempt to detect internal spark discharge, bearings were operated within an electrically screened enclosure. A high sensitivity, wide band, radio receiver was then used within the enclosure to monitor both radiative and conductive emissions from the bearing; experience having shown that radio waves are generated by even the smallest electric spark. No radiation could be detected.

A high voltage generator was then connected in series with a resistor and loudspeaker across the bearing clearance. By gradually increasing the voltage and listening for audible sounds of breakdown, it was established that the breakdown potential was in the region of 100 volts for a 120 micro-inch (3 micro metres) clearance.

5.10 Detection of Rotor Charge (Continued)

It has been observed that the D.C. resistance across the bearing clearance was less than infinite during normal bearing operation. To eliminate humidity effects, a bearing was sealed in a glass jar, together with a quantity of phosphorous pentoxide dessicant, and run against one thrust plate for 24 hours to ensure adequate circulation of air within the bearing. No change in air film resistance could be detected.

5.11 Differential Coefficient of Expansion

Unless this expansion coefficient for the bearing materials is accurately known, the running clearance at operating film temperature will be in question, and this error will be transferred to the calculation of the appropriate compressibility number.

A typical set of bearing components were wrung axially onto an optical base plate, and an optical flat then wrung across the polished end face of the rotor (Fig. 11). The bearing components and base-plate were then immersed in an oil bath, which could be heated electrically, and whose temperature could be measured on a mercury-in-glass thermometer. Interference fringes between the optical flat and the shorter journal shaft could then be counted through a microscope and graticule system as the relative rotor and journal lengths changed with temperature.

A ruby laser* was originally used to illuminate the fringe area but the specular nature of the reflected light made fringe counting difficult and later measurements were carried out with a mercury vapour source of known frequency.

* The equipment was operated by Mr. S. Searle of Smiths Industries Limited

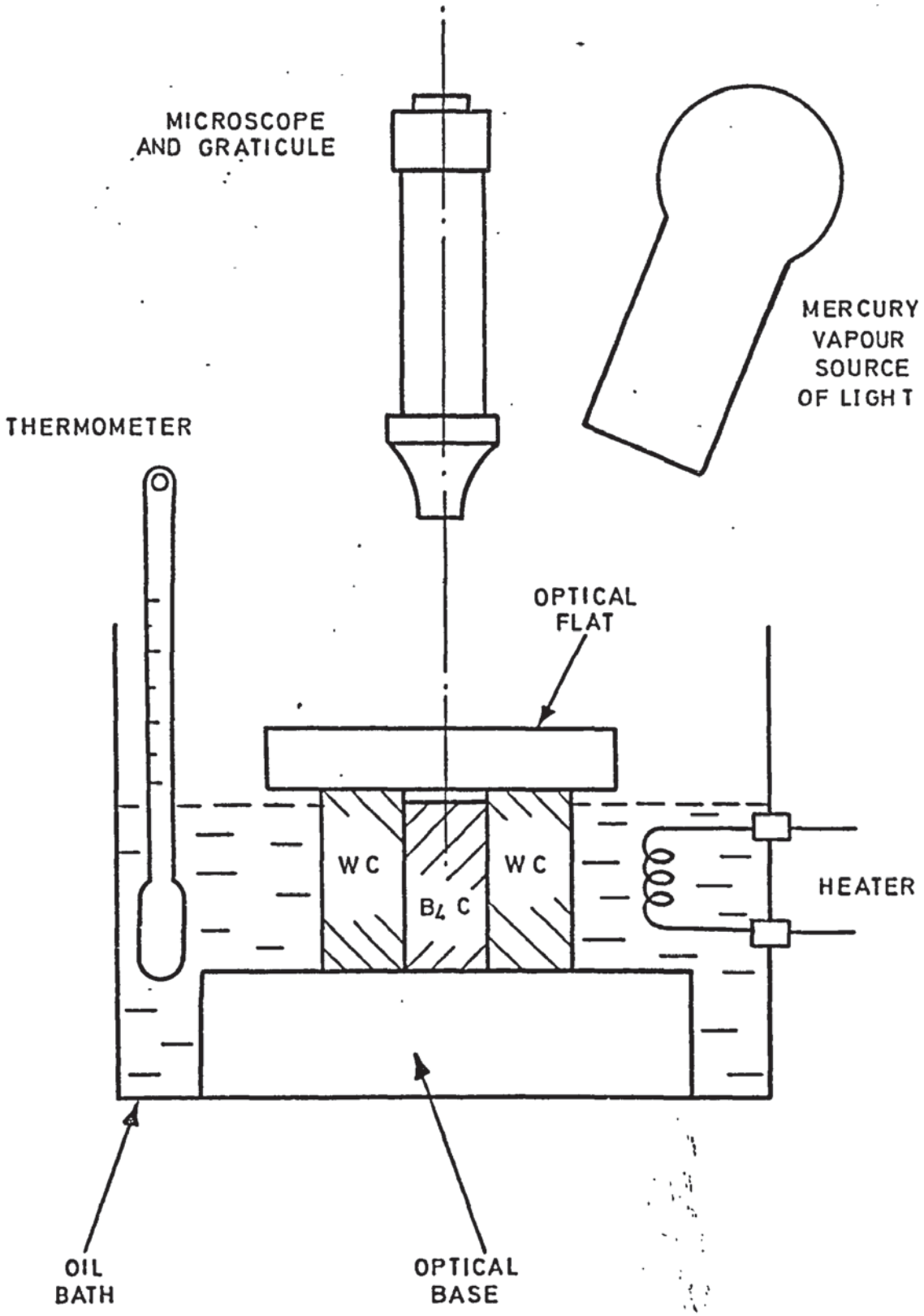

FIG. 11
EXPERIMENTAL
MEASUREMENT
OF DIFFERENTIAL
EXPANSION
COEFFICIENT

5.11 Differential Coefficient of Expansion (Continued)

The mean differential coefficient was measured over the temperature range +20°C to +120°C and it was assumed that the axial (measured) and radial coefficients would, for all practical purposes, be equal. Caution is normally necessary when using published expansion coefficients, as these are frequently measured over inappropriate temperature ranges, and small errors in the nominal values can lead to large errors when the differential coefficient is derived.

When measuring differential coefficients, the major problem lies in isolating the metrology equipment from the imposed temperature changes, and for this reason, optical methods are generally more suitable. An alternative optical arrangement allows the differential expansion to tilt a beam bridging the two components, on which is mounted the mirror of an autocollimator measuring system. Direct measurement of the expansion coefficient may be carried out using either a quartz dialotometer or a calibrated strain gauge. The numerical value tends to decrease as the purity of the material improves, and care is required to ensure that the samples chosen are fully representative.

If only a quick verification of the differential coefficient is needed, sophisticated equipment is not essential and by selecting a journal bearing with a sufficiently small (known) clearance, the temperature at which the shaft no longer slides freely in the rotor can be established. This temperature change, together with an accurate knowledge of the bearing geometry, yields a useful value for the differential coefficient.

5.12 Statistical Investigation of Geometry and Performance

Early experimental work (116) seemed to indicate significant changes in bearing test performance as a result of sequential variations in environmental and operating conditions.

It was decided to investigate these changes in a quantitative manner on a larger sample of bearings, to determine the true significance of the changes, and, in particular, to establish if any correlation existed between performance and bearing geometry.

5.12 Statistical Investigation of Geometry and Performance (Continued)

Selection of the parameters to be investigated was based partly upon previous laboratory experience, and partly on a knowledge of the specialised setting-up and 'burn-in' procedures that are required on production instruments. The measured performance variables were further limited by the dual requirement of being non-destructive measurements that could eventually be implemented by non-specialised personnel.

A total of 83 bearings were used in the investigation and 17 geometric parameters were recorded for each. Thirty one stylus traces were taken at selected positions over the surface of each bearing and the resulting graphs (at linear magnifications up to 14,000) provided a permanent record of their major geometric features. The principal performance features under investigation, including bearing friction, time to reach synchronism and coasting time were measured using methods already discussed. Friction was recorded at two circumferential positions around the journal bearing and after changes in performance had been evaluated, a total of 55 variables were available for analysis.

Since some of the above variables were also a function of spin motor performance, special care was taken to stabilise the motor characteristics by repeated temperature cycling and testing, during and after manufacture.

After initial assembly of the bearing, the appropriate parameters were measured at +20°C. The bearings were then placed in a sealed metal container and temperature cycled between -65°C and +110°C. Three cycles were applied with the bearing remaining at each temperature extreme for two hours. After re-measuring the performance at room temperature, each bearing was built into a gyroscope and the bearing performance assessed for a third time. Each instrument was then sealed in a metal container and the previous temperature cycling repeated. As before, the bearing remained un-energised throughout the cycling period.

5.12 Statistical Investigation of Geometry and Performance (Continued)

On reaching room temperature the performance was again checked before fitting into a temperature cabinet. The bearings were then energised and run at ambient temperatures of -30°C, +20°C and +70°C for periods of two hours. Two such cycles were carried out and limited torque loads were applied to the rotor while at each steady temperature.

After the usual measurements, each bearing was then made to perform 200 start/stop cycles in each of the orientations used for friction measurements, after which all measurements were repeated.

Finally, each bearing was run continually for two periods of 40 hours at +20°C before its performance was measured for the last time.

In this way, a complete history of selected aspects of the bearing's performance was obtained over a sequence of different environments and operating conditions. The parameters measured are of particular interest, since it was believed that these had a significant influence on the operational life and reliability of the bearing, and the test sequence was closely related to that which a typical bearing might undergo prior to and during normal service.

On completion of the above tests, approximately 10% of the test sample were subjected to mandatory environmental testing (necessary to obtain Civil Aviation Authority approval for the complete gyroscope) and system testing on a simulated aircraft flight control system rig. The remainder were fitted to commercial passenger carrying aircraft and operated under normal service conditions. Bearing reliability and life were continuously monitored throughout.

5.13 Flow Visualisation Rig

Measurement of viscous power loss eventually led to the discussion of a number of possible flow patterns around the grooved region of the bearing (section 6.3). Because these flow patterns were of a purely speculative nature and not readily predictable by analytic methods, it was considered important to attempt an experimental investigation of fluid flow in the region of a typical groove.

In order to examine the flow pattern in detail, it became clear that a large scale model would be required. The use of such a model, in conjunction with a suitable liquid, would allow incompressible flow patterns to be studied fairly easily, but for visualisation of compressible flow, some form of high pressure wind tunnel would be required in order to match both the Reynold's and compressibility numbers to those in the actual bearing. Whilst the latter arrangement would have been preferable it was decided to limit this particular investigation to incompressible flow in view of the prohibitive cost of constructing a compressible flow rig.

The incompressible flow rig (Plate 15) was constructed from a domestic baking tin of 190 mm diameter. A thin plastic window was formed in the wall of this container, through which the flow patterns could be observed. This window was curved to match the radius of the wall, in order to minimise its influence upon the adjacent flow pattern. The stationary grooved surface was fabricated from expanded polystyrene ceiling tiles and secured to the base of the tin with adhesive. This material proved to be ideal for modelling the bearing surface, since it could be easily shaped with the aid of either a hot wire or a razor blade. Additional sections could be added if desired after the chamber had been filled with liquid and secured in place with pins. The surface texture of the land or groove surface could be modified with the aid of a heated blade, but it was noted that polystyrene in the 'as moulded' condition had a scaled-up surface texture corresponding closely to that obtained on boron carbide by the ion-machining process.

PLATE 15
EXPERIMENTAL RIG FOR FLOW VISUALISATION.

5.13 Flow Visualisation Rig (Continued)

The moving surface was provided by the circular base of a second baking tin which could be rotated about its axis with the aid of an electric power drill. By using the drill gearbox in conjunction with an electronic speed controller, the rotational speed of the simulated bearing surface, and hence the Reynold's number, could be varied at will, though in order to obtain the very lowest speeds it was necessary to disengage the gearbox and rotate the drill spindle by hand. The whole assembly was mounted on a vertical drilling stand, which allowed the rotating plate and power unit to be raised or lowered in order to vary the separation between the stationary and moving members. Glycerene ($C_3 H_8 O_3$) was chosen as the most suitable fluid because its high viscosity allowed the model to operate at very low Reynold's numbers, while maintaining realistic rotational speeds and clearances. Magnesium swarf was broken into small chips and suspended in the glycerine. These magnesium particles were clearly visible under strong illumination, and allowed the flow of fluid past the window to be observed. In order to obtain extra contrast, the polystyrene surfaces and the interior of the enclosure were painted matt black. Magnesium was selected as a tracer material because its specific gravity (1.74) was sufficiently close to that of glycerine (1.26) to allow it to remain in suspension for the duration of the experiment. In practice, the use of flat chips of metal as opposed to rounded granules assisted in this respect, and allowed viscous forces to predominate over gravitational forces at the very lowest rotational speeds involved (0·016 revolutions per second).

Using this rather rudimentary apparatus, it was possible to observe and photograph the flow characteristics around a variety of groove formations as the rotating disc caused the fluid to circulate within the chamber. In addition to observing the overall flow pattern, study of the movement of an individual tracer particle allowed the relative velocity components to be estimated at low Reynold's numbers, and any regions of either stagnant or reverse flow could quickly be identified.

5.13 Flow Visualisation Rig (Continued)

While visual observation of the various flow patterns presented few problems, successful photography of the flow proved to be more difficult. Suitably chosen time exposures allowed each magnesium particle to form a continuous trace of its motion across the film; each streak on the photograph corresponding to a streamline in the flow pattern. This arrangement worked very well for some configurations, but limitations associated with the lighting and film speed eventually restricted the use of photography when running clearance fell below about 0·5 inches (13 mm).

CHAPTER 6

DISCUSSION OF RESULTS

In this chapter, the experimental and theoretical results are discussed in detail, and comparisons made with prior work where appropriate.

6.1 Low Speed Contact Characteristics

Low speed bearing contact was investigated using the electrical continuity method described in Section 5.7. The principles of this technique are considered in CHAPTER 2.

Despite the limitations outlined in CHAPTER 2, it is thought here that continuity methods are still a useful tool for investigating low speed contact characteristics and that many of the problems associated with their application to oil bearings will not necessarily apply to gas lubrication. While the validity of their use for contact area measurement is in doubt, they provide a valuable comparative assessment of the bearing behaviour.

Bearing contact as the rotor coasted to rest was recorded for a number of experimental bearings and a selection of the traces obtained is included in this report. In most cases, three distinct phases of contact could be identified (Figs.12 and 13). Initially, contact was intermittent as the rotor appeared to be bouncing over the tips of the asperities on either bearing surface. This bounce-contact region was followed by an intermediate or transition phase which probably corresponded to more frequent contact between the asperity regions. The third region was characterised by a smooth trace which indicated a gradual decrease in contact resistance and culminated in a sudden increase in current as the rotor assumed its fully grounded state. As far as could be ascertained, this final jump in current corresponded to the instant that rotation ceased. The preceeding trace is believed to correspond to a region of true sliding contact between rotor and journal. On bearings with good overall geometry and surface finish the three regions were generally well defined, but as these properties deteriorated, their boundaries grew less distinct and bounce-contact predominated. Where the overall bearing geometry was good, the bounce-contact region and the transition phase occupied approximately equal

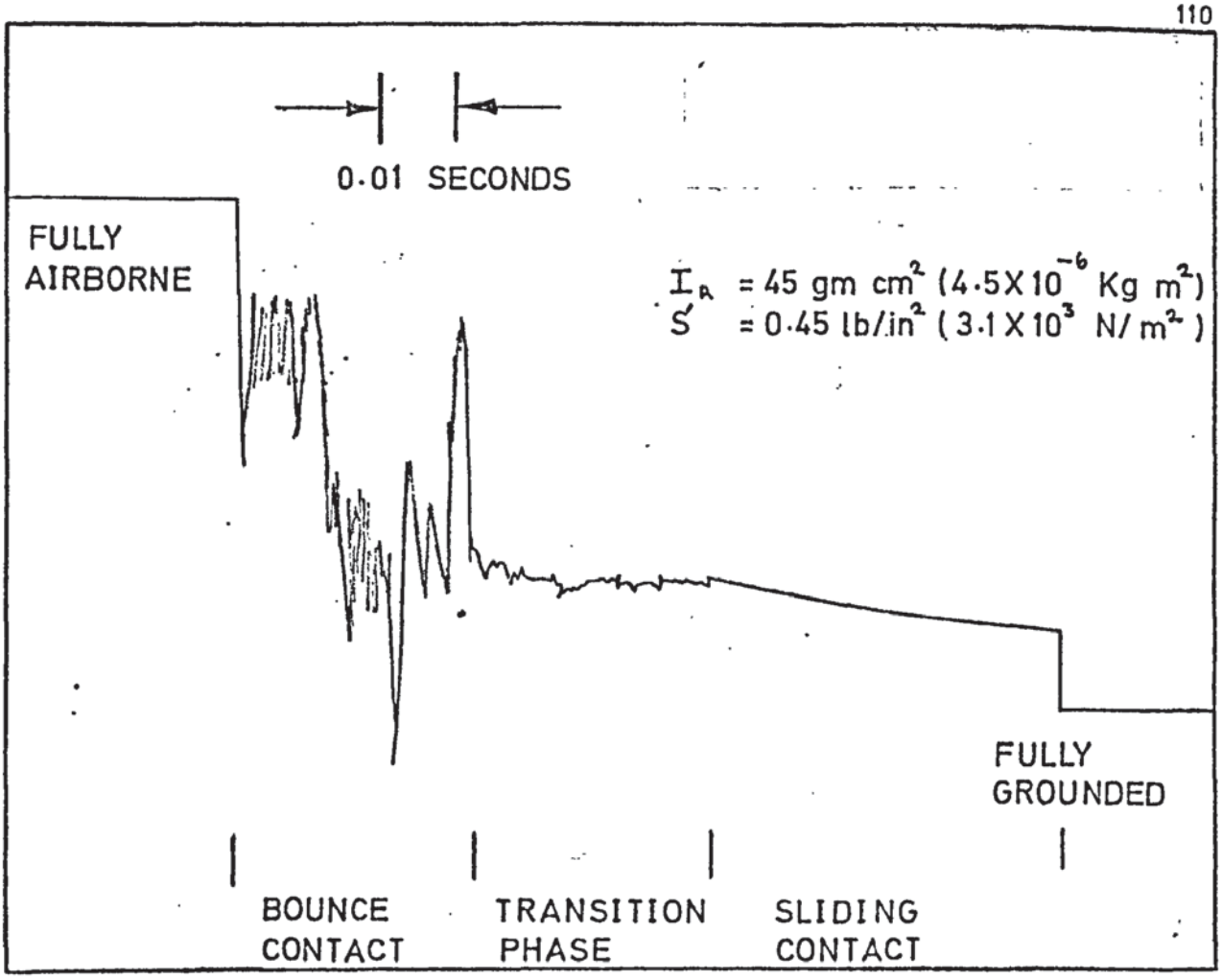

FIG. 12 BEARING CONTACT DURING TOUCH-DOWN (Experimental)

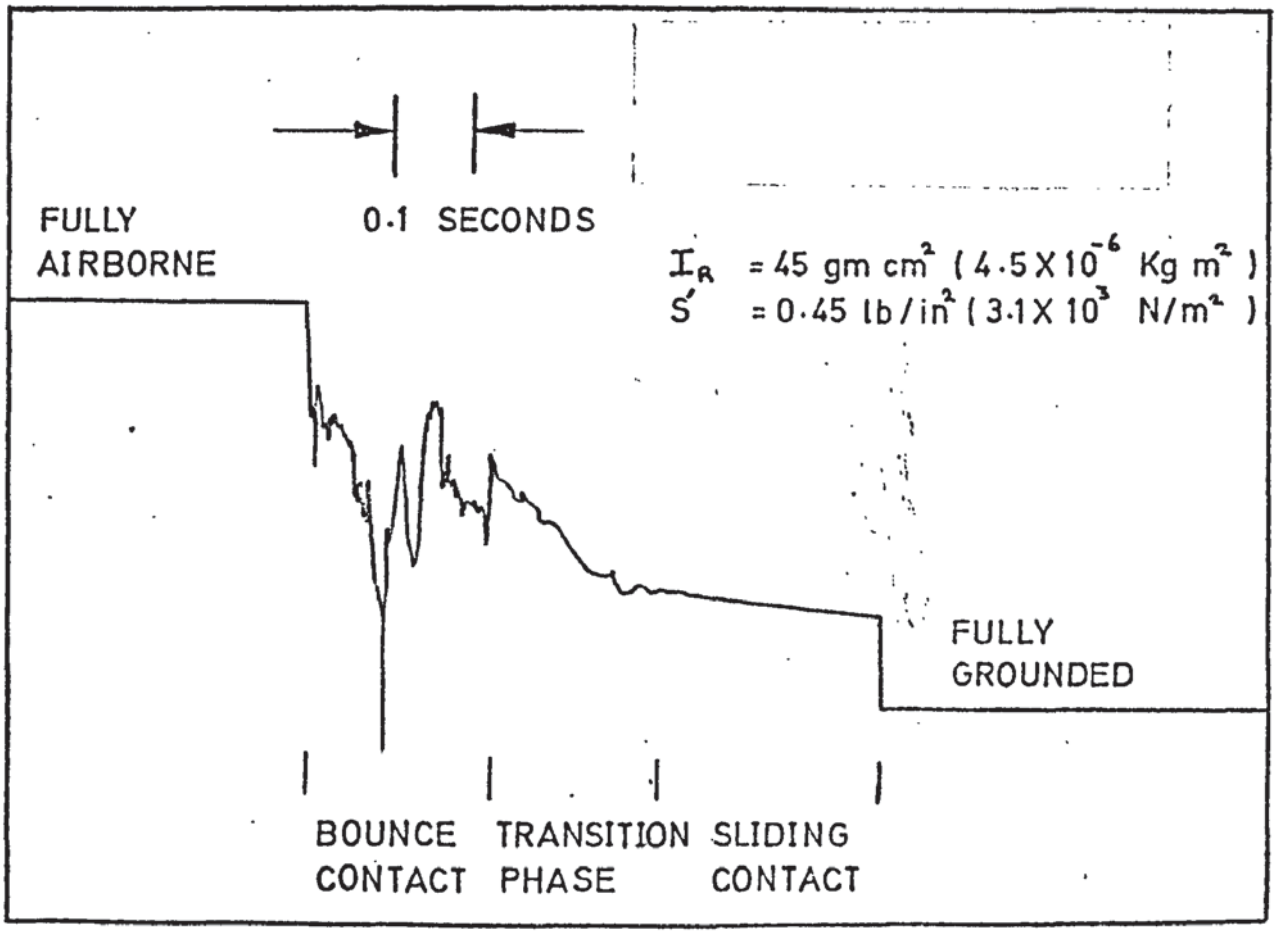

FIG. 13 BEARING CONTACT DURING TOUCH-DOWN (Experimental)

periods of time but sliding contact normally continued for a rather longer period. The entire contact period varied considerably from one bearing to another for no clear reason and periods of between 0·7 seconds and 0·11 seconds were recorded, with sliding contact periods of 0·3 and 0·05 seconds respectively. Despite careful adjustment, brush friction considerably increased the rate of speed decay and since the total run-down period was decreased by 25%, it is assumed that a similar error is present in the overall contact period. Over the region of bounce-contact, the continuity trace was not repeatable and jumped from one mean level to another in an unpredictable fashion. In contrast, the transition and sliding regions were found to be fairly repeatable and the mean current flow between different bearings of identical design was very similar.

The traces shown in Figures 12 and 13 were obtained from tungsten carbide - boron carbide bearing surfaces. When using this latter material, a characteristic squeak is occasionally audible during the touchdown period. The frequency of this sound is approximately 3 K c/s and its duration has been estimated to be in the order of 0·25 seconds. It was first noted here during 1968 and has since been confirmed by other workers (107). Only boron carbide appears to demonstrate this effect in gyro bearings and it is almost certainly due to some form of stick-slip motion during the region of sliding contact. Its approximate duration, and the fact that its amplitude builds up gradually and decays abruptly, both tend to confirm this assumption. A similar noise has been noted by Bowden & Tabor (39) between heavily loaded steel surfaces and in this case, the frequency could be associated with the natural frequency of the support. For this bearing, the natural frequency of the stationary members to both axial and lateral vibrations was shown by calculation to lie well above the audible range. Audible vibration must therefore be due to variations in angular motion of the rotor about its spin axis during contact. The occurrence of the squeak in a gas lubricated bearing invariably corresponds to a higher level of starting friction and is more likely to occur at high specific loadings. In practice, the squeak may not persist for long and its intermittency and infrequency have so far frustrated all attempts at serious investigation and measurement.

6.1 Low Speed Contact Characteristics (Continued)

In Figures 14 and 15, the combined effects of rotor inertia and poor bearing geometry are clearly illustrated, For the bearing shown in Figure 14, occasional contact is recorded up to 26 seconds before the rotor came to rest and severe contact took place over the last five seconds of the run-down period. In this case, the intermittent contact is attributed principally to roundness errors in the rotor bore and the mechanism of this contact is discussed more fully in section 7.3.2. For this particular rotor, roundness errors of up to 20 micro inches (0·5 micrometres) were recorded and these errors alone accounted for over 20% of the mean radial clearance. Bearing contact remained irregular throughout the actual touch-down period and there was no evidence of true sliding contact, though this may also be due to the comparatively poor surface finish on these bearing surfaces (up to 3 micro inches C.L.A., 0·07 micro metres C.L.A.). Figure 15 shows that as roundness and geometry in general are improved, intermittent contact prior to touchdown is reduced and evidence of transition-type contact can just be seen. Roundness in this case was 10 micro inches (0·25 micro metres) and both surfaces finishes were around 1 micro inch C.L.A. (0·02 micro metres C.L.A.). For the bearing shown in Figure 14, the theoretical touchdown speed was computed to be 0·8 revolutions per second, while the actual measured speed immediately prior to rotation ceasing was 1·0 revolutions per second. However, it is evident from the trace that substantial contact occurs long before the nominal touch-down period and in the case considered, initial contact corresponded to rotational speeds of around 20 revolutions per second. Similar findings are obtained from the bearing in Figure 15 where theoretical touchdown speed was 0·96 revolutions per second, rotation actually ceased at 1·5 revolutions per second and first contact corresponded to a speed of over 4 revolutions per second. These two bearings should be compared with those in Figures 12 and 13 in which the overall contact periods were considerably shorter and rotation ceased at a little over one revolution per second in each case.

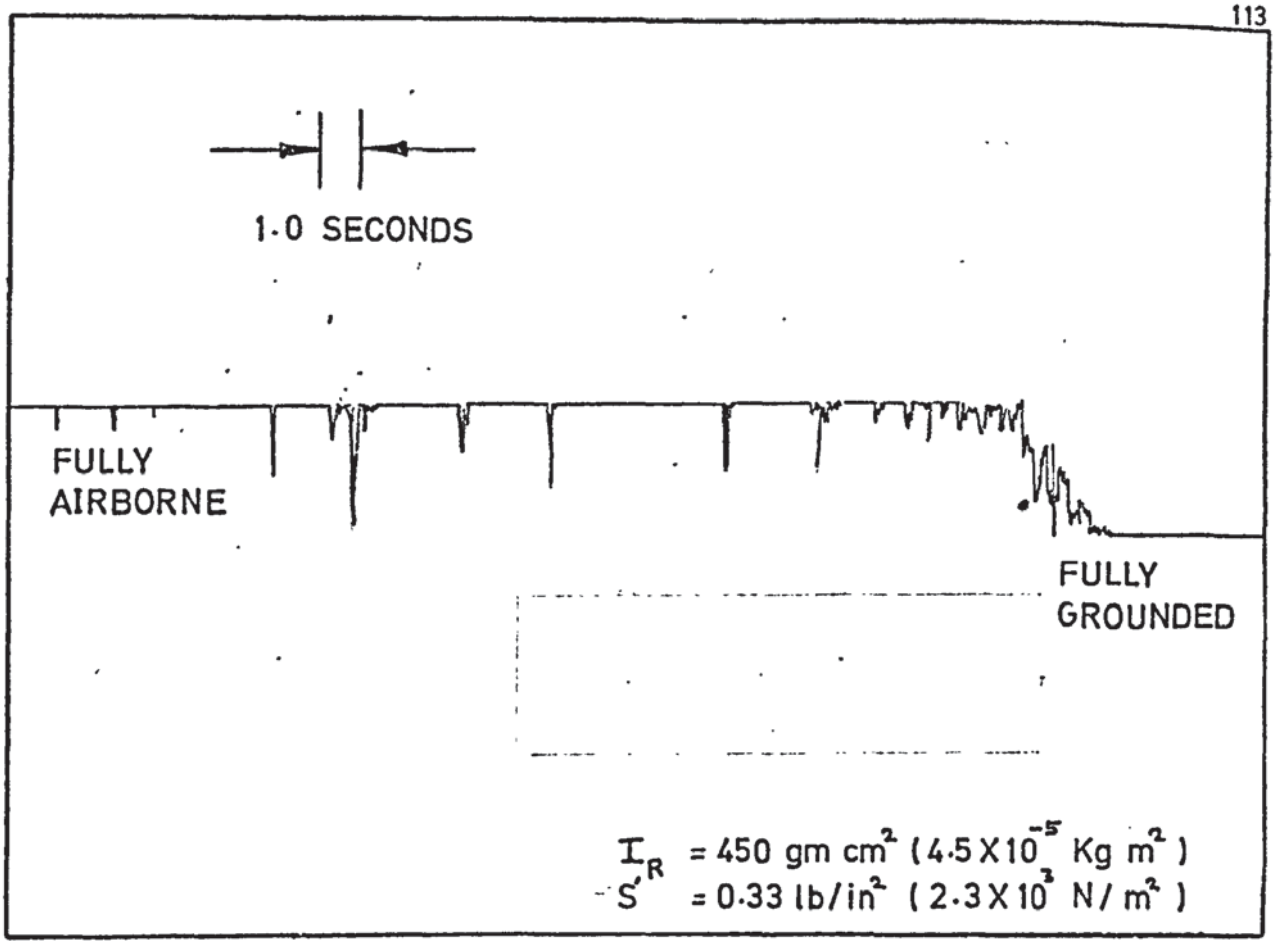

FIG. 14 BEARING CONTACT DURING TOUCH-DOWN (Experimental)

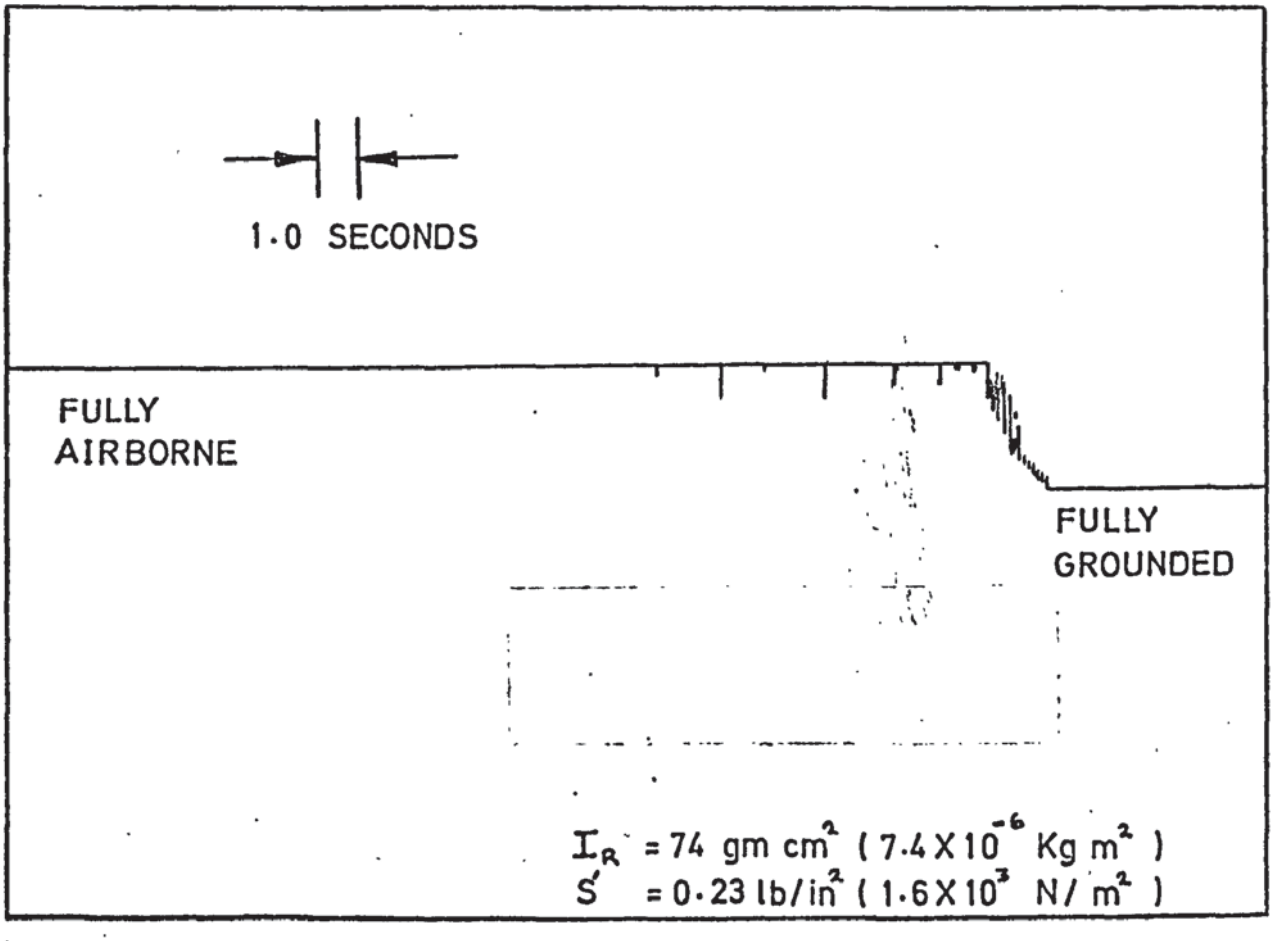

FIG. 15 BEARING CONTACT DURING TOUCH-DOWN (Experimental)

6.1 Low Speed Contact Characteristics (Continued)

Bearing contact was also recorded as the rotor became airborne and some of the traces obtained are shown in Figures 16, 17, 18, 19. In each case, irregular and intermittent contact occurred from the instant power was applied. For bearings where the overall geometry and finish were good, i.e. similar to that indicated on page 23, the rotor became fully airborne after a well defined period of time, as shown in Figures 16, 17 and 18. Where the geometry and finish were less perfect (corresponding to that previously described for Figure 15), intermittent contact was noted for up to 0·5 seconds after the rotor first became substantially airborne, as illustrated in Figure 19. In general, the rubbing period was surprisingly brief and for a well made bearing, was found to be in the region of 0·15 seconds. This could be reduced to 0·075 seconds by an increase in starting torque of only 10·5%, as demonstrated in Figures 16 and 17. Linear interpolation from the respective run-up curves indicated that these two rubbing periods corresponded to fully airborne speeds of 5·5 and 2·7 revolutions per second. Even allowing for experimental error and the small increase in bearing load due to brush pressure, it is clear that the take-off speed is significantly higher than the touch-down speed in each of the three bearings examined. Brush pressure and drag effects prevented recording of contact over a wide range of starting torques and the largest of the three sizes of bearing used would not start unaided with the brush gear in position. Visual examination of starting characteristics as the available torque is reduced suggests that, provided the bearing is free from gross contamination, the contact period is progressively lengthened until the rotor continues to rotate without becoming airborne. Rotor motion may be either smooth or stick-slip and successful take-off has occasionally been observed after several complete revolutions in this fashion.

Figure 18 is of particular interest because it illustrates an effect seen on several occasions on boron carbide - tungsten carbide wear surfaces. Contact resistance is seen to decrease almost immediately after rotation commenced and to regain its nominal value halfway through the rubbing period. The most satisfactory explanation of this effect is that oxide or contaminating films are temporarily

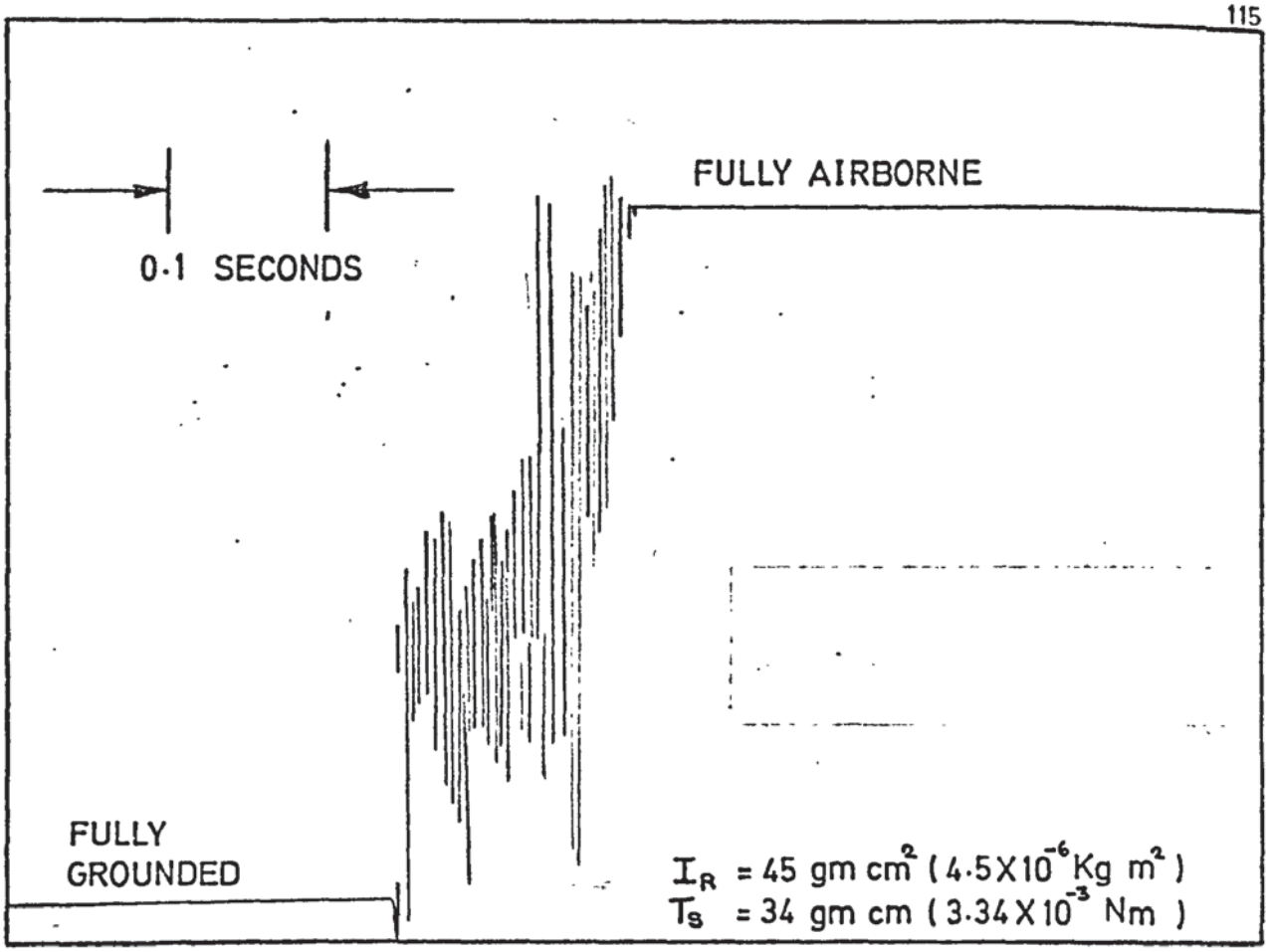

FIG. 16 BEARING CONTACT DURING TAKE-OFF (Experimental)

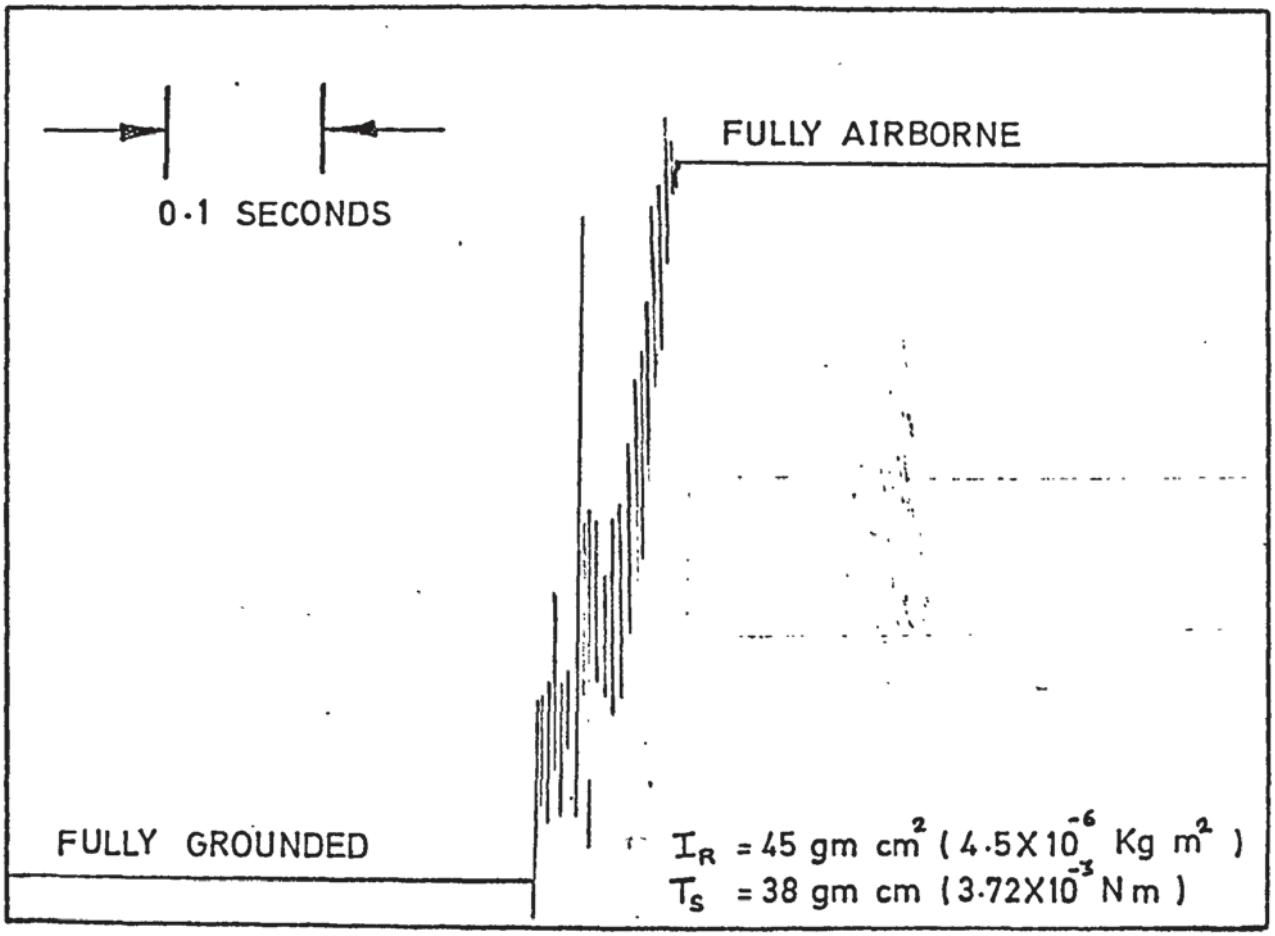

FIG. 17 BEARING CONTACT DURING TAKE-OFF (Experimental)

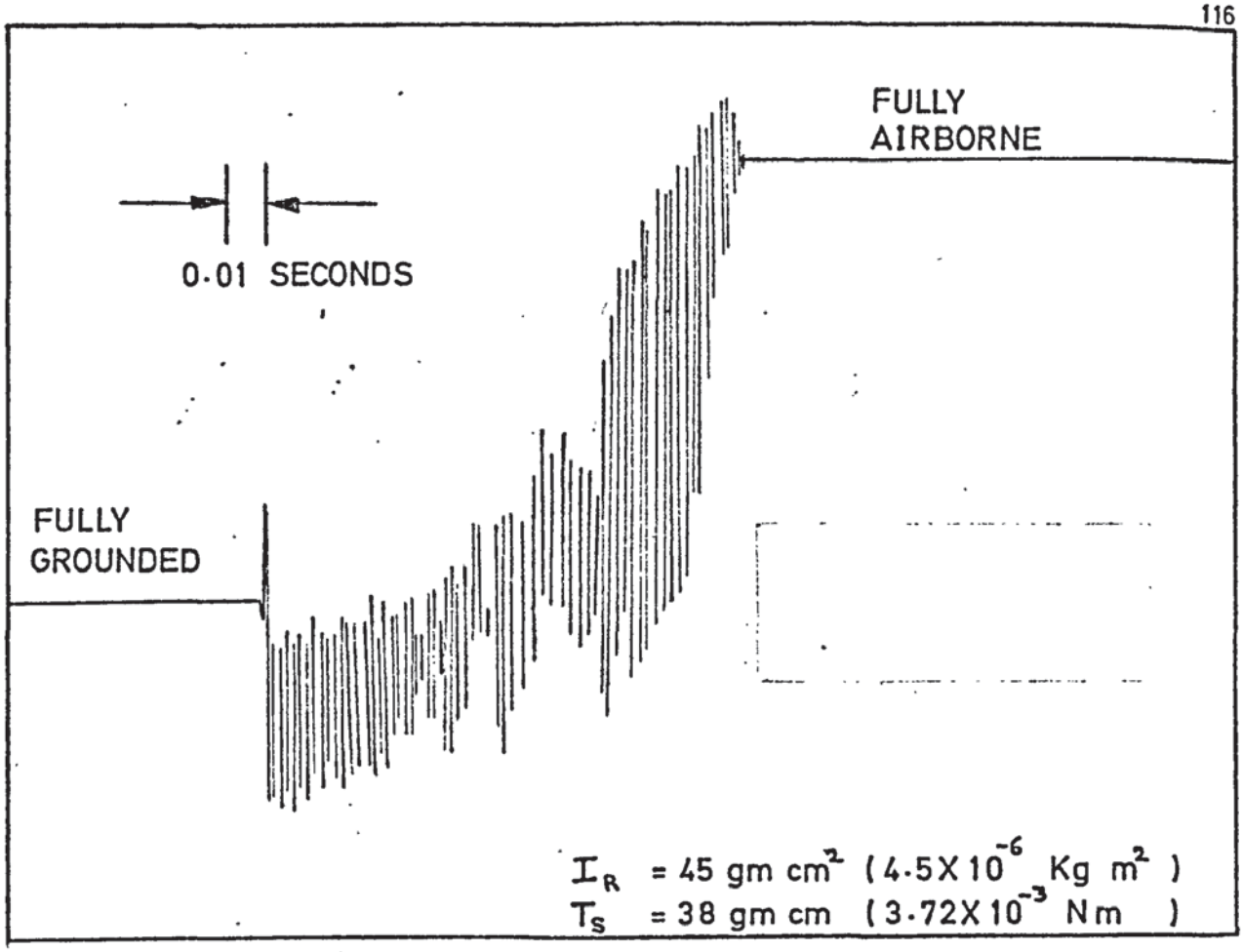

FIG. 18 BEARING CONTACT DURING TAKE-OFF (Experimental)

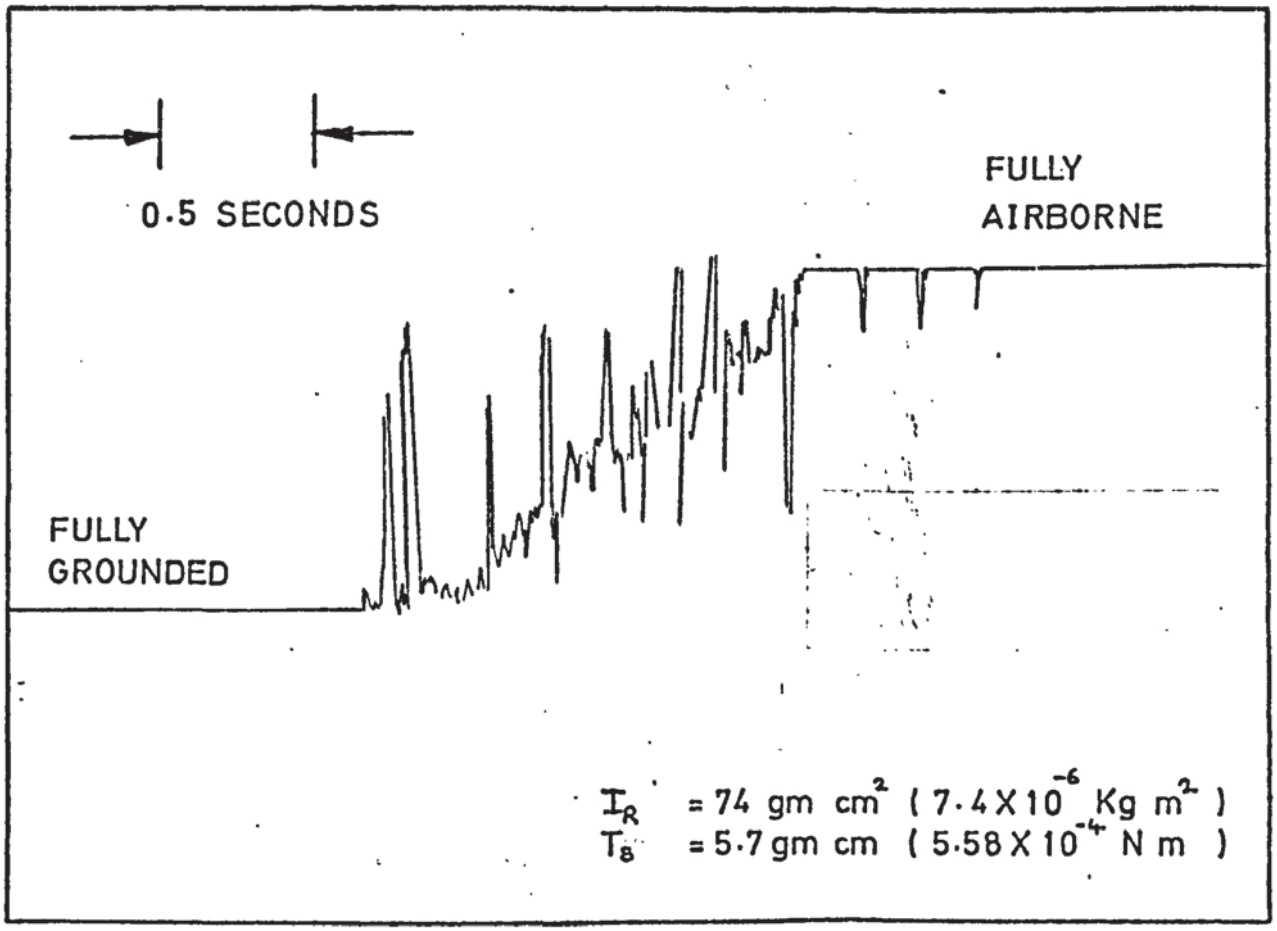

FIG. 19 BEARING CONTACT DURING TAKE-OFF (Experimental)

6.1 Low Speed Contact Characteristics (Continued)

rubbed away as the rotor starts to move and improved electrical contact is established between the opposing surfaces. This is supported by Wilson's work, referred to earlier in CHAPTER 2. Resistance changes of this order are not seen on the touch-down traces, though occasionally, a small and gradual increase in contact current could be observed over the first few seconds after the wheel had come to rest. The larger changes seen on starting may result from an increase in specific loading due to radial motor forces under these conditions.

From these results, a number of deductions can be made. The effects of geometry, rotor inertia and motor torque upon the nature and duration of the two rubbing periods are as might be expected, though the take-off period in particular is very sensitive to variations in starting torque. The apparent difference between take-off and touch-down speed is important because in all previous literature, the two parameters are implied to be identical. Explanations may lie in the additional support due to residual pressurisation of the bearing clearance during run-down, and this is discussed further in sections 7.16 and 8.1.1.

The reverse effect may also occur and the very brief period of take-off may be insufficient to allow complete pressurisation of the bearing to take place. It would explain why very close agreement is often obtained between theory and practice when measuring touch-down speeds on plain journal bearings, and where support is assumed to be due to instantaneous hydrodynamic action alone. It might also be argued that radial motor forces could produce the same effect, but they could also assist take-off when acting in opposition to the rotor weight and lower take-off speeds have not been observed here.

6.2 Speed Decay Measurements

A large number of speed decay measurements have been made on coasting bearings. Though initially recorded as a means of measuring power dissipation, the curves are of interest in their own right and several typical plots are included in this report. (Figures 20 and 21).

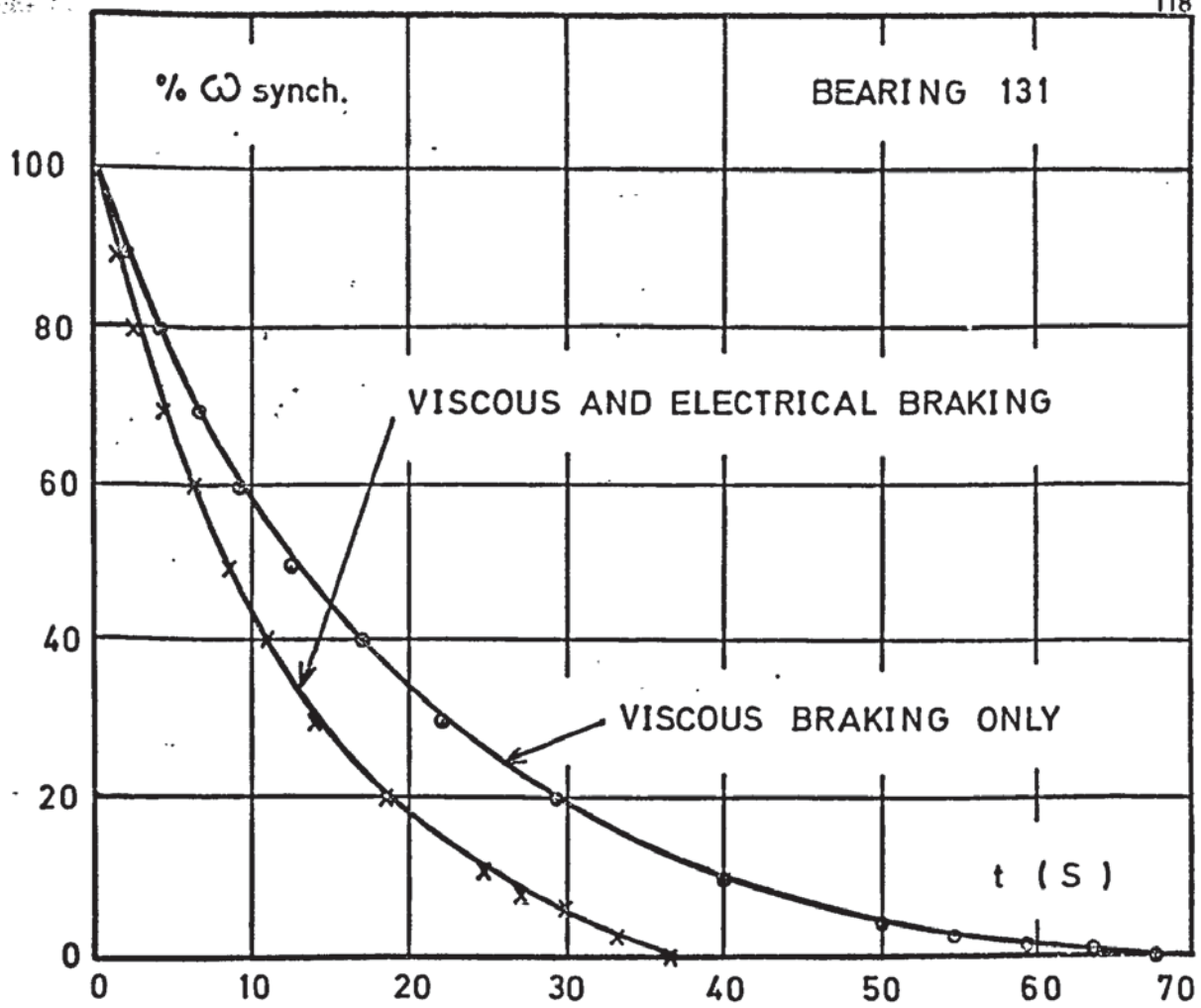

FIG. 20 ROTOR SPEED vs TIME (RUN-DOWN)

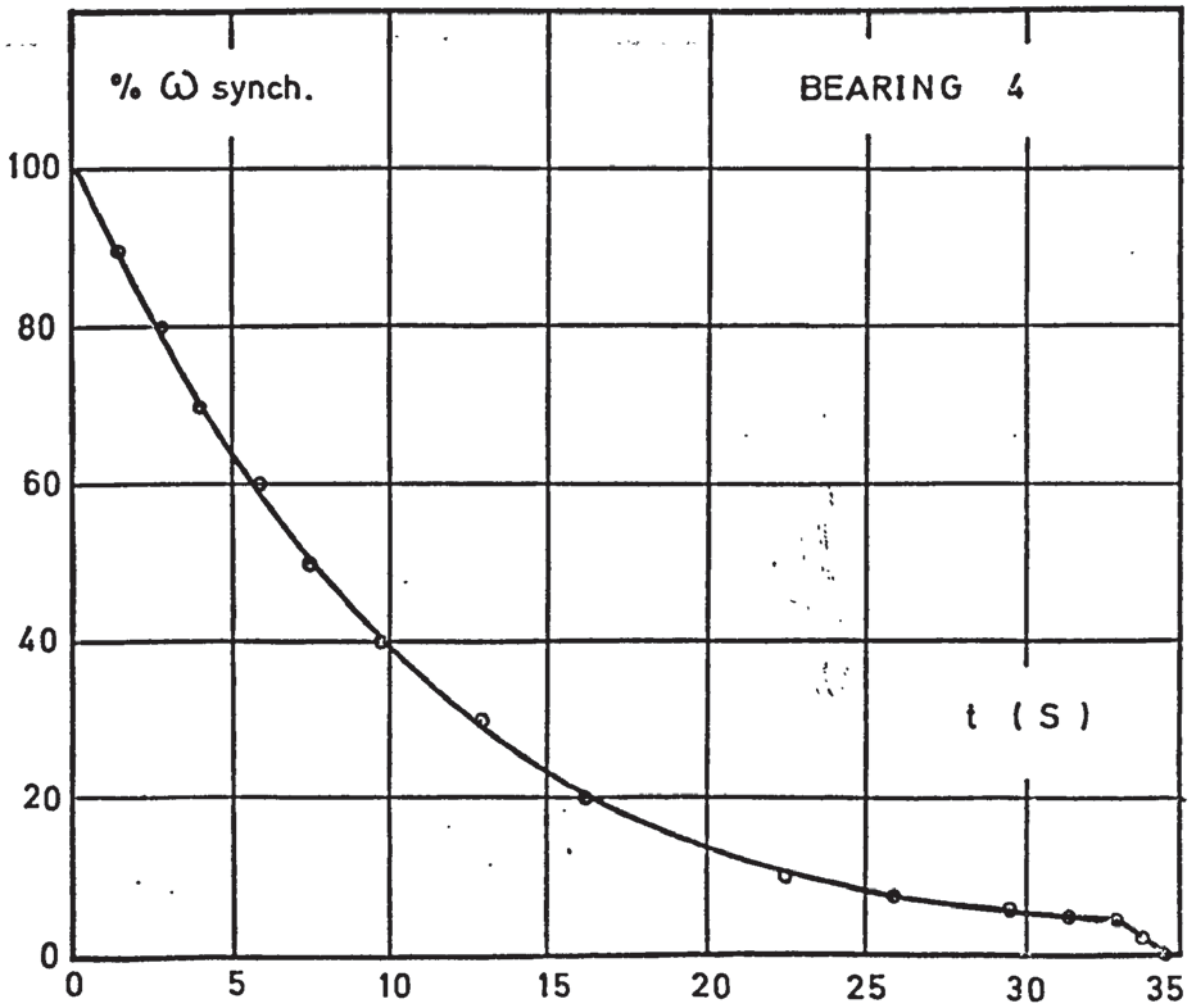

FIG. 21 ROTOR SPEED vs TIME (RUN-DOWN)

6.2 Speed Decay Measurements (Continued)

In each case, similar characteristics were obtained; the initial rate of decay is almost linear and the rate of decay reduces rapidly at low speeds as the viscous drag acting on the rotor diminishes. For almost all the bearings examined, the initial sections of the curves were practically identical. Significant divergence only occurred during the latter stages of run-down and these deviations were found to be more closely related to geometry and cleanliness than to the nominal bearing clearance. All the curves shown are for bearing assemblies running with their spin axes horizontal.

Figure 20 illustrates the very considerable effect of electromagnetic braking on the run-down characteristic. This dependence on the electrical characteristics of the drive system tends to detract from the usefulness of run-down information as a measure of bearing quality, and reference has already been made in section 5.5.7. to the effect of supply voltage variations on the residual magnetism in the hysteresis material of the motor. Where the rotating magnetic driving field is generated by a true three-phase winding, the residual magnetism and hence the braking effect will not be a function of the point on the supply waveform at which power is interrupted.

At very low rotational speeds where $\varepsilon \to 1$, the decay characteristic is influenced almost entirely by the local topography of the wear surfaces. Debris and surface contamination may exert a considerable braking torque under these conditions and this form of contact may not necessarily be evident from electrical continuity traces.

In severe cases, the run-down plot is seen to terminate abruptly and the rotor appears to dive into full contact with the shaft. This is illustrated in Figure 21. It can be seen from the curves that the overall run-down time is largely determined by the portion of the run-down trace obtained below 5% of synchronous speed, and that this time may thus be used as a useful measure of bearing quality. Freeman (4) also concludes that both the decay curve and run-down period can be used to indicate surface distress, but fails to highlight

6.2 Speed Decay Measurements (Continued)

the precautions required when making these measurements. Decay curves were also plotted for bearings operating at reduced ambient pressure but no significant variations were measured.

Run-up curves have also been recorded (Figure 22) and are all characterised by the same rapid increase in speed which gradually diminishes as synchronism is approached. Both the shape and duration of the run-up curve will be strongly dependent upon the speed-torque relation of the drive system. Whereas the coasting rotor spends a large proportion of its time at high eccentricity ratios, the accelerating rotor will normally spend a negligible proportion of its run-up period in this region. This, together with the very short period of rubbing contact, make both the curve and the overall run-up time almost indpendent of bearing surface conditions. Practical experience here has supported this view and only in severe cases of surface deterioration has a significant reduction in run-up time be observed.

By plotting rotor speed against time over a range of applied torques, the angular acceleration of the rotor from rest can readily be calculated from the tangent to the curves at t = O. Figure 23 compares this experimental acceleration with the corresponding theoretical value neglecting friction. The theoretical curve is evaluated from equation 70.

Discrepancy between the theoretical and experimental curves is due to the influence of static and sliding friction between the bearing surfaces during the take-off period. The contribution of viscous friction can be shown to be negligible at the rotational speeds involved. From the experimental plot, calculation shows that this friction torque corresponds to an average friction coefficient of 0·17 throughout the take-off period. This is considerably less than the static friction coefficient, which for the bearing illustrated was measured to be 0·25. It is also higher than the arithmetic mean coefficient, indicating, as might be expected, a non-linear variation in friction throughout the rubbing period. Knowing

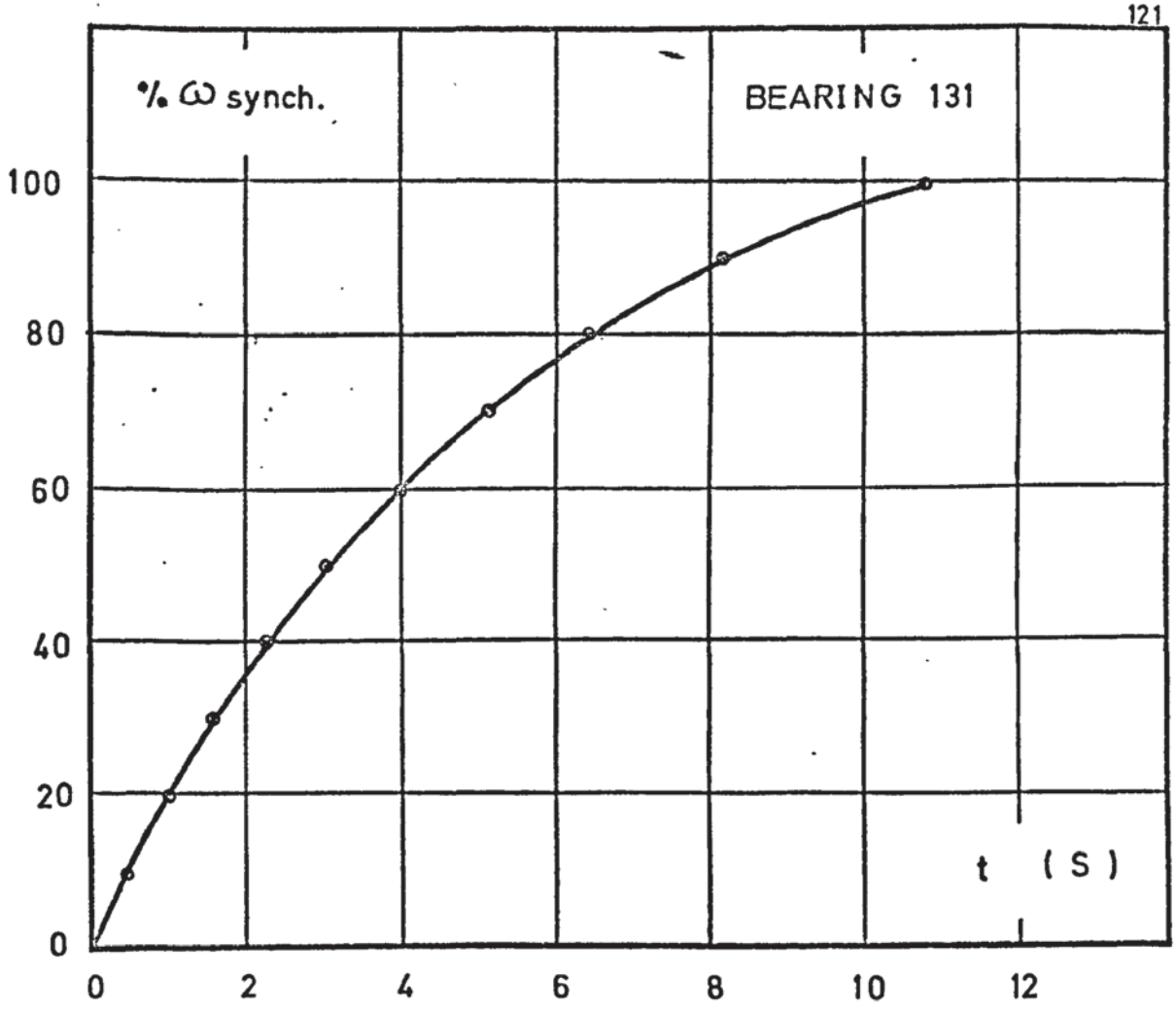

FIG. 22 ROTOR SPEED vs TIME (RUN-UP)

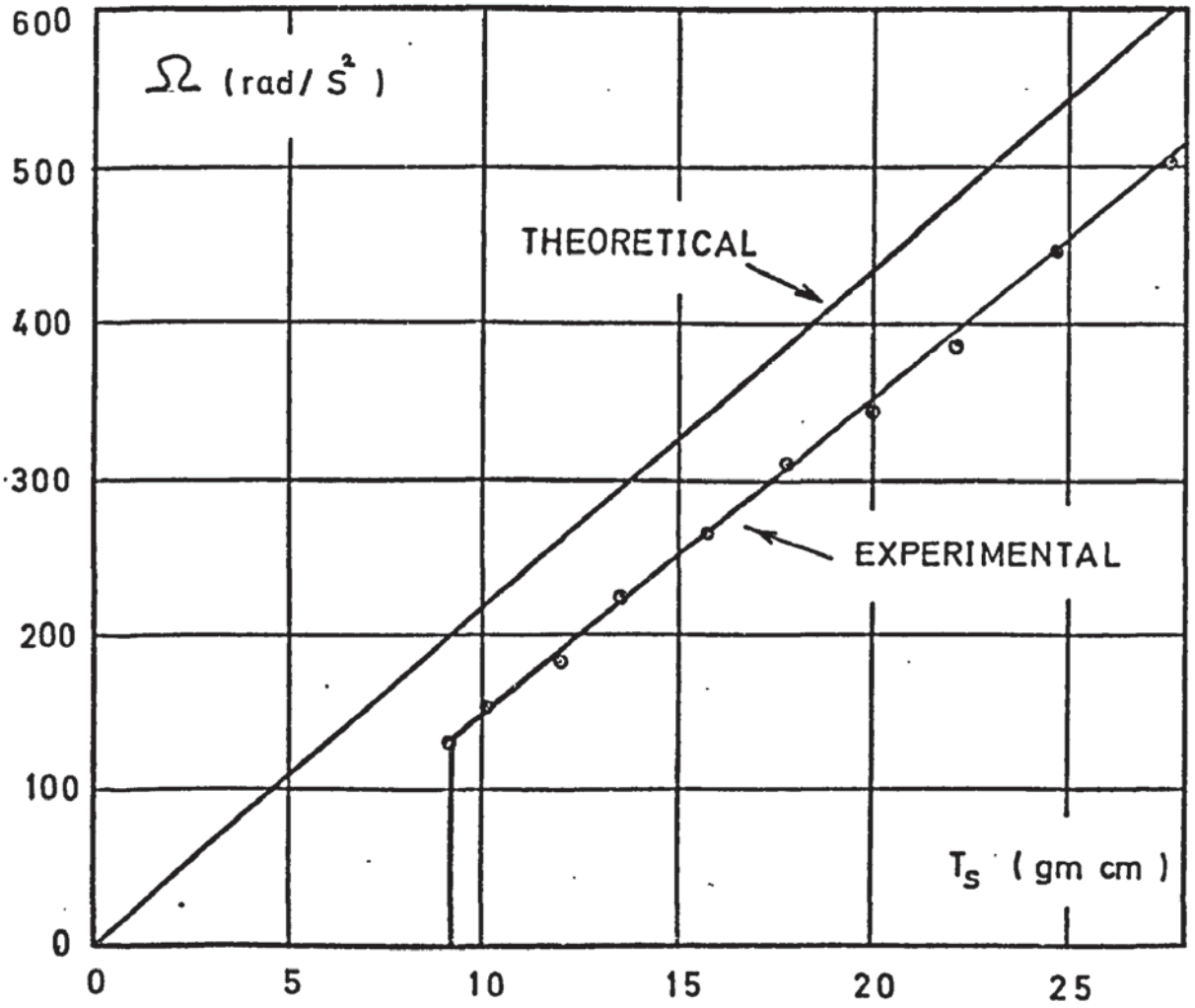

FIG. 23 ROTOR ACCELERATION vs STARTING TORQUE

the average friction coefficient, it is now possible to calculate the frictional power dissipation during lift-off. It can readily be shown that:-

$$\text{Energy Loss} = \tfrac{1}{2} \times f.m_R.R.\delta t^2.Go.\frac{d^2\omega^4}{dt^2} \qquad (72)$$

From relation 72 the lift-off dissipation is found to be 3,500 microjoules. This compares with a value of 90 microjoules for the total energy loss during touch-down, estimated from the kinetic energy of rotation at the moment of contact. Knowing also the reduction in rubbing period for a given increase in accelerating torque (Figures 16 and 17), it can be shown that a 10·5% torque increase will reduce the energy loss during lift-off by over 70% on this particular design.

It is reasonable to suppose that some positive relationship will exist between the energy dissipation during contact and the amount of wear damage produced. On very smooth surfaces where a thermal wear mechanism may predominate, i.e. welding-tearing at the tips of the asperities, it may be more appropriate to consider the rate of energy dissipation rather than the total energy alone. In such a case, it is found that for the bearing considered, lift-off under nominal torque conditions involved a power dissipation of 23 milliwatts, which could be reduced to 13 milliwatts by a torque increase of only 10·5%. This compared with a maximum dissipation rate of 1·0 milliwatts under normal touch-down conditions.

The above figures are of considerable importance, for they indicate that mechanical wear damage during the starting period will be far greater than that experienced during touch-down. They also suggest that quite small increases in starting torque may result in significant improvements in wear life.

In Figure 23, the theoretical and experimental curves diverge slightly as the accelerating torque is increased. This may be due to there being insufficient time for the bearing to fully pressurise at higher angular accelerations, as discussed in section 6.1.

The effect should be more pronounced on very small rotors where high angular accelerations are possible. Gas lubricated gyro rotors have until recent years been comparatively large in size and this might account for there being no previous reference to this effect.

6.3 Viscous Power Measurements

Practical measurement of viscous torque and power dissipation is required on a fully grooved H-form bearing configuration because, unlike its ungrooved counterpart, no direct analytic method is available for the grooved journal component. This is because of difficulties arising from sudden changes in clearance created by the helical grooves around the circumference of stationary journal members. In contrast, the power dissipations for a plain journal bearing and a spiral grooved thrust member are readily estimated from the following relations, and offer a useful basis of comparison with the experimental results for grooved bearings.

$$\text{JOURNAL DISSIPATION (84)} = \frac{746\pi\mu LR^3\omega^2}{3300C\sqrt{1-\varepsilon^2}} \text{ Watts} \qquad (73)$$

$$\text{THRUST DISSIPATION (31)} = \frac{746\pi\mu\omega^2 r_o^4}{24 \times 550h} \cdot \frac{(r_o)^4}{(\overline{ri})-1} \cdot \frac{a+b}{b\,(a+1)} \text{ Watts/plate} \qquad (74)$$

$$(\overline{ri}) = \frac{(r_o)^4}{(\overline{ri})}$$

Both these expressions assume laminar, vortex free flow over each portion of the bearing surface. Practical measurements cannot be made on an assembly incorporating a plain journal bearing, which would be inherently unstable over the range of rotational speeds involved.

The gyro designer is interested in two principal aspects of viscous dissipation; variation with speed and variation with angular misalignment. Both characteristics have been investigated. Operation of grooved bearings at high rotational speeds will later be shown to offer a number of important advantages. Gyroscopic torque loads (resulting in angular misalignment) are, in many applications, the most severe that the bearing will encounter in normal service.

6.3 Viscous Power Measurements (Continued)

Figures 24 and 25 show the power loss for grooved H-form bearing assemblies as a function of rotor speed. Initially, the increase in dissipation with speed is quite gradual, but at speeds approaching 800 revolutions/second, the power dissipation for one of the bearings investigated begins to increase rapidly. Figures 24 and 25 also show the theoretical bearing dissipation computed from equations 73 and 74, assuming the assemblies contain plain journals. This assumes the mean radial clearance of the plain bearing to be equal to the mean radial clearance of the grooved bearing measured over its land region.

At low speeds (N_R < 12,000 R.P M.), the recorded power consumption agreed closely with the predicted value for an assembly containing a plain journal on all the bearings investigated. As the rotational speed was increased, the measured power consumption always fell below the predicted value and, with the exception of bearing 101, remained below it at speeds up to 48,000 R.P.M. One possible explanation for the different behaviour of bearing 101 is suggested on Page 130. The divergence between the predicted and experimental curves varied from one bearing to another in a random way.

Reynold's number was evaluated for each bearing, based upon the mean measured pressure and clearance in the groove region. For both journal and thrust elements, the Reynold's number did not exceed 31 for the range of rotational speeds recorded in Figures 24 and 25. Over the land regions alone, it did not exceed a numerical value of 11·5 in each case. These exceptionally low values of Reynold's number effectively preclude any form of turbulent flow within the bearing, and turbulence cannot therefore be used to explain any rapid increase in power dissipation at higher rotational speeds. Further, from Constantinescu's work on turbulent lubrication (108), it can be shown that for the bearing in question, rotational speeds of 3×10^6 R.P.M. and $9{\cdot}5 \times 10^6$ R.P.M. will be required in order to achieve large scale turbulence within the thrust and journal bearings respectively. For an equivalent plain journal, the corresponding speed will be 45×10^6 R.P.M.

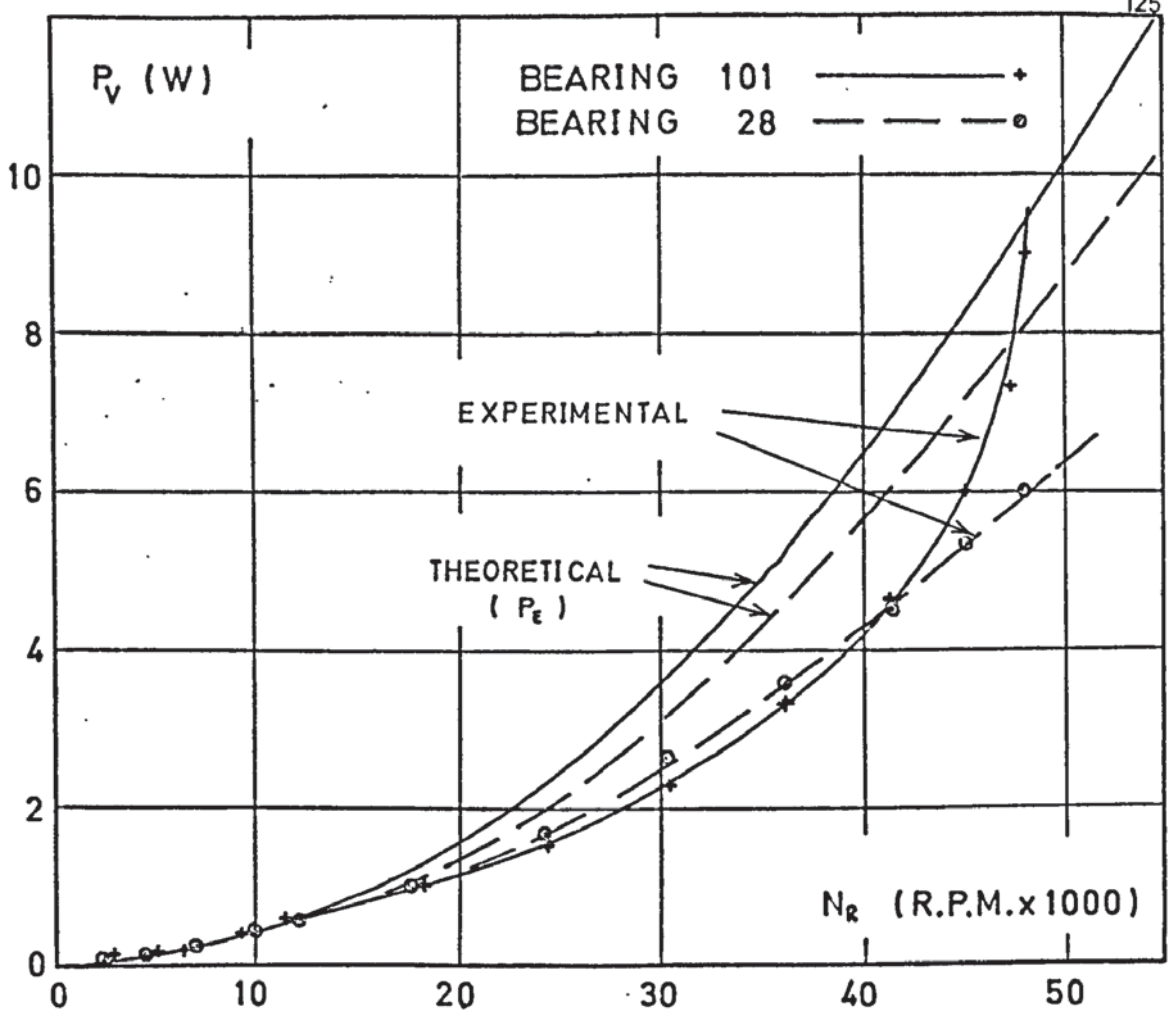

FIG. 24 POWER LOSS vs ROTOR SPEED

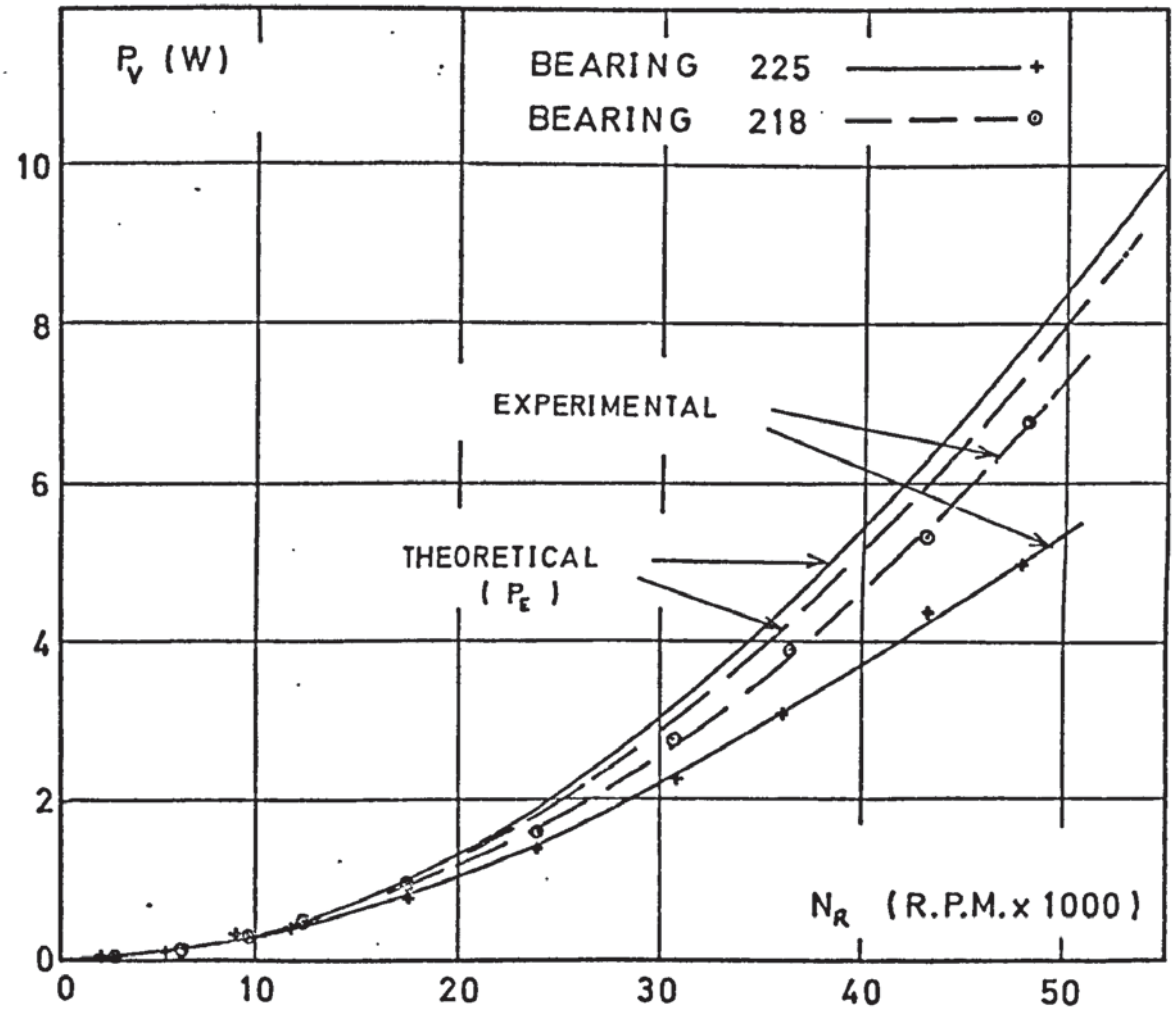

FIG. 25 POWER LOSS vs ROTOR SPEED

6.3 Viscous Power Measurements (Continued)

Fleming (1) has also encountered divergence between grooved and plain bearings at high speeds, using larger (38 mm diameter) herringbone-grooved journal bearings where the grooved member was rotating. He suggests the development of laminar eddies within the grooves to explain the increased power consumption he observed at high speed compared with an 'equivalent' plain bearing. At lower speeds, the slow viscous flow is said to result in a lower average velocity gradient in the groove region, in comparison with that over the land region. This in turn reduces the average power dissipation in comparison with that for a plain bearing. At very high speeds, it is suggested that the laminar eddies become 'fully developed' and may account for the levelling-off in relative power loss observed by Fleming. Figure 26 shows the relative power loss plotted against Reynold's number. At very low Reynold's numbers, the relative power losses are found to be sensibly equal to those for assemblies containing plain journals, and only decreased as the rotational speed was increased.

For the majority of the bearings examined here, the increase in relative power consumption at high speeds as reported by Fleming could not be confirmed. It is suggested that the increase in relative power loss may occur at rotational speeds above the range investigated, and that the precise point at which laminar eddies form might be influenced by the local geometry and texture of the individual bearing.

Over intermediate speeds, the lower relative consumption of the grooved bearing described by Fleming is confirmed.

At very low speeds the equality of power loss between grooved and equivalent plain bearings has not previously been reported. In order to explain this phenomena, it is proposed here that a fourth type of flow pattern may be possible, in addition to the three proposed by Fleming (1). This takes the form of a slow viscous flow over both the land and groove region, with the fluid within the groove remaining essentially stagnent. Such a situation would arise where the transfer of energy from the moving surface is insufficient to influence the bulk of the fluid within the groove.

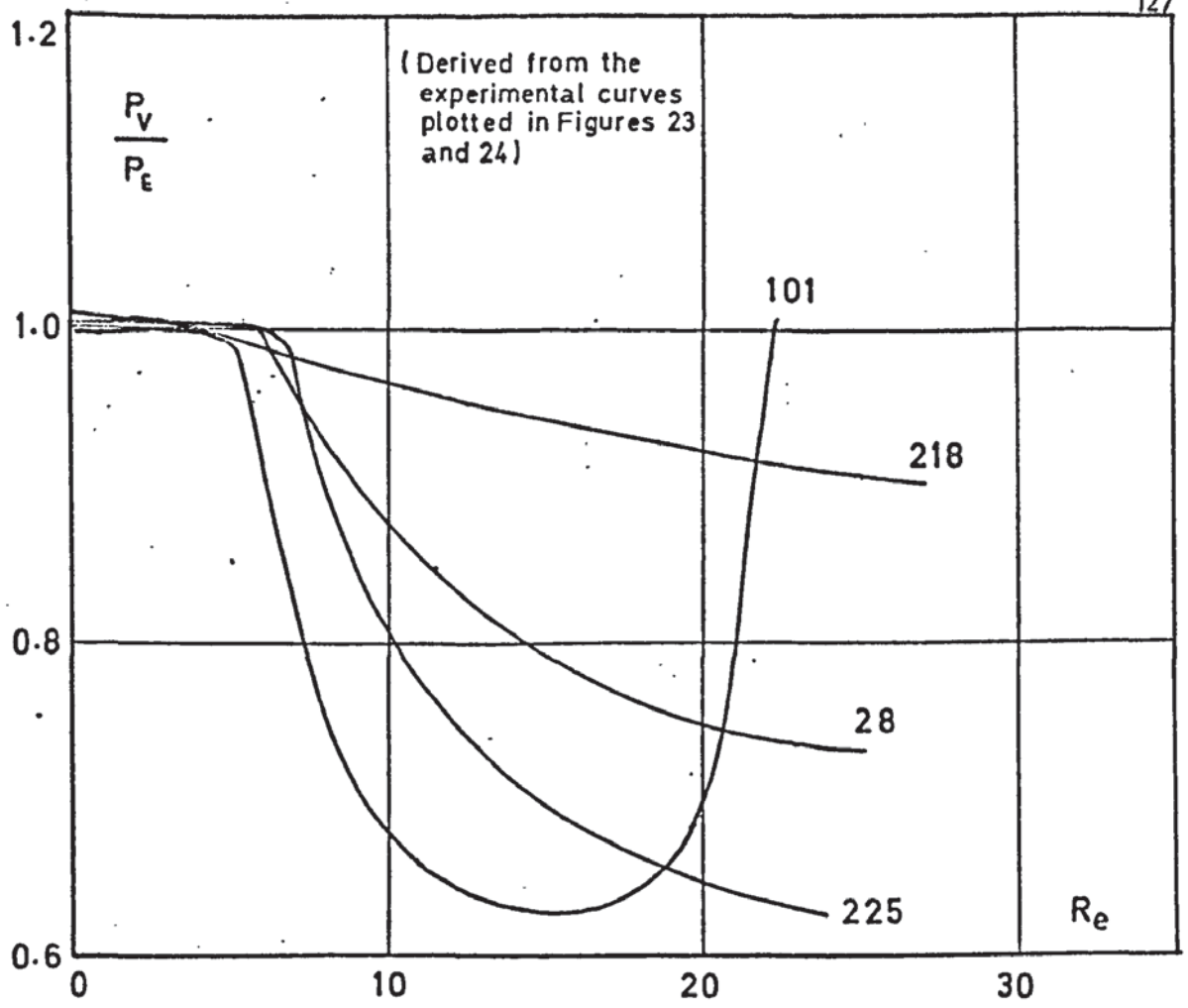

FIG. 26 RELATIVE POWER LOSS vs REYNOLD'S NUMBER

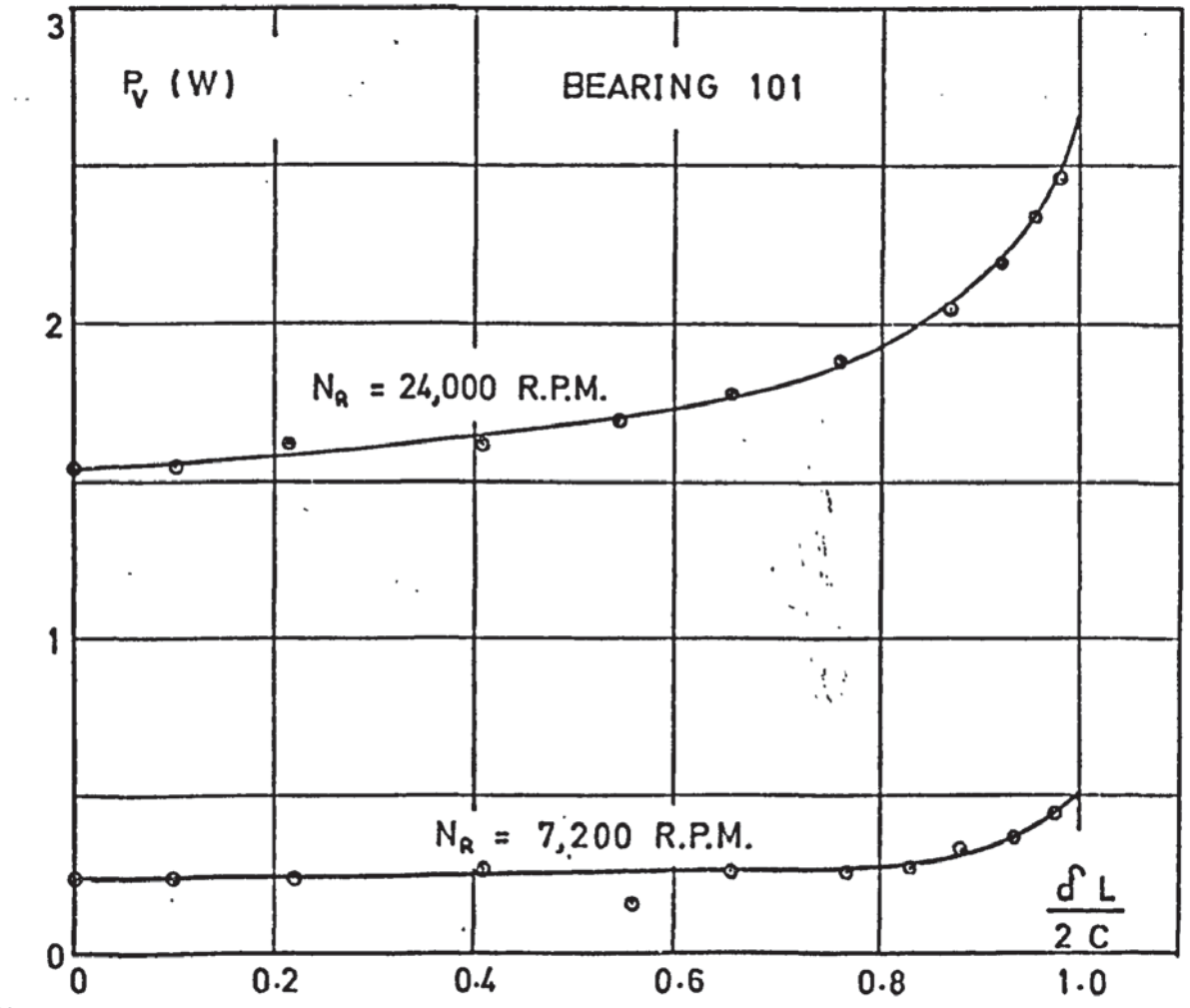

FIG. 27 POWER LOSS vs ANGULAR MISALIGNMENT

6.3 Viscous Power Measurements (Continued)

The average transverse velocity gradient would remain practically constant over both the land and groove region and the bearing would tend to behave as if the groove were no longer present; the viscous power dissipation then being approximately equal to that of an equivalent plain bearing. The four possible stages of flow are illustrated in Figure 28 and, together, offer a reasonable explanation of all the observed effects. They apply equally well to pumping grooves in both journal and thrust elements, and since none of the experimental results show any sudden discontinuities, a smooth and gradual transition can be expected between each flow pattern as the rotational speed is progressively increased. This is in contrast to the change between true laminar and true turbulent flow, where a sudden transition is invariably observed (108). If the observed changes in relative power loss are indeed due to changes in streamline flow within the bearing, some correlation with Reynold's number might be expected. Here, experimental power consumptions were found to be sensibly equal to predicted plain bearing consumption at Reynold's numbers of 7 or less. This may explain why this same equality of power consumption was not noted by Fleming, who does not record relative power loss at very low Reynold's numbers. In addition, fluid stagnation will also depend upon the relative groove numbers and dimensions and these were different to those used here.

The experiments clearly indicate the practical problems of operating a grooved bearing of this form at speeds substantially higher than the design speed of 400 revs/second, where viscous power losses may be considerable. Calculations based upon work in reference 108 (Page 17) show that the introduction of pumping grooves will considerably reduce the speed at which true turbulence will occur, though for all conceivable gyro bearings this speed will be of only academic interest. Fleming's experimental results are only partly confirmed for small scale bearings, and the rotational speeds available were insufficient to confirm the development of the laminar eddies. The fact that possible evidence of eddy formation could only be observed on one bearing cannot be

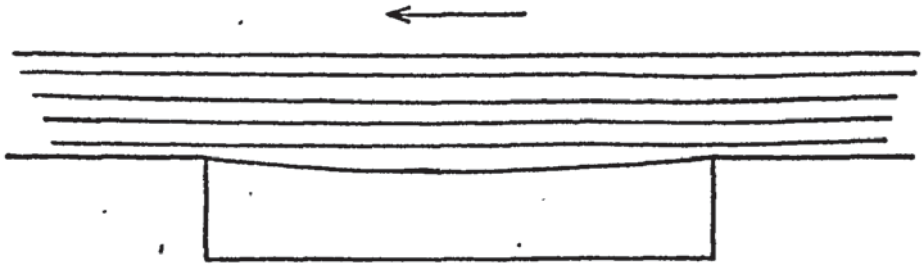

a) Slow viscous flow with stagnant fluid in groove (BEARDMORE)

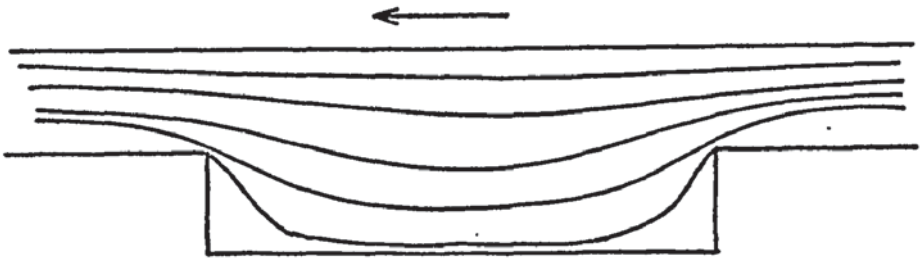

b) Slow viscous flow filling groove (FLEMING)

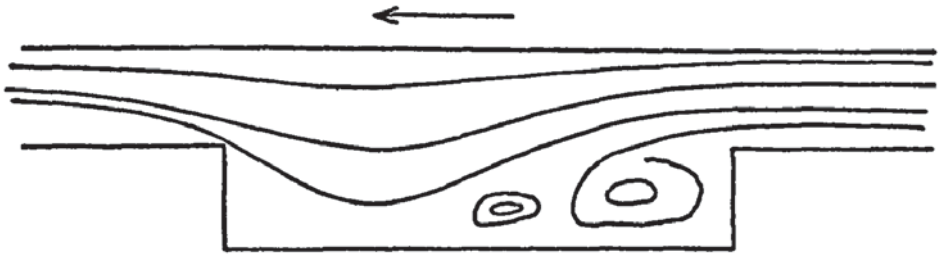

c) Formation of laminar eddies (FLEMING)

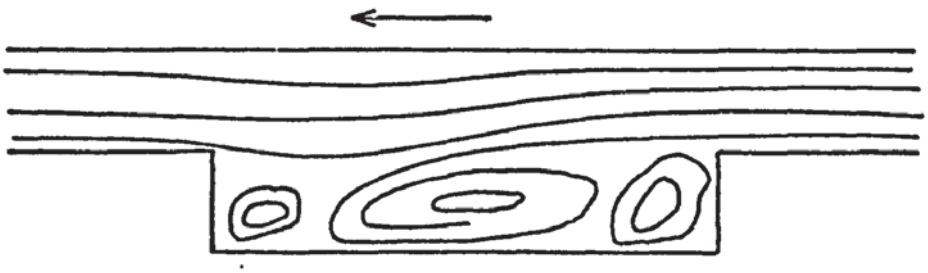

d) Fully developed laminar eddies (FLEMING)

FIG. 28
PROPOSED FLOW PATTERN IN GROOVE REGION WITH INCREASING ROTATIONAL SPEED.

6.3 Viscous Power Measurements (Continued)

explained in terms of Reynold's number alone, for in each case, the maximum Reynold's numbers were found to be very similar. It is considered that the results obtained from bearing 101 may be spurious, and no firm conclusions can therefore be drawn from them. However, this particular bearing originated from an early experimental batch in which the surface finish and groove profile were inferior to those later tested. It therefore seems possible that the development of laminar eddies might be influenced by small variations in groove and surface definition, and that the power consumption of very smooth grooved bearings may not exceed that of an equivalent plain bearing until higher Reynold's numbers are reached. Similar differences in bearing quality may also explain the varying correllation previously noted between the experimental and theoretical curves. Power supply limitations restricted the rotational speed of the test rig to 800 revolutions per second, and testing to higher Reynold's numbers was not possible.

Figures 27 and 29 show the change in power dissipation as the bearing is progressively misaligned for various values of N_R. Journal contact corresponds to $\frac{\delta L}{2C} = 1 \cdot 0$ in each case. As misalignment increases, so the power consumption rises, and in each test, a more rapid increase occurred as the contact condition was approached. The average slope of the power dissipation curve was found to increase with rotor speed and the sharp increase just prior to contact was more noticeable at lower speeds.

Two mechanisms may contribute to the increase in power dissipation as the rotor and shaft axes are misaligned. At those places within the bearing where misalignment causes a reduction in local clearance, an increase in velocity gradient will occur across the air film. Additional energy losses occur as the fluid is pressurised in the constricted clearance and the corresponding increase in shear force will increase the nett viscous torque acting on the rotor. As contact is approached, the local clearance will approach zero over the land region, and some finite value (corresponding to the groove depth) over the groove region. At opposing sections of the bearing the local clearance will increase

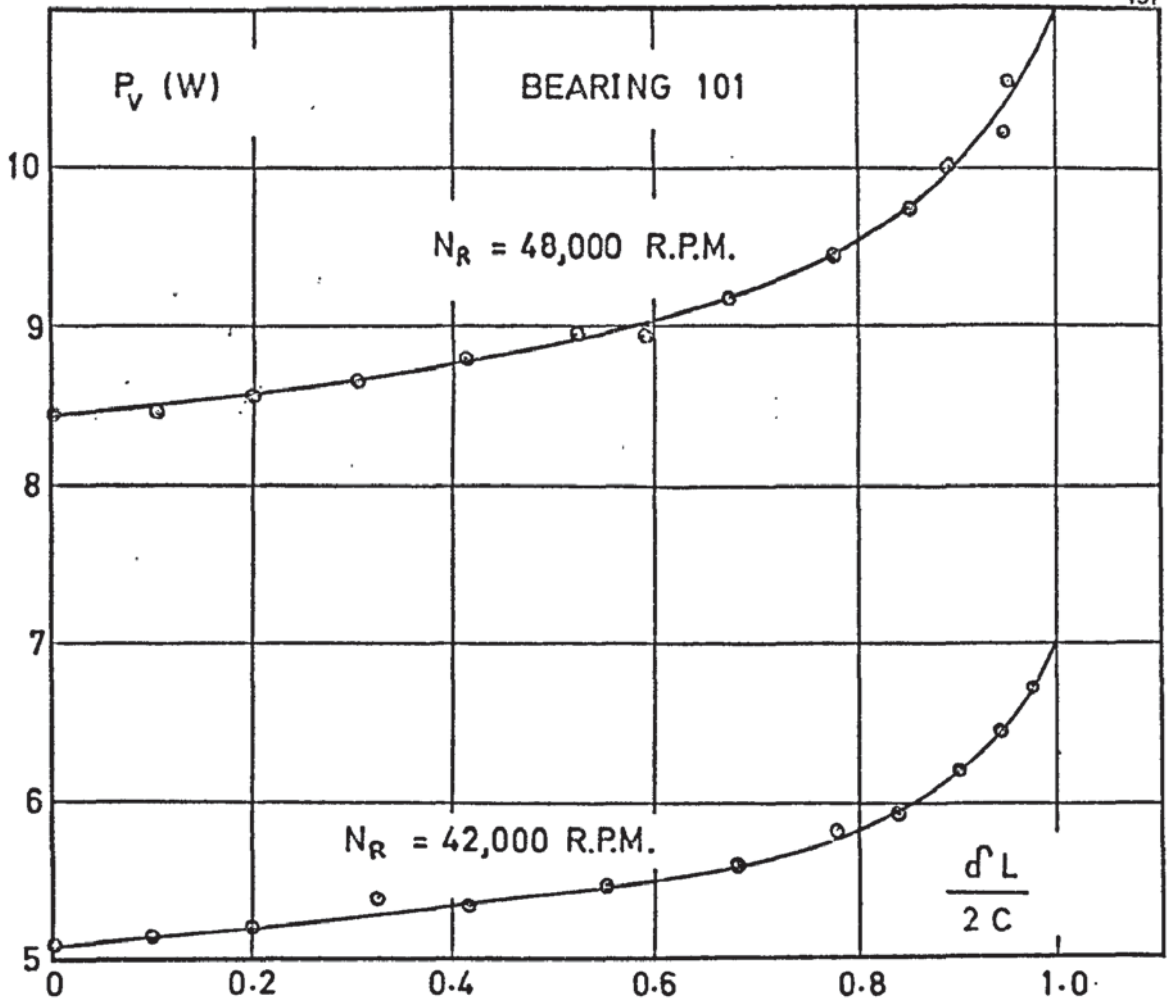

FIG. 29 POWER LOSS vs ANGULAR MISALIGNMENT

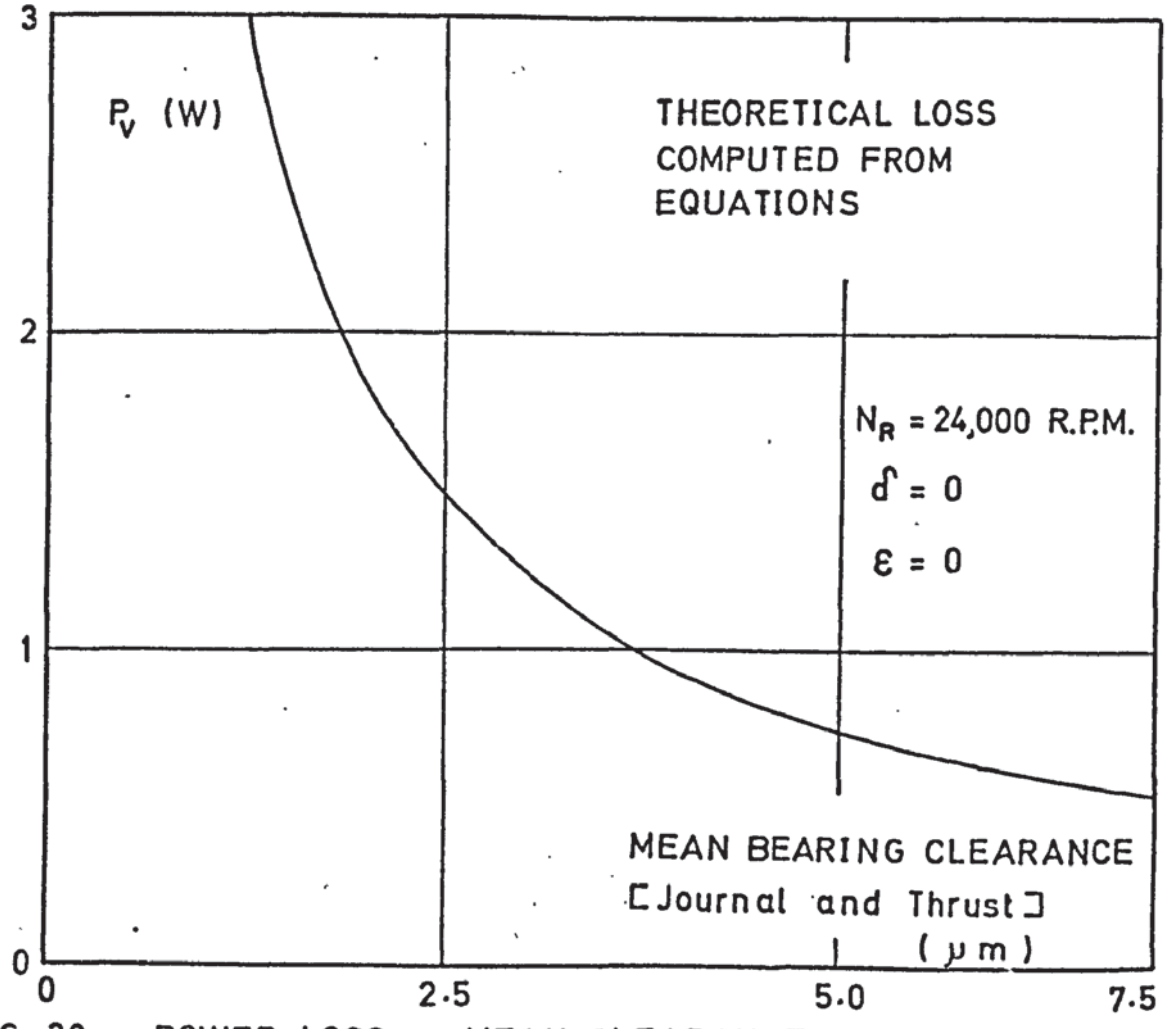

FIG. 30 POWER LOSS vs MEAN CLEARANCE

6.3 Viscous Power Measurements (Continued)

with misalignment, approaching double the mean value over the land region and a correspondingly higher value over the groove area. Under these conditions, the local Reynold's numbers may increase and, for the bearing in question, approach those at which laminar eddies are said to form near the leading edge of the groove (Figure 28). The formation of laminar eddies would account for the sharp rise in dissipation at high misalignments, and would also explain the increasing slope of the dissipation curves at higher rotational speeds, where some of the eddies may already be partly developed before misalignment commences.

The practical implications of these findings in relation to gyro applications may now be considered. Providing the bearing can be operated outside the laminar eddy region, the increase in power dissipation with angular misalignment will be small and will cause no embarrassment to the rotor drive system. Once any section of the bearing leaves the true laminar regime, either as a result of speed or local clearance changes, variation of viscous dissipation with misalignment may be more significant and, depending upon the torque-speed characteristics of the drive system, could lead to a loss of synchronous rotor speed.

6.4 Experimental Studies of Fluid Flow

The flow of an incompressible fluid around a number of groove formations was studied experimentally with the aid of the flow visualisation rig described in section 5.13. Reynold's numbers between 0·1 and 100 were considered and the initial investigations concentrated on rectangular section grooves of various aspect ratios; the aspect ratio being defined as the local groove width divided by the local groove depth.

With aspect ratios in the order of 1 or 2, a single laminar vortex was visible over the entire range of Reynold's number employed (See Plate 16). This laminar eddy almost filled the entire groove section and appeared to be fully developed at a Reynold's number as low as 0·1. Only a very small proportion of groove fluid appeared to be stagnent at the lower corners, and linear streamline flow was maintained throughout the clearance region

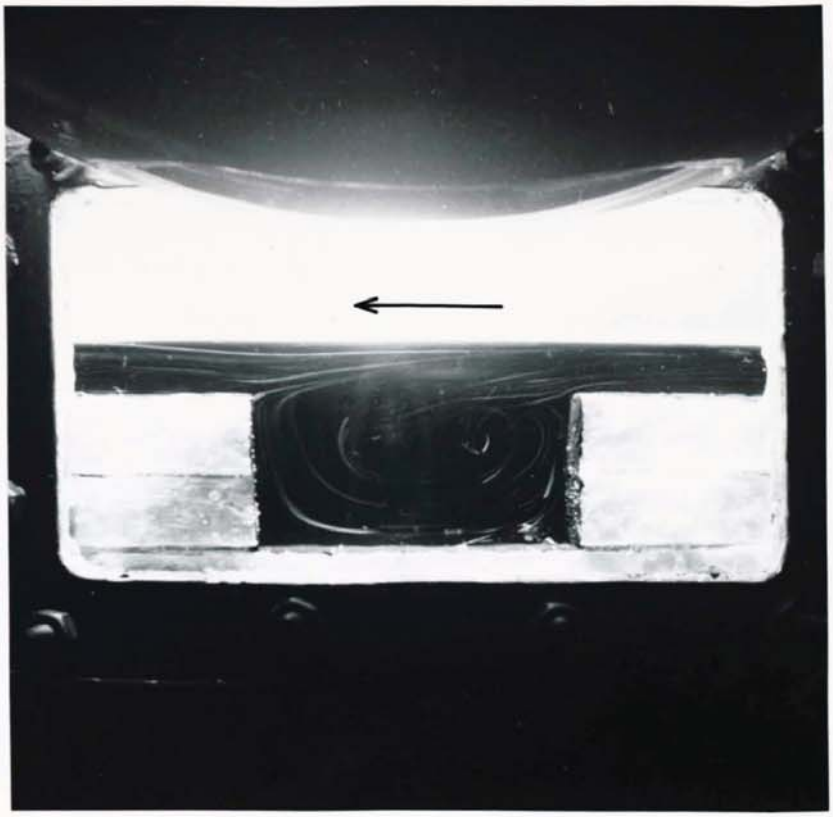

PLATE 16
FULLY DEVELOPED VORTEX FLOW AT Re = 5 .

PLATE 17
VORTEX FLOW AT Re = 100 .

6.4 Experimental Studies of Fluid Flow (Continued)

above the upper corners of the groove. The overall size and shape of this vortex remained essentially unchanged in response to variations in both running speed and clearance, through with Re → 100 and clearance in the same order as the groove depth, there was a slight tendency for the vortex to include fluid in the region above the upper corners of the groove (See Plate 17). As the running clearance was reduced until it became very much less than the depth of the groove, the vortex tended to assume a more rectangular shape, especially at Reynold's numbers of less than unity. The velocity gradient was approximately linear across the region of linear streamline flow, and measurements taken at Re = 5 suggested that the maximum velocity of reverse flow within the groove was about 10% of the mean flow velocity over the land region.

When the aspect ratio was increased to 10, and the running clearance over the land region was about eight times the depth of the groove, streamline vortex-free flow filled both the land and groove region at Reynold's numbers up to about 50, as shown in Plate 18. Stagnant fluid occupied the lower corners of the groove. Higher Reynold's numbers introduced an additional flow component along the length of the groove (Plate 19), but even at Re = 100, no trace of reverse flow could be seen. As the running clearance was reduced until it became comparable with the groove depth, a single laminar eddy formed within the groove region at all Reynold's numbers between 0·1 and 100. In common with the previous configuration of groove, this laminar eddy appeared to be fully developed at all times and extended across the entire section of the groove.

If the aspect ratio were reduced below unity and the groove width made small in comparison with its depth, a single laminar eddy was visible in the upper region of the groove at Reynold's numbers of 10 or less; the rest of the fluid in the groove remaining almost stagnant (Plate 20). With an aspect ratio of approximately 0·4 the vortex occupied the upper 30% of the groove at Re = 0·1, and progressively increased in size until it occupied between 50 and 60%

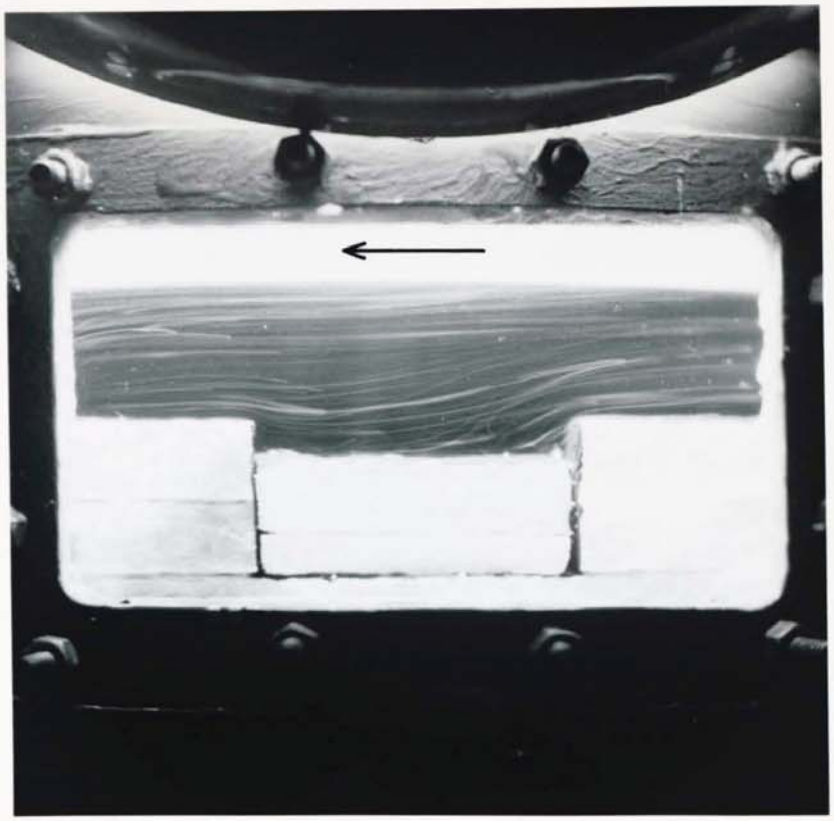

PLATE 18
STREAMLINE VORTEX-FREE FLOW AT Re = 0·1 .

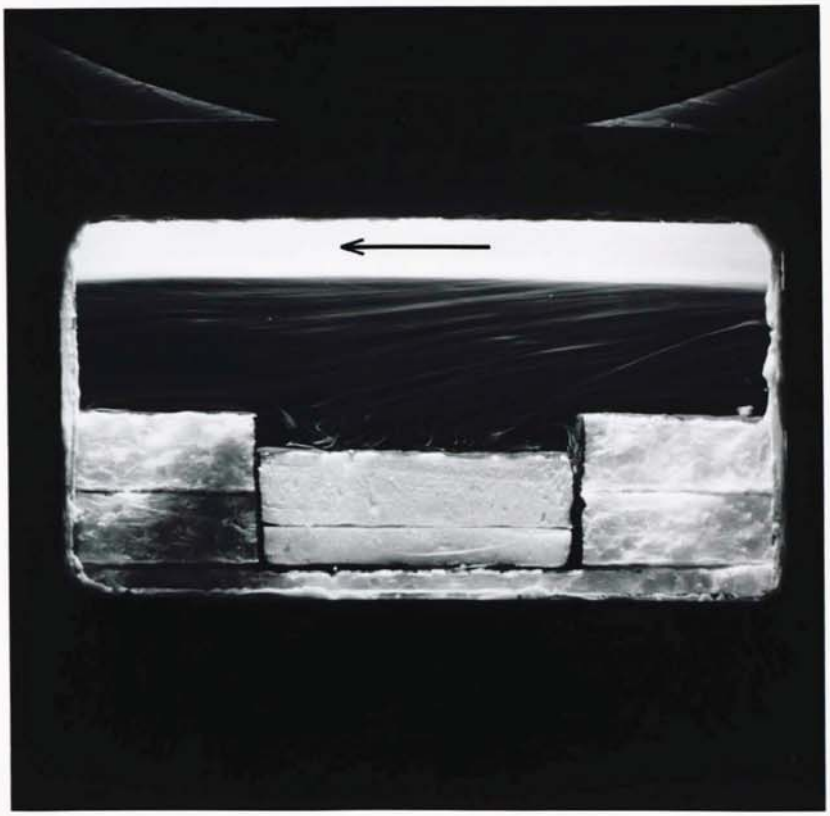

PLATE 19
ONSET OF LENGTHWISE FLOW AT Re = 100 .

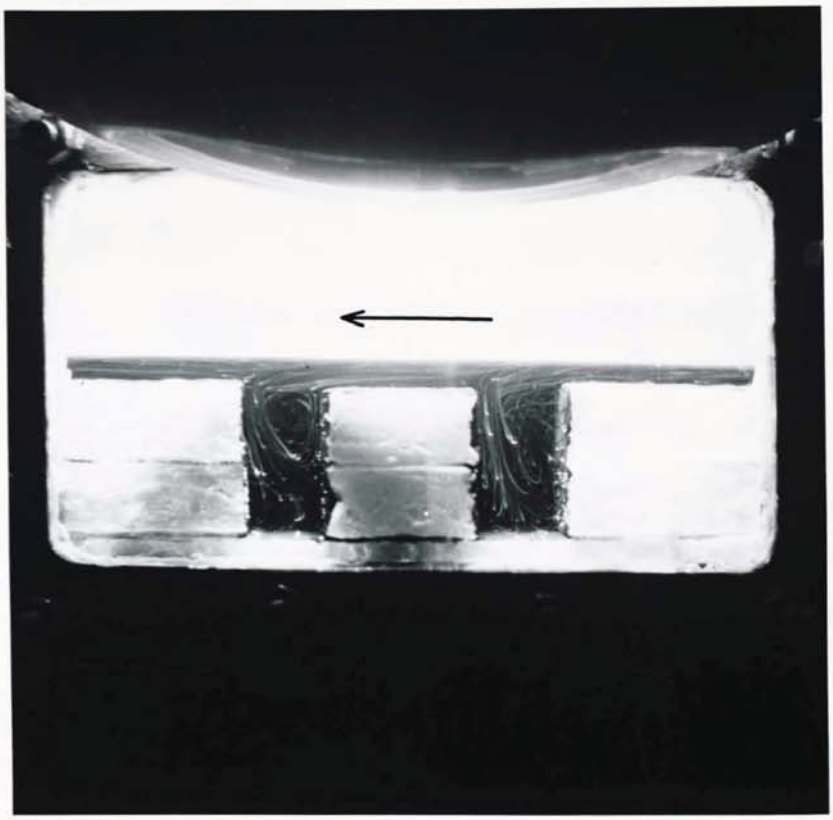

PLATE 20
PARTIAL VORTEX FLOW AT Re = 5.

PLATE 21
STAGNANT FLOW IN NARROW GROOVE AT Re = 0·1.

6.4 Experimental Studies of Fluid Flow (Continued)

of the groove volume as the Reynold's number was increased to approximately 5. Further increases in rotational speed progressively superimposed a flow component along the length of the groove and the streamlines within the groove boundaries assumed a two dimensional helical shape. Eventually, as $Re \rightarrow 100$, this lengthwise component became predominant and no reverse flow could be observed; the flow pattern then corresponded to that illustrated in Figure 31. Here, flow enters the groove at the outer edge and leaves just before reaching the inner blocked end.

A further decrease in aspect ratio to 0·4 or less allowed almost all the fluid within the groove to remain stagnant at Reynold's numbers of less than unity (Plate 21). Above unity, a very small vortex commenced in the upper section of the groove and as the Reynold's number increased towards 100, lengthwise flow appeared to be taking place throughout its entire volume. At aspect ratios of less than 0·5, the flow pattern within the groove appeared to be independent of the nominal running clearance.

Subsequent experiments showed the flow patterns were not significantly influenced by wide variations in groove shape and surface texture. It could also be demonstrated that linear streamline flow was regained immediately the fluid left the groove region and that the flow around one groove was not influenced by the presence of adjacent grooves. These observations justified the use of only one groove in the simulated bearing surface. By immersing a small light source in the glycerene, it was occasionally possible to follow the flow of clear fluid alone, without the addition of tracer particles. This confirmed that the particles themselves were not influencing the flow pattern.

On the basis of these rather elementary experiments, it is possible to make a number of general observations and deductions concerning the flow pattern in an actual bearing; at least under incompressible conditions.

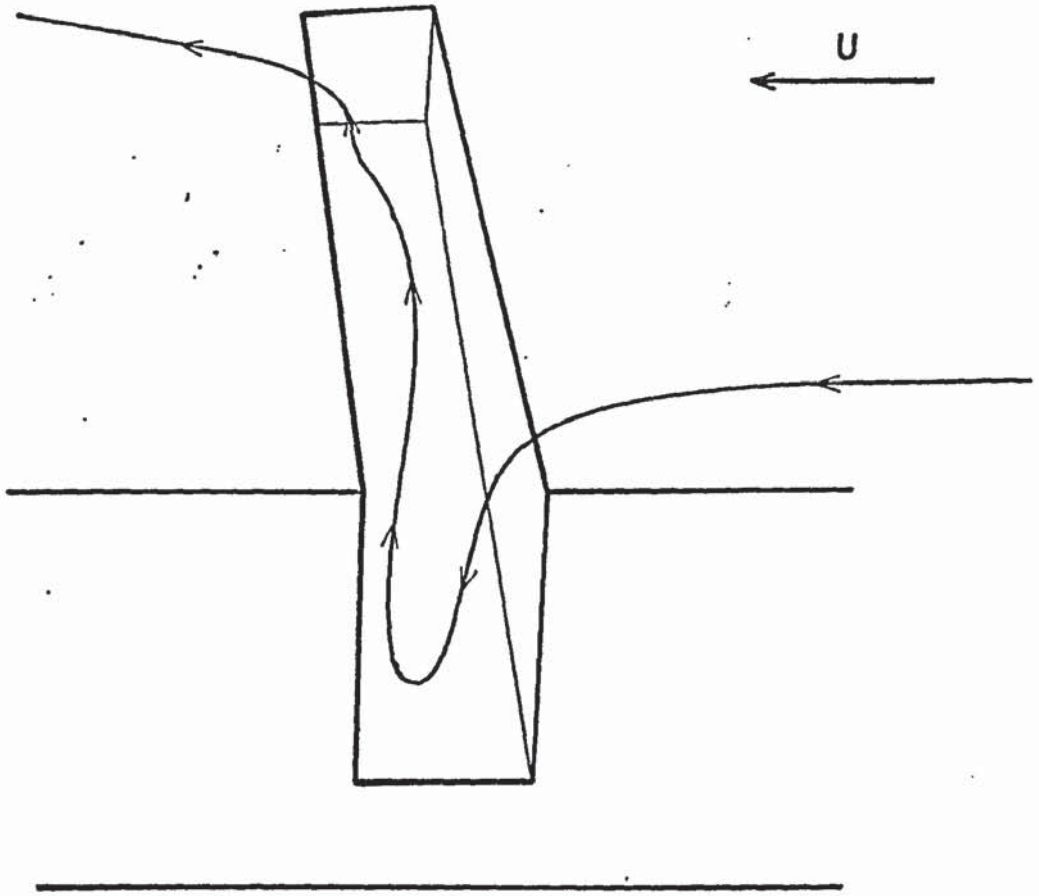

FIG. 31
LENGTHWISE FLOW ALONG GROOVE AT HIGH REYNOLD'S NUMBERS

6.4 Experimental Studies of Fluid Flow (Continued)

It is clear that both laminar eddies and fluid stagnation can occur, and that under suitable conditions, a streamline vortex-free flow can occupy the whole of the groove and clearance region. Reynold's number is apparently less important in determining the flow pattern than the overall geometry of the groove and clearance section. In particular, the aspect ratio of the groove plays a decisive part in shaping the flow, and at high aspect ratios, the running clearance over the land region is also important.

Perhaps the most important finding is that, on the model bearing, no single form of groove geometry could support each of the four flow patterns suggested in Figure 28. While the laminar eddies predicted by Fleming are confirmed, they are always fully developed unless the geometry begins to approach that of a bearing with an infinite number of grooves. Similarly, the predicted (Fig.28) stagnant flow region can only be demonstrated under conditions approaching those of infinite grooving, and where the groove aspect ratio is very low. The full linear streamline flow which Fleming used to explain his low power loss measurement (in comparison with an equivalent plain bearing) was only observed where the running clearance was considerably greater than the groove depth at high aspect ratios, and would certainly not occur under conditions of infinite grooving. Only when the aspect ratio fell below unity did the flow pattern change progressively with the Reynold's number, and only three distinct types of flow pattern were identified in this case. At higher Reynold's numbers, the onset of axial flow along the length of some of the groove formations examined was very marked, and would undoubtedly result in a considerable increase in viscous dissipation in an actual bearing. Once again, the onset of lengthwise flow appears to be more likely as the condition of infinite grooving is approached.

Since bearings tested here and by Fleming fall very much short of the concept of infinite grooving, it is instructive to consider the case of a practical bearing in which the aspect ratio may be as high as 300 and in which the normal running clearance is comparable with the depth of the grooves. In this case, the model predicts a

6.4 Experimental Studies of Fluid Flow (Continued)

single laminar vortex at all Reynold's numbers between 0·1 and 100, with no stagnant, linear streamline or lengthwise flow. The performance of the incompressible model conflicts with the flow pattern predictions made by Fleming and herein (Section 6.3) and does not account for the relative power loss variations on actual bearings. The explanation of this conflict is as yet obscure, and may require additional work on a compressible flow rig in order to confirm the true flow pattern under fully realistic operating conditions. It is possible that under incompressible conditions, the flow behaviour might be different to that under compressible conditions, where energy storage and release can occur with changes in film pressure across the groove-land region. Under these conditions, surface texture may play a more important part in determining the flow characteristic, whereas in the compressible model, it was shown to have anegligible effect.

It is considered that the onset of lengthwise flow along the groove (Figure 31) could be considered in addition, or as an alternative to the laminar eddy hypothesis, in order to provide an explanation for the sharp increase in viscous dissipation at high misalignment or rotational speed.

6.5 Statistical Correlation of Bearing Data

Data collected from some 83 bearings (as described in section 5.12) was processed by a standard statistical analysis programme (I.C.L. Statistical Package Mark II) on a digital computer, to determine if any significant correlation existed between the variables.

This data was examined by a number of appropriate statistical techniques (113), (71) and covariance and linear correlation matrixes generated for all possible combinations of parameters. Examination of the results available to date leads to the conclusion that no significant correlation exists between either geometric errors and test performance, between geometric errors and bearing failure, or between test performance and bearing failure. The implication of these results is that the geometric errors obtained

6.5 Statistical Correlation of Bearing Data (Continued)

from current manufacturing techniques are acceptable, and do not significantly influence either test performance or reliability, They also suggest that data from existing acceptance testing cannot be used to predict subsequent failure, although this does not mean that the inability of a bearing to meet the acceptance tests should not be used to justify its rejection.

The sample size quoted is large for a bearing of this quality, but small by statistical standards, and for this reason, the results should be viewed with some caution until more data becomes available.

This investigation also highlighted two unexpected problems which tend to limit the value of the results obtained to date.

Firstly, it was found in practice that the spread of geometric tolerances obtained was very much smaller than anticipated, and it is concluded that to obtain a wider variation from the specialised manufacturing equipment employed would be both costly and difficult; many of the machining operations being either fully or partly automatic. It is believed that in order to detect significant correlation (if any) and so either proove or disproove the relationships proposed in CHAPTER 7, a sample having a numerically wider range of tolerances will be required.

The second difficulty is that the initial reliability of the bearings included in this investigation has proved to be so high that only a minimal number of true failures have been recorded to date. An accurate correlation between bearing failure and other parameters will only be possible when a higher proportion of the test sample have failed, and present indications suggest that this position may not be reached for a number of years.

6.6 Electrostatic Discharge and Associated Effects

Gas bearing literature contains numerous references, e.g. (17) (103) (78), to the observed increase in starting friction of a self-acting bearing assembly following periods of continuous running. For many early gyro bearings, this friction increase culminated in a serious reduction of start/stop life and a series of

embarrassing failures during service. Young (103) observed that the surface friction continued to rise with the length of time the rotor remained at rest after a period of continuous operation, regardless of the number of start/stop cycles accomplished. This deterioration of performance with running hours proved to be very disturbing, for it challenged prior assumptions that continuous running caused no deterioration in service. Various explanations were proposed and Young (103) suggests that either organic contamination or migration of the boundary lubricant (believed to be residual 'Freon' cleaning solvent) or a combination of these two effects were responsible. Here, it is considered that contamination could occur as organic vapours are circulated within the bearing due to assymmetric pumping (80), with temperature and other effects eventually leading to their polymerisation into high friction materials. Migration of any original lubricating material may be due to a combination of internal temperature gradients and connected flow between the thrust elements. Alternatively, it has been proposed (107) that internal gas circulation within the bearing might scour the bearing surfaces perfectly clean and that any boundary lubricant molecules may then exhaust from the bearing during the rundown period. The immediate problem was reduced to acceptable proportions by improved techniques of cleaning and boundary lubrication, but it is still acknowledged that thin films of boundary lubricant will either deteriorate or disappear during extended periods of continuous running. Neither of the above proposals offer an entirely satisfactory answer to the observed increase in friction and an alternative explanation is proposed here based upon electrostatic effects within the bearing clearance. (See also reference 55.).

During routine laboratory testing, it was noted that a pitted 'wear' pattern appeared around the circumference of a plain toolsteel bearing shaft after some 2000 hours of continuous running. Two pitted tracks were formed around the entire circumference of the shaft with their axial position corresponding to the two high points along the journal surface, despite the fact that only one start/stop

cycle had been accomplished. Under optical examination, the pitting effect was similar to that previously observed on spark-machined surfaces, and it was decided to investigate the damage further with the aid of a scanning electron microscope. Plate 22 clearly shows that each track is due to a large number of individual craters in the surface of the shaft. In Plate 22 (c) and (d) it can be seen that many craters have had more recent craters superimposed upon them and in the top left hand corner of Plate 22 (d) the remains of circumferential polishing scratches can be seen on the undamaged surface. The craters vary in diameter from approximately 40 micro inches (1·0 micrometres) to 324 micro inches (8·0 micrometres) and each is characterised by a relatively smooth central region and an irregular raised rim. 'Talysurf' traces across the crater region (Figure 32) indicate that the raised rims are up to 8 micro inches (0·2 micrometres) above and the central region a similar amount below the mean bearing surface. Each crater may be deeper than indicated because the diamond measuring stylus is probably too large to provide an accurate trace of so small a feature. The average width of the pitted region was 0·003 inch (0·076 mm). No corresponding damage could be observed on the rotor bore which, unlike the shaft, was fabricated from a hard cermet material of high melting point. The form of each crater compared closely with craters subsequently produced by a single spark discharge form the tip of a fine tungsten wire, and with craters known to have been formed when a focussed laser pulse was used to vapourise part of a metal substrate. In each case a smooth central depression was surrounded by an irregular spattered rim, though the laser produced a more circular cavity. Comparison was also made with craters previously investigated by the writer (72) and known to be due to spark discharge from an Argon plasma. Once again, the smooth depression and raised rim are common features, though in the latter case, the rim had a more regular profile. Subsequent investigations failed to reveal any crater damage on ceramic or cermet surfaces after long running periods and it proved difficult

a) X 74

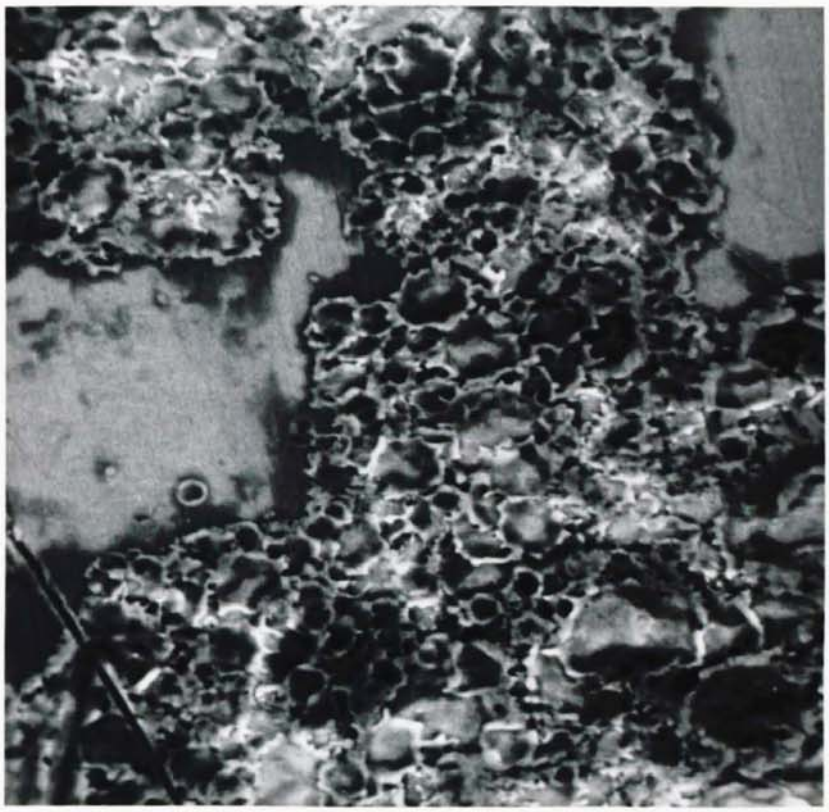

b) X 1,500

PLATE 22
STEROSCAN EXAMINATION OF ELECTROSTATIC DISCHARGE TRACK ON TOOLSTEEL BEARING SURFACE

c) X 7,400

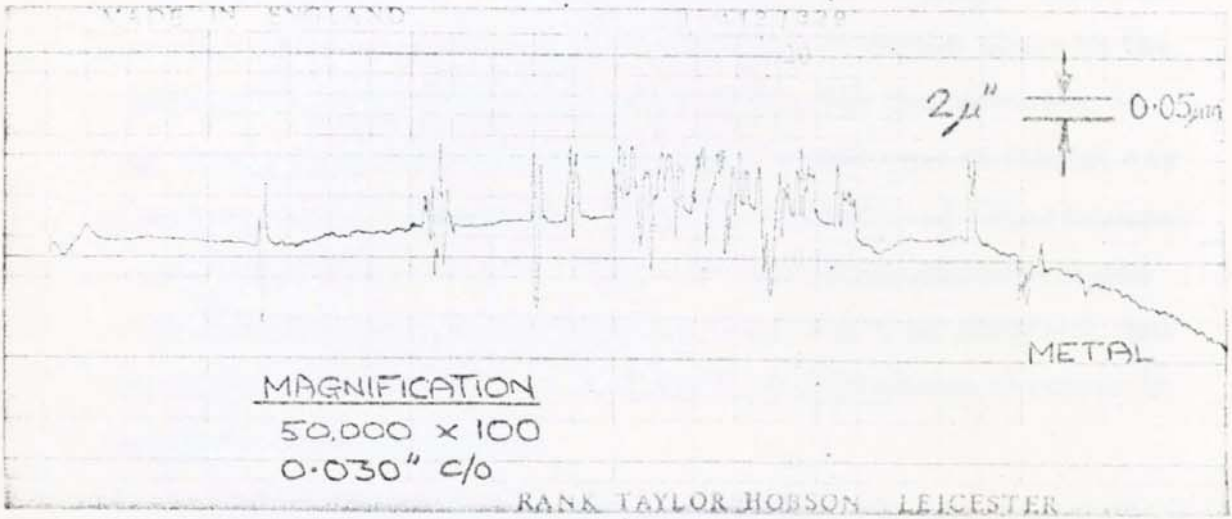

FIG. 32
TALYSURF PROFILE ACROSS AN ELECTROSTATIC DISCHARGE TRACK

to repeat the original damage on a second toolsteel shaft, though unavailability of suitable hardware prevented the original conditions from being duplicated.

On the evidence available, it was concluded that the craters were due to some form of spark discharge across the bearing clearance from the spinning rotor. Rapid movement of an insulated body through a gas is well known to result in an electrostatic build-up of electrical charge on the body, as, for example, on an aircraft skin during flight. The rotor of a self-acting gas bearing is electrically insulated from its surroundings while airborne and the viscous friction dissipation over its surface has been found to be in excess of 1·5 watts (Figure 27). Under these conditions, electrostatic charging of the rotor must take place. Once an appreciable amount of charge has been generated, it will eventually take the most convenient path to earth, which in this case will be across the bearing clearance at its narrowest point. At 400 revolutions/second, this particular bearing design is known to run at very low eccentricity; below 2 micro inches (0·05 micro metres) under one - 'G' conditions, and this would account for the fact that discharge tracks were observed around the entire circumference. At high eccentricities, it might expected that the cratered area would be confined to a region close to the point of minimum radial clearance, subject to the influence of high local pressures at this point which would tend to inhibit any form of electrical discharge. Despite a number of experimental investigations (see section 5.10), no conclusive measurements of electrical charge on the spinning rotor could be obtained, but this is believed to be due to the practical difficulties involved in this type of measurement.

Following the discovery of crater damage, a series of experiments were carried out with the object of producing and examining spark damage on various bearing surfaces. The materials examined were hardened toolsteel, tungsten carbide and boron carbide, and each surface was initially polished to within 0·5 micro inches C.L.A. (0·012 micrometres C.L.A.).

6.6 Electrostatic Discharge and Associated Effects (Continued)

Each discharge was initiated from the tip of a fine tungsten electrode, which was in turn attached to the spring-loaded armature of an electrical solenoid. The discharge current was arranged to flow though the solenoid, which would in turn pull the electrode away from the surface. With this apparatus and a suitable power supply, a series of reasonably distinct spark discharges will occur as the electrode is gently stroked across a conducting surface forming part of the electrical circuit. (Similar commercial equipment is frequently used in industry to indelibly mark metal components). All the craters were formed by the same discharge potential (4 volts), chosen to give small but optically visible damage on the surfaces concerned.

On toolsteel, two distinct types of discharge damage were observed, depending on the polarity of the bearing surface (see Plate 23 (a) and (b)). Where the bearing surface was negative with respect to the discharge electrode, the damage took the form of a small circular crater with a smooth base and a raised and spattered rim. The surrounding area often contained solidfied debris, and sometimes showed an etched appearance, characteristic of ion bombardment. No coloured oxide films were visible, indicating that little heat had been generated in the surrounding region. Where the bearing surface was positive with respect to the discharge electrode, a larger circular crater was formed and the raised rim was far less evident. Concentric circular interference fringes radiated from the centre of the crater to the surrounding bearing surface, indicating that considerable heating had taken place during its formation. The fringe pattern indicated that maximum heat generation had occurred at the centre of the crater, and the overall surface damage was characteristic of that produced by electron-beam spot welding equipment.

It is clear that in the first case, with the bearing surface negative, damage is predominantly due to positive ion bombardment, and subsequent removal or displacement of surface material. Local heating and fusion is undoubtably involved, but oxidation

a) Surface negative X 200

b) Surface positive X 100

PLATE 23
DISCHARGE DAMAGE PRODUCED EXPERIMENTALLY ON A HARDENED STEEL SURFACE.

fringes are probably unable to form under ion bombardment conditions. In the second case, with the bearing surface positive, damage is predominantly due to electron bombardment, and subsequent heating of the surface structure. The heating effect of electron bombardment is considerable, and vapourisation eventually occurs in the discharge region. Similar damage was noted on sintered tungsten carbide, but coloured oxidation fringes were not formed in this case. The craters were only half the diameter of those produced in toolsteel, and where damage was due to electron bombardment, extensive cracking of the surrounding surface had occurred. Both types of crater are illustrated in Plate 25.

On boron carbide, spark damage was found to be very difficult to produce, especially if the sample was of high purity. Where the carbide surface was at a positive potential, distinct craters could not be formed and a lighter coloured patch suggested that the heating effect had slightly oxidised the surface layer (See also section 7.15). With the surface negative, small craters with raised and spattered rims were occasionally formed, and one of these is illustrated in Plate 24.

From these simple experiments, a number of important conclusions can be drawn. Boron carbide is well protected from extensive spark damage by its higher resistivity and melting point, and in comparison with hardened toolsteel, some protection is also afforded to tungsten carbide by these same parameters. Comparison of craters discovered on actual bearing surfaces with those induced experimentally (Plates 23, 24 and 25) indicate that the stationary bearing shaft was at a negative potential during the discharge period, and that the spinning rotor must therefore have acquired a positive charge. In order to become positively charged by viscous effects, the rotor material must loose electrons to the surrounding air as a result of frictional motion between the two media. Loss of electrons under these conditions is in agreement with the observations of Tribo-Electronic Emission described by Kitamura (41). Charge storage over the rotor surface

X 200

PLATE 24
DISCHARGE DAMAGE PRODUCED EXPERIMENTALLY ON A BORON CARBIDE SURFACE (surface negative)

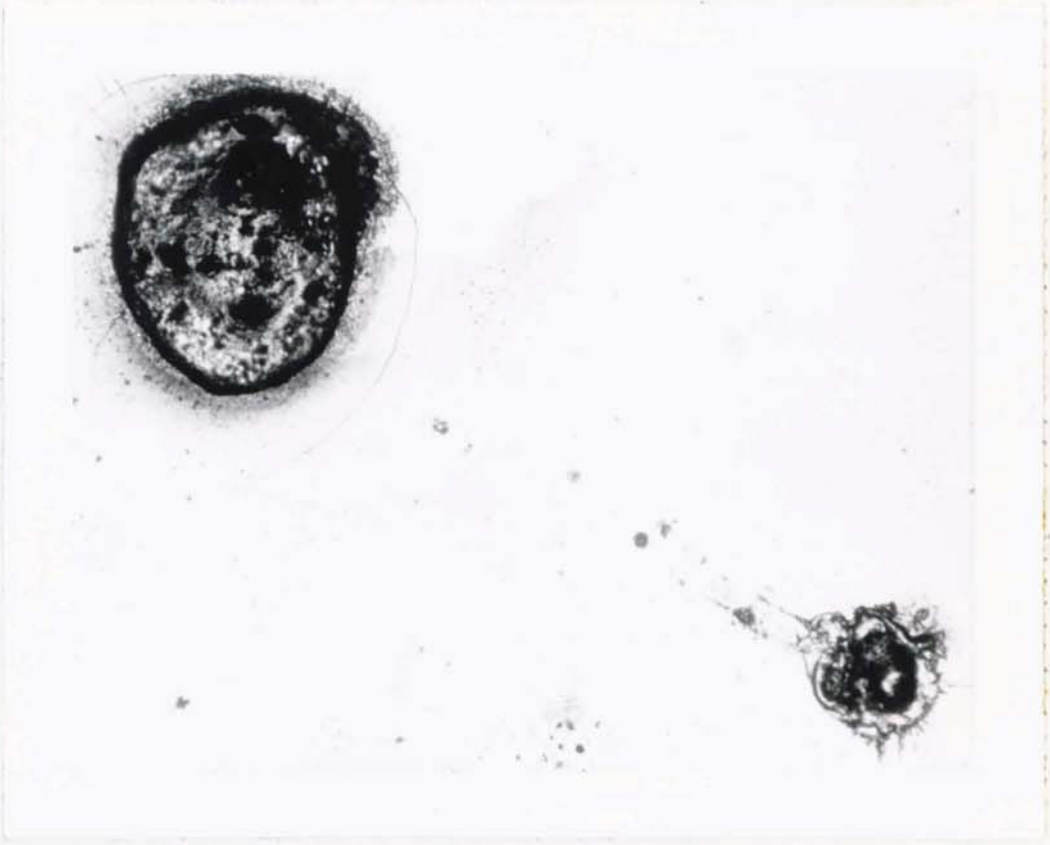

X 200

PLATE 25
DISCHARGE DAMAGE PRODUCED EXPERIMENTALLY ON A TUNGSTEN CARBIDE SURFACE (Upper - surface positive, Lower - surface negative)

will be related to the electrical capacitance between the bearing surfaces. For the bearing in question, this capacitance may be shown by calculation to be 456×10^{-12} farads, and knowing the approximate breakdown potential of the bearing clearance to be 100 volts (section 5.10), a value for the stored energy may readily be obtained. This energy storage was found to be 2.3 microjoules, and establishes an approximate upper limit for the dissipation due to each discharge, assuming that 90% of the rotor charge is lost at each breakdown. Reference 114 suggests that the size of a discharge crater is determined by the total energy dissipation during the discharge. Assuming the craters in Plate 22 to be hemispherical,* the energy required to vapourise this volume of material can be shown to be smaller than 2×10^{-12} Joules. This is very much less than the amount of energy estimated to be available from the charged rotor and the balance will be available for heating the surrounding bearing material and lubricant film.

Prior disclosure of this work (55) has allowed additional evidence of discharge phenomena to be obtained from other sources. Kilmister (56) (55) describes circular craters with raised rims of up to 200 micro inches (5 micro metres) in height discovered on an externally pressurised bearing, but unfortunately the cause of the phenomenon was not investigated in detail. Boyer (55) states that similar damage has occasionally been observed on steel gyro shafts as a result of electrostatic discharge from the operator's body during handling. Experiments later showed that identical damage could be produced by sparks of approximately 100 volts. Electrical fretting of ballrace bearings while operating at high speed in the full fluid film region has been known for many years (40) and is a frequent source of radio noise in aviation systems, unless measures are taken to earth the

* van Osenbruggen (50) suggests that for very small spark craters, the diameter/depth ratio can exceed 10, and in this case, the calculated vapourisation energy would be even smaller.

rotating element. Continuity measurements across the clearance of a self-acting gas bearing invariably suggest that the D.C. resistance of the gas film is significantly lower than would be expected and this low resistance has formerly been attributed to moisture within the bearing (55) (84). Experiments here (section 5.10) now suggest that moisture alone is not necessarily responsible. It appears more likely that some form of continuous electrical discharge may be taking place within the bearing and that the effective impedance of the lubricating film is lowered in the region of this discharge. Stephenson (55) observed that continuity measurements across energised gyro bearings had occasionally indicated rotor touch-down, despite the fact that no corresponding mechanical drag had been detected on the rotor. These apparent contacts may have been merely a transient electrical effect within the bearing, which would explain the absence of mechanical drag on the rotating member. A very recent paper by Freeman (4) makes brief reference to "... static charge attraction between rotating and stationary elements and attraction of contaminants to surfaces and grooves..." as possible causes of gyro bearing failure.

If the principle of internal electrostatic discharge is accepted, and there appears to be ample circumstantial evidence to support this view, then possible discharge mechanisms may now be considered in greater detail.

Electrical breakdown of the supporting gas film may occur either as a series of intermittent arc discharges, or as a slow leakage of current between the bearing members concerned. A continuous arc is theoretically possible but Plate 22 suggests that bearing damage was due to a large number of discrete events. Under pressure and temperature conditions normally encountered in gyro bearings, a potential in excess of 15 volts is required to start and maintain an arc, with a large proportion of this voltage being used in the anode and cathode fall regions (43). The voltage drop across the arc is well known to be only slightly dependent on current flow once the arc is established and varies marginally with

6.6 Electrostatic Discharge and Associated Effects (Continued)

the length of the discharge path. The temperature at the centre of a plasma arc is believed to be in the region of 5000°C; sufficiently hot to vapourise all known bearing materials. Boto's (40) examination of arc damage to metal roller bearings revealed substantial tempering at the crater floor, compared with the rim which was later confirmed by Fiennes (43) who observed that the floor of a similar crater was readily scratched by a measuring stylus. This suggests that most of the thermal energy is focussed at the centre of the crater and conducted into the bulk of the material rather than along its surface.

Referring to the damage illustrated in Plate 22 and Figure 32, it is possible to make some approximate calculations concerning the duration of each individual discharge. If the bearing rotates at 400 revs/second, the relative velocity between the two surfaces will be 500 inches / second (12·7 m/s). Taking a typical crater to be 162 micro inches (4 micrometres) diameter, this distance will be traversed in 0·3 micro seconds; suggesting a maximum duration for the discharge to produce a single quasi circular crater. Craters of various diameters were visible on each photograph and these dimensions corresponded to spark durations of between 0·08 and 0·65 microseconds. The calculation is only approximate because one end of the arc may either rotate a short distance with the moving surface or continue to discharge across the shortest path for a slightly longer period. Once an arc has been initiated, vapourised boundary lubricant, organic contamination or surface material will assist in maintaining it until either the charge is exhausted or geometric conditions change. The theory of sparking between electrical contacts is considered more fully by Holm (44) but does not include the effect on harder wear resistant materials.

The alternative to a plasma arc is a slow discharge of electrons across the bearing clearance. The mean free path of an electron in air at +20°C and atmospheric pressure is in the order of 7 micro inches (0·18 micrometres) and avalanche breakdown of the film will therefore be unlikely. Ionisation of the film is more probable and would result in a small leakage of charge

6.6 Electrostatic Discharge and Associated Effects (Continued)

across the bearing clearance. The presence of organic contamination within the bearing would assist ionisation and no crater damage would occur on either surface. This form of discharge would also explain why no electromagnetic radiation could be detected while the bearing was running (section 5.10).

Breakdown of the gas film may be initiated by a number of mechanisms and a detailed mathematical investigation of these is presented by Fiennes (43). Some caution is required in interpreting Fiennes' work because this considered oil films and will not necessarily apply to gas lubrication. The mechanisms of conduction and breakdown in thin gas films are considered to be very complex and are probably modified further by the local geometry and texture of the opposing surfaces. For these reasons, attempts to calculate the breakdown potential proved to be fruitless. Under certain conditions it is clear that a plasma arc discharge can take place, and that this can cause severe physical damage to the wear surface. The combined thermal and electro-chemical effects of the arc will either destroy or modify any boundary lubricant and the condensation of vapourised surface material could alter the friction properties of the surrounding area. Fortunately, it appears in practice that this form of discharge is quite rare and has only been observed occasionally on steel components running at comparatively large clearances, $\geq$150 micro inches (3·8 micrometres). For ceramic and cermet bearings operating at clearances of 90 micro inches (2·3 micrometres) or less, a slow ionising discharge may be more probable, and it is known that weak ion bombardment will progressively remove films of boundary lubricant or contamination from a metal or ceramic surface (86) without causing mechanical damage to the surface itself. Even under sparking conditions, the comparatively high resistivity and melting point of most ceramic materials will afford some protection. Both forms of discharge could be expected to leave a residual electrostatic charge on any debris particles within the bearing and, depending upon the nature of the charge, may result in the particles either clustering together or adhering more firmly to the wear surface. Examination of stripped bearings after life testing

6.6 Electrostatic Discharge and Associated Effects (Continued)

has shown the boron carbide debris adhering strongly to the parent surface, whereas sub-micrometre powder sprinkled over the surface could be easily blown away. In all the bearings examined here to date, distribution of the debris appeared to be influenced by hydrodynamic rather than electrostatic forces. Where the floated gimbal structure is electrically insulated from the gyro case, as in certain inertial quality instruments, it is considered that transfer of charge from the rotor to the gimbal assembly may result in electrostatic forces between the gimbal and the case causing deflection of the entire gimbal. This will in turn produce an error in the gyro output signal.

6.7 Numerical Programme and Associated Experimental Results

Despite precautions outlined in section 4.12, very considerable numerical stability problems were encountered while running the final version of the programme, and acceptable solutions could not be obtained consistently above $\Lambda \simeq 6$ and $\varepsilon = 0{\cdot}4$. Corresponding financial and time restrictions prevented further work and severely restricted the range of solutions obtained.

These limitations prevented the development of a corresponding numerical programme for the grooved thrust bearing, and experimental measurements of the thrust exhaust pressure were therefore taken as the effective ambient pressure in the numerical journal solution. It is considered here that the connected thrust and journal bearings can be treated seperatly in this way because the twin chamfers at each end of the journal form an annular reservoir whose volume is many times that of either bearing clearance. This reservoir seperates the journal and thrust elements, while still allowing the thrust exhaust to pressurise the journal clearance.

The final numerical programme could only be run for a total of twelve grooves, whereas the actual experimental journals had thirty six grooves at each end. Prior work (31) (67) has shown that bearing performance decreases from an asymptotic limit as the number of grooves is reduced from infinity. The restricted

6.7 Numerical Programme and Associated Experimental Results (Continued)

numerical results also mean that previously completed experimental data cannot always be compared directly, and direct comparison with prior work is also more difficult because of the practical features of this design.

6.7.1 Pressure Distribution

Initially, the numerical programme was run with the groove depth equal to zero; a solution thus being obtained for a plain journal. An additional computer programme was then prepared to yield a corresponding plain journal solution based on Ausman's small pertubation analysis (3) and the two results are compared in Figure 33. Agreement is seen to be excellent at small eccentricity ratios and reasonably good up to an eccentricity ratio of 0·3. In common with other numerical solutions (23), the pressure exceeds that predicted by the small pertubation analysis as the eccentricity increases. The axial pressure profiles were also found to be in close agreement.

Thus encouraged, a solution was then obtained for the pressure around a grooved journal, as shown in Figure 34. Here, the pressure component due to the grooves alone is clearly evident at zero eccentricity, as is the distinctive 'pressure ripple' over each land-groove pair predicted by previous workers (19) (31).

Both the theoretical and experimental results indicate that the pressure at any point within a typical H-form bearing assembly is, to at least a first approximation, equal to the algebraic sum of the components due to thrust exhaust, journal groove pumping and journal eccentricity or misalignment. This principle of pressure superposition is considered here to be important and is best illustrated in Figures 35 and 36. It is concluded that provided the rotational speed is high enough, the grooves will maintain super-ambient pressures throughout the bearing at any eccentricity or misalignment, and this excess pressure will help to prevent condensation and contamination within the bearing clearance. Experimental and theoretical results illustrated in Figure 37

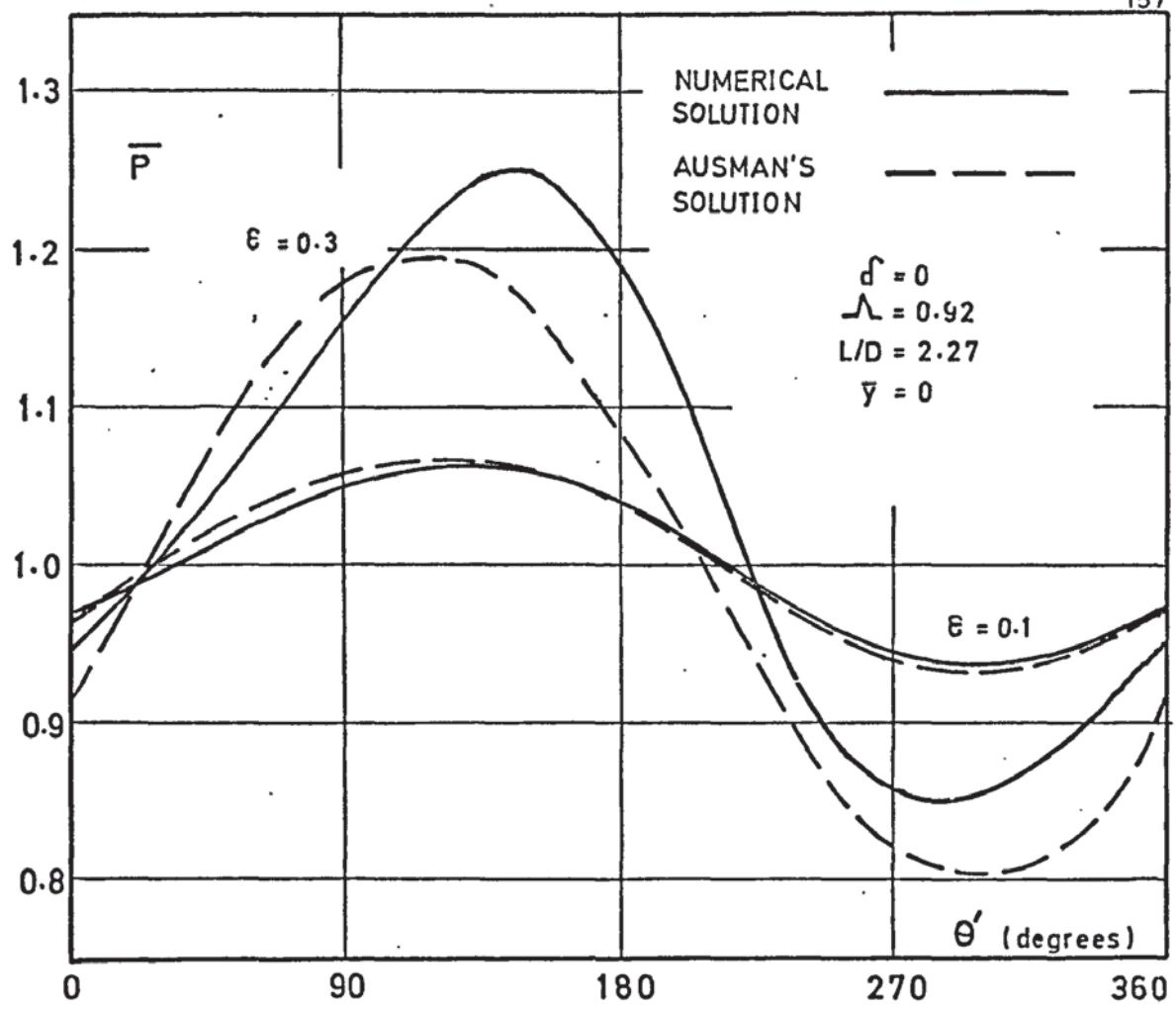

FIG. 33 COMPARISON OF THEORETICAL PRESSURE DISTRIBUTIONS AROUND A PLAIN JOURNAL BEARING

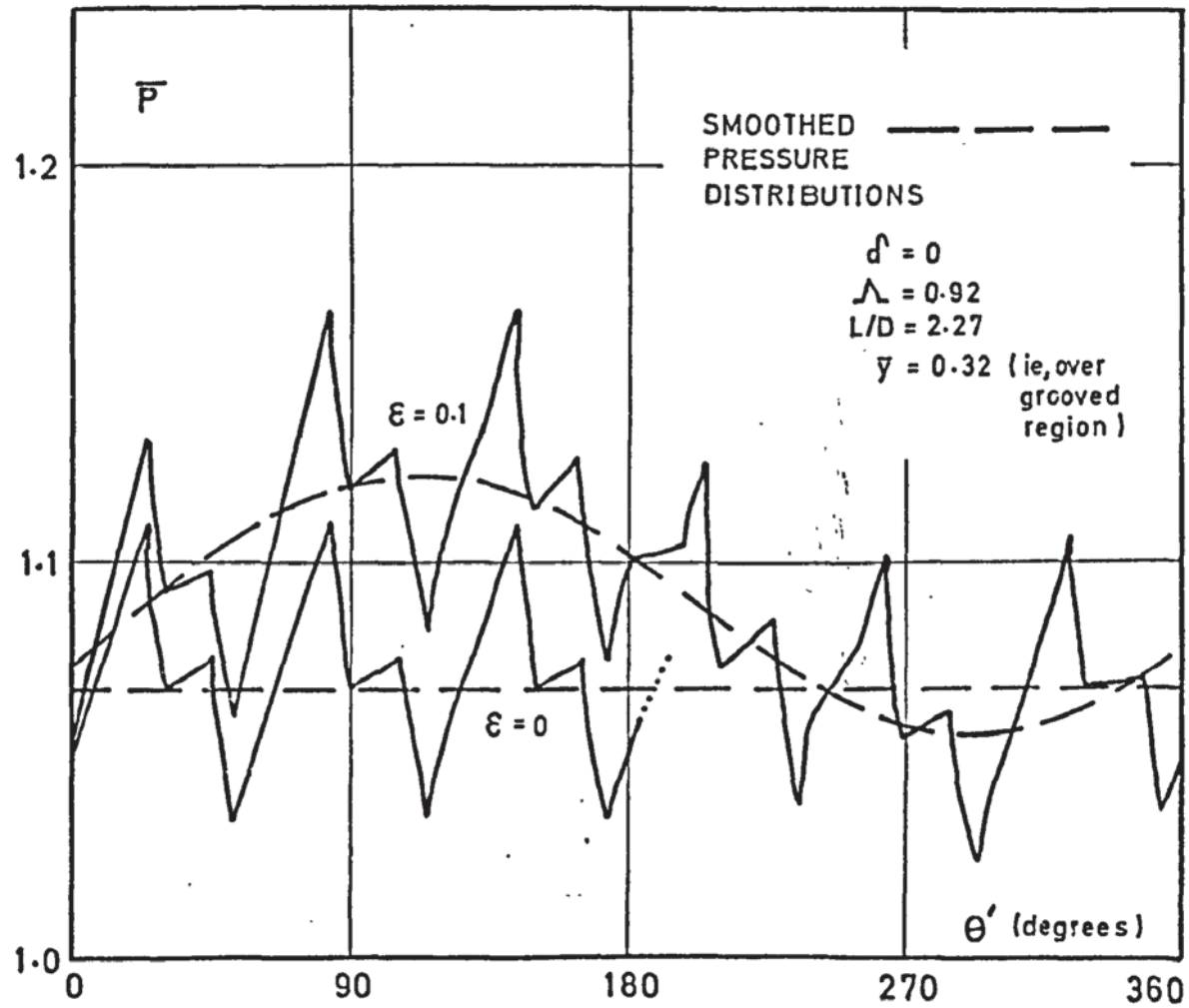

FIG. 34 THEORETICAL PRESSURE DISTRIBUTION AROUND A GROOVED JOURNAL BEARING

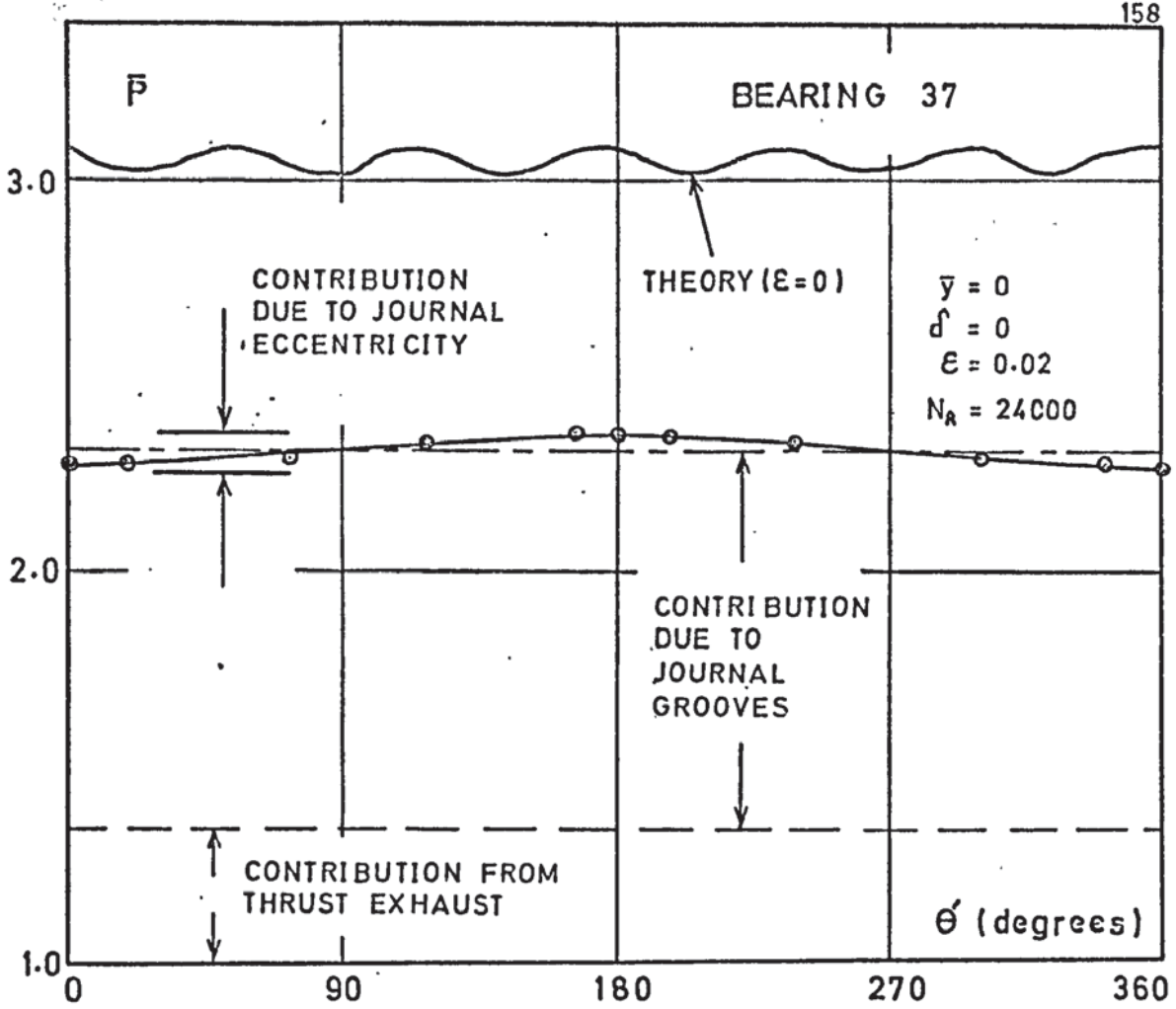

FIG. 35 PRESSURE SUMMATION AROUND CENTRE OF JOURNAL

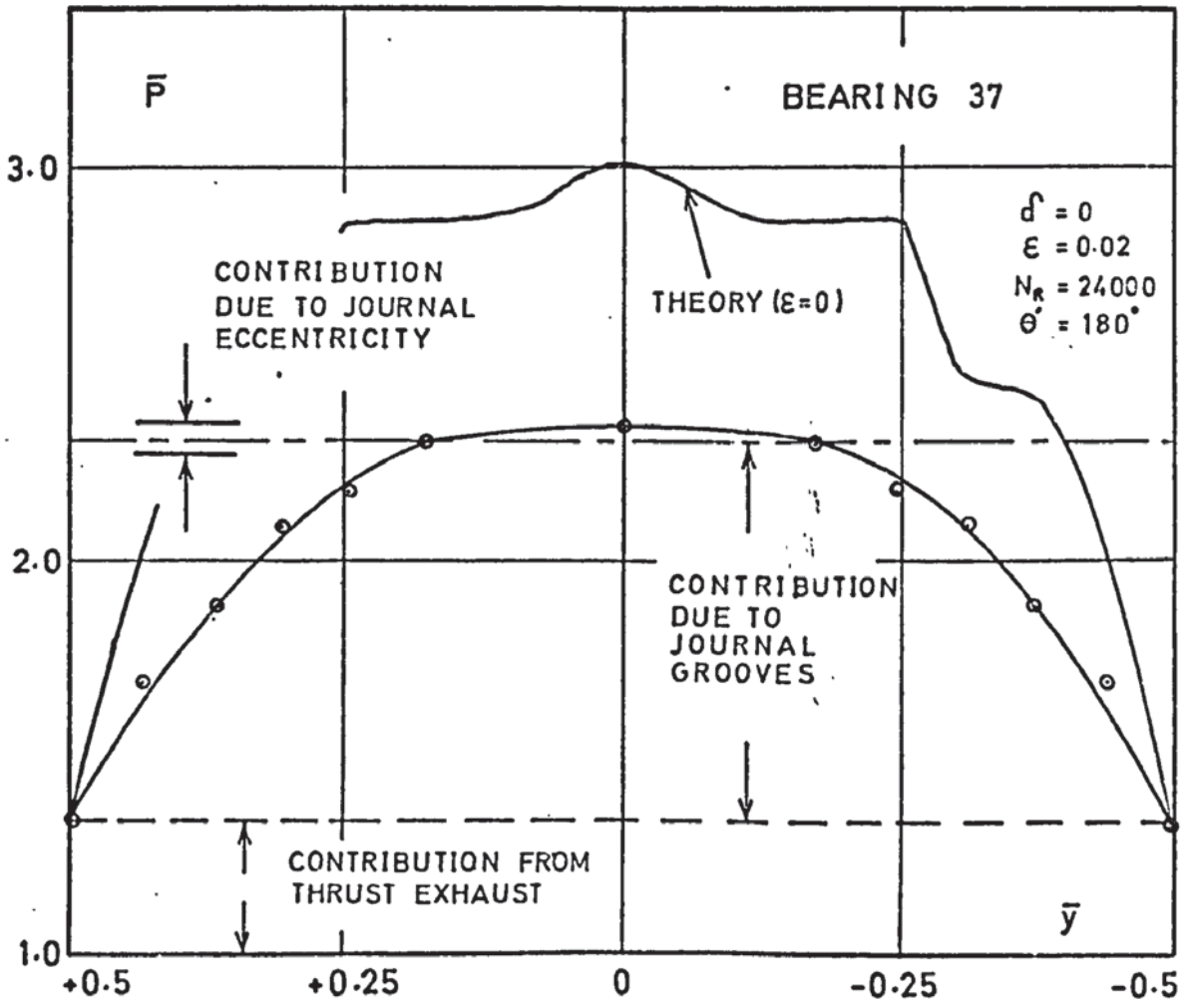

FIG. 36 PRESSURE SUMMATION ALONG JOURNAL AXIS

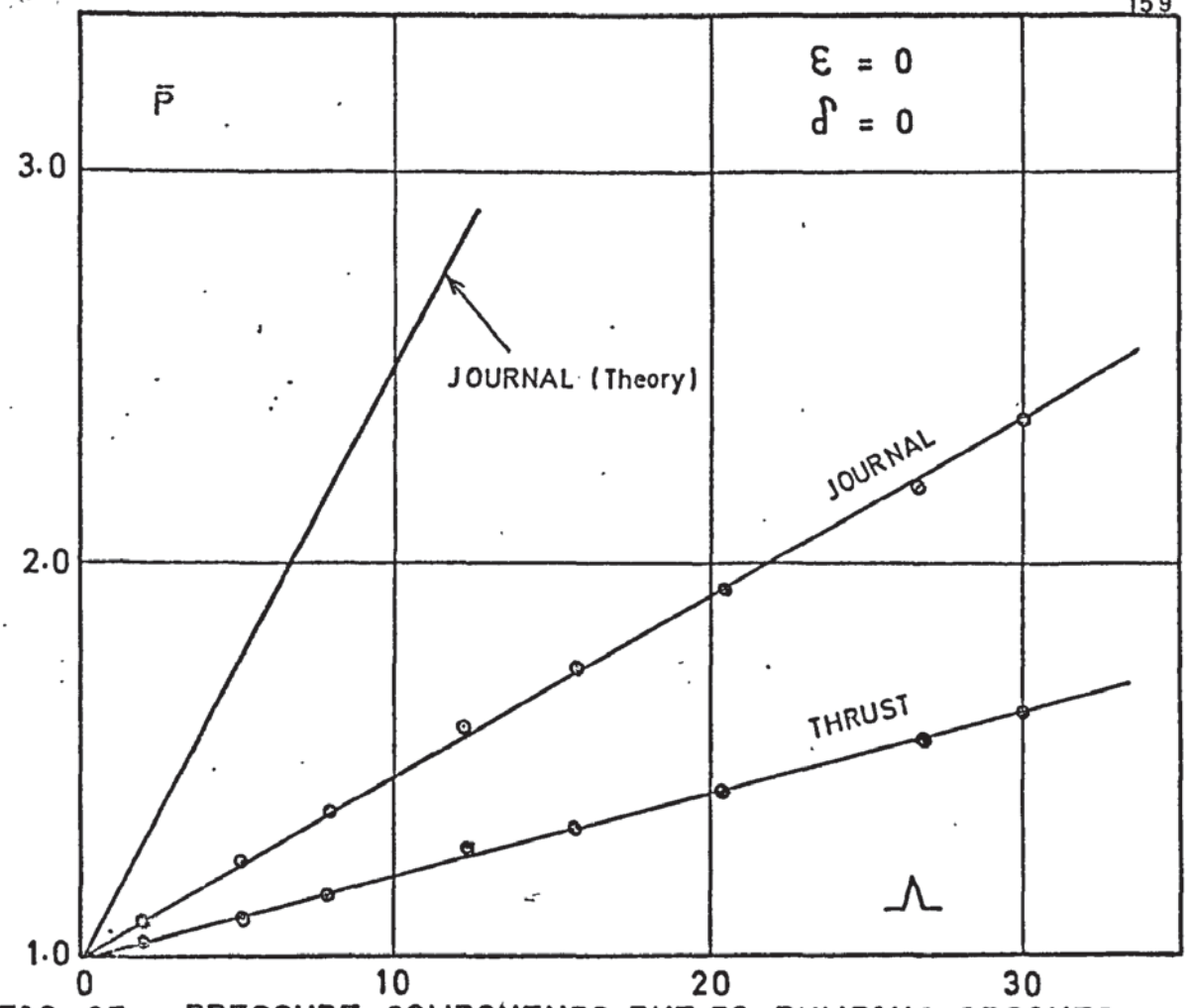

FIG. 37 PRESSURE COMPONENTS DUE TO PUMPING GROOVES vs COMPRESSIBILITY NUMBER

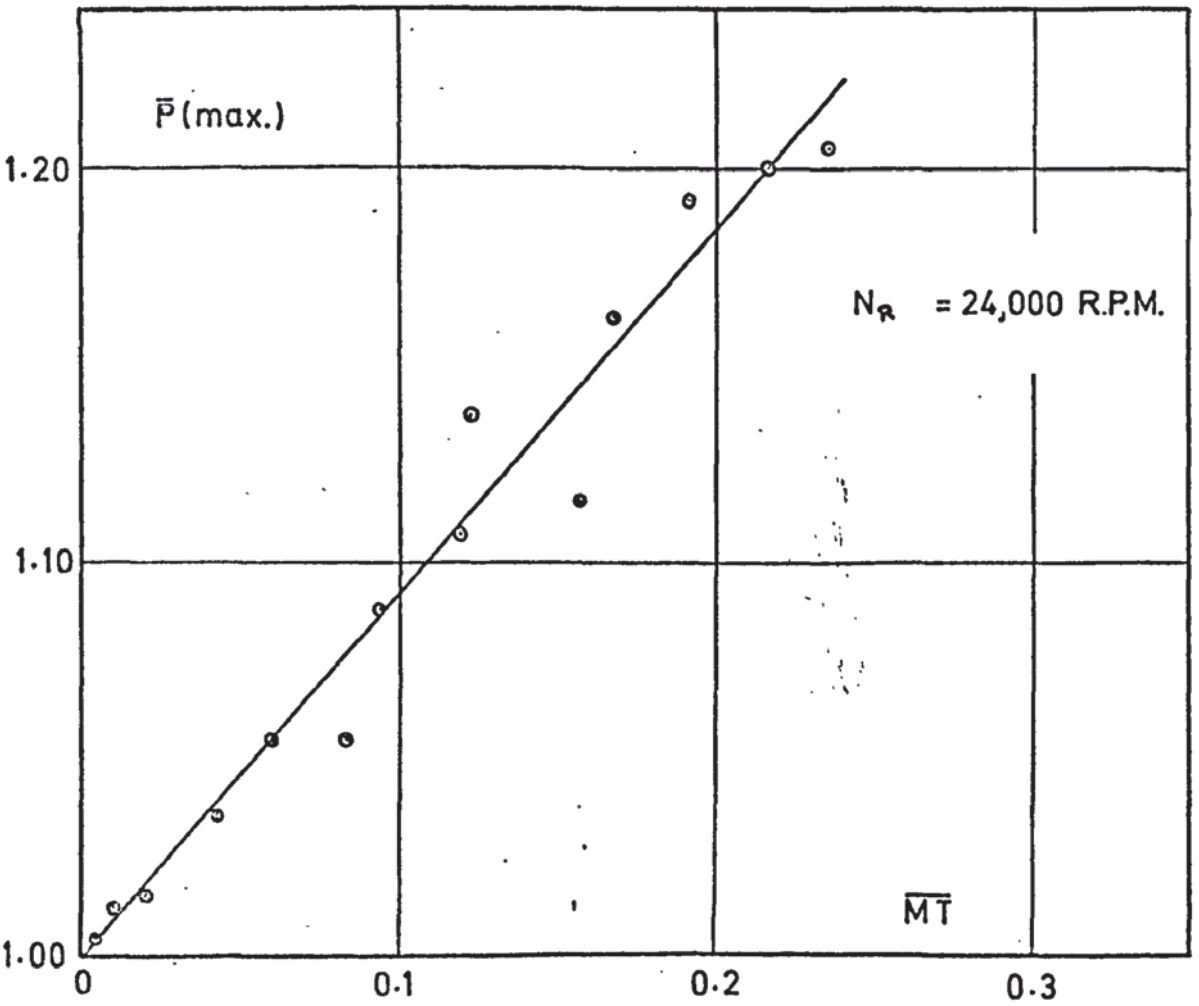

FIG. 38 PRESSURE CHANGE vs MISALIGNMENT TORQUE

6.7.1 Pressure Distribution (Continued)

show that the pressure contribution due to the pumping grooves increases linearaly with compressibility number, but the measured values are much lower than those predicted numerically. Figures 35, 36, 39 and 40 show a range of theoretical and experimental pressure profiles for a grooved journal and thrust assembly, and it is evident that the numerical programme is predicting higher pressures than those measured in practice, though their overall shapes are seen to be very similar. In Figures 35 and 39, the'pressure ripple' due to the journal grooves is still visible at the centre of the bearing, showing that the local influence of the groove extends completly across the plain central region of the shaft.

Under angular misalignment conditions, the experimental pressure change profile (Figure 41)compares closely in shape with those generated by the small pertubation programme (Figure 42) but this latter-programme subsequently developed a fault and did not give results for comparable compressibility values. Pressure change appeared to vary linearly with misalignment torque (see Figure 38) and it is clear that the pressure changes involved in angular misalignment are of a much lower order than those due to radial misalignment. This observation helps to explain why resistance to torque loading has often been a limiting feature of many gyro bearing designs (16).

When running the numerical programme, evidence was obtained that 'negative pressure' values were occasionally generated during some of the intermediate iterative cycles, and increasingly frequent reductions in relaxation factor were necessary to ensure convergence as both Λ and ε were increased.

It was found that both numerical stability and convergence were degraded each time Λ was increased, and the number of iterations required to converge the solution increased progressively with ε Up to 150 iterations were required for some cases and there was evidence that an even larger number would have yielded several more solutions before instability finally became the overriding factor.

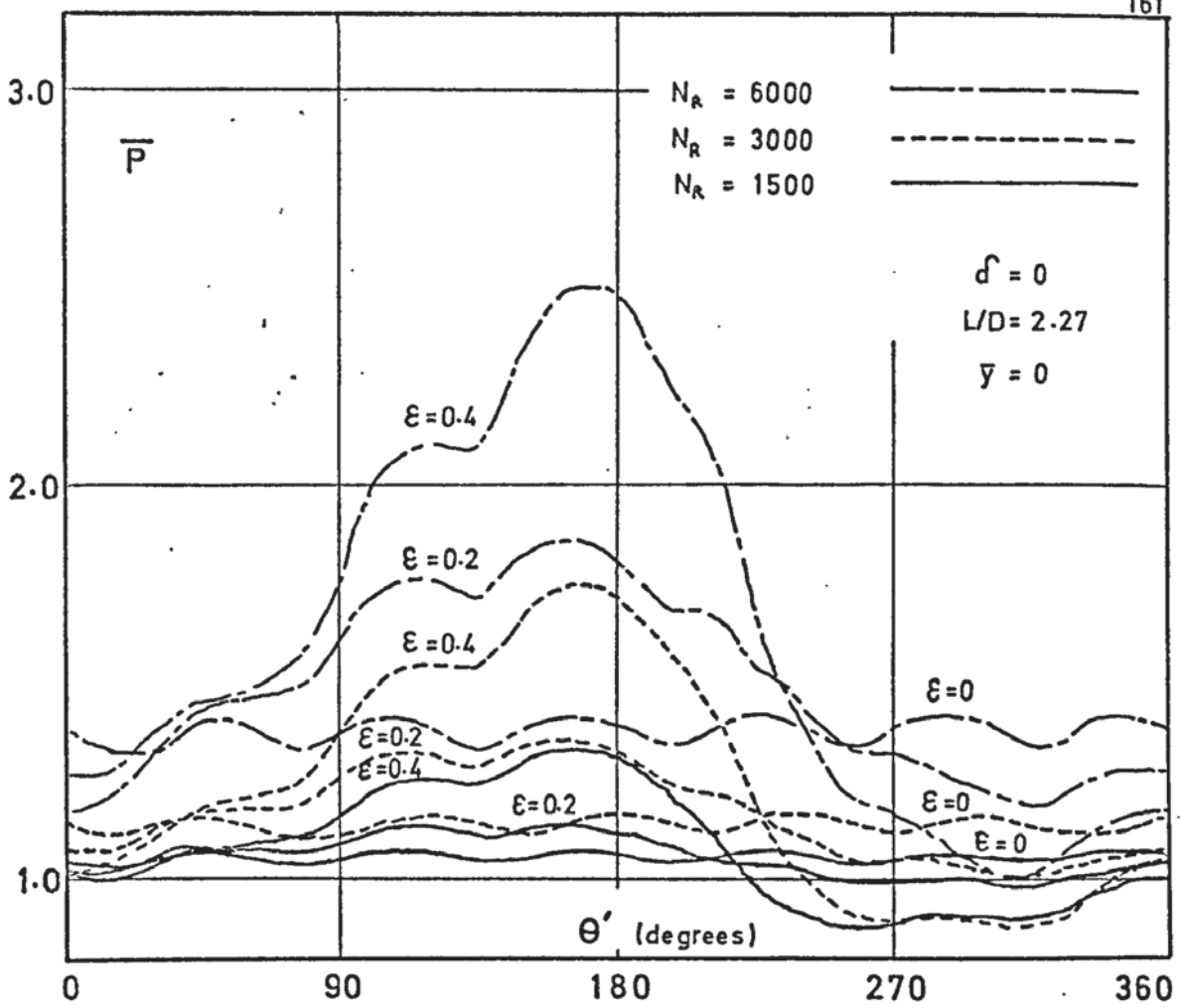

FIG. 39 THEORETICAL PRESSURE DISTRIBUTION AROUND A GROOVED JOURNAL AND THRUST ASSEMBLY

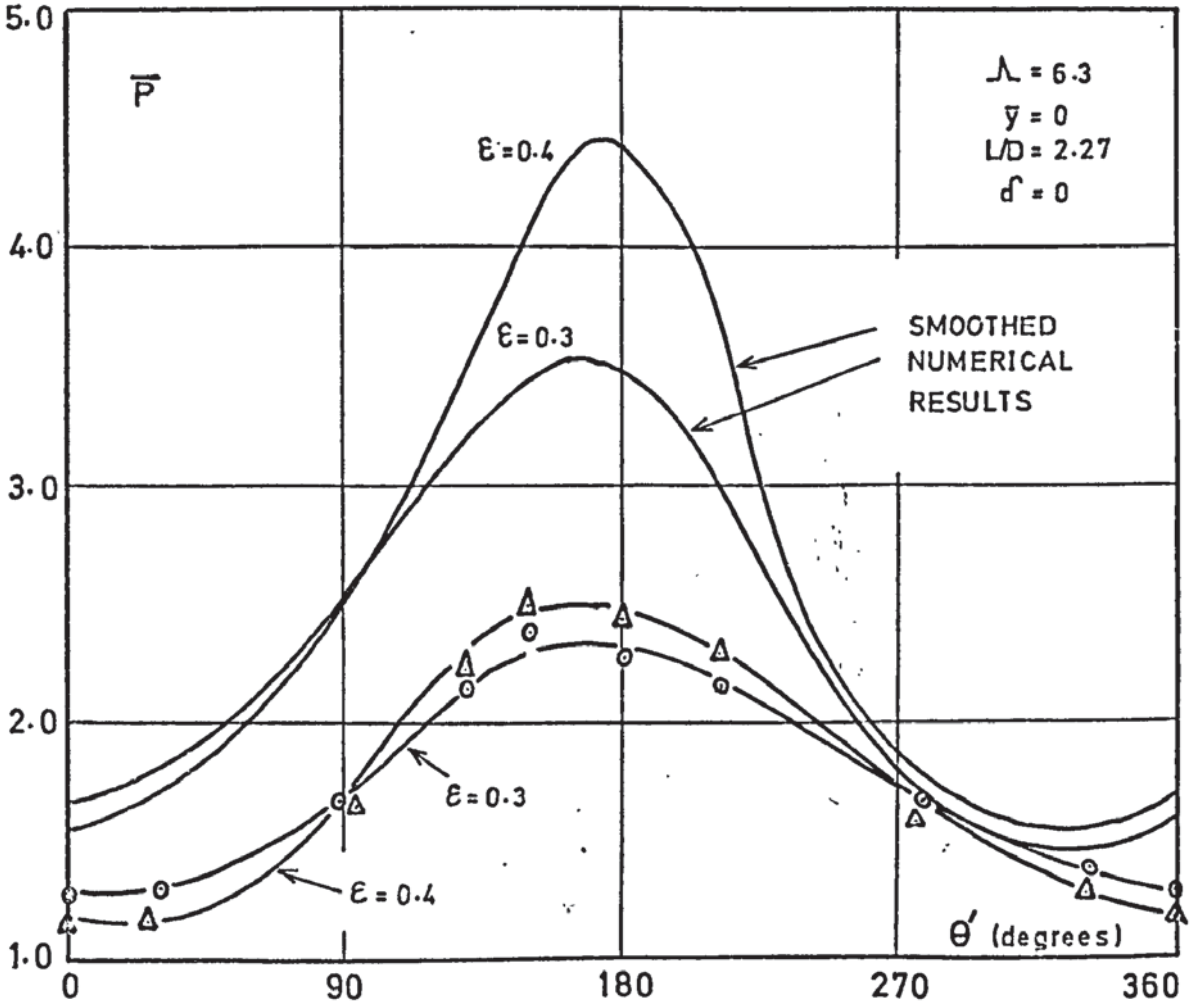

FIG. 40 COMPARISON OF NUMERICAL AND EXPERIMENTAL PRESSURE DISTRIBUTIONS

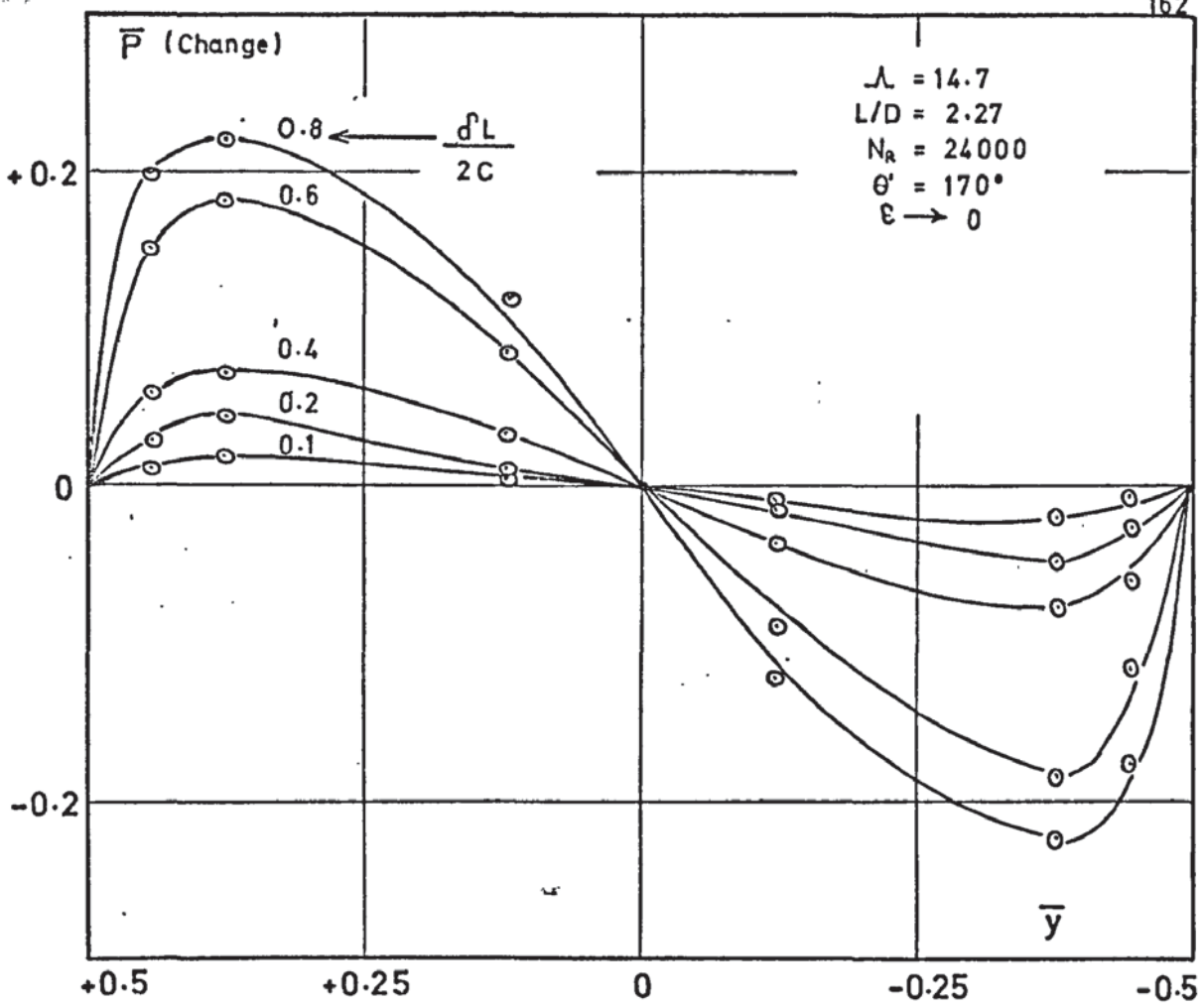

FIG. 41 – CHANGE IN AXIAL PRESSURE DISTRIBUTION DUE TO ANGULAR MISALIGNMENT

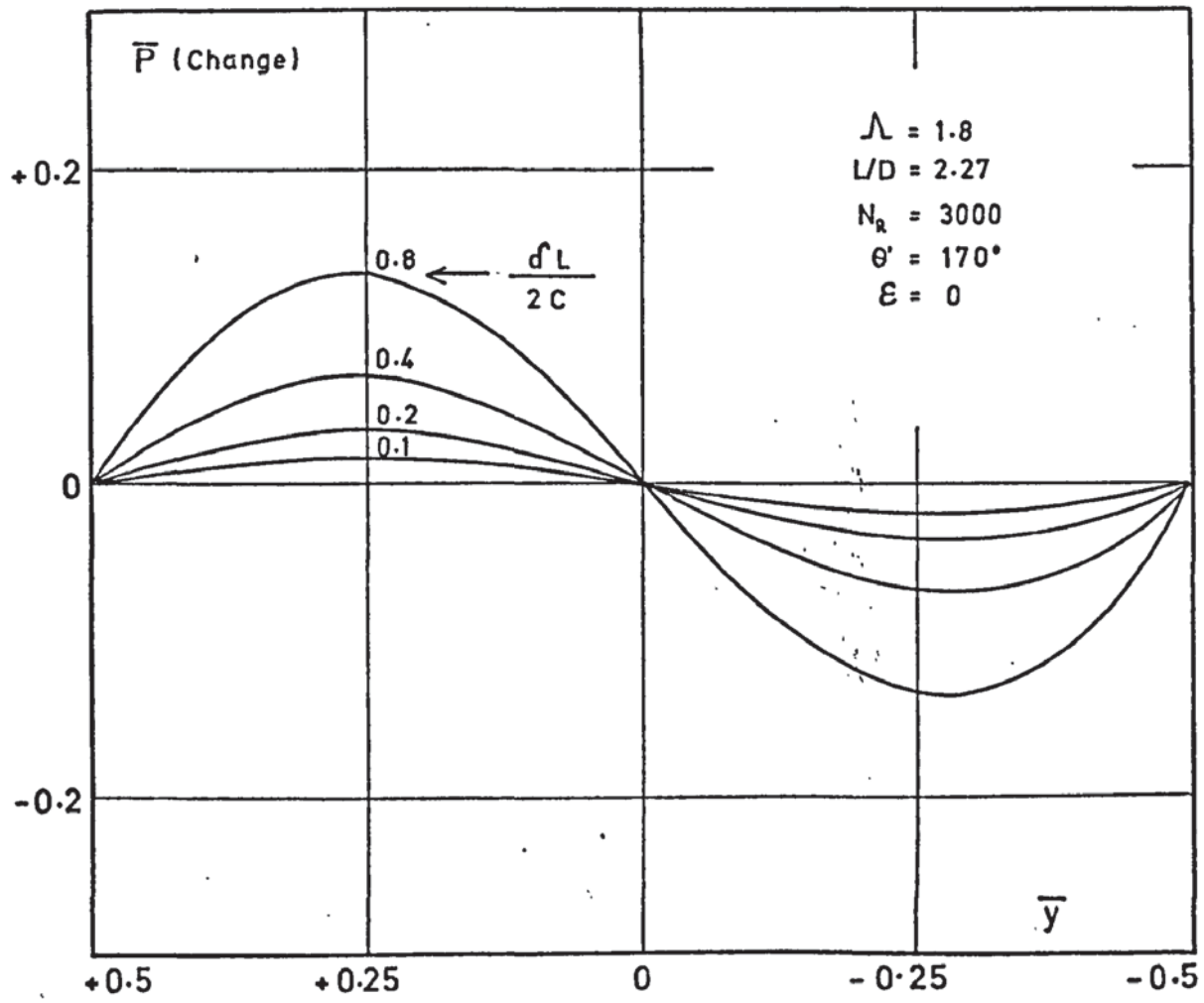

FIG. 42 CHANGE IN AXIAL PRESSURE DISTRIBUTION DUE TO ANGULAR MISALIGNMENT (Small pertubation theory)

6.7.1 Pressure Distribution (Continued)

Throughout the experimental measurements of bearing pressure, it was noted that considerable reductions in pressure could occur if the bearing were allowed to become 'dirty', and pressure changes of up to 50% were noted. The level of contamination was clearly very small, and was certainly insufficient to significantly modify the bearing geometry. Full pressure could be restored by careful cleaning and re-assembly. Quantitative measurements could not be obtained and the phenomena remains unexplained. It may however account for at least some of the discrepency between the experimental values and the numerical predictions.

While the basic assumptions listed in section 4.1 and the loss of experimental pressure due to contamination can clearly account for some of the observed discrepancy, it is believed here that a contributing factor is likely to be the influence of the large pressure ripple over the groove region and its effect on the local stability and accuracy of the solution. It is concluded that an increase in both the number of grooves and the number of mesh points* defining each land/groove pair would lead to an improved solution, and that the inevitable increase in computational time might be partly offset by a more sophisticated method of controlling the relaxation factor during each iteration (See section 4.12(a)).

Alternatively, an empirical 'correction factor' could be used to force the solution to agree with known experimental results and thus allow comparative investigations of manufacturing defects to be made.

6.7.2 Radial Load Parameter

Figure 43 shows the theoretical variation in radial load parameter with compressibility number for a grooved journal and thrust assembly. Comparison with the numerical solution presented in reference 23 shows the radial load capacity of the assembly to be less than that of an equivalent plain journal for $\Lambda < 1$ and increasingly greater for $\Lambda > 1$. Figures 44, 45 and 46 show this same parameter

* Castelli (11) also observes that as the pressure gradients and their derivatives become sharper, it may be that no real solutions to the difference equations exist unless the mesh is fine enough.

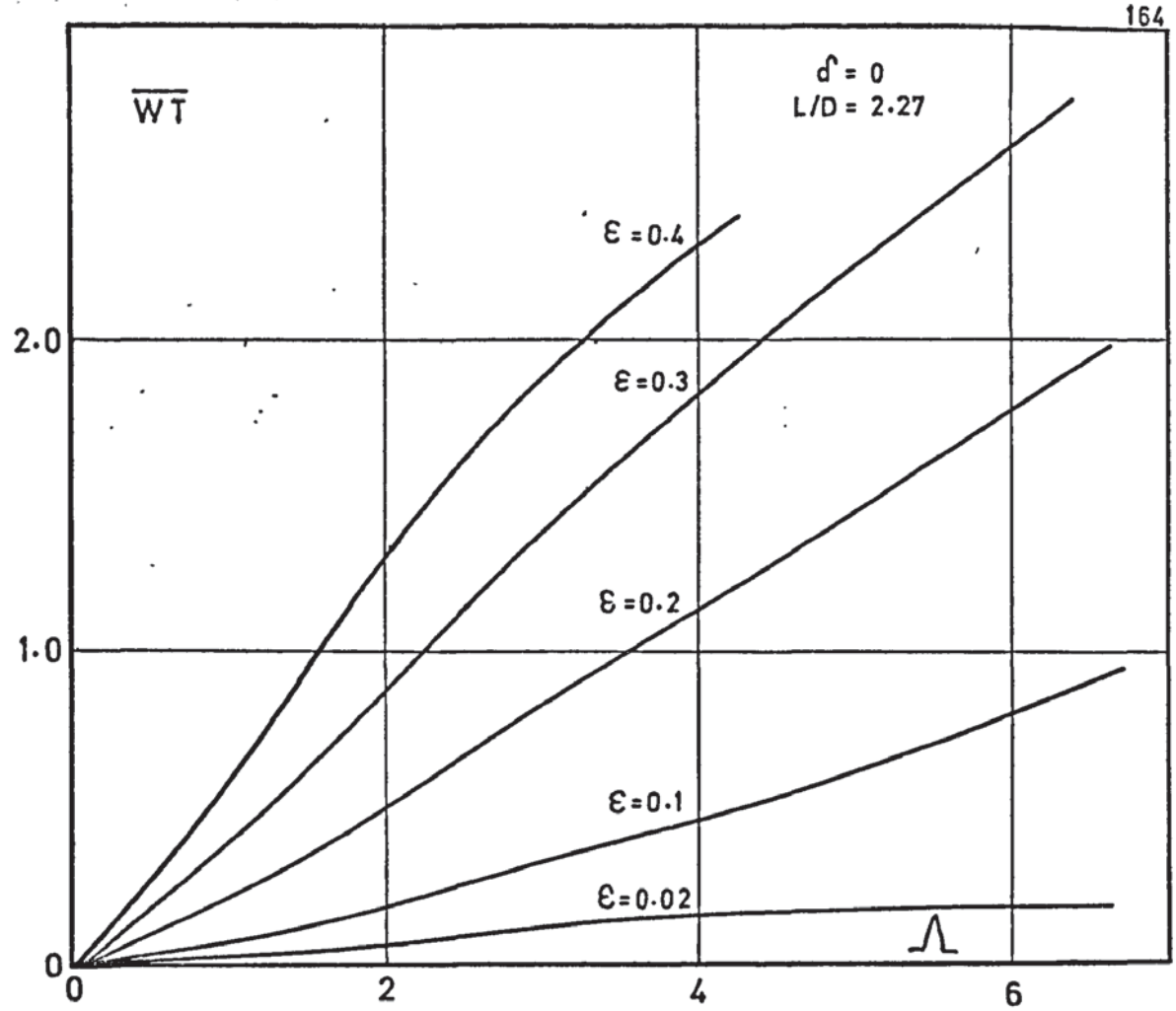

FIG. 43 RADIAL LOAD PARAMETER vs COMPRESSIBILITY NUMBER

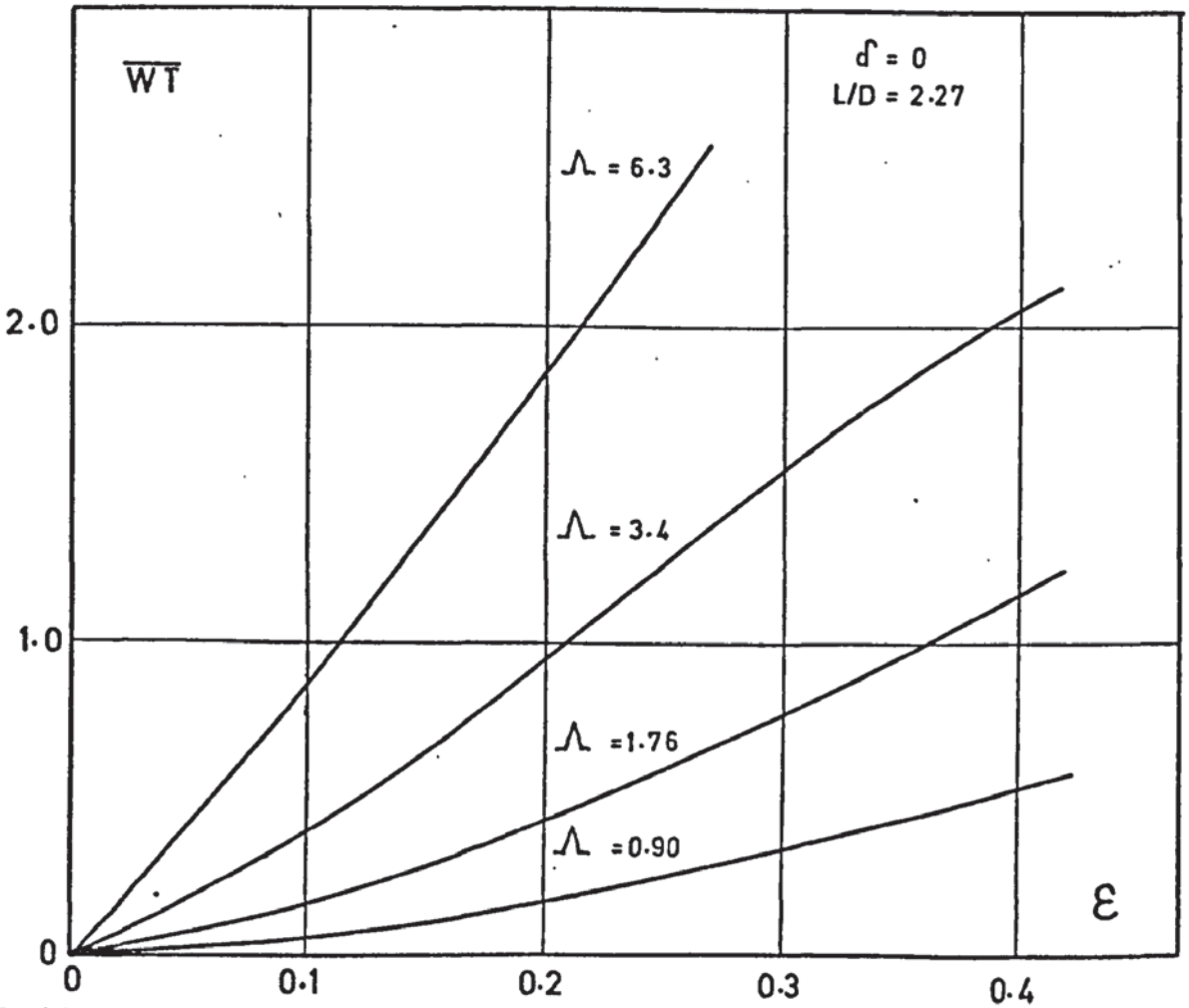

FIG. 44 RADIAL LOAD PARAMETER vs ECCENTRICITY RATIO

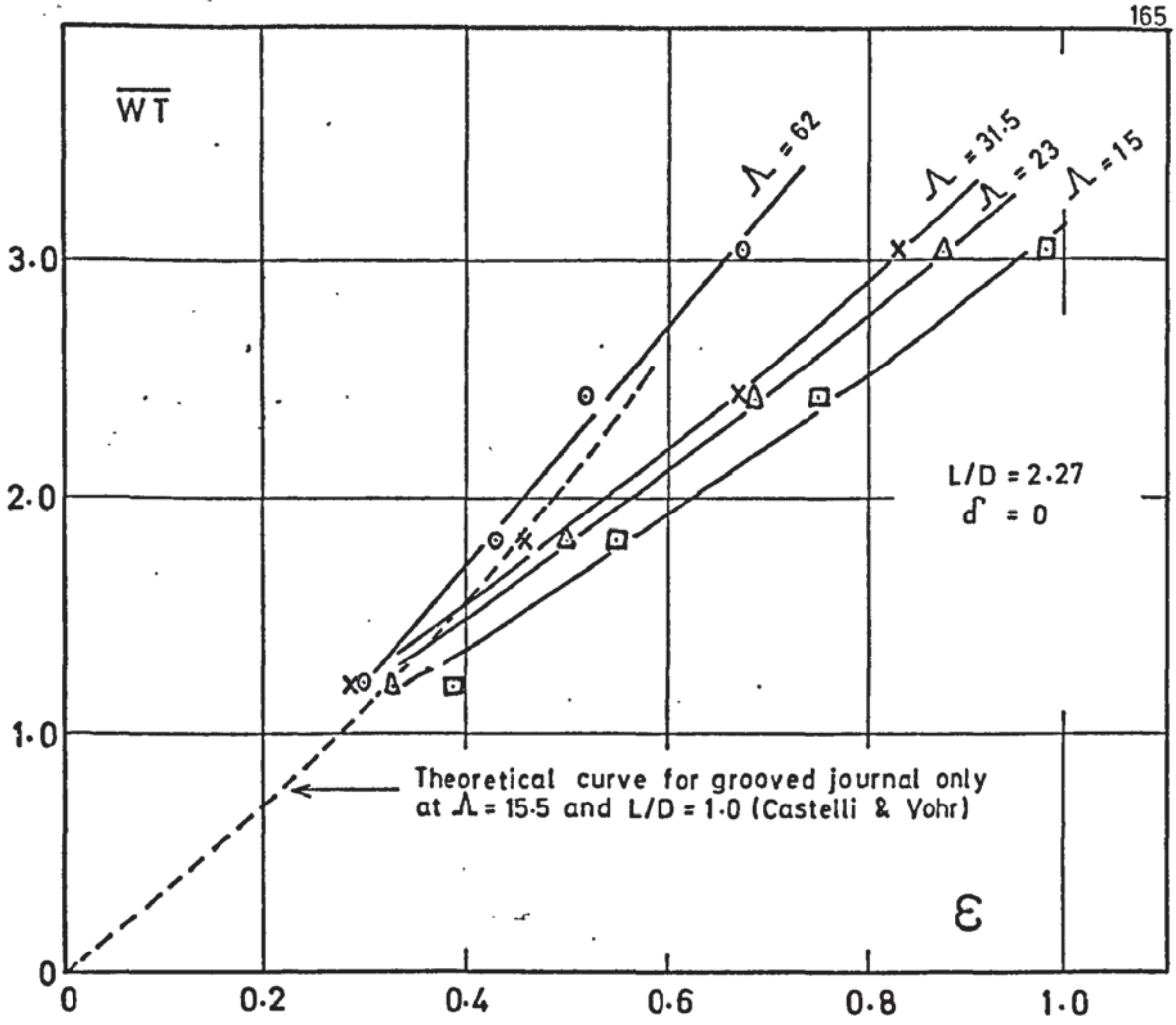

FIG. 45 RADIAL LOAD PARAMETER vs ECCENTRICITY RATIO

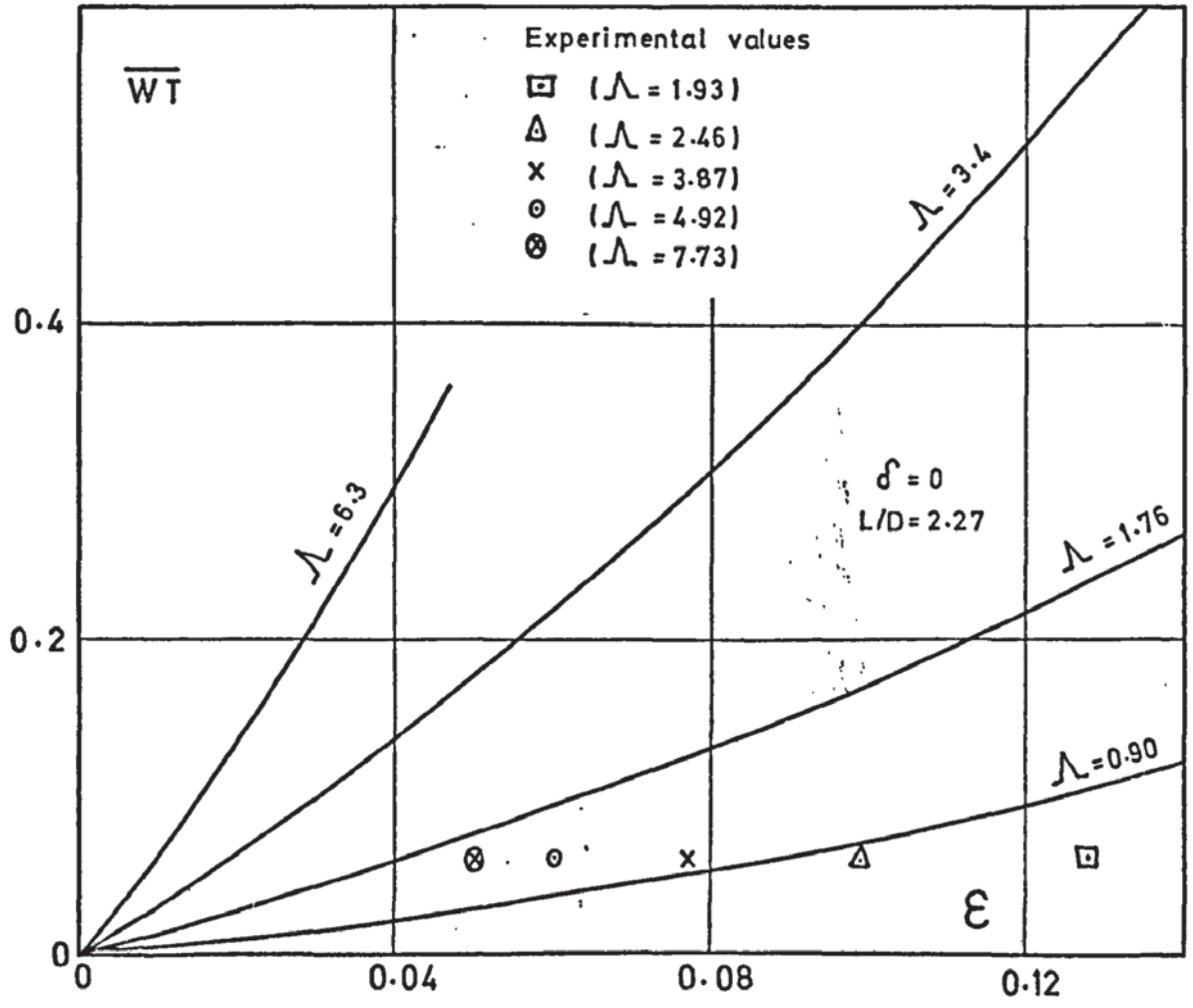

FIG. 46 RADIAL LOAD PARAMETER vs ECCENTRICITY RATIO

6.7.2 Radial Load Parameter (Continued)

plotted against the eccentricity ratio and the progressive increase in radial load capacity with both ε and Λ is again self evident.

At small eccentricities (Figure 46) the agreement between theory and experiment is very poor, with the measured eccentricity ratios being consistently high in each case, and this may be related to the practical difficulties involved in measuring such small deflections. For higher eccentricities (Figures 44 and 45) agreement is still poor, with the numerical programme predicting considerably higher load capacities than are realised in practice.

6.7.3 Attitude Angle

Figures 47 and 48 show the theoretical and experimental variation of attitude angle with compressibility number. Here, the numerical predictions are reasonably good, though in common with prior numerical work (17) (23), the theoretical angle is always smaller than the corresponding experimental value. The polar plot in Figure 49 shows the change in attitude angle with eccentricity ratio and here the agreement is less good, though the general shape of both the theoretical and experimental locii are similar to those determined for a plain journal (21) (3) (32).

In contrast with a plain bearing, it is observed that the attitude angle does not tend to 90° as the compressibility number is reduced to zero, but to some lower value. This can be seen theoretically and practically in Figures 47 and 48. For this particular design, the numerical programme predicts a maximum angle of 80°, whereas a semi-analytic solution given in reference 91 for a similar grooved journal suggests a value of 68°. However since prior analytic work (19) has shown the attitude angle to be sensative to several groove parameters (which were different here), direct comparison is inappropriate.

6.7.4 Torque Load Parameter

This parameter is shown plotted against the misalignment ratio in Figure 50. The experimental results show that over the range of compressibility numbers and angles investigated, the restoring torque increases linearaly with misalignment and this is in agreement with the semi-analytic results of Castelli and Vohr (91).

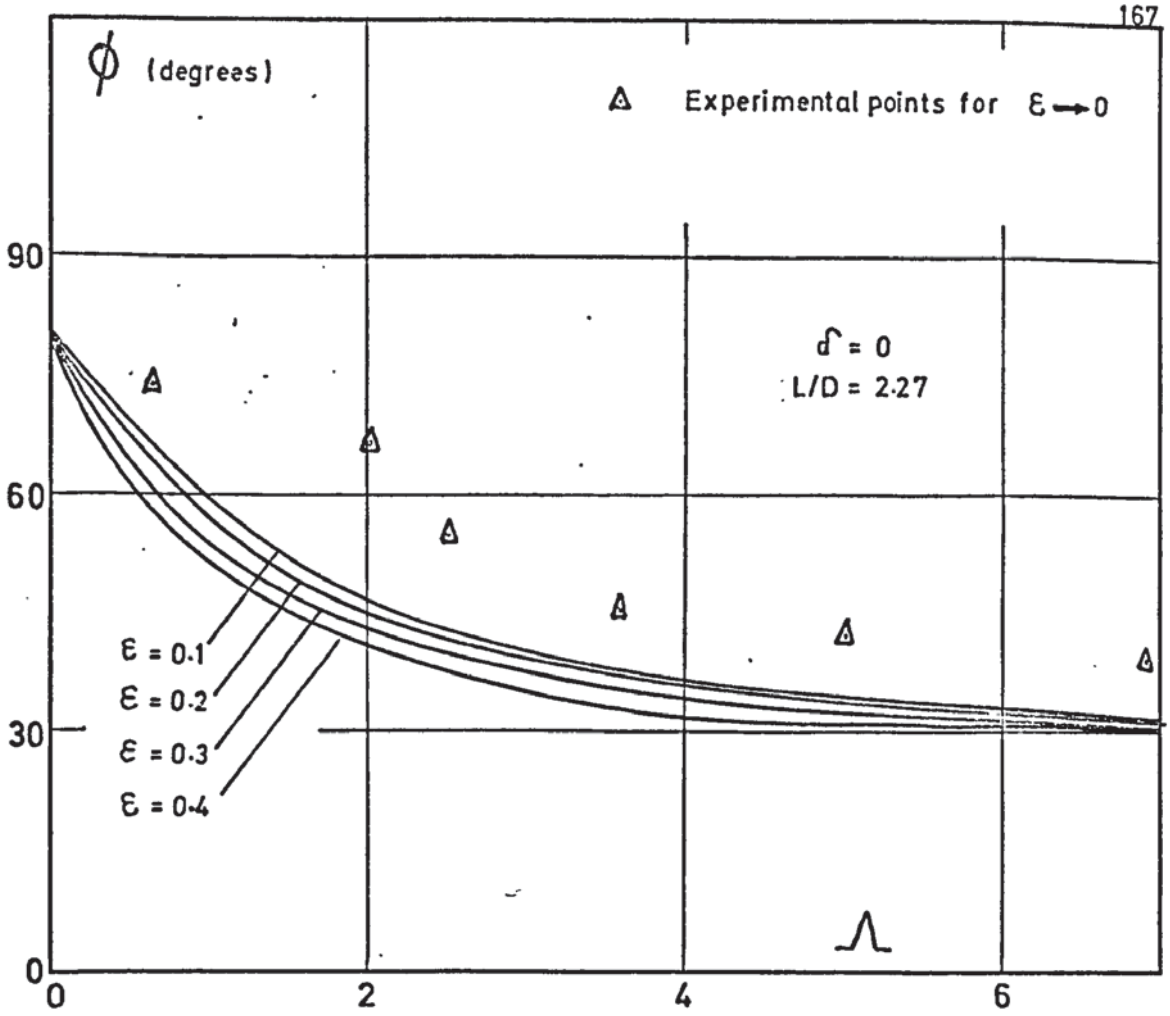

FIG. 47 ATTITUDE ANGLE vs COMPRESSIBILITY NUMBER

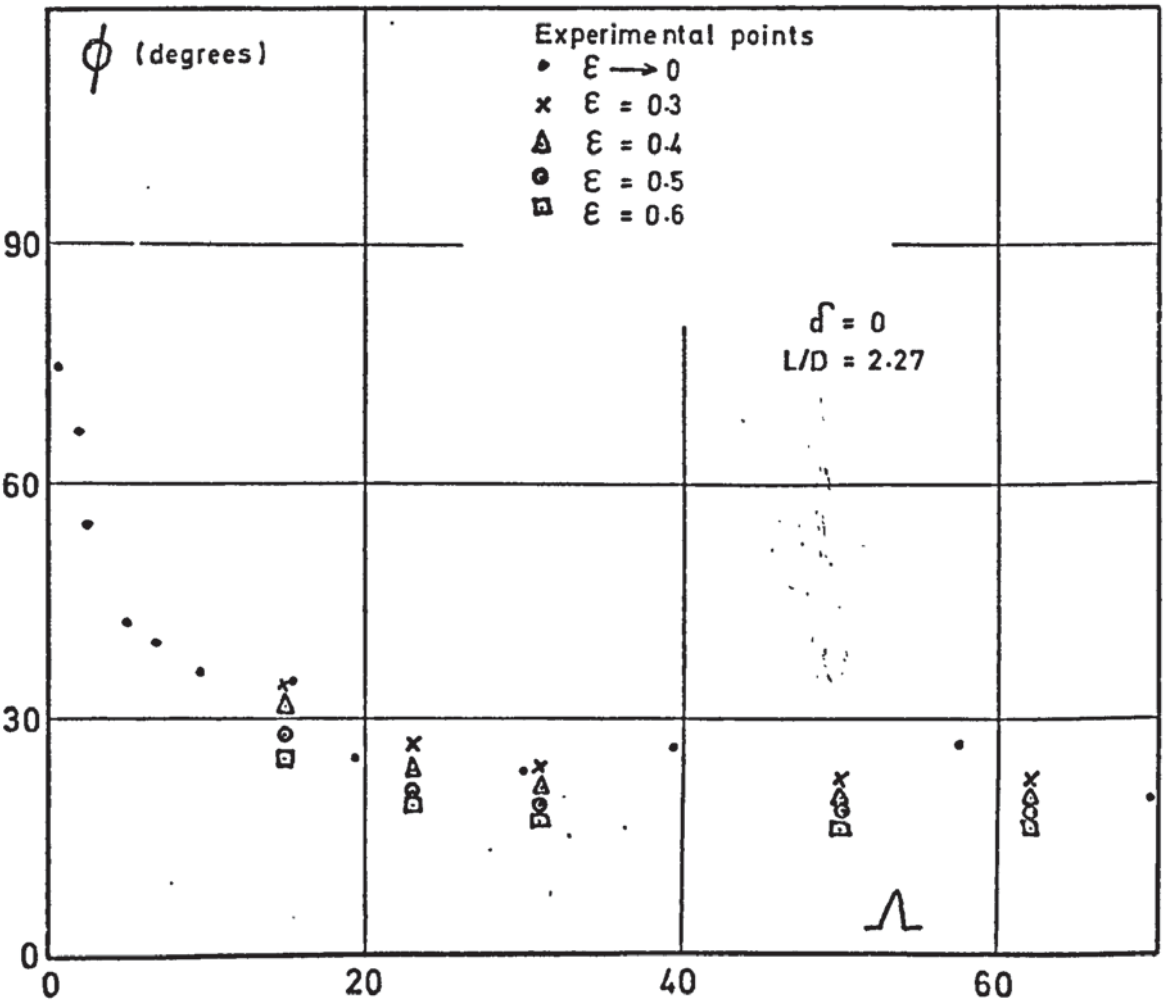

FIG. 48 ATTITUDE ANGLE vs COMPRESSIBILITY NUMBER

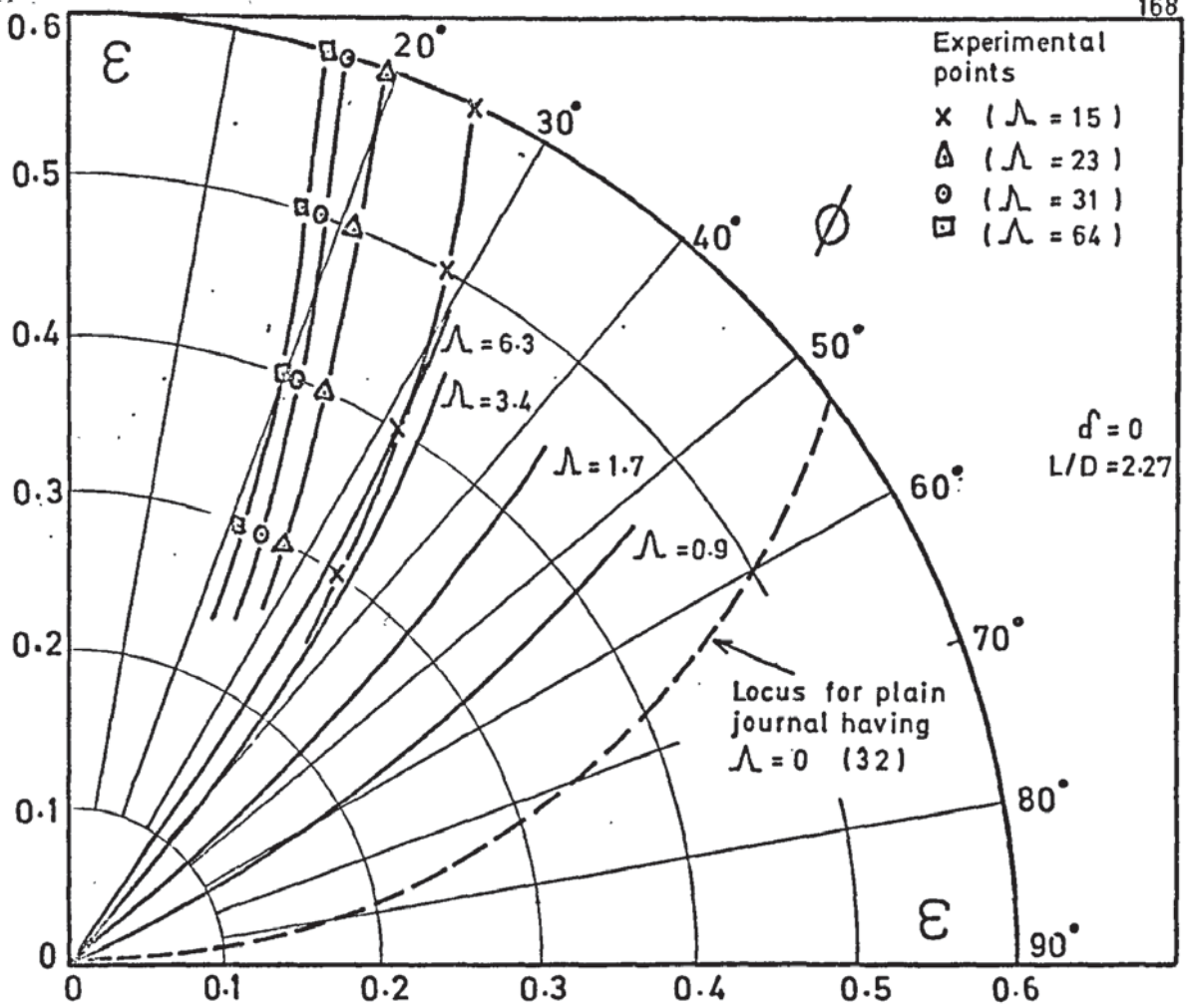

FIG. 49 ATTITUDE ANGLE vs ECCENTRICITY RATIO

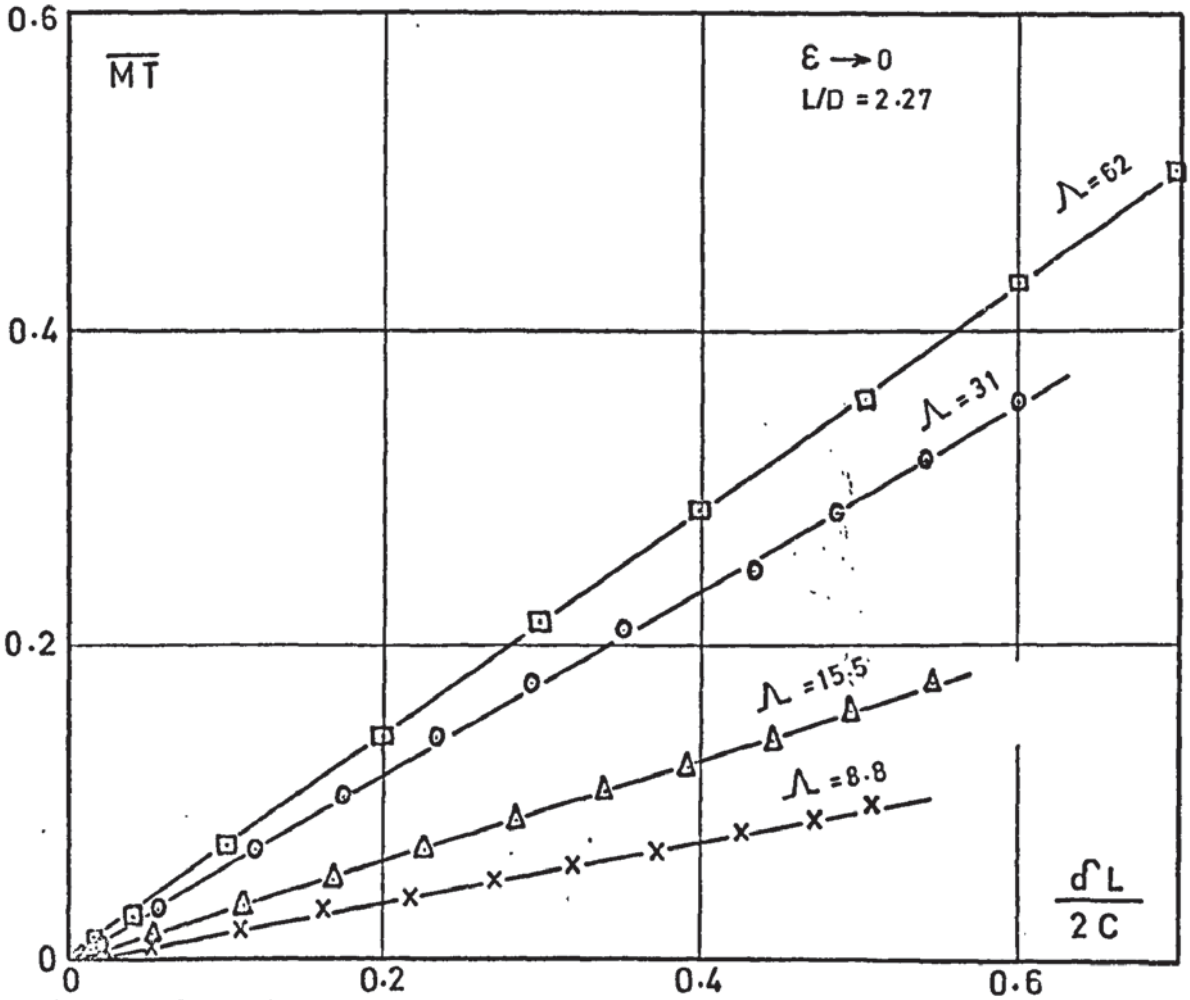

FIG. 50 MISALIGNMENT TORQUE vs MISALIGNMENT RATIO

6.7.5 Attitude Angle Under Torque Loading

This angle is plotted against the compressibility number in Figure 51 and also in polar form against the misalignment ratio in Figure 52. In common with the attitude angle under radial loading, it is seen to decrease with both increasing deflection and increasing compressibility number. Where a gyroscope gimbal is supported by a flexure suspension (as opposed to a rigid ball-bearing) it is considered that this angle may be of some significance because where it exceeds zero, it will allow a component of the gyroscopic torque to deflect the suspension about an axis other than the true output axis of the gyroscope (see Appendix I). This in turn may result in either a spurious output signal or even in damage to the suspension itself and no reference to this aspect of bearing operation has been found in prior literature.

6.7.6 Radial and Angular Compliance

These parameters were not computed directly by the numerical programme, in its present form, but it is clear from the curves presented in Figures 44, 45 and 50 that the compliance is, for all practical purposes, constant over the range of deflections considered. The experimental results also support this conclusion, as can be seen from Figures 45 and 50.

Numerical results could not be obtained for the normal operating condition of the bearing ($\Lambda \simeq 15$), but experimental measurements indicate an average radial compliance of 5·5 micro inches/lb (303 micrometres/N.) and an average angular compliance of 30 sec. arc/lb ins ($2{\cdot}55 \times 10^6$ sec. arc./N-m.) under these circumstances.

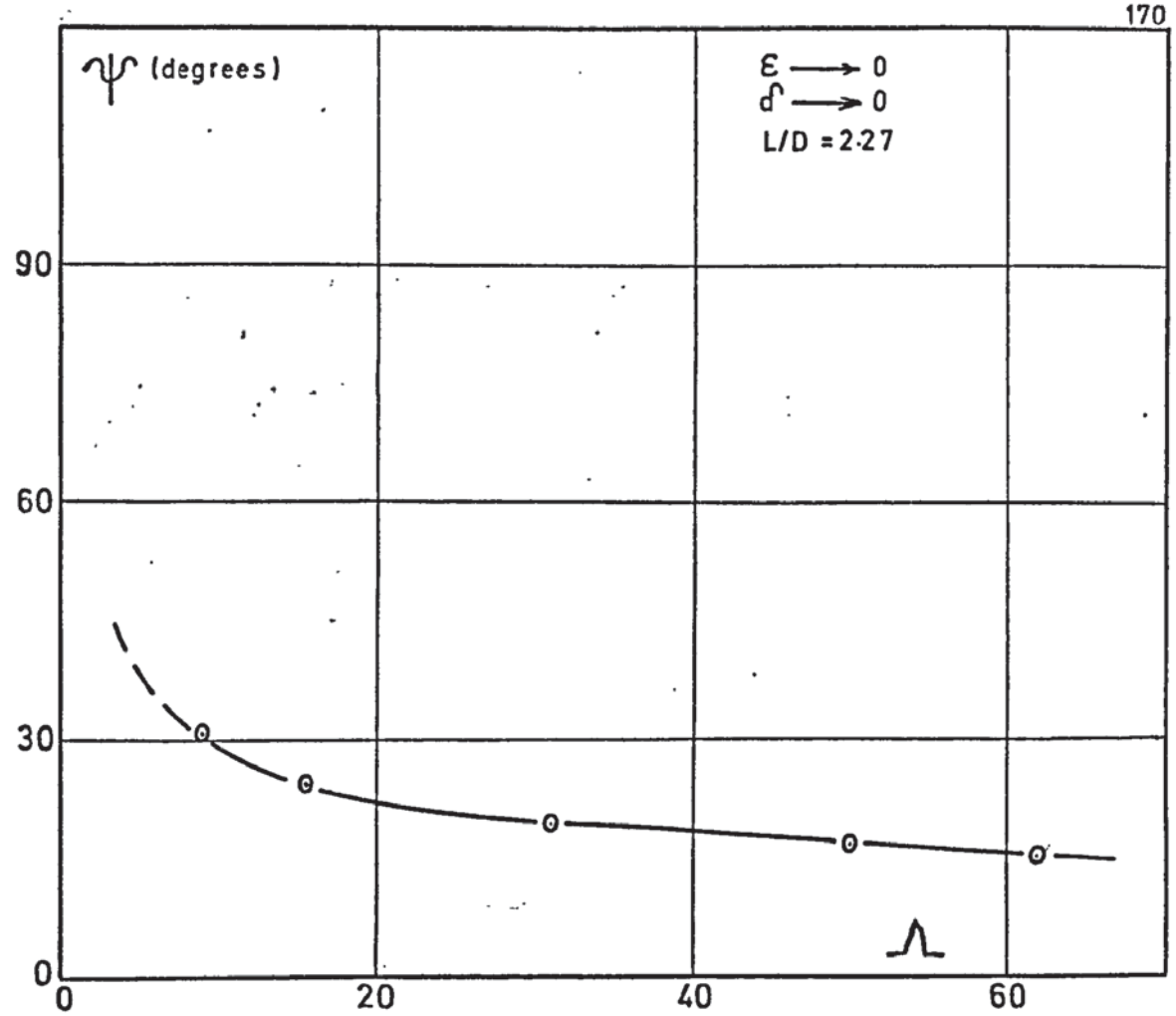

FIG. 51 ANGLE BETWEEN APPLIED TORQUE AND AXIS OF DEFLECTION vs COMPRESSIBILITY NUMBER

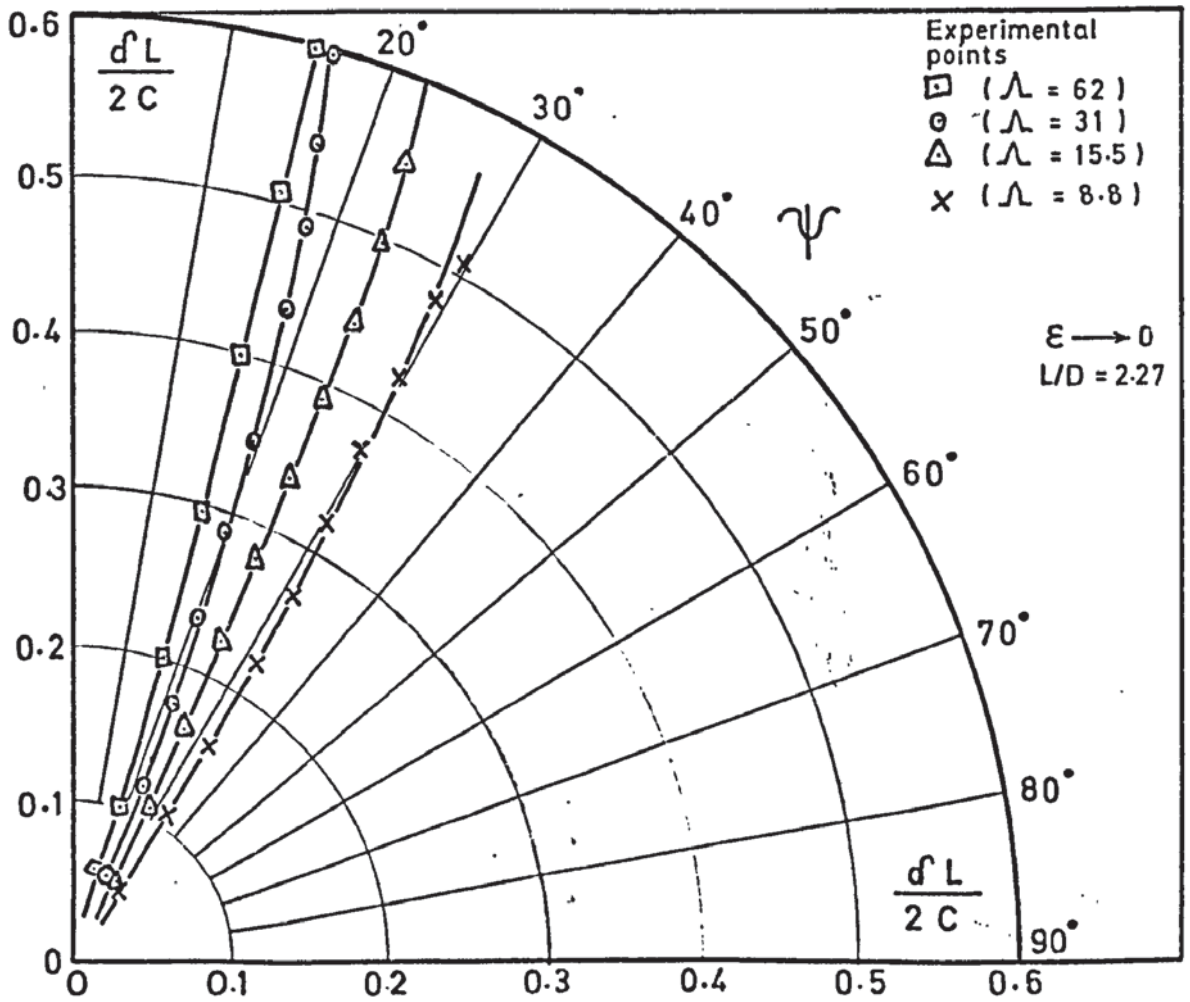

FIG. 52 ANGLE BETWEEN APPLIED TORQUE AND AXIS OF DEFLECTION vs MISALIGNMENT RATIO

CHAPTER 7

DISCUSSION OF FACTORS INFLUENCING OPERATIONAL LIFE

7.1 Introduction

The inter-relation between hydrodynamic theory, bearing design, material properties, manufacturing limitations, operational life and reliability is very complex and it seems unlikely that their true relationship will ever be fully understood. Some areas (for example Boundary Lubrication and Materials Selection) have been investigated in great detail by previous workers, but many equally important regions have been neglected. Prior work has tended to concentrate upon improving the life and reliability of existing bearing designs. Design criteria for optimising the operational life at an early design stage have not been considered.

In this discussion, the broader aspects of bearing design will be considered to determine if any general principles can be established with reference to operational life.

Some of the relationships discussed will be obvious on first inspection, but it is only by considering each one formally that a true picture of their combined effect can be formed.

Before considering individual aspects of bearing design in detail, it is necessary to define 'operational life' and 'reliability' for the type of bearing under discussion.

'Operational life' differs from a simple definition of running life, because it must take into account many aspects of the bearing's behaviour in service. Four principal aspects of life may be considered, viz:

(a) Storage or Shelf Life.
(b) Start/Stop Life.
(c) Continuous Running Life
(d) Overload Life.

In service, each instrument will be subject to some particular combination of the above. The precise pattern of operation will normally be difficult to predict and will invariably lie beyond the designer's control.

7.1.1 Definition of Operational Life and Reliability (Continued)

In general, the relative proportion of each will depend upon the particular application for which the bearing is intended, but wide variations may still be expected between individual instruments.

7.1.1.1 Storage or Shelf Life

For a hydrodynamic gas bearing, storage life is determined by the bearing's ability to re-start and run up to synchronism, after remaining unenergised for a long period. In a commercial application, the instrument would usually be stored in its protective packaging, but military applications may require a bearing to remain installed for many years before power is applied.

For civil aviation or marine use, a storage requirement of two years could be considered to be typical.

7.1.1.2 Start/Stop Life

Few applications are known in which a bearing may be allowed to run continuously and gyro applications normally involve a considerable number of start/stop cycles throughout the working life of the instrument. Starting ability depends upon the available motor torque overcoming the friction torque between the bearing surfaces. Friction torque, in turn, is influenced by many factors, including wear and contamination of the bearing surfaces.

Start/stop life is therefore the number of start/stop cycles that can be accomplished before the bearing fails to start. For an instrument in civil aviation service, an average of 1000 start/stop cycles per annum might be expected over an airframe life of about ten years.

7.1.1.3 Continuous Running Life

The ability to run continuously is not normally a limiting factor in any aerodynamic bearing design, since in almost all respects, this is the ideal mode of operation. Physical contact between the bearing surfaces is eliminated and the bearing should continue to perform as long as driving power is available.

7.1.1.3 Continuous Running Life (Continued)

Unfortunately, while running may have no effect upon the ability to continue running (because physical contact is prevented by the fluid film) it almost certainly influences the ability to re-start if the bearing is later stopped. It is this aspect of continuous running that will be of primary interest here.

In civil aviation use, continuous running may account for up to 6000 hours each year, with a maximum period of 20 hours between each start and stop. For marine applications, up to 7000 hours running may be completed during each start/stop cycle.

7.1.1.4 Overload Life

If a bearing is progressively operated beyond its design limits, the lubricating gas film must eventually break down and high speed rubbing will occur between the bearing surfaces.

Two forms of failure are then possible. The bearing may seize, either suddenly or gradually, or it may recover once the overload condition has been removed and prematurely fail to re-start at some later date. In commercial applications, impairment of starting ability may not be too serious, since the possibility of overload would normally be known and a full inspection or overhaul could be initiated. For critical aviation applications, such a procedure would of course be mandatory.

Seizure is more important and, unlike impaired starting ability, is more easily measured. It is therefore best to define overload life as the degree of overload that can be sustained before the bearing fails to recover and regain its design speed.

7.1.1.5 Reliability

Reliability is a measure of the confidence that can be expressed in a bearing's ability to operate for a specified period without failure. Failure in general must be defined as an inability to meet the full performance specification, rather than simply a complete failure to operate.

7.1.1.5 Reliability (Continued)

In practice, progressive failure of rotating a hydrodynamic bearing is unlikely and by far the most predominant failure mode is the inability to re-start when power is applied. This freedom from progressive performance deterioration is one of the gas bearing's most useful features, but it does not necessarily follow that the failure mechanism itself is not progressive.

Reliability is expressed in a quantitative manner as the Mean Time Between Failures (M.T.B.F.) in hours, Where failure mechanisms are complex and insufficiently understood (as in all aerodynamic bearings) the M.T.B.F. cannot be predicted analytically, and must be derived statistically from experimental data. It is important to make a clear distinction between M.T.B.F. and mean life, for the terms are often confused. By way of an example, the mean life of the human body is around 70 years, whereas the corresponding M.T.B.F., where failure is defined as a premature death, is approximately 300 years.

Reliability of the bearing alone is usually of little interest to the user, who is rightly concerned with the overall reliability of the complete instrument. In an instrument constructed from many separate components, the unreliability of each component will obviously degrade the overall M.T.B.F. of the assembly. Initially, a large improvement in bearing reliability will result in a corresponding increase in overall M.T.B.F., since the failure rate contribution from (ballrace) bearing sources is relatively high. Later, because of this contribution to total failure rate from other sources, and the fact that the failure rate in many areas, (for example windings, electrical and mechanical fastenings, etc.) cannot easily be improved, a point will eventually be reached where very large improvements in the M.T.B.F. of the gas bearing will cease to yield significant improvements in the M.T.B.F. of the instrument as a whole. It therefore follows that a limiting level of reliability will eventually be reached, beyond which, improvements to the reliability of the gas bearing alone will no longer be effective.

A complete discussion of the selection and properties of gas bearing materials must be outside the scope of this thesis. The number of possible combinations of bearing material is very large indeed, and their manufacture has developed into a very specialised branch of materials science.

The selection of materials for the larger hydrodynamic applications has been discussed at some length (84) (104) but little really detailed information has been published on suitable hydrodynamic bearing materials. If the discussion is limited to materials that are likely to be suitable for use in precision hydrodynamic bearings of small dimensions, the list of possible choices becomes quite small. While many combinations of material have been suggested for this purpose, few have withstood the test of time, and a mere seven materials account for over 90% of the gyro bearings that are known to be in current production, throughout the world.

For the purpose of this discussion, material properties in general will be considered, but with special reference to Tungsten Carbide and Boron Carbide. There are several reasons for this choice.

Both materials are reasonably typical of many gyro bearing materials in current use. They are both used extensively by a number of gyro manufacturers and illustrate the general trend towards ceramic and cermet wear resistant surfaces for gyro applications. In addition, considerable practical experience has been gained here with each material and the unique properties of Boron Carbide make it worthy of special mention in its own right.

For similar reasons, only the properties of solid materials will be discussed, but many of these are obviously applicable to thin surface coatings. Surface treatments have many special problems which are often related to the method of coating rather than to the material itself. In general, flame sprayed coatings tend to be inferior to the properties of the bulk material while coatings deposited by vacuum techniques are often superior to the parent material.

7.2.1 Materials Currently Used in Hydrodynamic Gyro Bearings

The following materials are widely used for forming the wear resistant surfaces of self-acting gas lubricated gyro bearings. Their selection has largely been the result of practical tests and working experience over a period of at least fifteen years, and each has demonstrated its ability to provide a useful operational life under service conditions.

Material	Chemical Formula
Aluminium Oxide	Al_2O_3
Tungsten Carbide	WC
Boron Carbide	B_4C
Chromium Oxide	Cr_2O_3
Beryllium Oxide	Be O
Carbon Bronze	(Composite Material)
'Stellite'	(Cobalt based Alloy)

Two other materials, Silicon Carbide (SiC) and Titanium Carbide (TiC) have been the subject of recent interest, but are not in general use.

7.2.2 Discussion of Physical and Chemical Properties

Each property will be considered in turn and its influence on operational life examined. Methods of material selection will then be discussed.

7.2.2.1 Hardness

In the absence of any alternative criteria, hardness has often been the principal physical property upon which the suitability of a given material for gyro bearing applications has been based. A high hardness has been equated with a low wear rate and for bearing clearances of 100μ inch (2·5 μm) or less, the volume of wear products necessary to promote bearing failure by direct obstruction of the clearance is clearly very small. This reasoning is considered to be sound for wear surfaces incorporating little or no lubrication, but where boundary lubrication or self lubricating materials are used, hardness alone may be a less important factor in deciding wear rate.

7.2.2.1 Hardness (Continued)

Plain oil-lubricated bearings have traditionally used one hard bearing member running against a much softer material (e.g. hardened steel vs tin-lead alloy). Here, the softer material can readily deform to accommodate high spots in the harder surface, and under contact conditions, the load can be spread more evenly over the usable bearing area. In addition, the soft surface can absorb hard fragments of wear debris and contamination, while at the same time providing a degree of dry lubrication under start/stop conditions.

Such a strategy is considered to be of limited use in small gas bearings, where the relatively large volume of wear product that would be evolved under dry rubbing conditions could not be removed by the fluid lubricant. In order to achieve take-off at relatively low rotational speeds, hydrodynamic gas bearings are normally designed to have a low specific loading in comparison with plain oil lubricant bearings. This, together with the very high standard of geometric accuracy now being achieved, effectively eliminates the need for surface deformation to spread the static load.

Where homogenous materials of high hardness are used throughout the gas bearing structure, the useful property of one soft surface absorbing and retaining hard particles is believed to be lost. This may not necessarily be the case for two-phase materials such as sintered tungsten carbide, where very hard grains are embedded in a soft matrix. In this case, the exposed matrix at the bearing surface is probably capable of absorbing loose debris; albeit on a microscopic scale.

Hardness, by definition, is a measure of the ability of a surface to resist local indentation or deformation under a point contact load. High hardness values for both bearing surfaces therefore imply that any solid particles trapped between them will, under suitable circumstances, be crushed into finer and possibly less harmful debris, and that the bearing surfaces will sustain little damage in the process. This does occur in practice, but it is felt here that the ability to crush must also be

7.2.2.1 Hardness (Continued)

linked with the relative bond strengths of particle and surface rather than just their relative hardnesses alone.

Materials spanning a wide range of hardness values have been used in self-acting bearings, both in the writer's laboratory and elsewhere, and it is possible to make a few general observations on their performance. For hardness values below 1000 knoop, dry wear rate is usually too high (giving a low start/stop life) and performance during overload conditions unacceptable. For materials in excess of 2000 knoop, start/stop wear rate is found to be very small and overload tolerance is usually exceptional. Boron Carbide at 3000 knoop offers an exceptionally low wear rate and is successfully used on bearings of only 40 micro inches (1·0 micrometre) mean radial clearance. Up to 227,000 start/stop cycles have been obtained here using 60 micro-inch clearances (1·5 micrometre). Plate 26 depicts a boron carbide - tungsten carbide bearing after 1000 start/stop cycles. No wear of any kind can be observed. Plate 27 shows a different boron carbide journal after 40,000 repetative starts and stops. A very small degree of wear is visible in this case, but since the shaft had a rather lower standard of surface finish, direct comparison is inappropriate. Most current bearing materials lie within the range 1000 to 2000 knoop and wear life in this region is less easily related to the actual numerical value of hardness. Certainly materials at the upper end of the range, i.e. tungsten carbide at 1700 knoop and aluminium oxide at 2000 knoop, are well known to be capable of surviving a high number of start/stop cycles, but anomalies do suggest that relative hardness is not the sole factor in deciding wear rate. Beryllium oxide for example has a knoop hardness of only 1200, and yet Hall (58) reports that it survived at least 100,000 start/stop cycles in four typical gyro assemblies. Materials of around 1000 knoop and lower were found here to be most susceptible to damage from ingested airborne grit particles. This is readily explained by reference to the particle crushing concept, and the fact that fine sand grains make up a large proportion of airborne particles. Quartz

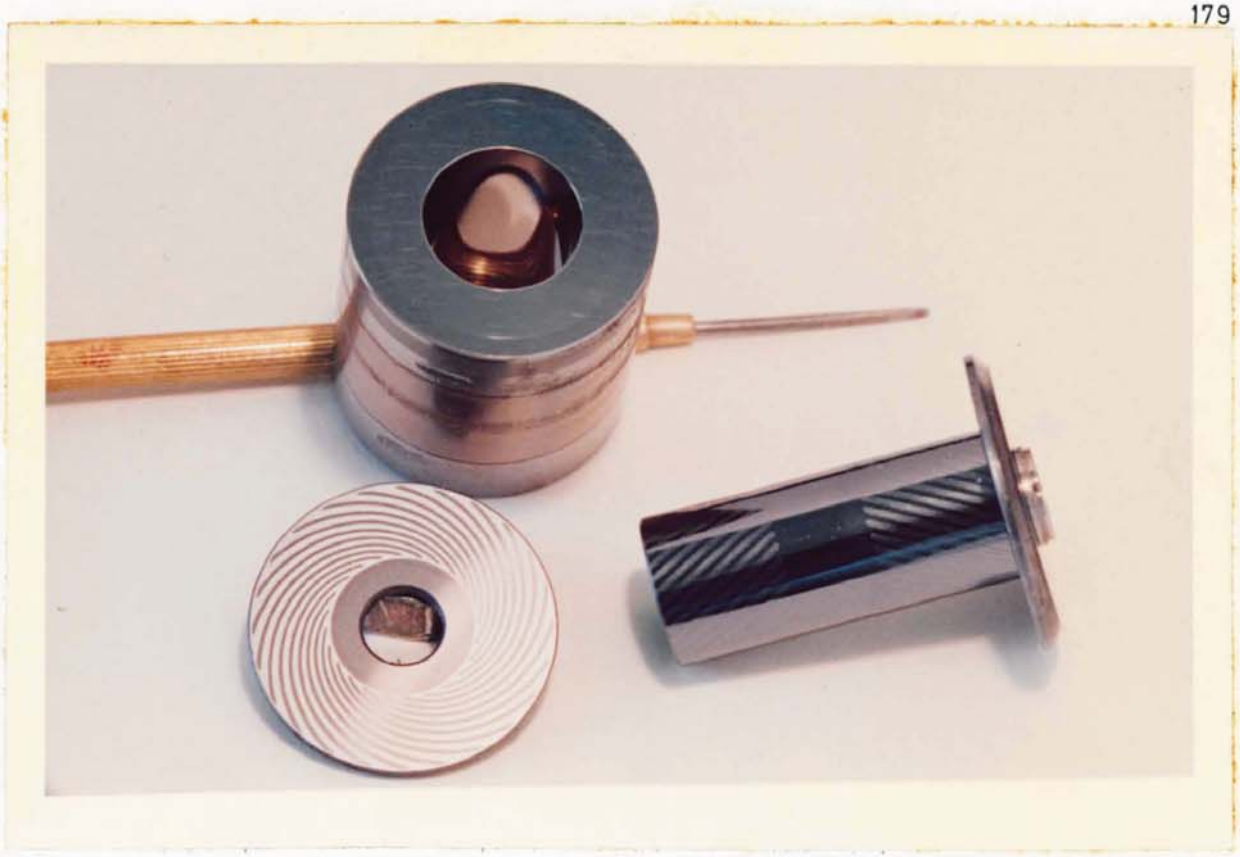

PLATE 26
GAS BEARING COMPONENTS AFTER EXTENSIVE LIFE AND ENVIROMENTAL TESTING

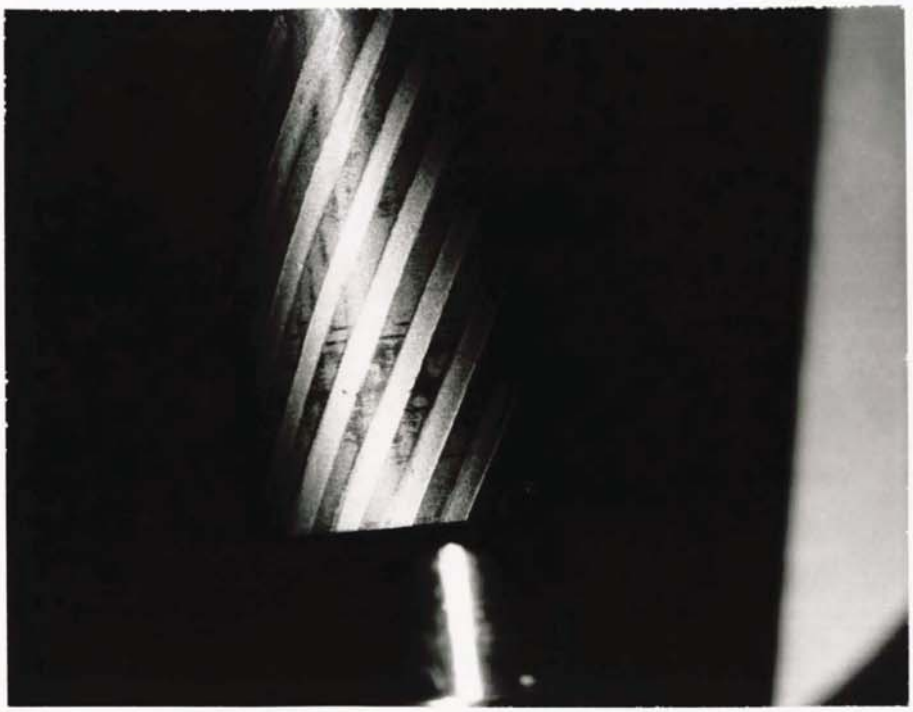

PLATE 27 X 2
STOP/START WEAR PATTERN ON BORON CARBIDE JOURNAL SHAFT

7.2.2.1 Hardness (Continued)

has a hardness of 800 knoop and can therefore cause severe damage to bearings manufactured from softer materials.

Survival under high speed rubbing conditions does at first sight appear to be closely related to hardness, but it will be shown later that this is largely a coincidence and that other properties are more likely to be responsible.

The choice of high hardness materials is considered to bring other advantages which are rarely recognised in the initial design phase. Surface damage during inspection, transportation, cleaning and assembly is either reduced, or for materials like boron carbide, practically eliminated. This in turn preserves the original design features and serves to contribute to operational life and reliability as a whole.

The subject of hardness cannot be left without reference to the problems of its measurement. Caution is essential when interpreting published hardness figures for many are believed to refer to measurements taken on single crystals of very pure material. This may not always be made clear in the literature. Crystal hardness varies considerably as the measurement plane moves relative to the crystal lattice and often only maximum values are quoted. These values are of little use to a bearing engineer working with dense compacts, and accurate readings of hardness can only be obtained from a polished bearing surface. This not only includes the influence of any binder which may be present, but also allows for the effect on hardness of the machining processes themselves.

7.2.2.2 Melting Point

Melting point is a significant factor in dry lubrication (39) (31) and is believed here to influence several aspects of operational life.

7.2.2.2 Melting Point

It is well known that, under high speed rubbing conditions caused by overload, local frictional heating causes an appreciable rise in surface temperature at the point of contact. If the melting point of either or both materials is approached, momentary welding and tearing will occur and transfer of material will take place between the bearing surfaces (39). Massive local damage will be caused and in an extreme case, total seizure has been found to take place.

The actual temperature rise is considered to be a function of the rubbing velocity, contact load, surface roughness, thermal conductivities, densities and specific heats. Rubbing velocity will depend not only upon the rotational speed and contact radius alone, but also on the nature of the overload condition itself. For a simple radial, axial or slew overload, rubbing velocity is given by the relation:-

$$V_o = R\omega \qquad (75)$$

When overload is due to half speed whirl-induced rubbing, the velocity will be given by:-

$$V_W = R\omega + \tfrac{1}{2} R\omega \qquad (76)$$

The extra term is due to the superimposed orbiting velocity of the moving member as it whirls about its equilibrium position at an angular velocity $\frac{\omega}{2}$. Rubbing velocity in this case is clearly 50% greater than for a simple overload condition and for the more unlikely case of synchronous whirl, a 100% increase can occur. If other factors are held constant, it could be expected that whirl-induced rubbing might generate a higher surface temperature than that produced by a simple overload; thereby increasing the chance of exceeding the melting point. This is offset to a certain extent by the fact that under whirl rubbing conditions, the contact point rotates around the circumference of the stationary member, as opposed to the case of a simple overload where heat is generated at a fixed point on the non-rotating surface. Comparative tests by the writer (116) on twelve bearing assemblies confirms that half speed whirl rubbing (induced on a shaker table) generates a higher surface temperature than slew rubbing at high input rates.

7.2.2.2 Melting Point (Continued)

The above discussion does suggest that materials of high melting point should be capable of surviving a higher degree of overload than those of lower melting point. It can also be inferred that a higher melting point is necessary for the stationary member, where unlike the moving member, heat generation may be confined to only part of the surface and windage cooling may be less effective.

Under start/stop conditions, temperatures approaching the melting point are unlikely to be achieved on a macroscopic scale, though at a molecular level they are believed to occur on the peaks of the surface asperities. Intermittent welding and tearing can therefore take place at these peaks and the result will be small scale surface damage at the points of contact. These molecular level welds must be broken each time the bearing starts from rest and the effective starting friction is therefore increased. Starting reliability will be reduced.

Figure 53 shows a hypothetical asperity of triangular section in which the frictional heat input at the tip is represented by Q_F and the temperature gradient after a short increment of time depicted by isotherms T_o (minimum) to T_4 (maximum). If the material has a high melting point corresponding to T_4, only material above the T_4 isotherm will melt and the rubbing contact width will be small. For material were $T_m = T_3$ (say), all material down to T_3 might be expected to melt and the contact width will be correspondingly large. The proposed model is a very simple one, and does not take into account the dynamic situation over a longer period of time. Nevertheless, it does illustrate how the melting point can influence the extent of microscopic surface damage under start/stop conditions.

It may be concluded that high melting point materials will reduce the extent of molecular welding at surface peaks and result in an improved start/stop life.

It is well known that storage life of a conventional bearing is limited by gradual deterioration of the fluid lubricant, but even under dry lubrication conditions, storage life cannot be assumed

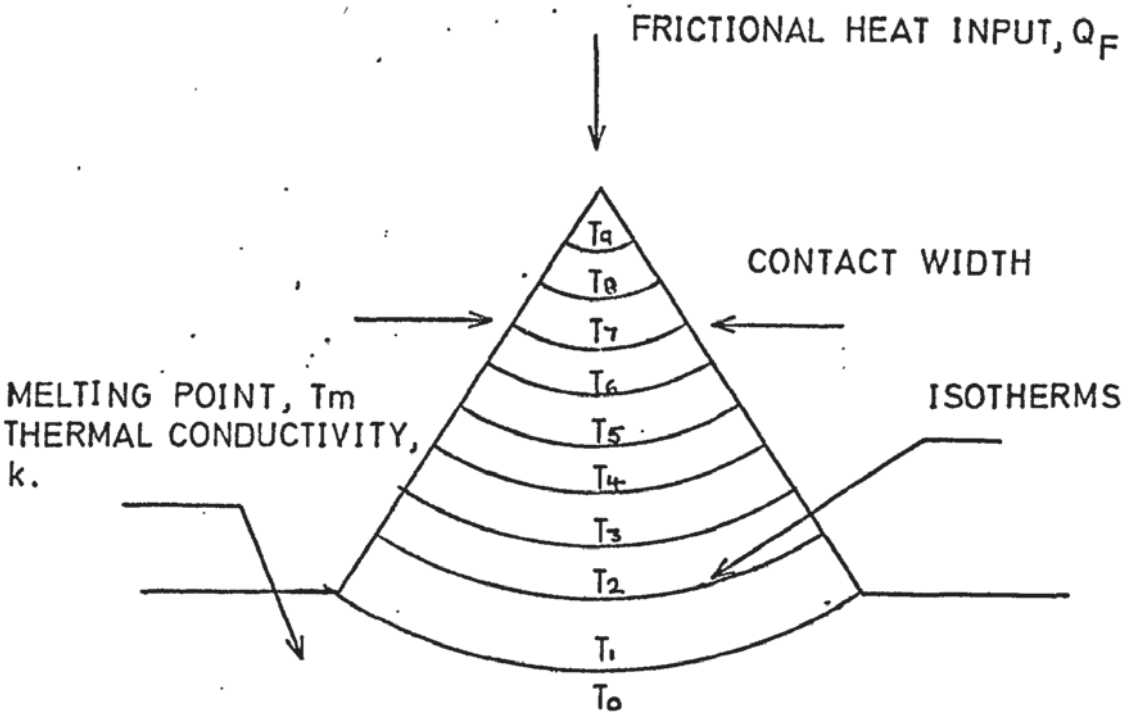

FIG. 53
SIMPLIFIED THERMAL MODEL OF SURFACE MICRO-PEAK.

to be infinite. Where very smooth surfaces are maintained in intimate contact, mutual transfer of material can occur at a molecular level across the interface. This 'growing together' effect is well known in industry, and wrung steel slip gauges are often inseparable after a period of several years.

In a gas bearing, the motor starting torque must therefore overcome the shear force of the material at the diffused junctions if a successful take-off is to be made. This progressive increase in starting friction may represent a limiting factor in the bearings shelf life.

For a solid material, the binding energy of the molecules is known to be considerably greater than their kinetic (thermal) energy. As the melting point of a material is approached, intermolecular cohesive forces become less important in comparison with the increasing kinetic energies, which allow the molecules to vibrate with increasing amplitude and frequency about their mean position in the crystal lattice. At the melting point, the cohesive forces are no longer sufficient to prevent the molecules from moving freely past and around each other and the substance becomes a liquid. This increasing level of molecular vibration as the melting point is approached is considered here to increase the probability of individual molecules transferring from one bearing surface to an adjacentone.

If this explanation of the phenomena is correct, it can be speculated that the choice of high melting point materials should reduce the likelihood of molecular diffusion across a stationary bearing interface and result in a relatively long storage life. An additional implication is that the storage life of an assembled bearing could be increased slightly at low temperature and decreased at very high temperatures.

The operational performance of most bearing materials shows good agreement with their melting point. Materials like Carbon (M.P. 3700°C), Boron Carbide (M.P. 2400°C) and Silicon Carbide (M.P. 2300°C) show excellent resistance to high

7.2.2.2 Melting Point (Continued)

speed rubbing, though the superlative performance of boron carbide in this respect is also due to its special chemical properties. Aluminium oxide (M.P. 2050°C) and Tungsten carbide (M.P. 2000°C) also show good resistance to overload, but lower down the scale, ferrous alloys (M.P.≃ 1500°C) have a marked tendency to seizure under identical conditions (116) (84).

Stop/start life is usually very high for materials like boron carbide, reasonably good for aluminium oxide and tungsten carbide and poor for hardened steel (116) (118).

Very little information is available concerning storage life. Hall (58) states that no problems were experienced over a six year storage period at room temperature when using beryllium oxide, and here, no change has been detected in starting performance over a period of two years on boron carbide - tungsten carbide bearings under similar conditions.

7.2.2.3 Boiling Point

In most materials, boiling point is closely related to melting point and much of the discussion in section 7.2.2.2. is also relevant here.

Local vapourisation of the bearing surface will be most likely to occur during high speed rubbing conditions and because the high temperatures involved are very local, it is believed that condensation will occur rapidly. Experimental work here (116) has shown that vapourisation occurs on hard steel, Stellite and various carbide bearings at rubbing velocities of 1000 in/sec (254 m/s) and relatively low contact loads (1 lb/ins^2 or $6{\cdot}9 \times 10^{-3}$ N/m^2). Very small amounts of material were involved and condensation took place on the stationary member close to the contact region. The condensed material was normally thin enough to produce interference fringes and these indicated a typical maximum thickness of some 20 micro inches (0·5 μm). In all cases the deposit adhered firmly and covered an area up to seven times larger than the corresponding wear region.

7.2.2.3 Boiling Point (Continued)

Vapour deposits are therefore believed to modify the friction coefficient of the surface over a wide area and in practice they appear to degrade it.

For good resistance to overload, it is considered that the boiling point, like the melting point, should be as high as possible.

7.2.2.4 Thermal Conductivity

Under overload conditions, the temperature rise due to frictional heating will be a function of the thermal conductivity of the bearing materials. High conductivity materials will transfer surface heat rapidly into the bulk of the material and will tend to prevent either the melting or boiling points from being reached.

On the asperity model shown in Figure 53 an increase in k could be expected to eliminate one or more of the upper isotherms and to re-distribute the remainder throughout the micro-peak. The temperature gradient will be decreased and the nett heat flow into the bearing improved.

This reduction of local temperature gradient has the added advantage that it improves the ability of the surface to withstand thermal shock, which might otherwise produce cracking, crazing or spalling at the point of contact. Many high conductivity materials have a good resistance to thermal shock, and silicon carbide is especially notable in this context.

Quite apart from any beneficial effects upon bearing wear, high thermal conductivity materials also assist in removing viscous frictional heat from the bearing, and in maintaining all parts of the bearing assembly at an even temperature. Design clearances can be maintained over a wider temperature range and it is considered that an overall improvement in performance can be realised.

7.2.2.5 Specific Heat

Specific heat indicates the thermal storage capacity of the material and, together with thermal conductivity, is believed

7.2.2.5 Specific Heat (Continued)

to play a major role in reducing the maximum surface temperature for a given frictional input. More correctly, the Density-Specific Heat product is a comparative measure of the thermal storage capacity of different materials.

A high value of specific heat is therefore considered to be an advantage in keeping local temperature low during rubbing conditions, and might be expected to contribute to the overall wear life of the bearing.

7.2.2.6 Latent Heat of Fusion

If circumstances are such that local frictional heating eventually causes the melting point of one of the bearing materials to be reached, fusion will be accompanied by the absorption of additional heat energy from the immediate surroundings. Since overload or start/stop conditions are usually transiatory, this latent heat of fusion serves to limit the extent of the surface damage that might otherwise occur.

Thus, where rubbing temperature are expected to exceed the melting point, a high value of this parameter is considered to be advantageous.

7.2.2.7 Latent Heat of Vapourisation

As previously stated, vapourisation of the bearing surface has only been observed during high speed rubbing and very small volumes of material appear to be involved.

When vapourisation occurs, additional energy must be absorbed and like the fusion process, this must tend to limit the extent of the surface damage.

For those cases where high speed contact is likely to take place, a high latent heat of vapourisation would seem to be desirable if the extent of the damage is to be minimised.

7.2.2.8 Grain Size

Grain size has long been considered to be an important factor in the manufacture of engineering ceramics, and has received much attention when some of these materials were later developed for gas bearing applications.

7.2.2.8 Grain Size (Continued)

Reduction in grain size is well known to increase the mechanical strength of all materials and this in turn permits the design of relatively thin section components where desired. Fine grain materials are better able to withstand machining stresses and allow well defined corners to be produced.

While mechanical strength is important in order to resist possible impacts due to shock loads, the prime reason for reducing the grain size in gas bearing materials has been to improve the small scale microstructure of the bearing surface. This helps to reduce the porosity of hot pressed or sintered composites and allows a better surface finish to be obtained. It is particularly important in polycrystalline ceramics like aluminium oxide in which intergranular fracture and pull-out occur during final machining, but far less important in a material such as boron carbide where each grain can be individually levelled during polishing and pull-out is virtually absent. This is clearly illustrated by the fact that for aluminium oxide compacts, a reduction in grain size from 15 micrometres to 2 micrometres will improve the ultimate surface finish from about 6 micro inches C.L.A. to 0·5 micro inches C.L.A., (0·15μm C.L.A. to 0·008μm C.L.A.), whereas 0·1 micro inches C.L.A. (0·0025μm C.L.A.) can readily be obtained on boron carbide up to a grain size of at least 5 micrometres (116).

If maximum compaction (and therefore minimum porosity) is to be achieved in hot pressed or sintered materials, an adequate range of grain size is important. The smaller grains serve to partially fill the voids between the larger ones and improve the overall microstructure and strength of the material. A compact produced from grains of one size, however fine, would fall short of its theoretical density and would be unsuitable for bearing use. Where consolidation involves very high temperatures, allowance must be made for grain growth during pressing and a rather smaller average particle size selected.

7.2.2.8 Grain Size (Continued)

Under certain conditions, massive grain growth can occur, as depicted in Plate 28. Despite their size, the enlarged grains are invariably composed of pure material, the properties of which present no threat to the wear life of the surface. Transgranular defects (Plate 30) are found to be rare* unless growth has been excessive, and an exceptionally fine finish can be obtained on each grain. Occasionally, twinning can occur within a grain as shown by the light lines on Plate 30. This is a crystal defect which occurs when one section of the crystal lattice forms as a mirror image of the adjacent section and is not considered to be serious from the bearing standpoint. The main disadvantage of grain growth, the concentration of impurities, will be considered further in 7.2.2.11.

Practical restrictions appear to impose a limit on the minimum grain size that can be successfully used for ceramic and cermet materials. While certain materials (e.g. Boron Carbide) can be produced in 0·1 micrometre size or smaller, the excessive 'bulk' of the powder is known to make compaction difficult and porosity is generally poor.

One common method of producing the correct particle size and distribution is by ball-milling a relatively coarse mixture of aggregates. This has recently been questioned by Glasson & Jones (37). It appears that ball-milling fractures the larger crystals in an unnatural manner and the resulting material does not densify as readily as naturally formed crystals. Plate 30 shows a large grain within a boron carbide compact. Internal fissures are clearly visible but it is not clear if these are a result of the ball-milling process.

It is believed here that, for ceramics and cermets at least, the finer grain materials do provide longer wear lives in service. One again, a notable exception is the beryllium oxide bearing quoted by Hall (58) where a grain size of 20 micrometres was used.

* Based upon routine examination of boron carbide samples in the Material Research Laboratories of Smiths Industries Limited.

PLATE 28 X 5
OPTICAL PHOTOMICROGRAPH SHOWING SEVERE GRAIN GROWTH AND INCLUSIONS IN A BORON CARBIDE COMPACT

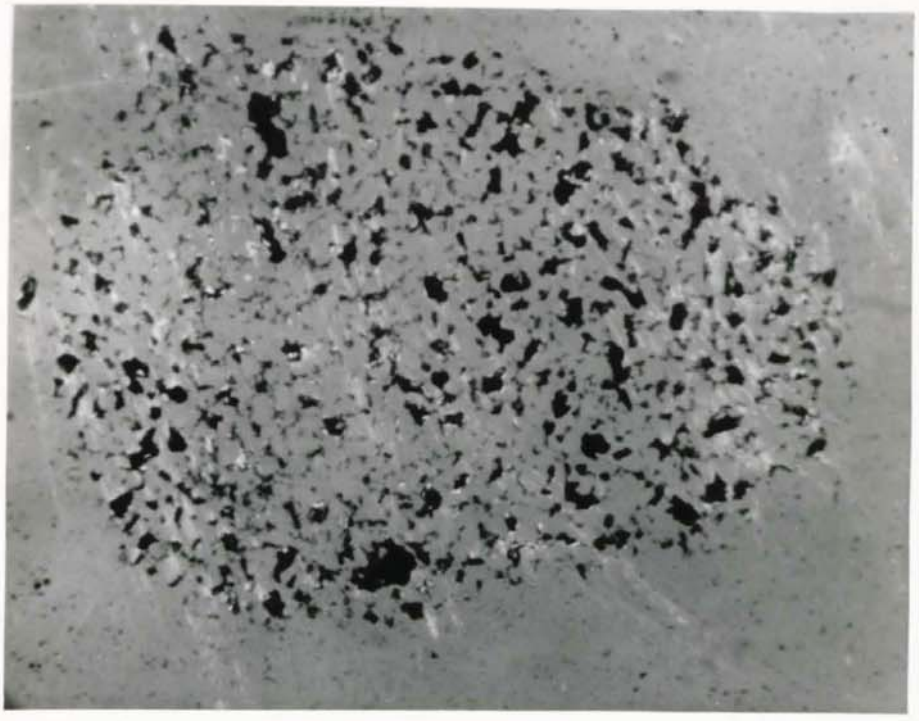

PLATE 29 X 200
OPTICAL PHOTOMICROGRAH ILLUSTRATING INCOMPLETE DENSIFICATION IN BORON CARBIDE

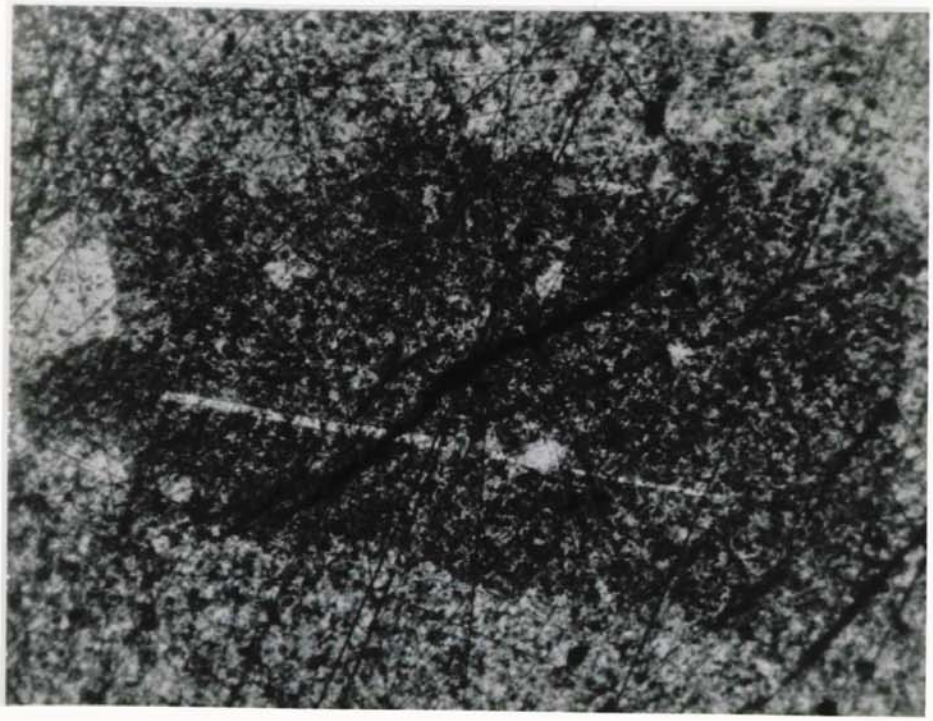

PLATE 30 X 150

PHOTOMICROGRAPH OF A LARGE GRAIN WITHIN A BORON CARBIDE COMPACT SHOWING INTERNAL GRAIN FISSURES (DARK LINES) AND CRYSTAL TWINNING (LIGHT LINE)

7.2.2.8 Grain Size (Continued)

This material survived over 100,000 start/stop cycles and was tolerant to high speed rubbing. The same reference conveniently compares coarse grained (> 20 micrometres) aluminium oxide with fine grained (1 micrometre) aluminium oxide. These gave 5000 and 15,000 start/stop cycles respectively. Unlike the beryllium oxide, the latter results were only achieved in conjunction with a sodium stearate boundary lubricant.

The conclusion by Young (78) that small grain size leads to good wear and high speed impact resistance may be correct, but it is considered here that the attendant benifits of lower porosity and improved surface finish might be responsible rather than grain size alone.

7.2.2.9 Grain Bond Strength

Whereas grain dimensions alone do not influence operational life, the individual grain bond strengths are belived to be of considerable importance.

The importance of grain bond strength in relation to various machining processes is discussed in Appendix IV where it is shown that superior surface finishes could be obtained if each surface grain were firmly anchored in position.

This same property is thought to be equally important under contact conditions. The welding and tearing action can pluck individual grains from the wear surface if the grain boundary is weak, and these loose grains then abrade (See Appendix IV Section 4) within the bearing. Severe shock loading might also cause bearing contact and the resultant 'hammering' action can then chip loose grains from the surface matrix. Reference has been made in section 7.2.2.1 to the very high

7.2.2.9 Grain Bond Strength (Continued)

micro-hardness measurements recorded on individual crystals in comparison with the average hardness of a compacted surface. This, together with their characteristic angularity (See Plate 31) may best explain the destructive and often cumulative action that occurs when individual grains are plucked from a bearing surface.

Though contact conditions are the most likely cause of grain dislodgement, grains are also well known to be thrown from the surface of a rotating member under the action of centrifugal force. For a cylindrical journal bearing this can only occur if the inner member rotates, and for the alternative case in which the outer member is rotating, centrifugal forces will assist in retaining the grains. Rotating thrust surfaces are generally under the action of tangential forces and it is concluded that grain movement would be less likely in this case.

In hot pressed materials like silicon or boron carbide where each grain is partially fused to its neighbours, boundary strength will be related to the mechanical properties of the material itself, whereas in sintered compacts, grain bond strength will be largely dependent upon the properties of the binder matrix. Single phase materials can therefore be expected to be more resistant to mechanical, thermal and chemical attack than composite structures. In particular, where the binder matrix has a lower melting point than the wear material, (as for example the glass phase in bonded aluminium oxide) softening could occur locally under frictional heating and individual grains could be torn free. Galvin (98) reports evidence that the cobalt binder in sintered tungsten carbide is attacked by fatty acids used for boundary lubrication, with the consequent release of tungsten carbide particles. Young (99) suggest similar experiences when using fatty acids with aluminium oxide.

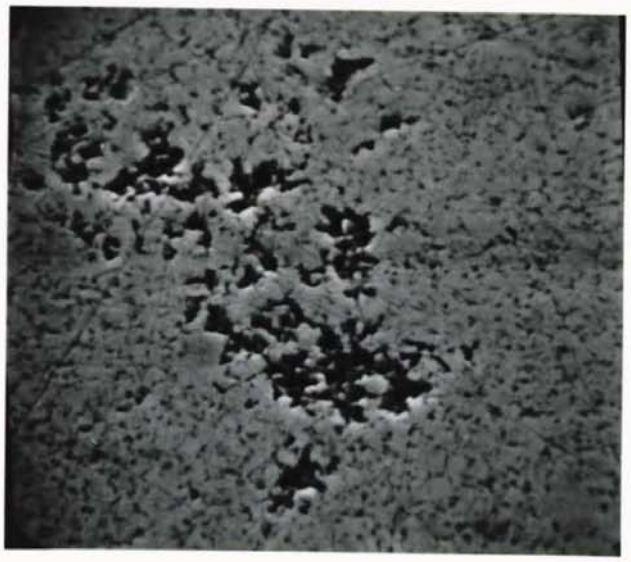

a) X 2,000

b) X 10,000

PLATE 31
STEROSCAN EXAMINATION OF A TUNGSTEN CARBIDE BEARING SURFACE SHOWING LACK OF COBALT MATRIX

7.2.2.9 Grain Bond Strength (Continued)

Comparative measurements of bond strength have been obtained for various materials by Stokes (36) who measured their energy absorption during grinding. These show the bond strength of hot pressed boron carbide to be far superior to that of all other ceramic materials investigated. High bond strength materials can often be identified by an examination of their fracture faces. Plates 32 and 33 are of a boron carbide fracture face and clearly show the areas of transgranular fracture which are characteristic of high bond strength materials. Fracture faces of low bond strength materials are characterised by areas of intergranular fracture and loosely attached debris.

It may be concluded that materials having a high bond strength will resist damage by all forms of rubbing contact and should be especially tolerant to high speed touchdown. Boron and silicon carbide, both high bond strength materials, are known (116) to survive repeated overloads at high speed and grain pull-out does not occur easily under these conditions. Medium bond strength materials like aluminium oxide and tungsten carbide survive a lesser degree of overload, but here, grain dislodgement has been observed on two occasions when using tungsten carbide. Low bond strength materials such as Porcelain and 'Steatite' quickly break down under similar conditions.

Where centrifugal forces become comparable in magnitude with the bond strengths of the looser grains, it is believed that reliability and life may also be affected for the continuous run condition.

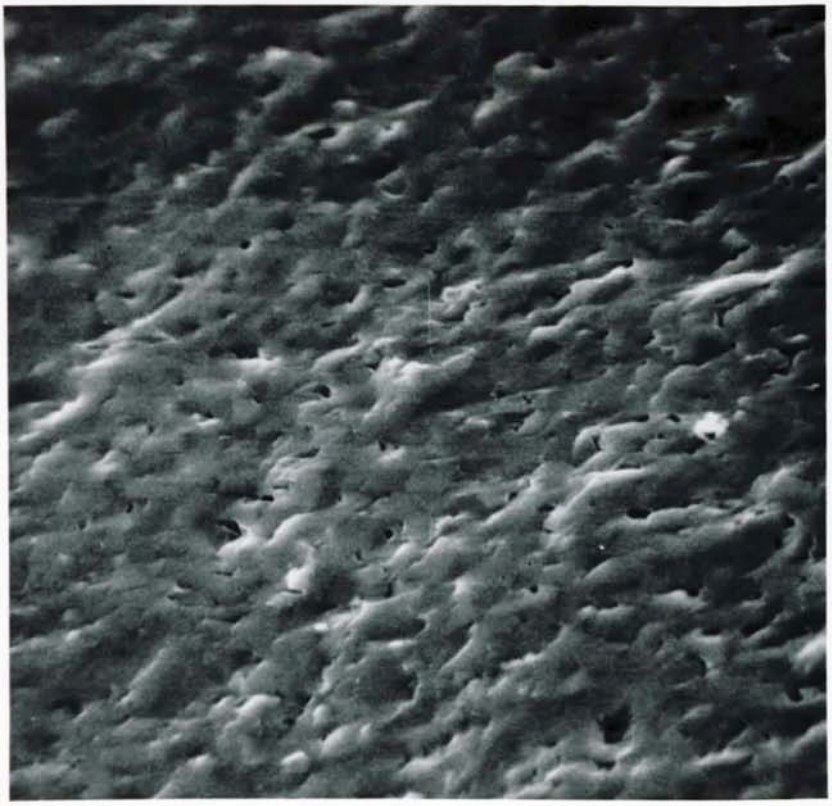

a) X 1,150

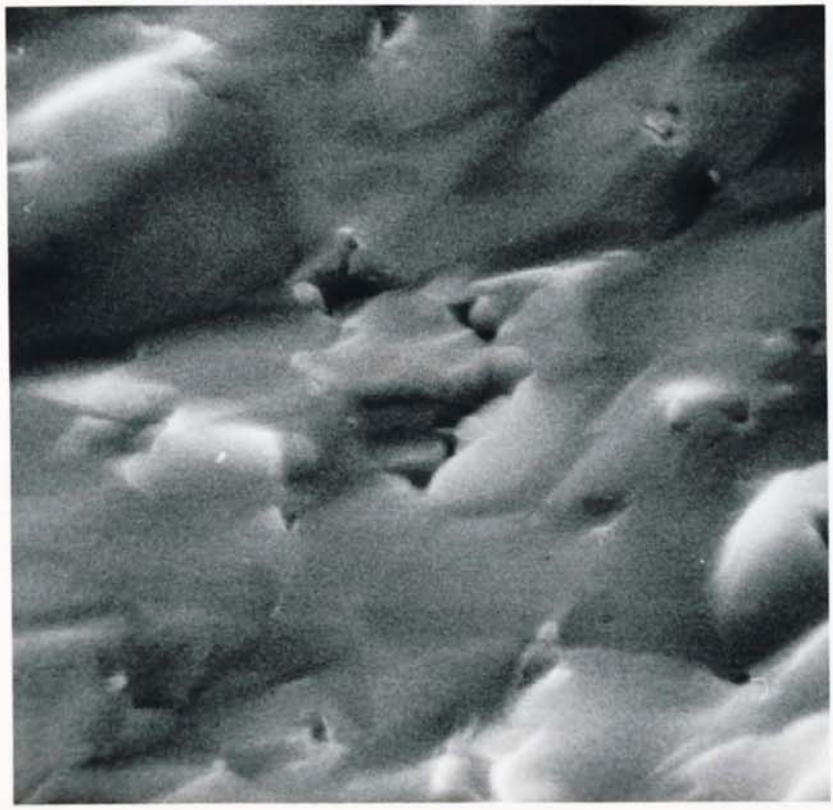

b) X 5,700

PLATE 32
STEROSCAN PHOTOGRAPHS OF A BORON CARBIDE FRACTURE FACE

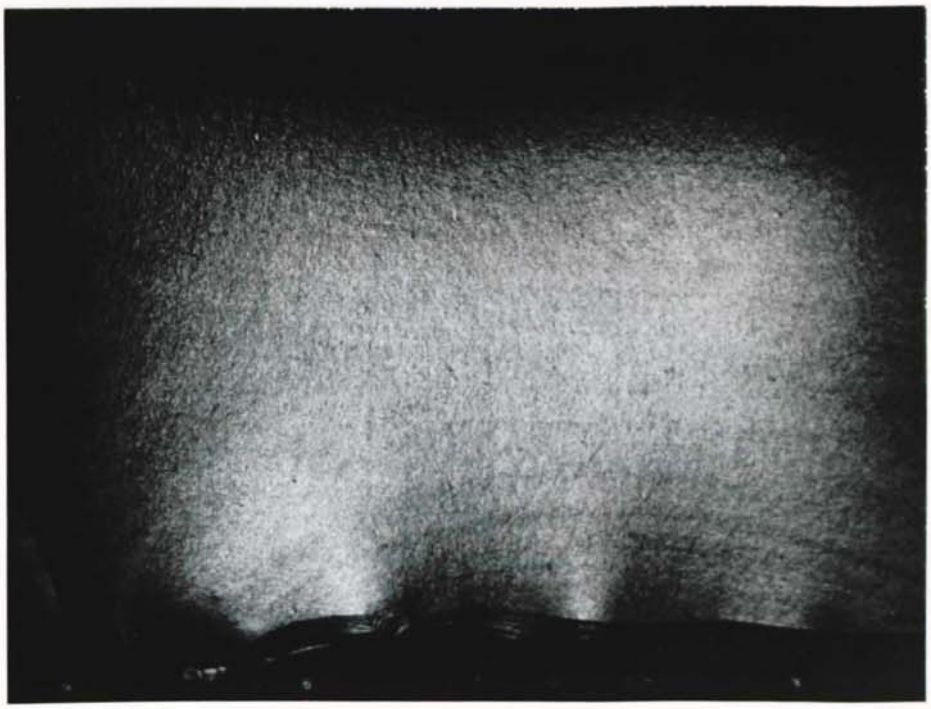

PLATE 33 X15
OPTICAL PHOTOMICROGRAPH OF BORON CARBIDE FRACTURE FACE

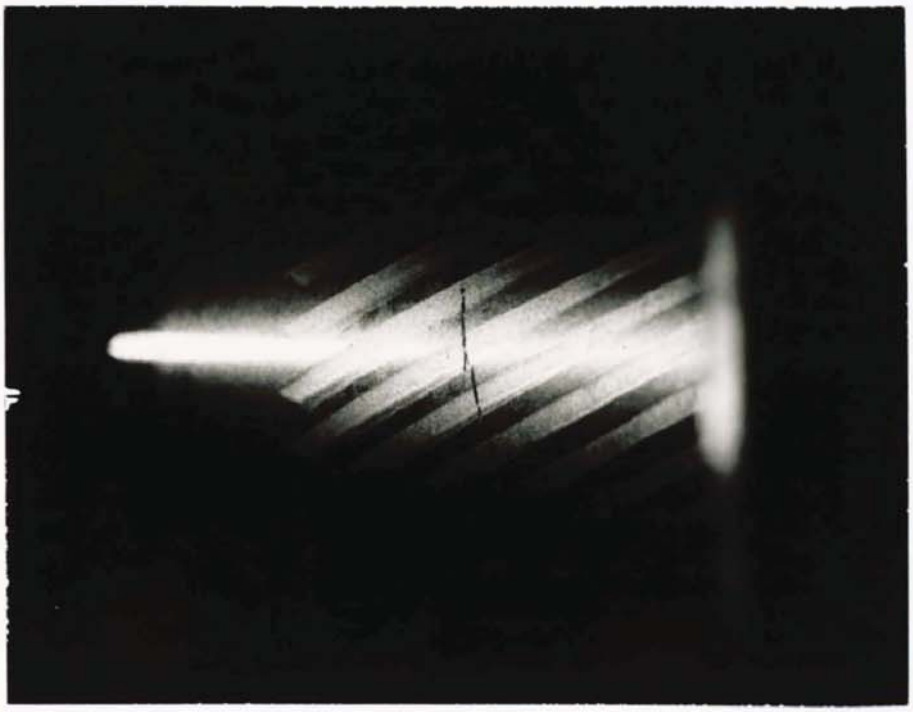

PLATE 34 X 2
PRESSING FISSURE IN BORON CARBIDE JOURNAL SHAFT

7.2.2.10 Porosity

All known bearing materials exhibit some degree of porosity and manufacturers claims to the contrary should be viewed with suspicion.

Two characteristic types of porosity can be identified. Interconnected or 'tunnel' porosity in which surface pores are connected to the interior of the material by a network of fine galleries and discrete porosity where the cavities are not joined. Examination of true porosity cannot be carried out on a polished surface where grain pull-out and other artifacts would be misleading. Fracture faces often reveal the inherent porosity of the material and Plate 32 shows evidence of discrete porosity in a boron carbide bearing sample. This is illustrated more clearly after ion bombardment, as shown in Plate 35(b).

Apart from the obvious limits to surface finish that a high porosity imposes, its influence upon the operational life as such is not entirely clear. The good start/stop life and high speed touch-down characteristics obtained from early aluminium oxide bearings were originally attributed to the relatively coarse 'tunnel' porosity of this material. Patterson (107) refers to the pores acting as "micro-dustbins" and preventing wear debris from circulating within the bearing where it would induce cumulative damage. More recently, Hall (58) has cast doubts upon this view by noting that a threefold improvement in start/stop life can be obtained on fine grain low porosity aluminium oxide, as compared with coarse grain high porosity material. Against this must be counted the now familiar exception of beryllium oxide which despite a very open pore structure yielded a sixfold improvement over fine grained aluminium oxide (58).

It seems more likely that the "micro-dustbins" will be full even before the bearing is assembled, having acted as a trap for machining debris, cutting fluids, cleaning solvents and other potential contaminants. This situation will certainly make cleaning difficult and may have a long term effect upon the friction coefficient, and therefore the start/stop life of the surface.

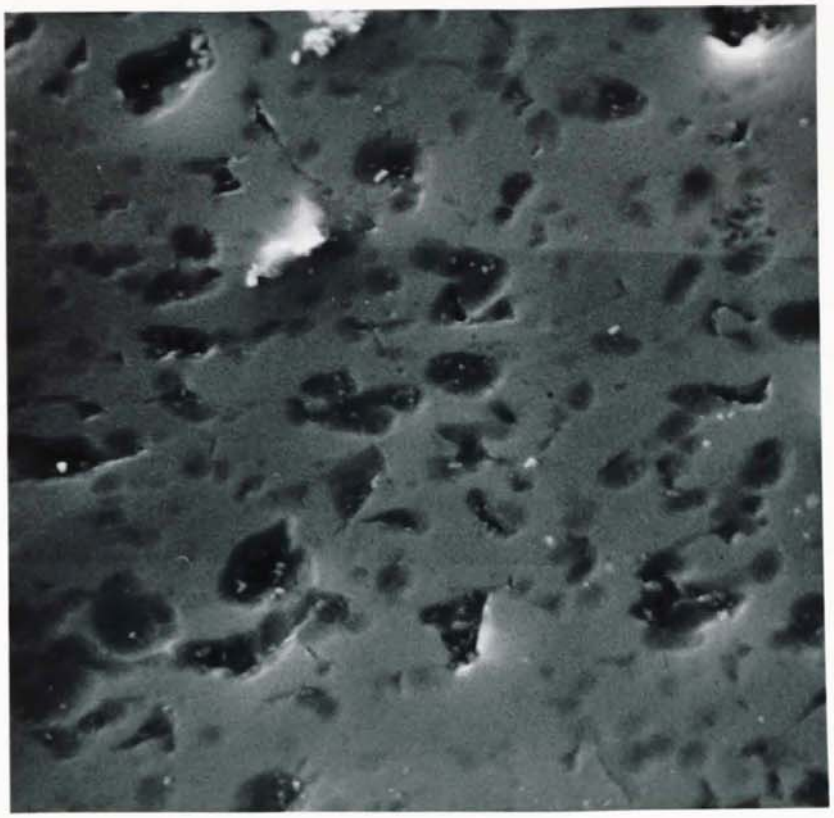

a) X 3,300

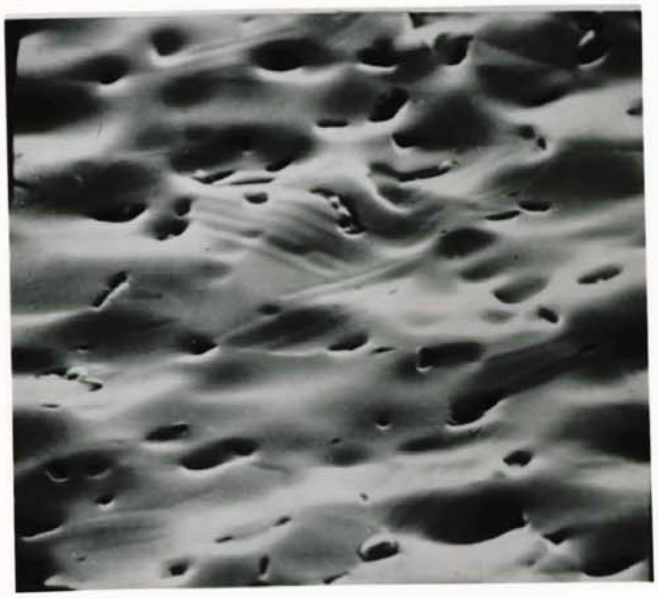

b) X 3,000

PLATE 35
STEROSCAN PHOTOGRAPHS SHOWING A TYPICAL BORON CARBIDE SURFACE AFTER ION-MACHINING.
SURFACE a) WAS FORMED BY LOW ENERGY ION BOMBARDMENT WHILE SURFACE b) WAS ERODED BY A HIGH ENERGY ION BEAM

7.2.2.10 Porosity (Continued)

Large scale porosity may however have a beneficial effect upon the storage life by discouraging the molecular diffusion effects discussed in section 7.2.2.2.

Plate 29 shows a small region of local porosity in a boron carbide compact; the result of incomplete mixing of some of the larger agglomerates. Plate 31 shows a similar region in sintered tungsten carbide, this time due to a local shortage of cobalt binder. In each case, the photomicrographs clearly show many loosely held grains and this type of manufacturing defect can have serious implications where life and reliability are concerned.

While performance is not of direct concern it should be noted that the permiability of high porosity materials will allow leakage through the bearing surface from regions of high gas pressure to those of lower pressure. This will be particularly acute in bearings operating at high compressibility numbers and may ultimately have an indirect effect upon the wear life of the assembly.

7.2.2.11 Purity

The effect of impurities on the properties of the basic bearing material are difficult to predict. Much will depend upon whether the foreign matter is present in discrete inclusions or evenly alloyed throughout the base material.

Where grain growth has taken place, impurities tend to be concentrated into the depleted intergranular region, forming pockets of high porosity and very low wear resistance. Differential hardness causes preferential machining of the impure areas during manufacture, surface finish is impaired and pressure leakage paths formed along the bearing surface. Plate 28 shows the impurity regions as medium grey between the lighter grains. The dark grey areas on this sample have been investigated with an Electron Microprobe Analyser and were found to contain large quantities of iron from the ball-milling process where cast iron balls are often used.

7.2.2.11 Purity (Continued)

Carbon is well known to be a common impurity in ceramic or cermet materials and usually diffuses into the outer skin of the compact from the graphite pressing moulds. Refractory materials like magnesium oxide are frequently added to ceramic powders in small amounts (typically 0·1%) to inhibit grain growth during pressing, and while their presence seems fairly innocuous from a chemical view, some reduction in grain boundary strength must be inevitable.

Where materials have been specially developed for use in gyro bearings (e.g. aluminium oxide, boron carbide and chrome oxide), improved purity has always been accompanied by superior physical properties and increased life (107). It can therefore be concluded that high purity materials are desirable where optimum wear life is required.

7.2.2.12 Young's Modulus

A high value of elastic modulus is useful in the overall design of a bearing, but is considered here to have little direct effect upon operational life. Increased component stiffness helps to maintain the design geometry and clearance while elasto-hydrodynamic effects and centrifugal distortion are reduced.

Even for a high modulus material like boron carbide, improvements in dynamic performance are very small and will have a negligible effect on operational life.

7.2.2.13 Rupture Modulus

Rupture modulus of the bulk material is closely related to the grain boundary strength and the comments already made under that heading are generally applicable here. While large scale rupture of the bearing structure is improbable, local rupture of individual micro-peaks may take place under some conditions of contact and a high modulus is therefore desirable.

7.2.2.14 Compressive Modulus

This is associated with the hardness of the material and is believed to be important if the bearing surfaces are to successfully crush entrapped debris. If the compressive strength of the bearing surface is exceeded, crumbling will take place and cumulative damage may result. For all bearing surfaces and especially for those disrupted by pumping grooves, a high compressive modulus is considered to be desirable.

7.2.2.15 Shear Modulus

When welding occurs at the peaks of the surface asperities, either due to frictional heating or to molecular diffusion, (Section 7.2.2.2) the bond will usually be broken under shear. Shear strength therefore makes an important contribution to the effective friction coefficient. If the motor starting torque is unable to provide the necessary shear force the bearing will fail to start, and if the synchronous torque is insufficient to overcome the weld strengths under overload conditions, the wheel will loose synchronism.

For lamellar bearing materials like graphite, shear strength is found to be low (31) (39) and rubbing friction is also small. Unfortunately, low shear strength is usually associated with low hardness and wear rate is consequently unacceptable on gyro bearings. One well known solution is to apply a molecular layer of low shear strength material (boundary lubricant) over a hard substrate. Direct welding of the hard substrate peaks is prevented,at least under start/stop conditions, and bearing friction reduced. The shear characteristics of boron carbide are a special case and will be discussed in section 7.2.2.24.

For optimum wear and storage life a low shear modulus is therefore considered to be desirable, but only if accompanied by adequate hardness.

7.2.2.16 Dimensional Stability

Young (78) quotes a dimensional stability better than 0·002% as being suitable for gyro bearing materials but since this corresponds to a possible movement of 20 micro inches (0·5 μm) over a one inch (25·4 mm) bearing dimension, the figure would appear to be rather high and a stability of around 0·0002% is considered here to be more compatible with current gyro tolerances.

All ceramic and cermet materials examined here appear to be within this limit (see Appendix III Section 6) but considerable difficulty was experienced on early experimental models constructed from Monel-K, stainless steel and chrome plated iron (Plates 1 and 2). Bearing geometry varied considerably with temperature and time and repeated temperature cycling failed to provide an acceptable level of stability.

If the bearing materials are very unstable, premature touchdown can occur and wear life will be impaired. It is considered that a dimensional stability of around 0·0002% is desirable.

7.2.2.17 Thermal Expansion Coefficient

Where two or more materials are used to form the bearing assembly, correct matching of expansion coefficients will be necessary to maintain the design clearances over the working temperature range. If clearances become excessive as a result of differential expansion, take-off and touch-down speeds will increase disproportionally and wear rate will increase. The start/stop life of the assembly will therefore be reduced.

In the case of high speed rubbing, local frictional heating will result in a considerable increase in local temperature as previously discussed. This in turn will cause local expansion within the bearing surface and considerable stress will be involved in resisting this expansion. Where the stresses exceed the structural moduli of the material, mechanical breakdown will occur and cracking or crazing will be visible over the contact region. A low expansion coefficient may therefore be expected to improve the material's ability to survive high speed rubbing.

7.2.2.17 Thermal Expansion Coefficient (Continued)

An inspection of those materials which are known to survive high speed rubbing without cracking or spalling, for example chrome oxide, silicon carbide, boron carbide and beryllium oxide, shows that all have low expansion coefficients, though clearly this is not the only factor involved.

7.2.2.18 Density

Density is considered to have no direct influence upon operational life. Indirectly, the density-specific heat product is a measure of the thermal storage capacity of the surface as discussed in section 7.2.2.5.

7.2.2.19 Electrical Conductivity

Electrical conductivity of either wear surface does not appear to influence operational life, but this is discussed more fully in CHAPTER 6.

7.2.2.20 Chemical Stability

All bearing surfaces are required to be chemically stable, but this is particularly true for small hydrodynamic gas bearings under service conditions. The high level of cleanliness leaves the surfaces especially vulnerable to corrosion, and this can have a disastrous effect upon both the starting and running characteristics of the bearing. Where the volume of the corrosion product exceeds that of the converted material, complete siezure will eventually occur. Even hermatic sealing does not necessarily guarantee immunity to chemical attack and previous workers have observed extensive corrosion on ferrous bearings after running in a 99% Helium atmosphere. A typical gyro assembly may contain traces of volatile halogens, phthalate esters and other materials, in addition to oxygen and water vapour, and the formation of acidic contaminants may therefore be possible.

7.2.2.20 Chemical Stability (Continued)

Most ceramic and cermet materials show a marked resistance to corrosion. Boron carbide for example is claimed* to be stable against all acid or alkaline solutions, regardless of temperature or concentration. Sintered cermet composites are limited by the chemical properties of their metal matrix but no corrosion problems have been experienced here when using un-lubricated tungsten carbide in a 6% cobalt matrix. The corrosive action of fatty acid boundary lubricants on this material was referred to in section 7.2.2.9.

Chemical stability is therefore seen to be an important pre-requisite of any bearing material, but the degree of stability required will depend upon the operating environment of the assembly.

7.2.2.21 Mutual Solubility of Mating Materials

This is really a particular aspect of the materials chemical behaviour, but important enough to be considered separately. So far, discussion has centred on the properties of either bearing material and the chemical interaction between like or dissimilar bearing surfaces has not been considered. In practice, a bearing material may be run against itself, or against another material. Neglecting mutual chemical action and assuming physical factors to be dominant, it may be assumed that the performance of a dissimilar combination would be intermediate between the performance obtained when each was run against itself. This presumption may not be entirely true but the performance of many chemically stable ceramic materials suggests that it holds reasonably well at high hardness values.

Conventional plain bearings are traditionally constructed from dissimilar materials and the mutual 'pick-up' and 'scuffing' associated with like materials is well known (39).

* Supplier's literature

7.2.2.21 Mutual Solubility of Mating Materials (Continued)

For bearing materials having a low chemical interaction, that is, those which are mutually insoluble and do not tend to form compounds, the frictional junctions at the tips of the asperities will be due to relatively weak van der Waal's forces, and easily sheared. For the case of mutually soluble chemically active surfaces, the common bonding will be by strong covalent or ionic forces and will only be sheared with difficulty.

In practice it is found here (116) that such combinations as hard steel on hard steel, Monel-K on Monel-K, hard chrome on hard chrome and both hard steel and Monel-K on hard chrome, all have very poor wear and friction characteristics when used in gyro bearings without deliberate boundary lubrication. All these combinations are mutually soluble at high temperature. In contrast, tungsten and boron carbide are not mutually soluble and chemical 'pick-up' and scuffling do not occur.

It is proposed here that one possible method of assessing the suitability of mating combinations might be to study the contact angle between the material of lowest melting point, in its molten state, and the higher melting point surface. Where the 'wetting angle' approached zero, it might be predicted that the rubbing characteristics would be unsuitable. Unfortunately, this information is not documented for many materials but Glasson and Jones (37) record a number of contact angles for various refractory boron compounds. From this it is seen that a strong reaction takes place between molten iron and born carbide, suggesting that ferrous materials will form an unsuitable bearing combination when run against boron carbide. Similarly, chromium has a zero contact angle with boron carbide and poor rubbing characteristics can be expected. Cobalt is seen to have a 90 degree angle against the same material, indicating that the wear properties of a tungsten carbide - boron carbide combination should not be unduly sensitive to the proportion of cobalt binder in the former.

7.2.2.22 Magnetic Properties

In electrically driven gyroscopes, the bearing materials will almost certainly be cut by magnetic flux from the spin motor and pick-off systems.

Where ferromagnetic materials are used, the induced magnetism may cause the bearing surfaces to adhere together, so raising the effective coefficient of friction between them. This occurred on an early experimental assembly (Plate 1).

The effect of magnetic debris within the bearing clearance, while less obvious, is probably more detrimental to the wear life than a direct increase of friction due to magnetic attraction. In a bearing using non-magnetic wear surfaces, any loose wear debris may be swept aside by the rotating member and allowed to take up a position where it is likely to do least damage. Grooved regions will later be discussed in this context. Inspection of debris patterns in dismantled bearings also suggests that particles are carried by the air flow and deposited some distance from their source. Where both debris and bearing surface are magnetised, this freedom of movement may be restricted by magnetic forces, and the debris may remain in the contact region long enough to cause further cumulative damage.

An additional consideration is the fact that elongated magnetic particles will tend to align themselves in the direction of the local magnetic field, which for the case of a journal will be perpendicular to the bearing clearance. Clusters of magnetised particles will eventually be formed and the clearance will be bridged. This effect has been observed here on many occasions in a 0·002 inch (0·05 mm) radial gap between two cylindrical magnetic surfaces in intermittent rubbing contact, and there seems to be no reason why it should not occur on a reduced scale within a gas bearing.

7.2.2.22 Magnetic Properties (Continued)

From the above it is concluded that magnetic materials are best avoided in the design of gyro bearings, and that where this is not possible, preference should be given to those materials having low susceptibility and low remanence.

7.2.2.23 Friction Coefficient

The friction coefficient between two bearing surfaces will be dependent on many of the factors discussed in this thesis. While some are obviously basic properties of the substance concerned, others are clearly independent of the individual material and are related to the circumstances in which the bearing pair is being used. For this reason, it appears wholly insufficient to refer to bearing materials as 'high friction' or 'low friction' as has been customary and for gyro bearings, where small changes can have a large effect, the measurement conditions must be very clearly stated. Boron carbide for example has a fairly low coefficient of friction when used against itself with a surface finish of 0·2 micro inches C.L.A. (0·005 μm C.L.A.) and a specific loading of 0·45 lbs/in^2 (3080 N/m^2) while at 1 micro inch (0·025 μm) C.L.A. and specific loadings above 1·5 lbs/in^2, (10,300 N/m^2) it is found to be quite unsuitable for gyro use.

In section 7.2.2.2, a simplified form of the Adhesion Theory of Friction has been used to explain friction and wear effects in bearing materials. This recognises the successive adhesion and shearing of opposing micro-peaks on the sliding surfaces, and has the merits that it is consistent with experimental evidence of metal transfer and also with Admonton's Law - that frictional force is directly proportional to load and independent of apparent contact area. It does not, however, account for the appearance of loose wear debris, nor does it predict the very high friction coefficients measured between super-clean surfaces. This simple theory can be extended to overcome many of its criticisms and invokes micro-fatigue of the asperities to account for the formation of free wear particles.

7.2.2.23 Friction Coefficient (Continued)

An alternative approach is the Coulomb Theory of Friction, which suggests that interlocking occurs between the asperities of each surface. Relative motion between the surface will then result in fracture of the most prominent peaks, with the consequent generation of wear debris and frictional force.

On examination of both theories in the light of actual experience with a large number of hydrodynamic bearings, no valid reason can be found here why both mechanisms should not occur together, with the relative local geometry deciding which takes precedence at any point on the bearing's surface. It seems reasonable to suppose that the Coulomb theory would be dominant where the surface texture is relatively coarse and that the Adhesion hypothesis will take over as very high orders of surface finish are achieved. This would explain the observed and very marked reduction in loose wear products as the surface finish is progressively improved below one micro inch C.L.A (0·025μm C.L.A.). It could also account for the observation that, on very smooth bearing surfaces, the difference between static friction and sliding friction is very small in comparison with that on rougher surfaces.

Returning again to Figure 53, it can be shown that the rate of frictional heat input is given by the expression:-

$$Q_F = f \cdot U \times \text{Contact Load} \qquad (77)$$

An increase in friction coefficient will therefore result in a proportional increase in Q_F, a higher temperature gradient and increased temperatures throughout the asperity.

Friction coefficient is therefore seen to be a primary factor in both the start/stop and overload life of a bearing assembly.

7.2.2.24 Self Lubricating Properties

Reference has already been made to the ability of certain materials to provide a degree of inherent lubrication when in sliding contact. Though the property is well known amongst various plastic and organic materials, the molecular structure

7.2.2.24 Self Lubricating Properties (Continued)

necessary to achieve this effect is not compatible with the very high hardness and stability that has been found to be so desirable in gyro bearings.

Most, but not all lubricating materials, are of a layer-lattice or lamellar construction in which strong ionic or covalent bonds exist between the atoms within a layer. Between the lattice layers, bonding is due to relatively weak van der Waal forces, allowing shearing to take place easily under certain conditions. These conditions are often complex, as in the case of graphite, where an adsorbed gas or vapour film appears to be necessary between the crystal planes for low friction to be achieved (31). Other types of non-laminar solid lubricants are of little interest in this context because it is unlikely that they can be formed into structural bearing members.

A clear distinction must be made between the use of solid lubricant materials to form bearing surfaces, and their use as boundary lubricants, for in the former case the lubricating property extends throughout the entire structure and not just at the surface. In reference (88) the author suggested that self lubricating wear surfaces could be artificially constructed using vacuum deposition techniques.

The self-lubricating properties of boron carbide are a rather special case and will now be considered in some detail.

Thermo-chemical polishing of boron carbide is discussed in Appendix IV where it is observed that this might play an important part in the wear process for that material. This is indeed the case, and the chemical action within the bearing is identical to that which takes place during the polishing process.

When high speed rubbing occurs, a relatively soft, low melting point oxide of boron is formed at the interface of the contact area. Unlike the abrasive debris from many other hard bearing materials, the diboron trioxide can cause no further mechanical damage to the bearing surface and is

7.2.2.24 Self Lubricating Properties (Continued)

easily swept, aside by the rotating member. Its low hardness, and the fact that it is continuously formed in a very finely divided state, suggests that it can behave as a solid lubricant around the contact region. During high speed rubbing, wear is belived to be primarily due to chemical oxidation across the surface of each individual grain, rather than either a micro-machining or welding-tearing action observed on most other materials. As a result, the wear surface can be smooth, almost down to a molecular level, and pick-up or scuffing does not occur. The exceptionally high bond strength of the material helps to preserve this effect on a macroscopic level. Very small degrees of rubbing produce a surface finish similar to that shown in Plate 27, but even where serious overload has occurred, the wear track is still remarkably clean and polished. Plate 36 and Figure 54 show a wear track some 75 micro inches (1·9 μm) deep around a boron carbide thrust plate; the result of prolonged overload at 400 revs/sec. Even in this case, the wear region has not suffered catastrophic damage, despite the sub-standard quality of the material on this particular sample. Plate 37 shows a sequence of Steroscan photomicrographs of boron carbide wear debris generated under similar conditions. The light grey debris has been deposited in the base of the pumping grooves and wear tracks may just be seen on the corresponding land region in Plate 37 (B). At higher magnifications (Plate 37 (c) and (d)) the deposit is seen to have coalesced into mounds and many fissures are evident, suggesting rapid cooling of hot material. Despite their loose and fractured appearance, the deposits adhered very firmly to the surface of the component and were not removed by prolonged ultrasonic cleaning. They were, however, considerably softer than the parent material and could be crushed with the blade of a scalpel. The volume of deposit was too small to be analysed by available laboratory methods but it was assumed, by comparison with the analysis of polishing debris (Page 331), to be diboron tetroxide.

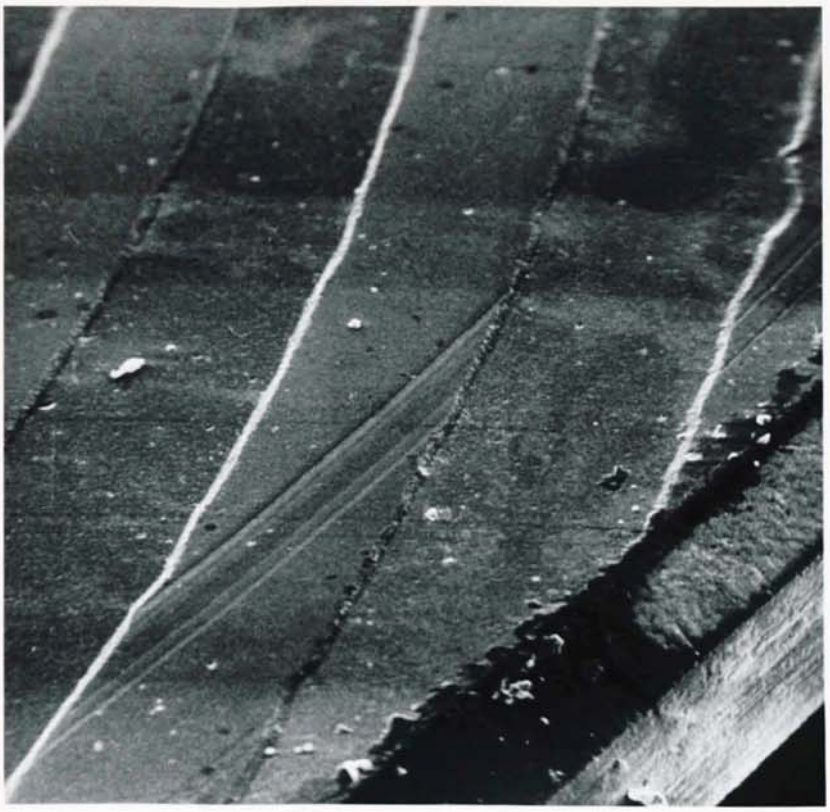

a) X 70

b) X 280

PLATE 36
STEROSCAN EXAMINATION OF WEAR TRACKS ON A BORON CARBIDE THRUST PLATE

c) X 1,400

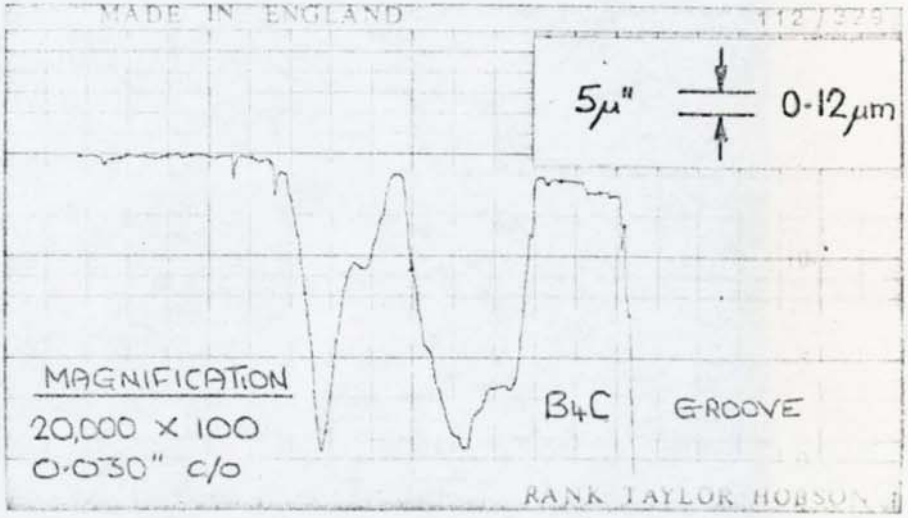

FIG. 54
TALYSURF TRACE TAKEN ACROSS THE WEAR TRACK SHOWN IN PLATE 36

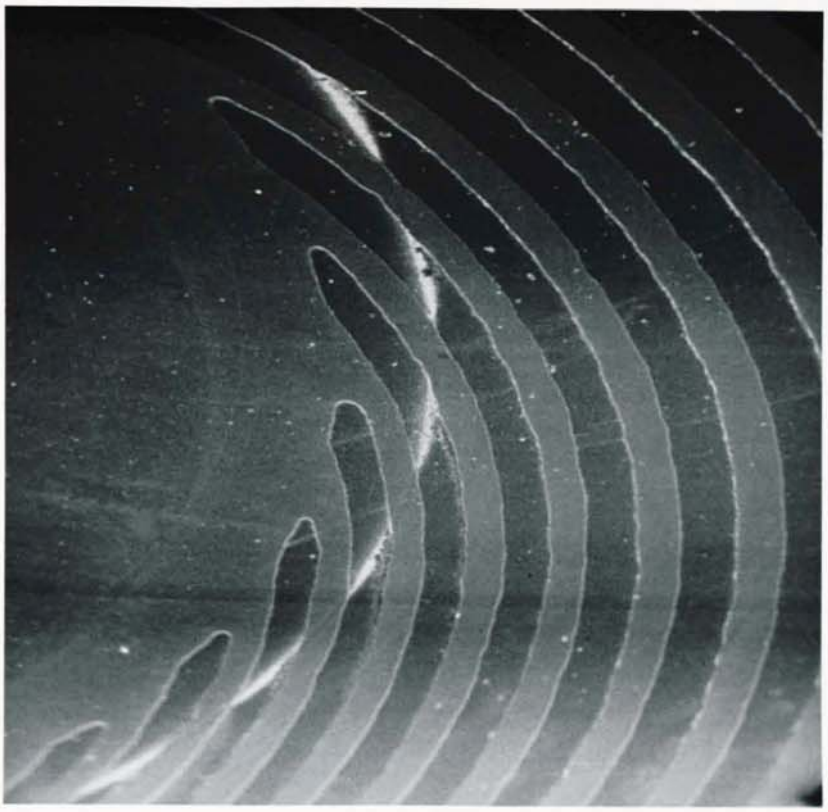

a) X 23

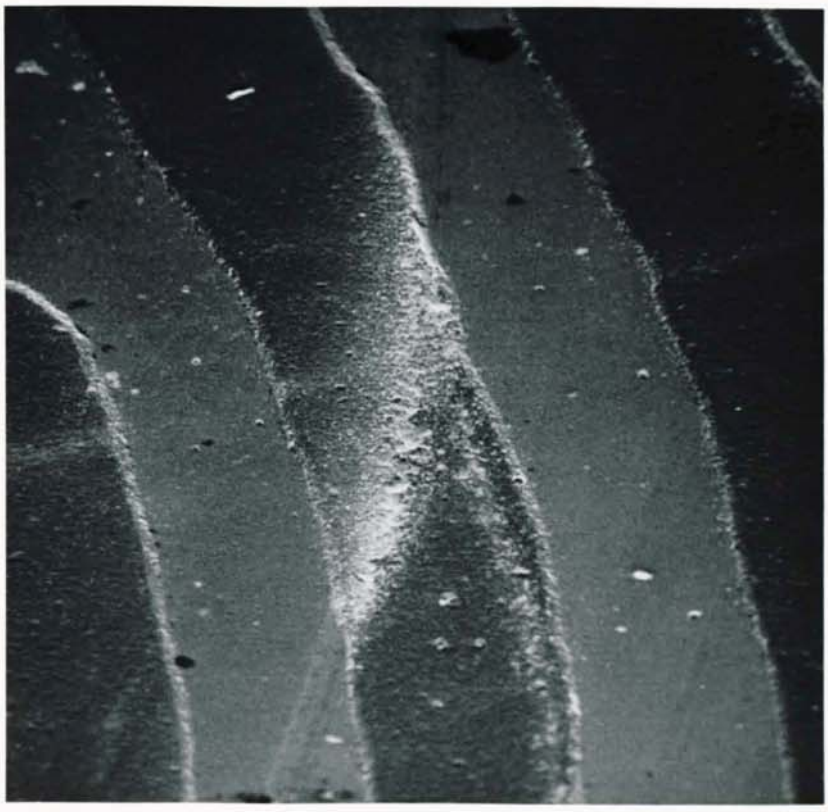

b) X 115

PLATE 37
STEROSCAN EXAMINATION OF BORON CARBIDE WEAR DEBRIS GENERATED DURING BEARING OVERLOAD

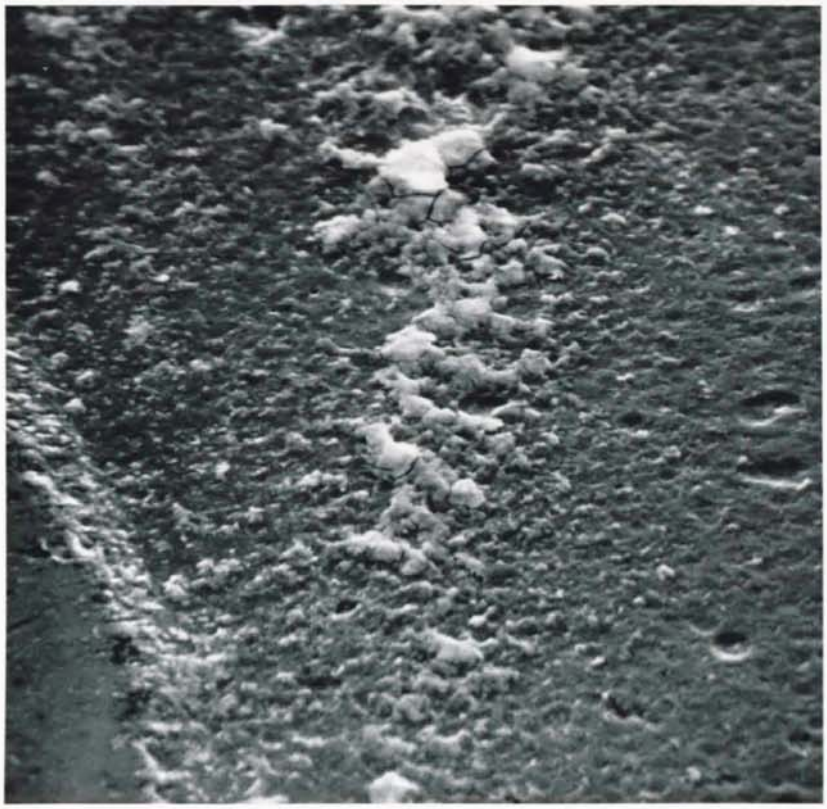

c) X 570

d) X 2,300

7.2.2.24 Self Lubricating Properties (Continued)

The mechanism of low speed rubbing, that is start/stop wear, on boron carbide is a little less clear. Certainly the wear scar appears as a highly polished region if the bearing surface is not already polished to a molecular level, after many thousands of wear cycles. Plate 27 shows wear damage on a boron carbide shaft of 1 micro inch C.L.A. (0·025 μm C.L.A.) surface finish after 40,000 start/stop cycles. The corresponding debris is, however, of a darker colour and a more powdery nature. It adheres quite firmly to the base of the grooves but is loosened by ultrasonic action. Nelson (59) has succeeded in photographing and analysing wear debris from a boron carbide gyro (6). He found that the wear products gathered to form minute dendritic growths in the groove region. Analysis revealed on anisotropic crystalline compound of boron, carbon and oxygen with a distinct crystallographic x-ray diffraction pattern, but Nelson is reluctant to suggest that this material contains diboron trioxide. In order to generate an appreciable volume of wear product, Nelson ran his bearing backwards for a period of time; pumping groove suction then causing continuous grounding of the rotating surface. It is believed here that this is an unrealistic method of generating 'start/stop' debris, since reverse rotation speeds of over fifty revolutions per second have been measured on laboratory bearings of similar design. At these speeds, the wear mechanism may be different to that taking place at typical touchdown speeds of one rev. per second or less.

Dendrite growths have not been observed among the debris examined here, and this may be due to the relatively low temperature of the wear product under realistic start/stop conditions. At very high speeds and temperature, temporary vapourisation of some of the wear product may account for the fissured mounds previously described.

The presence of contamination is also known to inhibit dendritic growth in pure materials (121), and in those bearings examined here, debris from the opposing surface (tungsten carbide) may also have influenced the final state of the wear product.

7.2.2.24 Self Lubricating Properties (Continued)

On the available evidence, oxidation of boron carbide is believed to occur at all rubbing speeds, and to be a primary factor in the remarkable wear properties of this material. If this is so, the lubricating gas should contain a proportion of oxygen. Experiments within Smiths Industries Limited have shown that very high concentrations of oxygen do not influence the oxidation rate under rubbing conditions, and this suggests that only a very small proportion of oxygen is necessary. Wear properties are retained in a helium atmosphere (5) and this may be due to residual oxygen within the gyro.

Boron carbide is reputed to maintain a low coefficient of friction when perfectly clean but there has been no opportunity to test this claim. If correct, it could be accounted for by frictional oxidation effects, Similar suggestions have been made with regard to chromium oxide but most materials show friction coefficients of up to 100 under these conditions. Hall (58) has shown that beryllium oxide maintains a friction coefficient of 0.17 after glow discharge cleaning but the explanation of this apparent self lubrication is still obscure.

7.2.3 Material Selection

Bearing materials are frequently evaluated on conventional wear testing equipment, such as the 'Shell four-ball', the Bowden friction tester and similar devices. These are considered to give totally misleading results when used to evaluate materials for gas lubricated gyro applications. Wear particles are allowed to escape easily from between the rubbing surfaces of wear test machines (92) and the cumulative surface damage and jamming action in real bearings cannot be duplicated. (See section 7.9) Contact geometry, frictional temperature and load dynamics will all differ from those in service and it is believed that conventional wear testing equipment can provide only the most rudimentary indication of operational life.

If the wear behaviour of a material is related to its properties in the manner suggested, it should be possible to select new bearing materials by inspection of their physical and chemical

7.2.3 Material Selection (Continued

characteristics, and predict their comparative performance in relation to that of established bearing materials. Final selection or verification can then be carried out using actual bearing assemblies. This approach, while more costly than the traditional wear-test method, may be more reliable, and was used here to successfully select boron carbide for the Series 700 bearing (See CHAPTER 3). Young (78) supports this view, but places greater emphasis on the value of friction and wear test equipment to carry out the initial screening on large numbers of samples. Clearly screening and much of the final elimination can now be replaced by selection based upon physical and chemical properties alone.

7.3 The Influence of Bearing Geometry

The geometric parameters defining the bearing surface or surfaces will now be examined for their influence, if any, on operational life and reliability.

7.3.1 Surface Finish and Texture

Surface finish is defined as the average value of the departures of the profile from its centre line, whether above or below it, throughout a prescribed sampling length. It is expressed as the sum of all the areas contained between the profile and the centre line, divided by the sampling length,in the British system.

Centre Line Average measurements only indicate the average level of roughness and tell little about the local texture of the surface. Below values of 0·5 μinch C.L.A. (0·01 μm C.L.A.). the accuracy of stylus instruments is questionable because the radius of the stylus becomes large in comparison with variations in surface height. Despite these limitations, surface contour traces can provide useful information on the nature of a bearing surface.

If each wear surface were perfectly smooth down to a molecular level, the generation of large wear particles by Coulomb action could not occur and friction levels would be determined by the

7.3.1 Surface Finish and Texture (Continued)

Adhesion hypothesis as discussed in section 7.2.2.23. Thermo-chemical polishing of boron carbide produces the closest approach to such a surface in practice and Figure 55 shows the essentially flat and level plateau, interrupted only by the inherent porosity of the material. Plate 38 also shows this porosity, but the surface is seen to be entirely free of polishing scratches.

Conventionally polished surfaces are by contrast covered in a fine network of scratches as shown in Plate 39. Figure 56 shows that the surface texture is less regular and the remaining land areas are bounded by sharp corners. Even at this scale, it is not difficult to imagine mechanical conflict between the corners of scratches on adjacent rubbing surfaces.

Plates 40 and 41 show the surface produced by conventional lapping, where pull-out is seen to play an increasing role in determining surface texture. In Figure 57, the surface is seen to contain many sharp asperities which, on this material, result in a high friction coefficient.

Where free abrasive lapping has taken place, Plate 42 shows that the surface texture of a boron carbide surface is entirely due to pull-out and transgranular fracture. Figure 58 shows this surface to be composed of a very large number of sharp cutting edges, and to be quite unsuitable for gyro bearing use.

Figure 59 shows the characteristic saw-tooth profile of a ground bearing surface, which is also illustrated in Plate 44. Note that in contrast to any of the lapped or polished surfaces, the surface peaks are approximately equal in height to the surface troughs. Figure 60 illustrates the improvement that can be obtained from a hydrostatic air bearing wheelhead, but this trace should be compared with Figure 52 where an identical C.L.A. reading was obtained.

A number of important conclusions can be drawn from the 'Talysurf' traces shown in Figures 55 to 60. The variation in C.L.A. value between each surface is quite small by normal engineering standards, and yet the surface textures are markedly

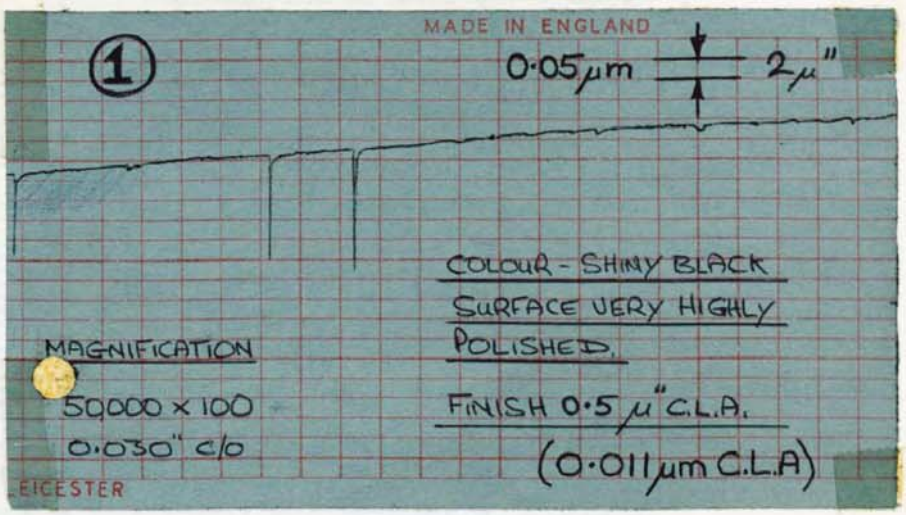

FIG. 55

THERMO-CHEMICAL POLISHING OF BORON CARBIDE AGAINST BORON CARBIDE

NOTE THE ESSENTIALLY FLAT AND LEVEL SURFACE

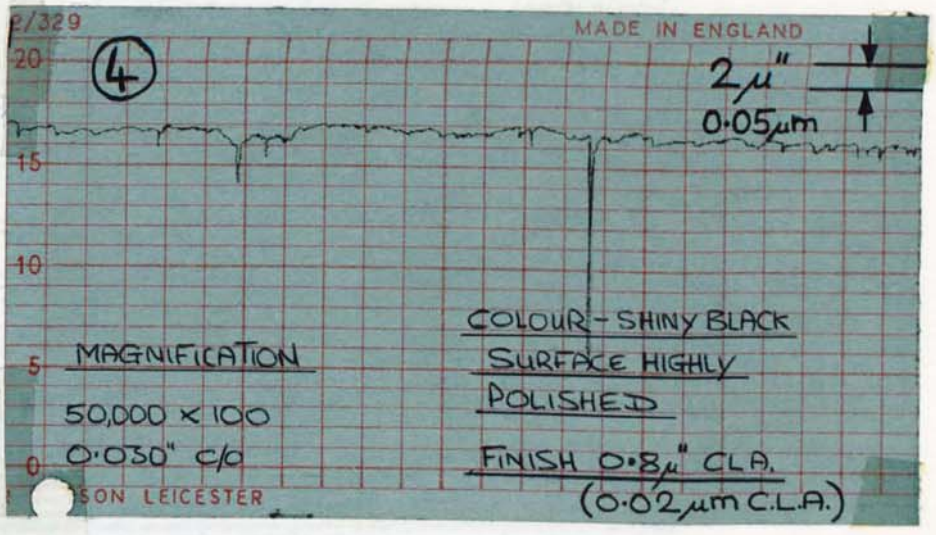

FIG. 56

DIAMOND POLISHING OF BORON CARBIDE ON A SOFT FOIL MATRIX

a) X 340

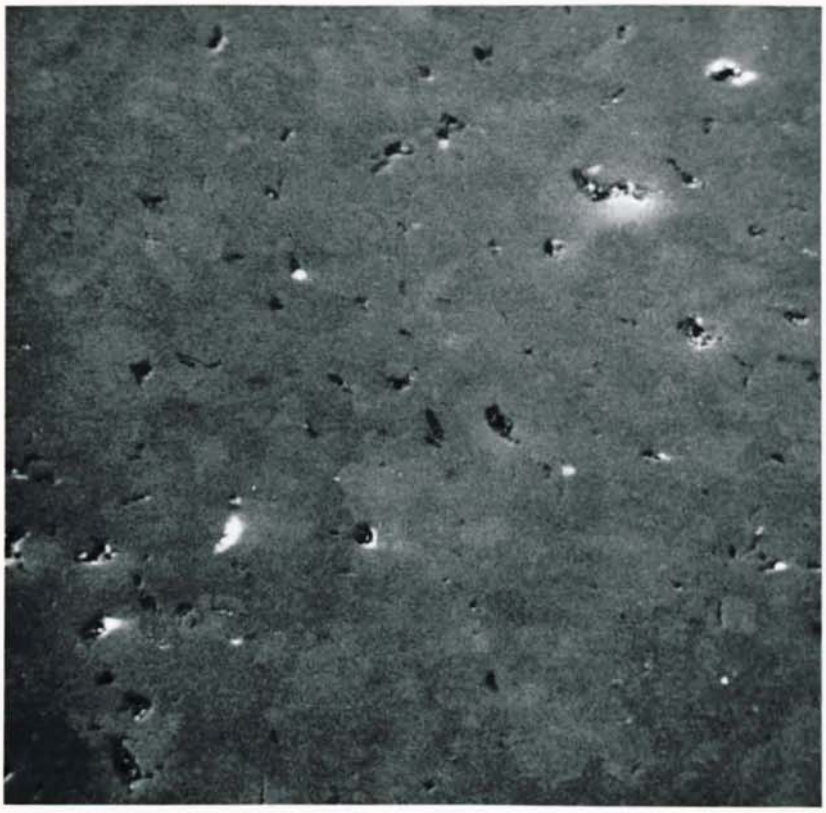

b) X 1,700

PLATE 38
STEROSCAN INVESTIGATION OF THERMO CHEMICALLY POLISHED BORON CARBIDE

c) X 3,300

d) X 33,000

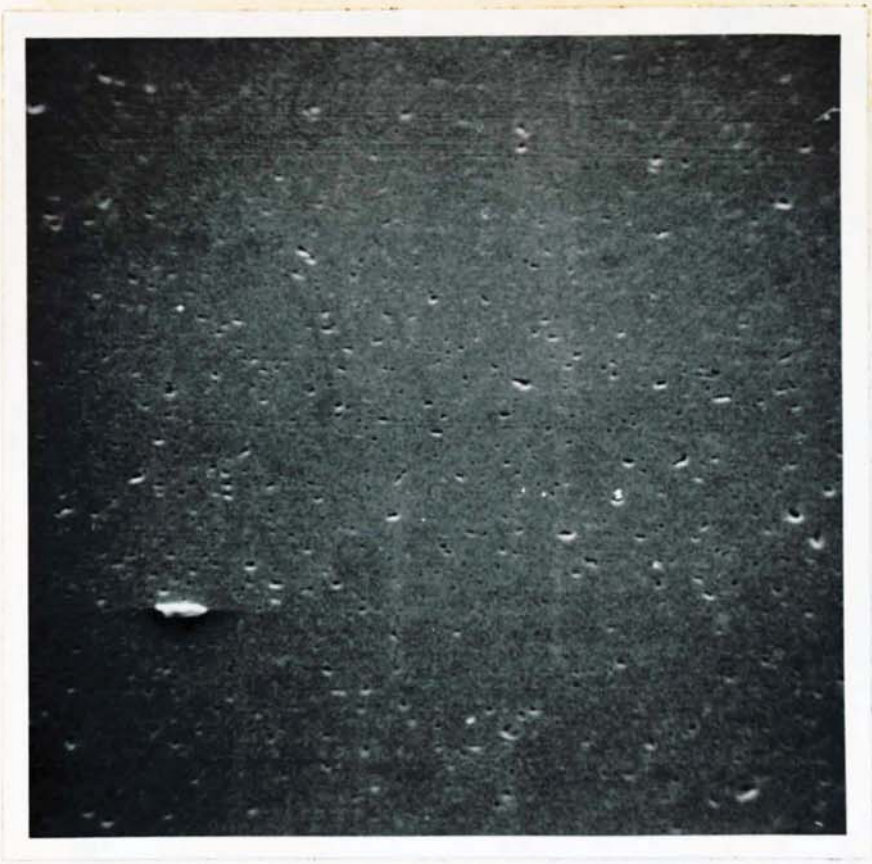

a) X 235

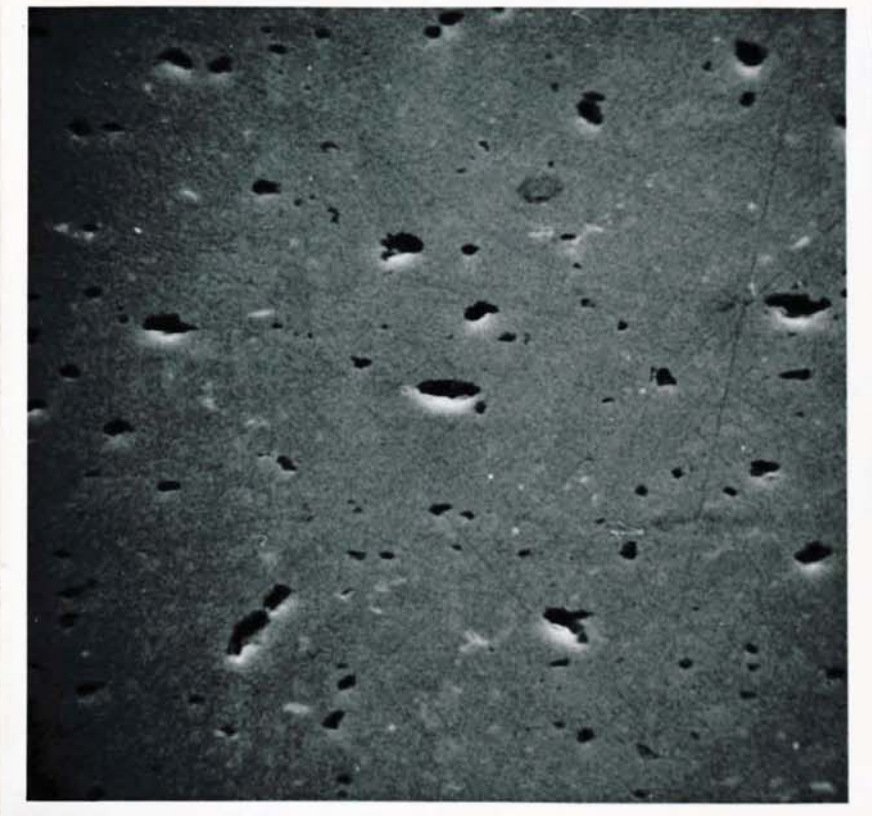

b) X 1,150

PLATE 39
STEROSCAN VIEWS OF BORON CARBIDE AFTER DIAMOND POLISHING ON A SOFT FOIL MATRIX

c) X 5,700

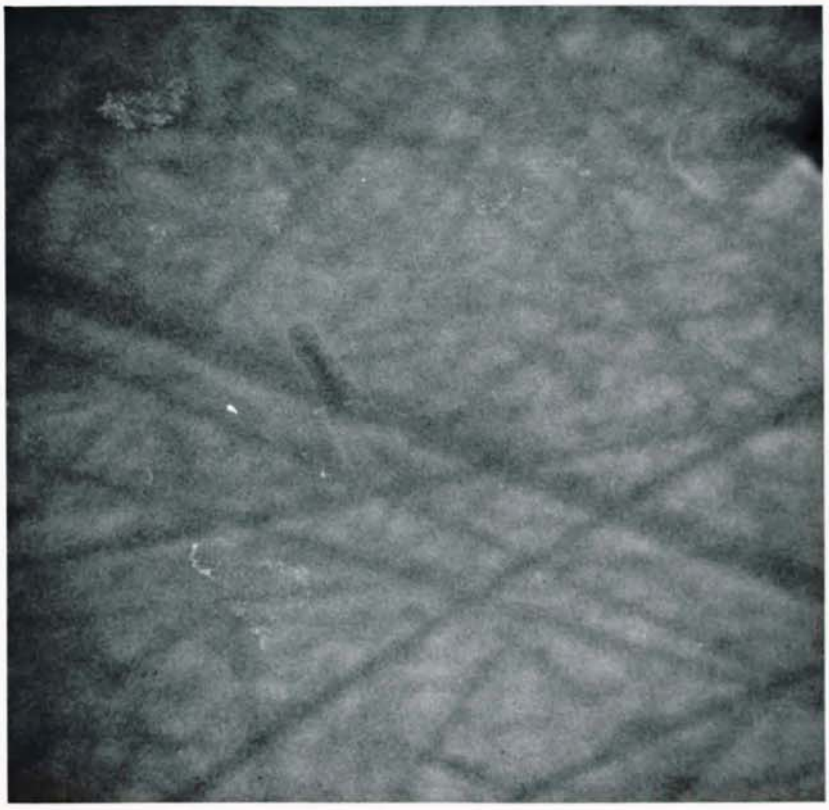

d) X 23,000

a) X 100

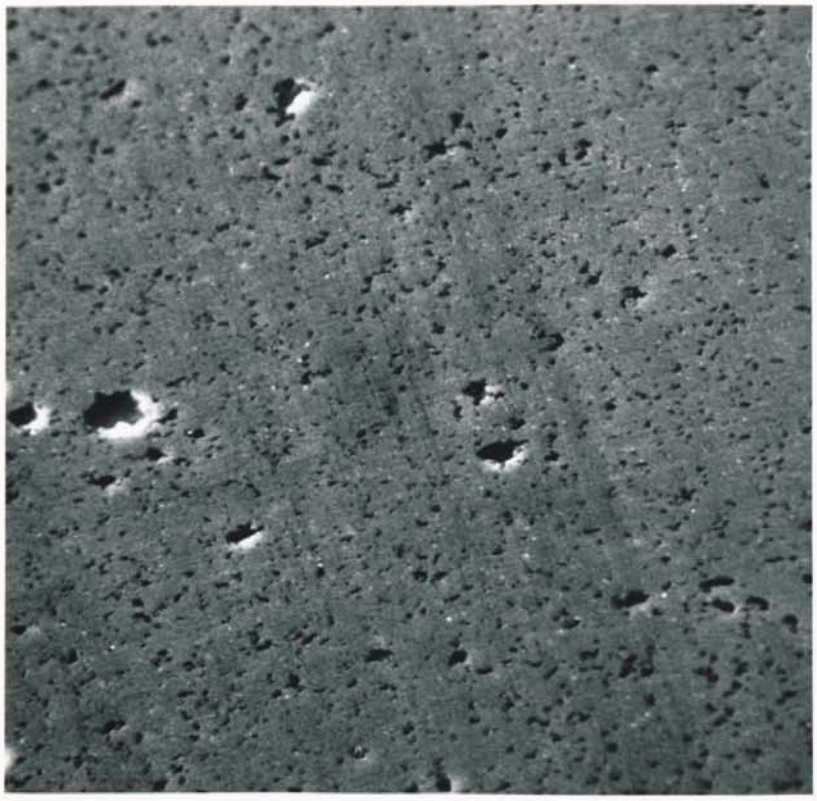

b) X 560

PLATE 40
STEROSCAN VIEWS OF BORON CARBIDE AFTER DIAMOND LAPPING (CONTAINED ABRASIVE) ON CAST IRON

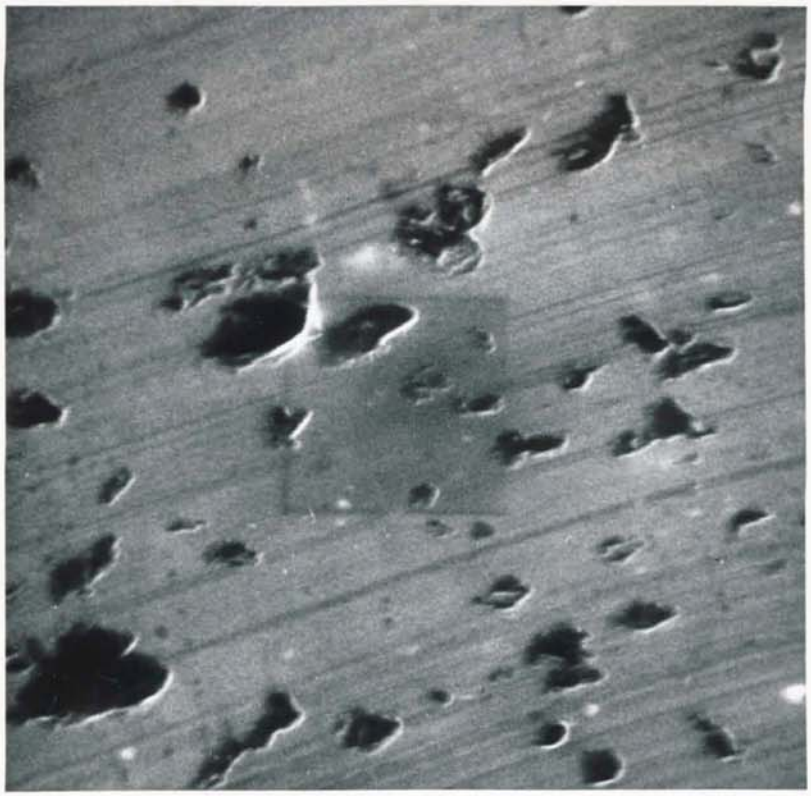

c) X 5,600

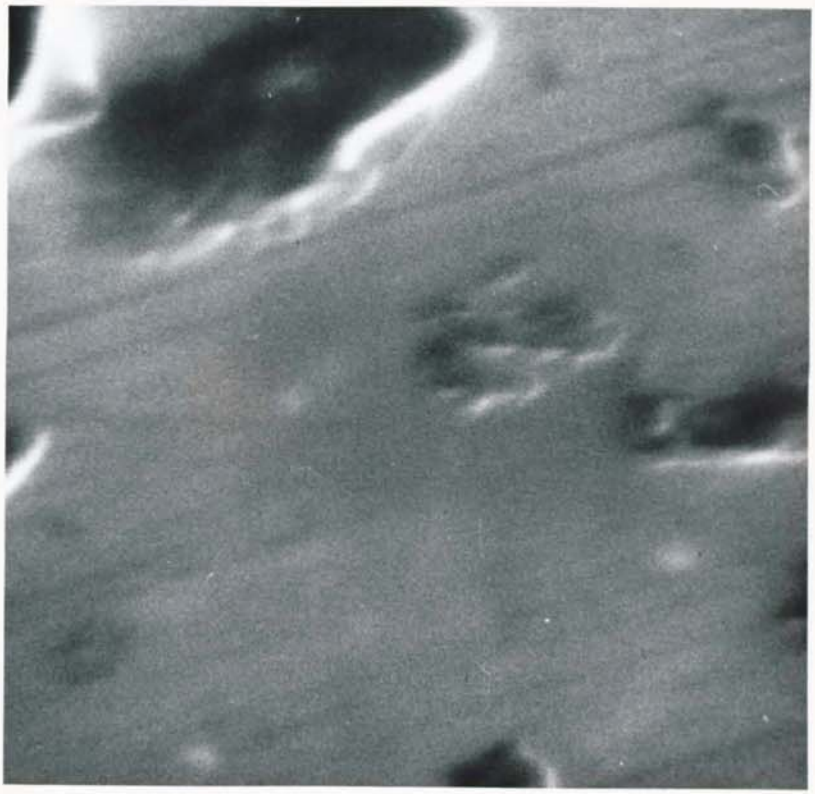

d) X 22,500

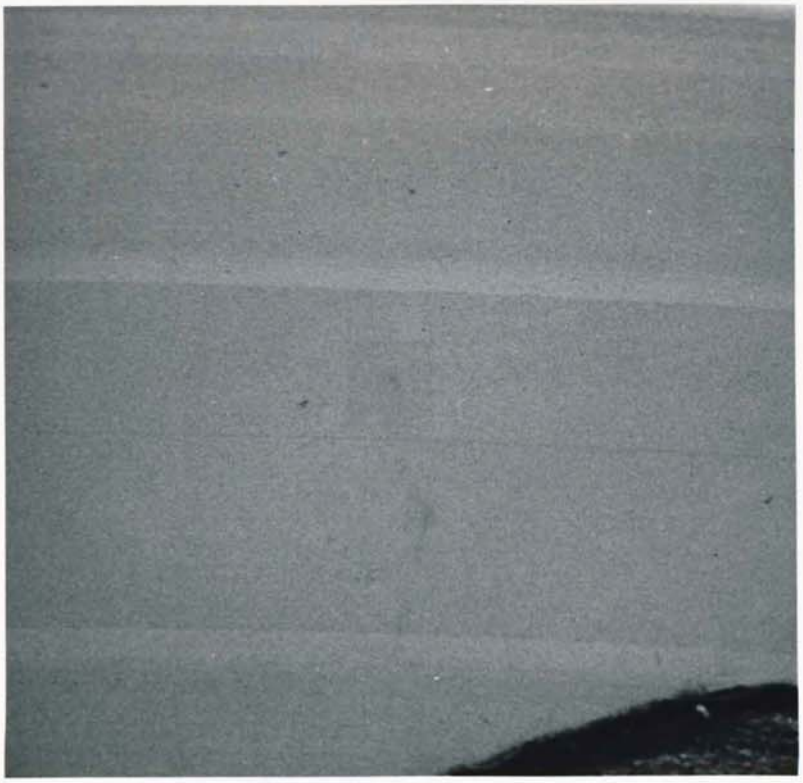

a) X 340

b) X 1,700

PLATE 41

STEROSCAN VIEWS OF A TUNGSTEN CARBIDE SURFACE AFTER DIAMOND POLISHING ON DRY CAST IRON

c) X 8,300

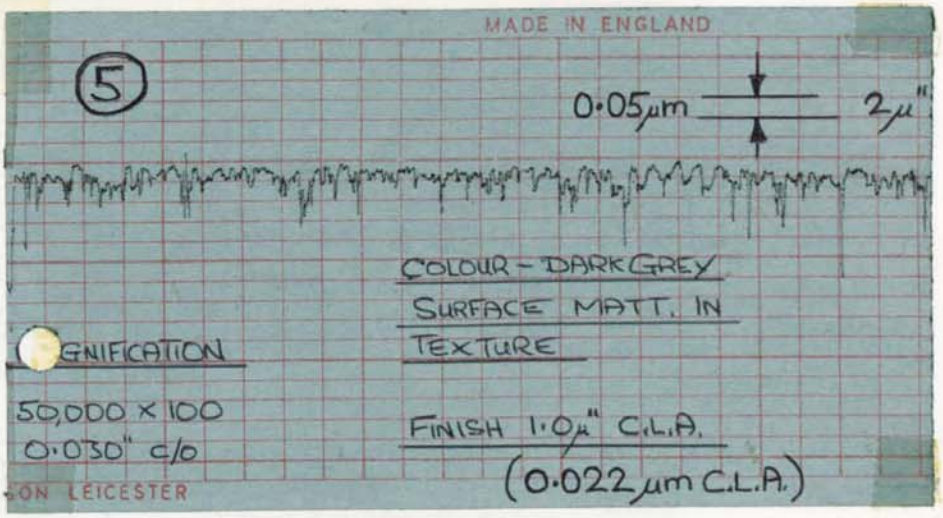

FIG. 57

CONTAINED ABRASIVE DIAMOND LAPPING OF BORON CARBIDE ON A CAST IRON MATRIX

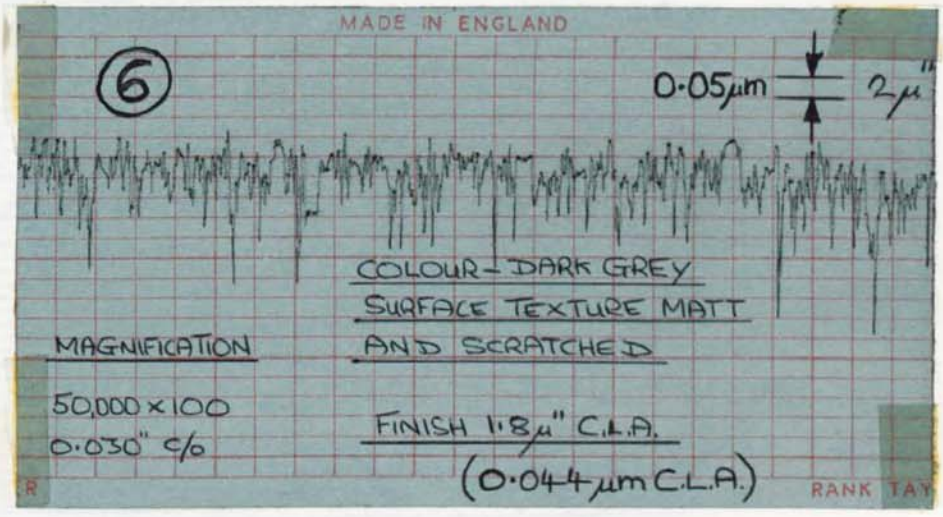

FIG. 58

FREE ABRASIVE DIAMOND LAPPING OF BORON CARBIDE ON A CAST IRON MATRIX

NOTE THE MANY DEEP SCRATCHES CAUSED BY ROLLING OF ABRASIVE GRAINS

a) X 235

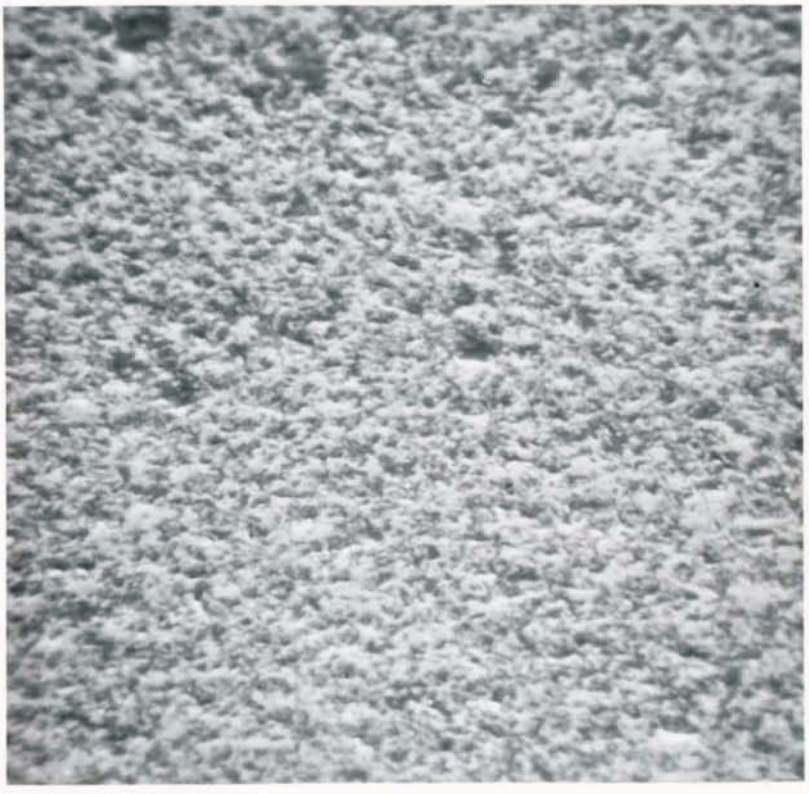

b) X 1,150

PLATE 42
STEROSCAN VIEWS OF BORON CARBIDE AFTER DIAMOND LAPPING (FREE ABRASIVE) ON CAST IRON

c) X 5,700

d) X 23,000

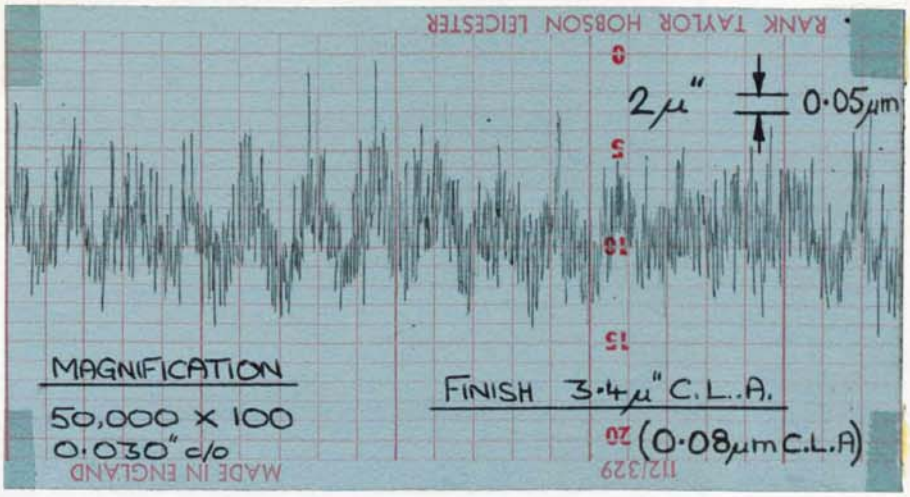

FIG. 59

GROUND FINISH OBTAINED FROM A HYDROSTATIC OIL BEARING WHEELHEAD (WHEEL GRIT SIZE 400)

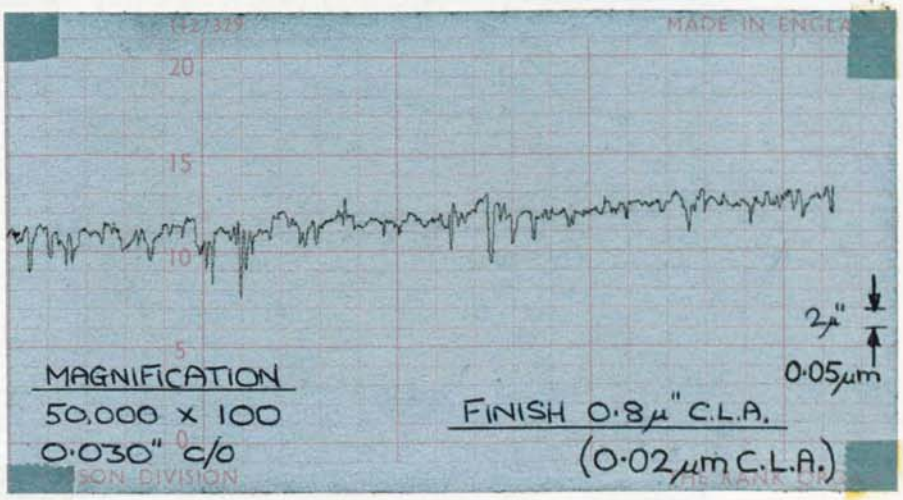

FIG. 60

GROUND FINISH OBTAINED FROM A HYDROSTATIC AIR BEARING WHEELHEAD (WHEEL GRIT SIZE 60)

a) X 32

b) X 158

PLATE 43
STEROSCAN VIEWS OF A BORON CARBIDE JOURNAL SHOWING GROOVE FEATURES AND SURFACE CONTAMINATION

c) X 160

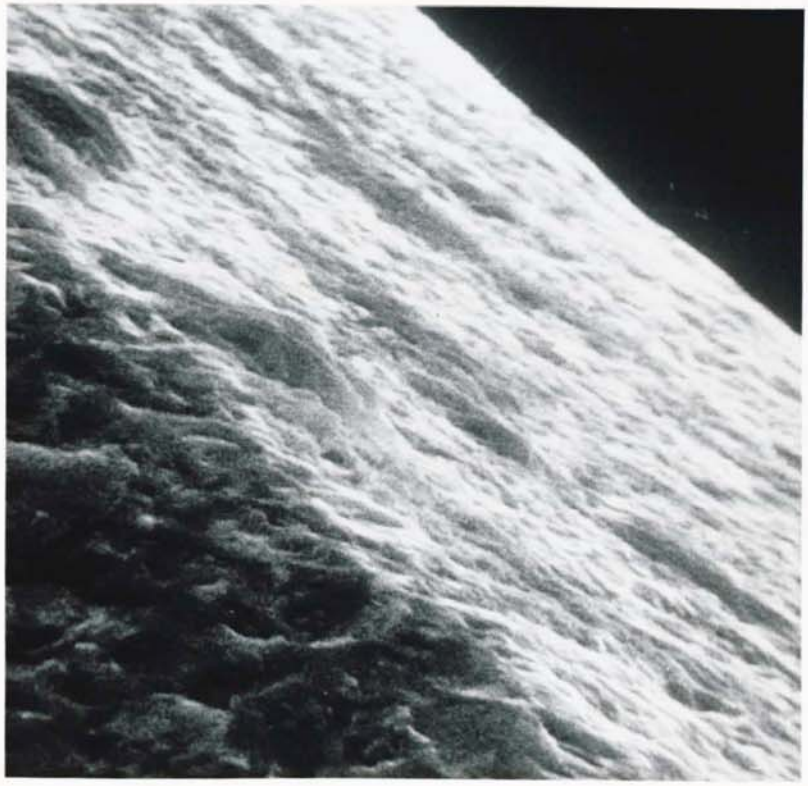

X 190

PLATE 44
STEROCAN PHOTOGRAPH OF A DIAMOND GROUND BORON CARBIDE SURFACE

7.3.1 Surface Finish and Texture (Continued)

different. This shows that C.L.A. readings alone are insufficient to determine the suitability of a surface finish for wear applications. Subtle changes in texture do result in very noticeable changes in colour and reflectivity, suggesting that optical measurements could provide a reliable method of assessment. Any conventional lapping or polishing process will tend to produce an assymmetric texture profile, where the protruding asperities are smaller in height than the surface depressions. Under wear conditions, this is clearly preferable to the symmetric texture profile produced by the grinding process.

In practice, the overall wear life of a bearing assembly is found (116) to be closely related to surface texture. While a coarse texture does not necessarily result in a low wear life, it does give a much wider scatter of performance under start/stop conditions. A sample of bearings whose surface finish corresponded to that shown in Figure 57 were found to have wear lives between 11,000 and 240,000 start/stop cycles, whereas those corresponding in texture to Figure 55 all completed at least 100,000 cycles under similar conditions. Plates 26 and 27 contrast components corresponding to the above surface textures. Wear damage on the irregular textured surface (Plate 27) is seen to be confined to the peaks of the asperities, while the very smooth surface showed no visible wear damage at all.

Where the texture of the wear surface has resulted in a series of sharp cutting edges, as for example in Figure 57, transfer films are sometimes obtained during rubbing contact with a softer material. Transfer films of tungsten carbide on boron carbide have been observed here and these usually coincide with an increase in friction coefficient.

Where a ground finish is used in a production instrument (100), there is clear evidence that the surface texture is at first unsuitable, and only improves after a lengthy running-in process. Case hardened steel journals are assembled into a bearing and subjected to 600 start/stop cycles, after which the bearing assembly is stripped, cleaned and fresh boundary lubricant applied.

7.3.1 Surface Finish and Texture (Continued)

This cycle is repeated until the friction coefficient remains constant over the wear period. The initial surface finish in this case is reported to be around 3μ inch C.L.A. (0·07 μm C.L.A) and the texture is presumably similar to that shown in Figure 59. Running-in is therefore flattening the highest peaks and producing an assymmetric texture profile similar to that observed in the lapping process. Only repeated cleaning and lubrication prevent cumulative damage by the wear debris.

Under overload conditions, qualitative tests (116) have shown that surfaces with a coarse texture (e.g. Figure 58) can occasionally shed a large wear particle, and that such a particle may prevent recovery of the bearing when the overload is removed. This has not been observed when testing very smooth ceramic surfaces.

The effect of surface finish and texture on storage life is less easy to predict. Wringing of slip gauges is found to become more difficult as the surface finish deteriorates, and from this observation, it can be concluded that long term molecular diffusion across a bearing interface is also reduced. True contact area is smaller and lubricant gas is trapped between the surfaces, thus preventing any large scale adhesion from taking place. This reasoning has often led to the choice of a ground finish where ferrous bearing materials are used and wringing/molecular diffusion effects are known to be pronounced. In section 7.2.2.2 it was shown that storage problems were not encountered on certain ceramic materials, even where very smooth surfaces were employed, and that this could be attributed to the higher bonding forces inherent in these substances.

Where the peak to valley height of the surface imperfections is an appreciable proportion of the local bearing clearance it is considered that pressure leakage will occur across the surface and at high pressure ratios, performance will be reduced. Any corresponding increase in take-off or reduction of overload capacity may reduce the wear life of the assembly. This brings

into question the practice known as 'nodular finishing', in which the softer matrix of a two-phase cermet material is buffed below the level of the harder ceramic grains to increase the effective hardness of the surface.

The preceeding discussion referred to the finish and texture of the wear surface but the surface finish at the base of any pumping grooves cannot be ignored. Here, the principal danger is belived to be that of residual debris from groove manufacture. This debris may be dislodged in service and cause premature failure. Removal of organic contamination is clearly more difficult on rough surfaces and its effect on operational life will be discussed in a later section. The merits of various groove cutting processes have been considered in Appendix IV., where it is shown that ion-maching leaves the surface totally free of loose debris and organic contamination. Plate 35 shows two such surfaces and should be compared with the texture of an electro-chemically etched groove shown in Plate 45. The latter shows many loosely attached grains and grain fragments, and the ragged profile presents a formidable cleaning problem. In Plate 35 (a) the shallow depressions result from preferential sputtering of various crystal orientations within the surface and the white objects are airborne dust and skin particles.

All the available evidence suggests that in order to achieve maximum operational life and reliability, each bearing surface should be finished to the smoothest possible texture, and that machining processes should be selected which leave the minimum surface damage and debris. This will minimise the friction coefficients and produce the smallest volume of wear product under all rubbing conditions. The only possible exception to this general rule is where surface finish below 1 μ inch C.L.A. (0·02 μm C.L.A.) may restrict the storage life of low melting point materials.

For journal bearings operating in a fixed attitude, the surface texture of the rotating member is considered to be more important than that of the fixed member, where only a portion of the surface is subjected to start/stop wear.

X 4,500

PLATE 45
STEROSCAN OF AN ELECTRO-CHEMICALLY ETCHED PUMPING GROOVE

X 740

PLATE 46
STEROSCAN OF AN ION MACHINED PUMPING GROOVE

7.3.1 Surface Finish and Texture (Continued)

This does not necessarily apply to flat thrust surfaces, or to journals experiencing whirl rubbing, where the entire surface of each component may contribute to the volume of wear product.

7.3.2 Roundness

The roundness of a bearing is defined as the total deviation of the wear surface from a true circle.

Roundness has not previously been considered to have a direct influence upon operational life. This is true once the rotor is completely airborne, but under take-off or touchdown conditions, large variations in roundness are believed to influence the wear life of the assembly.

Where roundness variations are confined to the stationary member of a journal pair, the rotor will touchdown normally where the touchdown area is undistorted, or prematurely where the contact point corresponds to a hump on the stationary shaft. When roundness variations are confined to the rotating member, hydrodynamic action will define the axis of rotation as coincident with the mean bore axis. Under touchdown conditions when $\varepsilon \to 1$, intermittent and abnormally fast contact is predicted between the most prominent point on the rotor bore and the journal shaft. These two situations are illustrated in Figure 61.

This intermittent contact may be more damaging to the bearing surfaces than a steady sliding action, where the wear will be spread over a larger proportion of the rotor surface. Repeated impacts may result in surface fatigue and the generation of abnormally large wear particles. The effect will be more noticeable during touchdown where the rate of angular deceleration, $-\frac{d\omega}{dt}$, is low, but will be less significant during the starting phase where $\frac{d\omega}{dt}$ is usually high. A similar situation will arise when the bearing is loaded to high values of ε in service and premature contact may then occur for $\varepsilon < 1$. The effect of hollows in an otherwise circular surface is not as obvious and will depend very much upon their proportions. In general, small hollows may be expected to have a negligible effect, whereas small humps will be significant.

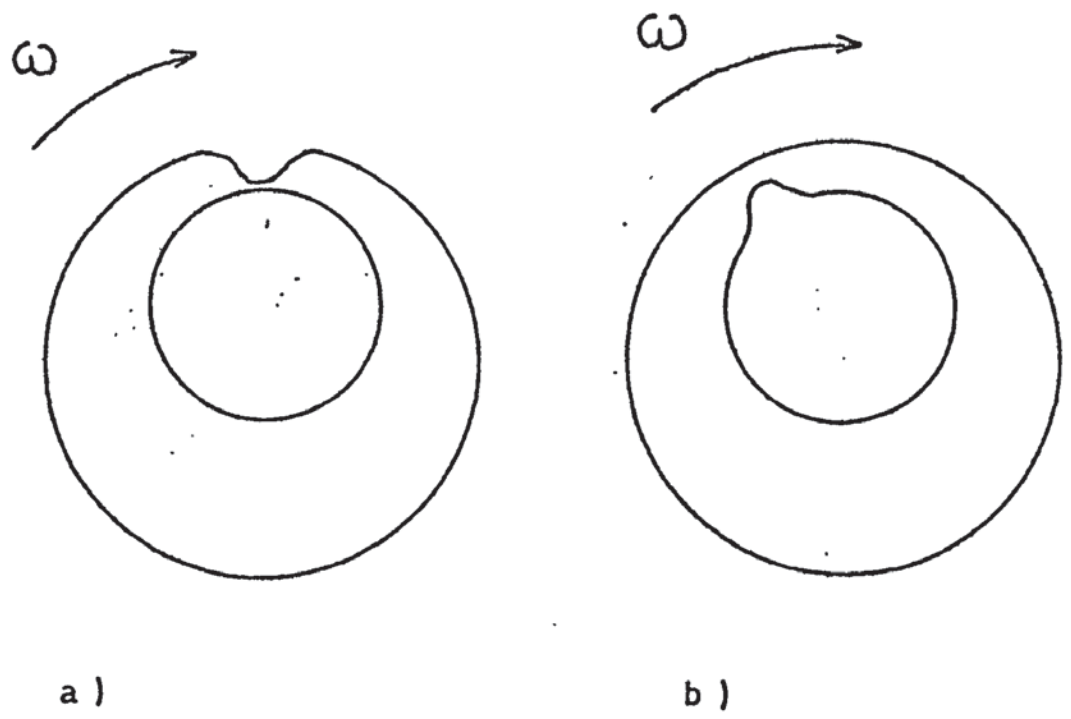

FIG. 61
THE INFLUENCE OF ROUNDNESS ON BEARING CONTACT.

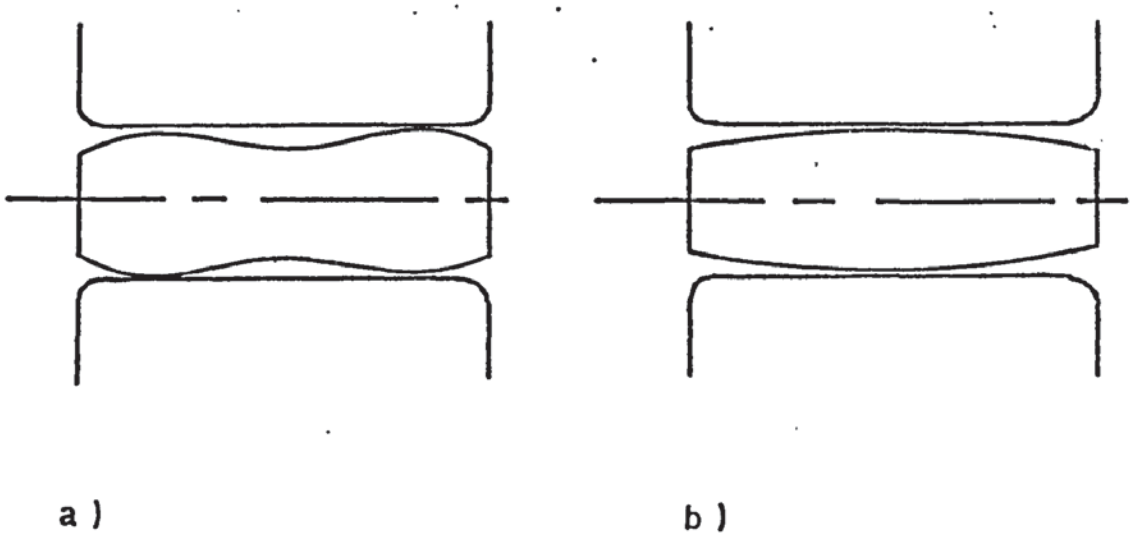

FIG. 62
THE INFLUENCE OF SHAFT GEOMETRY ON BEARING CONTACT.

7.3.2 Roundness (Continued)

For bearings in which the inner member rotates, a comparable situation will occur.

In practice, the concept of a single hump or hollow is unrealistic and a number of these features are usually detected around each bearing surface. Contact conditions will then be more complex but the principles outlined above should still apply.

Experimental investigations herein (section 6.1.) have shown that intermittent contact does occur during the rundown period, and that the effect is very marked where large roundness errors are present on the rotating member. Contact did not occur at each revolution as might be expected from the simple model illustrated in Figure 61, where ω decays and ε progressively increases with each rotation. The rotor apparently regained its fully airborne state for an appreciable period between each impact (see Figure 14) and a later study of the wear damage did not indicate that the obstruction had simply been swept aside on each occasion. To explain this discrepancy, consideration must be given to the extended Adhesion theory of friction (31), in which it is assumed that 50% of the asperity contacts between two surfaces are elastic. This is considered to account for the rotor bouncing during the touchdown period, - rather like an aircraft landing on an uneven runway.

Current manufacturing techniques normally allow the roundness of both journal components to be controlled to exceptionally close limits, as illustrated in Figure 63. On bearings of this quality, intermittent contact prior to touchdown has not been detected. Statistical analysis has shown no significant correlation between roundness of this order and either bearing failure or run-down time. (See section 6.5.).

Roundness is seen to be of some importance to both start/stop and overload life. It is believed to be more important on the rotating member than on the stationary one, but in both cases, the touchdown and take-off speed increase with the roundness error.

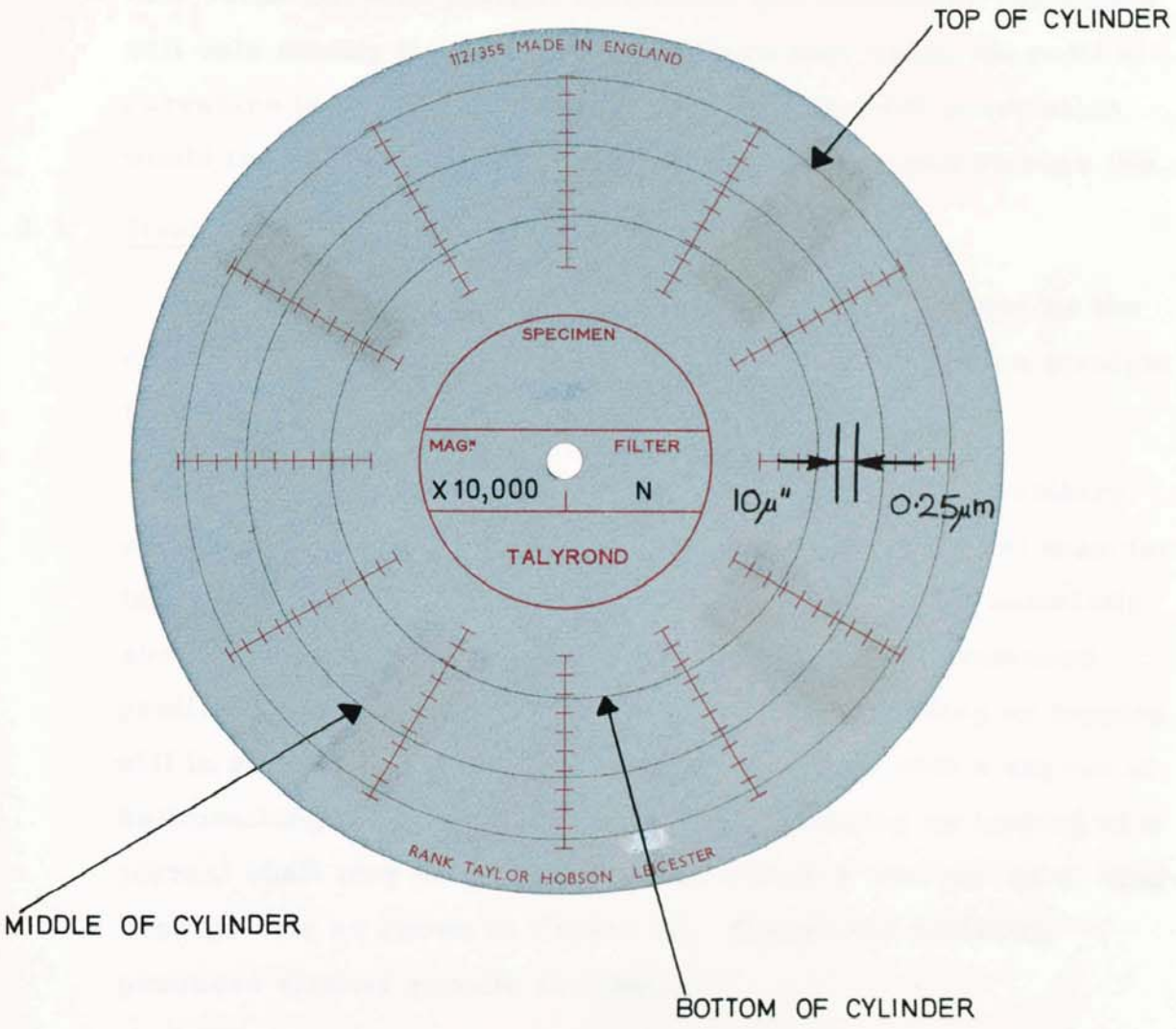

FIG. 63

THREE ROUNDNESS TRACES FROM A TYPICAL JOURNAL BEARING

7.3.2 Roundness (Continued)

Experimental evidence suggests that premature contact will be insignificant if roundness errors do not exceed 5% of the mean radial clearance. Under storage conditions, point or line contact may occur between journal members, and roundness variations will only modify this contact area where they cause the radii of curvature to be equal and coincident. No general correlation would therefore be expected between roundness and storage life.

7.3.3 Straightness

The straightness of a journal bearing is defined here as the deviation of the axial profile of the wear surface from a straight line.

While in theory, a bearing surface could have any arbitary straightness profile, in practice it is found that current manufacturing techniques (Appendix IV) produce several characteristic shapes. All tend to have circular symmetry and a radiused profile at the boundary of the surface. Bore grinding or lapping will in general result in a straight central area with a degree of bellmouthing at either end. Cylindrical grinding or lapping of a journal shaft may frequency produce either a 'Barrel' or a 'Dog-bone' profile as shown in Figure 62. Controlled polishing produces similar results to lapping.

Like roundness, errors in straightness are thought to result in premature contact under high eccentricity conditions, for the bearing's load capacity and touch-down speed are related to the mean radial clearance rather than to local clearance. Take-off and touch-down speed should therefore increase with the straightness error and start/stop wear should be proportionately greater. Unlike roundness, straightness is considered equally important on both the fixed and rotating surfaces.

Perhaps the most important feature of bearing straightness is that it defines the point or points of contact under touchdown conditions. Where the component is Barrel-shaped as in Figure 62 (b), normal touchdown or radial overload contact will occur at the shaft centre, while contact due to angular misalignment will

7.3.3 Straightness (Continued)

take place at either end of the component. In the case of a 'Dog-bone' profile illustrated in Figure 62 (a), all three forms of contact will occur at approximately the same position, a short distance from each end of the shaft and rotor. Although in this latter case the wear will be shared between two areas of the bearing, there is the added possibility that overload damage due to angular misalignment will impair the starting ability. In each case, the bell-mouthing of both rotor and shaft will help to prevent rubbing contact by the sharp corner of the rotor bore. This form of contact is found to be particularly destructive under angular misalignment conditions and a polished radius is frequently introduced at each end of the rotor bore as an additional precaution.

Where a partially grooved journal is employed, bearing straightness will determine whether rubbing contact occurs over the grooved or the ungrooved region, and the relative merits of each case are discussed in section 7.3.12.

In practice, the axial position of the wear scar corresponded exactly to the known straightness profile on all the experimental bearings examined, and the wear damage illustrated in Plate 27 represented a 'Dog-bone' straightness of 7 micro inches (0.18 micrometres).

Statistical analysis reveals no significant correlation between straightness and either bearing failure or run-down time over the range of variation examined (see section 6.5). Figures 64 & 65 show the order of straightness tolerance that can be maintained by current manufacturing methods.

Straightness errors prevent full line contact between rotor and journal under storage conditions, and an improvement in storage life could be expected where this life is limited by molecular diffusion across the interface.

7.3.4 Parallelism

Parallelism of a journal component is defined as the divergence between two straight lines drawn axially through the mean wear

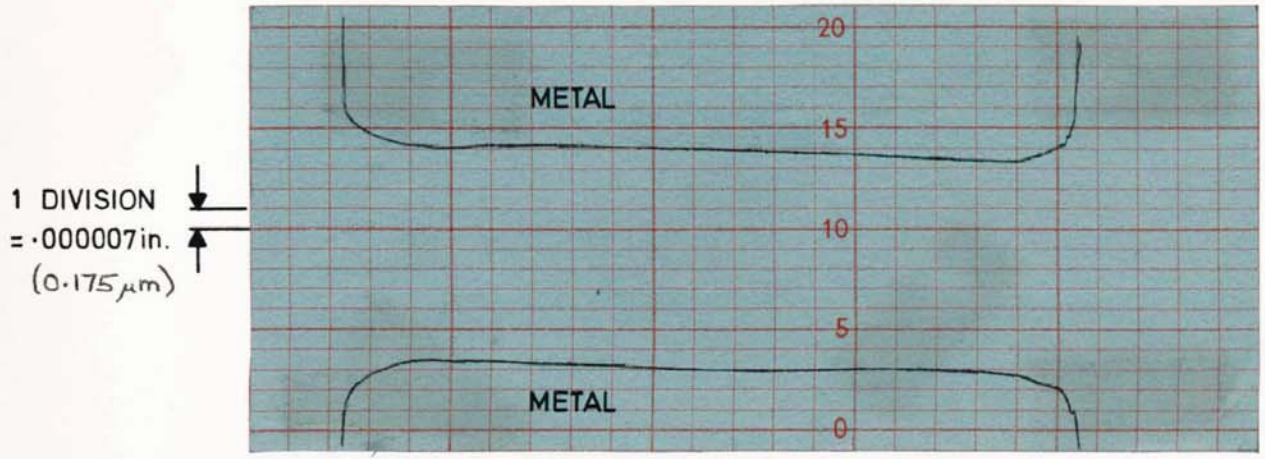

VERTICAL MAGNIFICATION X 14,000

FIG. 64

TYPICAL ROTOR BORE STRAIGHTNESS AND PARALLELISM TRACE

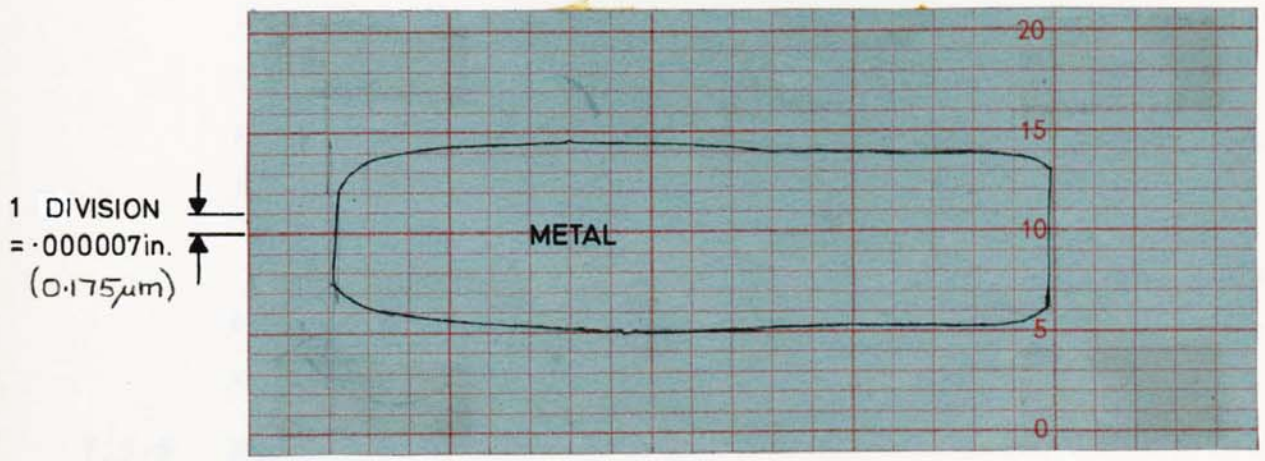

VERTICAL MAGNIFICATION X 14,000

FIG. 65

TYPICAL JOURNAL SHAFT STRAIGHTNESS AND PARALLELISM TRACE

7.3.4 Parallelism (Continued)

surface at each end of a diameter.

Errors in parallelism will in general produce an axial variation in bearing clearance. This variation may be either accentuated or cancelled out if similar errors are present in each mating component. Where the bearing rotor can be assembled in either direction, appreciable differences in mean radial clearance can result.

Like roundness and straightness errors, lack of parallelism will result in premature contact under high eccentricity conditions, and in addition, will cause a symmetric loss of slew capacity if misalignment contact takes place at the position of minimum radial clearance.

Where pumping grooves are present, an axial variation in clearance will cause unequal pumping. This is because optimum pumping will only occur at a fixed ratio of h_g/C (91). Trevorrow (80) has shown that axial flow will reduce the performance of the associated thrust element, though he considers the assymmetric pumping as due to thrust clearance variations alone.

Axial flow, however caused, has been shown (80) to reduce the overall performance of the bearing and increase the likelihood of overload. It also brings with it a more insidious problem; ingestion of external contamination. This contamination is considered to play an important role in deciding the overall operational life and reliability, and will be discussed in detail in sections 7.14., 7.18. and 7.19.

Experimental investigations here have shown no statistical correlation between shaft parallelism and the time taken for the rotor to coast to rest from synchronous speed. (See section 6.5).

7.3.5 Flatness

Flatness is defined as the total deviation of the wear surface from a true plane. Flatness variation over the component is referred to as its 'figure'.

7.3.5 Flatness (Continued)

In order to maintain design clearances, a high order of flatness is required on the thrust surfaces of a typical H-form bearing. This flatness can be achieved by either grinding (using an air bearing wheelhead) or lapping, but each method of manufacture leaves its own characteristic 'figure'. Where lapping methods are employed, the finished surface is invariably either convex or concave, and has circular symmetry about a central axis perpendicular to its mean plane. This axis would normally correspond to the spin axis of the rotating element. In contrast, a surface-ground component does not have circular symmetry but is often symmetrical about a diameter of the surface.

The 'figure' of a thrust surface will determine both position and area of contact, unlike a journal bearing where only line or point contact can occur. Where one surface is concave, contact will occur at the maximum possible radius, whereas if one surface is convex, the radius of contact will be minimised. For the design of bearing under consideration, line contact will occur in each case. Under starting conditions the friction arm, and therefore the friction torque, will vary by a factor of two or more between the best and worst case. This variation will be proportional to the ratio of thrust diameter to journal diameter.

If synchronous contact takes place, the rubbing velocity will be directly proportional to the radius of contact. Any increase in rubbing velocity will increase the likelihood of surface damage as discussed in section 7.2.2.2.

Where both mating surfaces are perfectly flat, area contact will occur over the entire thrust surface. It has been found (84) that this condition can promote 'wringing' as relative motion occurs between the surfaces during contact. Susceptibility to 'wringing' will also depend upon material properties, surface finish and specific loading, but if it should occur, it may not be possible to re-start the bearing.

7.3.5 Flatness (Continued)

'Wringing' can also occur slowly under storage conditions and the shelf life of the assembly may be impaired as the effective level of starting friction rises.

To overcome the disadvantages of high starting friction, high rubbing velocity and 'wringing', thrust bearings are often designed where one or both rubbing surfaces are 'crowned' (84). Deliberate 'crowning' can be accomplished by biasing the lapping or polishing process to produce a surface with a symmetrical convex 'figure'.

While 'crowning' reduces both contact area and friction radius, it has the disadvantage that a corresponding reduction in performance will also occur. This loss of performance will be most evident at low running clearances where touchdown and take-off speed will be increased. Wachmann & Malanoski (34) have analysed the load loss due to thermal distortion, but their results should be equally applicable to 'crowned' bearing surfaces, which are of a similar shape.

Where operational life is under consideration, the numerical value of flatness is seen to be of lesser importance than the surface 'figure'. Those manufacturing techniques based upon lapping are believed to offer many advantages, because they can produce an axially symmetric 'figure' of a pre-determined magnitude and sense. This is not true of a surface ground component where the axially assymmetric 'figure' can allow contact over an undefined region of the thrust surface. For those bearings where thrust contact is inevitable, a slightly convex thrust surface does appear to be advisable if wear life and reliability are important, but it is suggested that the degree of crowning be no greater than is geometrically necessary to define the desired contact condition.

7.3.6 Squareness

Squareness of each thrust surface is defined with respect to the journal bearing axis.

7.3.6 Squareness (Continued)

The most immediate effect of poor squareness of a fixed thrust element will be an assymmetric loss of maximum slew capacity as the rotor attempts to support a misalignment torque. Misalignment in one sense may bring the opposing thrust surfaces closer to parallelism, while misalignment in the opposite direction will eventually cause premature contact and high speed rubbing as the non-parallel surfaces move further apart.

Where a start/stop capability is required from a thrust surface, squareness errors, like certain types of flatness error, will clearly increase the friction radius and rubbing velocity. Rubbing velocity and heat generation will also be increased during axial overload at synchronism and wear will be concentrated on a limited portion of the stationary member. Wear on the rotating member will occur around its complete circumference. Crowning of one thrust surface will help to prevent premature contact but can only combat very small errors in squareness.

Where squareness errors are present on the rotating member alone, the loss of slew capacity will be symmetric and rubbing wear will be confined to a small portion of this component. Any corresponding wear pattern on the stationary member would be expected around its entire circumference.

Squareness errors on a stationary member alone must result in a change in pumping efficiency across the diameter of a grooved thrust plate as the thrust clearance changes. This is because optimum pumping will only occur at a fixed ratio of $\frac{C + h_g}{C}$ (84). The resulting diametral pressure difference will exert a small misalignment torque on the spinning rotor, but this misalignment is considered to be negligible in rate gyro applications.

Squareness errors on the moving member will produce a swash action as rotation occurs and Nahavandi and Osterle (18) have shown that this swash action alone is capable of generating support pressure against an ungrooved thrust surface.

In practice, squareness errors are usually present on both fixed and moving members and the situation is more complex

7.3.6 Squareness (Continued)

than suggested, though wear patterns similar to those described have occasionally been seen here on experimental bearings (116) where relatively large errors have been restricted to one component. Experimental measurements of maximum slew capacity by the writer have always shown a degree of assymmetry. In some cases, this has been as high as 30%, but has often been traced to poor assembly squareness of a fixed thrust member.

For maximum wear life and resistance to gyroscopic torque loads, close control is concluded to be essential over both machining and assembly squareness (see Figure 66). In reality, it is one of the most difficult parameters to control, and is a major mechanical limitation to the manufacture of very small thrust clearances.

7.3.7 Overall Dimensional Tolerances

These are considered to have no practical effect upon either operational life or bearing performance. This is due to the fact that all diameters and lengths must be closely controlled for tooling purposes during manufacture, and the resulting dimensional variations are less than 0.1%.

7.3.8 Journal/Thrust contact conditions

For any given H-form configuration, it can be shown that there will be a ratio of journal to thrust clearance for which simultaneous journal and thrust contact will occur under angular overload conditions. Above this ratio, slew contact will occur between the thrust surfaces, while below it, only journal contact may take place.

If high speed thrust contact due to misalignment can be prevented in this way, many of the problems associated with squareness and flatness errors will be avoided. The smaller journal radius will ensure a minimum rubbing velocity but any generated wear debris will be less easily accommodated. On balance, journal contact appears to be preferable in theory and in practice, and a smaller volume of wear product is generated in this case.

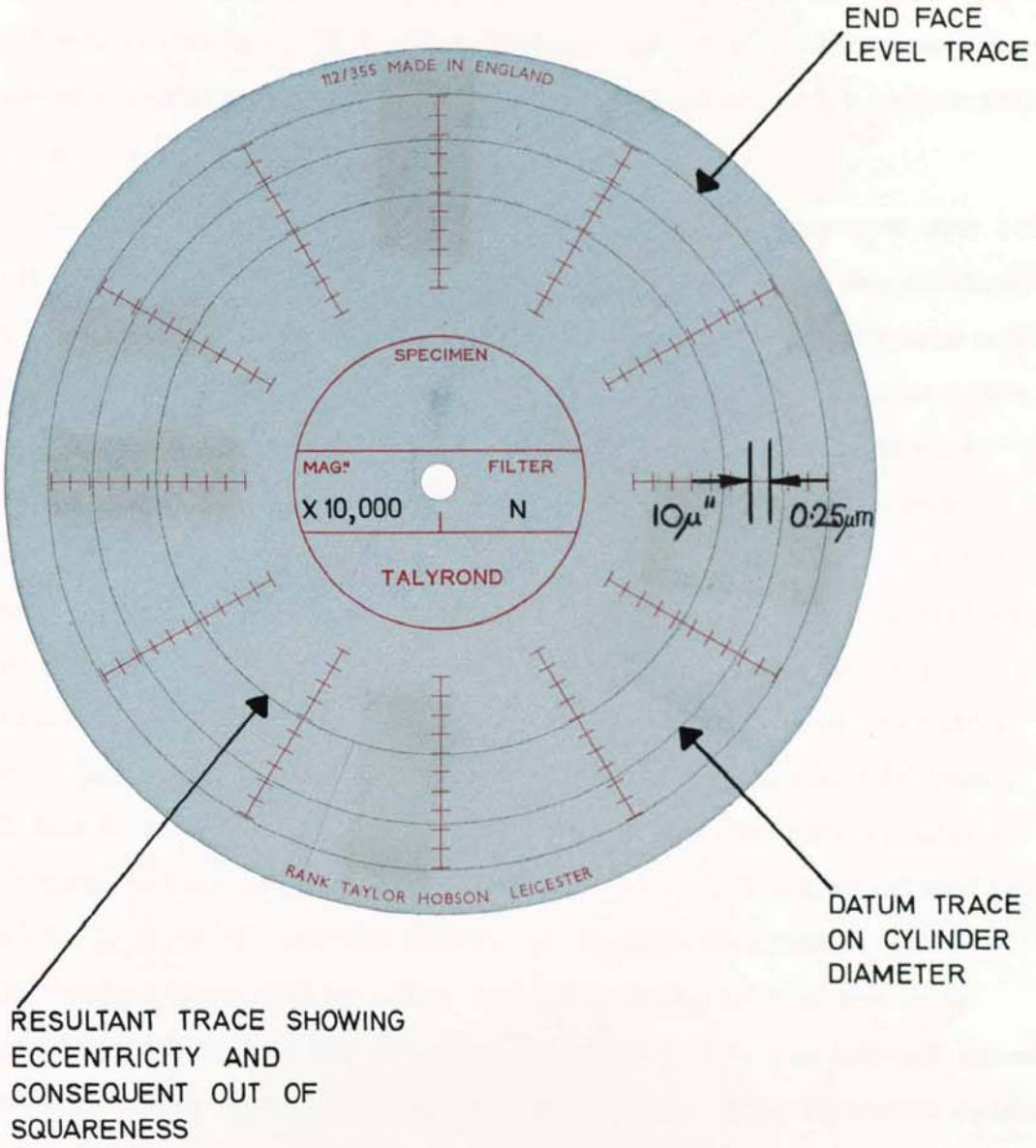

FIG. 66

END FACE SQUARENESS TRACE OF A TYPICAL BEARING ROTOR

7.3.9 Bearing Clearance

The range of radial and axial clearance that can be used in gyro bearings is very limited. Below 40 micro-inches (1 micrometre) clearance, manufacturing problems are significant, while above 150 micro-inches, (3.6 micrometres) bearing performance is usually unacceptable. All known gyro bearings work within this range.

In order to minimise start/stop wear, it is proposed that each clearance should be as small as possible, allowing the minimum rotor speed to be maintained prior to contact and after take-off. It has also been suggested that smaller clearances are to some extent self-sealing, and will prevent the ingress of external foreign matter, though this view does not support rigorous inspection since any gap will accept particles of sufficient size to jeopardize that particular bearing (Assuming a linear distribution of particle size). On the other hand, a small clearance will be more readily blocked by internally generated debris, and will only be practicable where the volume of wear product is small. It has been shown in sections 7.2 and 7.3.1 that this volume is determined principally by the properties of the material and it's surface texture. As the clearance volume increases, an increased time will be taken for the bearing to become fully pressurised and at high angular accelerations, the lift-off speed will increase beyond the touch-down value. Experimental evidence of this effect has been discussed in CHAPTER 6 and for minimum wear damage, the clearance volume should therefore be small.

In general, a reduction in bearing clearance will clearly be accompanied by a considerable improvement in load capacity and stiffness, and the likelihood of accidental overload will be reduced. If overload should occur, the previous comments relating to the volume of wear product will again apply. Where clearances fall below 50 micro-inches (1.3 micrometres) and the gap is comparable with the mean free path of the gas molecules, slip flow can occur and the resistance to overload will start to diminish in comparison with the theoretical value.

7.3.9 Bearing Clearance (Continued)

Wood (14) has proposed a simple design rule from which the loss in load capacity can be estimated.

Predicting the effect of clearance on storage life is more difficult and no experimental evidence is available. As the journal clearance is reduced, the shaft and bore radii approach a common value and for a finite level of surface roughness, the effective contact area must increase. This suggests a decrease in shelf life, but over the range of clearances available, the change may be negligible.

For the maximum operational wear life, it is therefore considered that all bearing clearances should be maintained at the smallest possible value consistent with material properties and manufacturing limitations.

7.3.10 Groove Depth

Where pumping grooves are formed on either thrust or journal surfaces, groove depth may be optimised to give either maximum load capacity or maximum stiffness (13) (91). Optimised depth will be a linear function of running clearance; normally taken to be the mean radial or axial clearance of the assembly. This arrangement will provide maximum rotor support where $\varepsilon \to 0$ but where $\varepsilon \to 1$, the contribution due to the pumping grooves will decrease, and any nett improvement will be due to the reduction in local running clearance. It follows that groove depth may be optimised for some value of $\varepsilon > 0$, and that such an arrangement will provide better rotor support at small running clearances. In this way, the theoretical take-off and touch-down velocities will be reduced and the ability to withstand overload will be improved. The arrangement might be expected to be most effective on the thrust surface, where axial loads allow the surfaces to remain parallel, less effective on a radially loaded journal and relatively ineffective under angular misalignment conditions, where only a small portion of either clearance is significantly reduced.

7.3.10 Groove Depth (Continued)

Experiments (116) have confirmed that no increase in maximum slew capacity is obtained by reducing below the optimised (84) (30) (13) value either journal or thrust groove depth, and any reduction in journal touch-down speed appeared to be masked by normal variations in parallelism. Thrust contact speed could be reduced by a factor of two by optimising for half the nominal clearance, but only if squareness and flatness tolerances were closely controlled.

As the depth of the pumping grooves is increased, the pressurized volume within the bearing becomes larger. On bearings where the initial rate of angular acceleration is high, this increase in volume may increase the lift-off speed as discussed in CHAPTER 6, and is an additional argument for keeping all groove depths to a minimum.

The foregoing discussion assumes that no other claims are made on groove depth, wheras in practice, this may not be the case. Inertial quality instruments are frequently required to have isoelastic bearings with linear load-deflection curves, and their groove depths are often tailored exclusively to meet these requirements.

In certain circumstances, it is seen that a reduction in groove depth can assist in reducing start/stop wear, but groove depth will have no influence upon continuous running or storage life. From the results of Whitley and Williams (30) it can be deduced that for spiral thrust grooves it is marginally better to over estimate the optimised depth at any chosen clearance if load capacity and stiffness are of prime importance.

7.3.11 Groove Profile

Groove profile has been the subject of widespread debate in recent years, closely reflecting the manufacturing difficulties and costs of producing a perfectly rectangular groove section, upon which most analytic methods are based. Elrod (61) has frequently stated that wide deviations from this classical shape are possible before the bearing performance is significantly

7.3.11 Groove Profile (Continued)

degraded, and analysis by Trevorrow (15), together with practical work by Patterson (65) have generally confirmed this view.

Where relatively ductile materials are employed, the upper corner of a groove may remain sharp without undue detriment to wear life. On brittle ceramic components, this sharp edge is generally considered to be highly undesirable, since under wear conditions it will crumble and introduce large abrasive particles into the bearing clearance. Denhard (77) has also encountered this problem and was obliged to choose a somewhat softer material for the bearing surface. Sharp ceramic corners may be radiused by buffing but control is difficult and the overall geometry and finish may be impaired. Where large numbers of grooves are involved, an uncontrolled edge radius will result in poor control of the effective groove/land width ratio, and rotor support will decrease rapidly as this parameter is reduced from its optimum value (30). Under take-off or touch-down conditions, it is probable that a radiused groove edge will provide additional rotor support as the moving surface drags gas from the main groove volume into the smaller wedge-shaped volume formed over the leading edge of the land. This additional method of pressure generation may well be more effective than the conventional pumping groove action where the bearing clearance is reduced to zero, and may help to explain the apparent ease (84) with which take-off can be achieved from a thrust bearing where the groove depth has been optimised for the mean axial running clearance. No previous reference has been seen to the groove radius behaving in this manner, and if the assumption is correct, further investigation is warrented.

The lower corners and base of a pumping groove are less important than the upper edges, but may provide a serious source of loose debris and contamination if very uneven (see section 7.3.1).

Plates 43 & 46 show typical groove profiles resulting from the ion-machining process.

7.3.11 Groove Profile (Continued)

Plate 46 clearly shows the radiused upper groove edge, together with part of a wear track passing over this edge. No breakdown of the corner is apparent, and this groove should be compared with one produced by more traditional methods in Plate 45. Here, debris from the corner has caused severe scratching over the land region. Figures 67, 68, 69 & 70 compare the base profile obtained by three different manufacturing methods, and the superiority of ion-machining is again clear.

It is considered that any justification for seeking a good groove profile should be based not upon performance criteria alone as has previously been suggested, (65) but on wear life and freedom from spontaneous generation of debris in service. In this respect, a smooth profile approaching that shown in Figures 67 & 68 is believed to be desirable. Ion-machining will produce the nearest approximation to this shape, and the process may be programmed to machine the upper edge radius directly without the need for subsequent buffing.

7.3.12 Groove Pattern

At high values of Λ, the radial support of a grooved journal bearing is known to be considerably greater than that provided by the equivalent plain bearing, but at very low values of Λ the ungrooved bearing may have a superior load capacity (10). Grooving therefore provides the bearing with a considerable resistance to overload, but does not necessarily reduce the rubbing velocity during the start/stop period. Where a groove pattern covers the entire journal area it is well known that the maximum possible stiffness can be achieved, whereas partial grooving will provide a higher load capacity. Full grooving will also provide the maximum level of stability and protection against whirl induced rubbing, but increases the pressurised volume of the bearing (see CHAPTER 6).

When a plain journal bearing is subjected to vibration during storage, squeeze-film action (119) will often protect the bearing surfaces from damage over a wide range of amplitudes and frequencies (116).

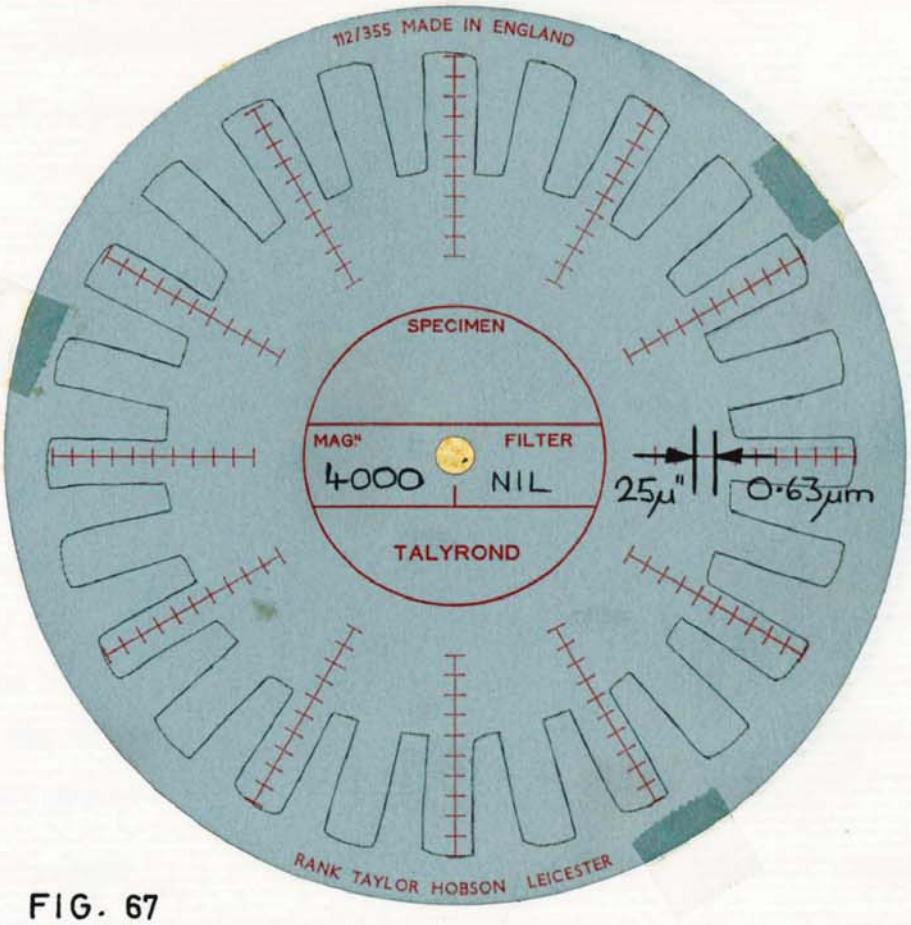

FIG. 67
ION-MACHINED PUMPING GROOVES IN A TYPICAL BORON CARBIDE THRUST PLATE

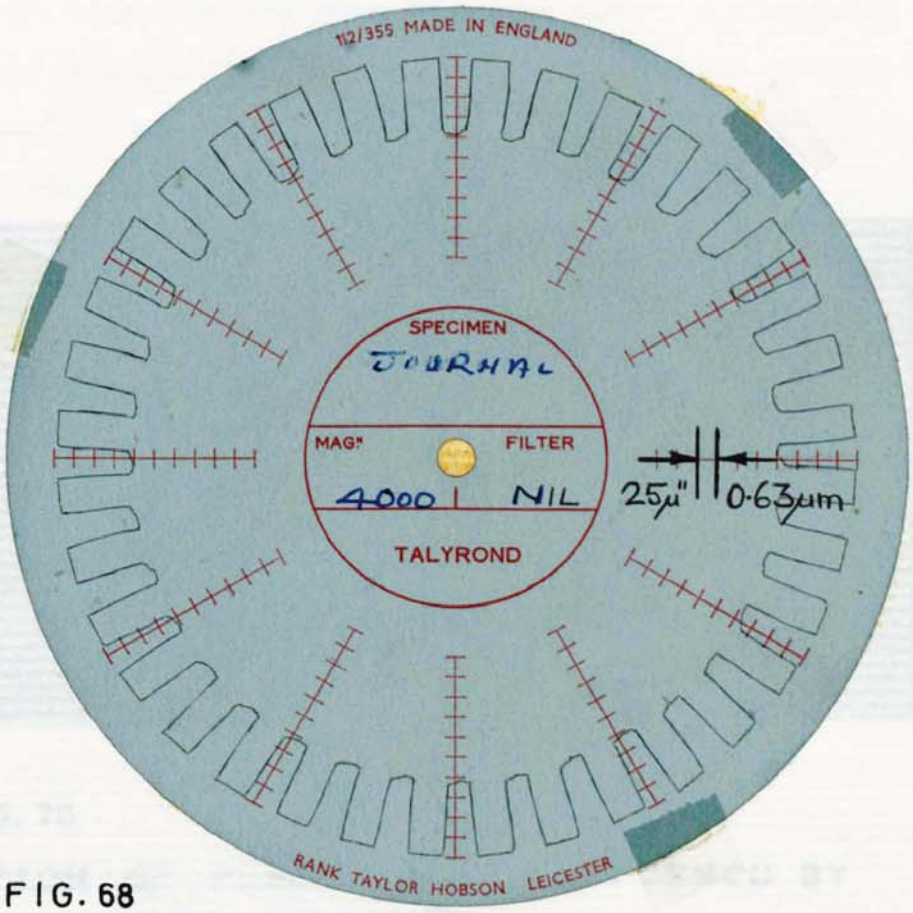

FIG. 68
ION-MACHINED PUMPING GROOVES IN A TYPICAL BORON CARBIDE JOURNAL SHAFT

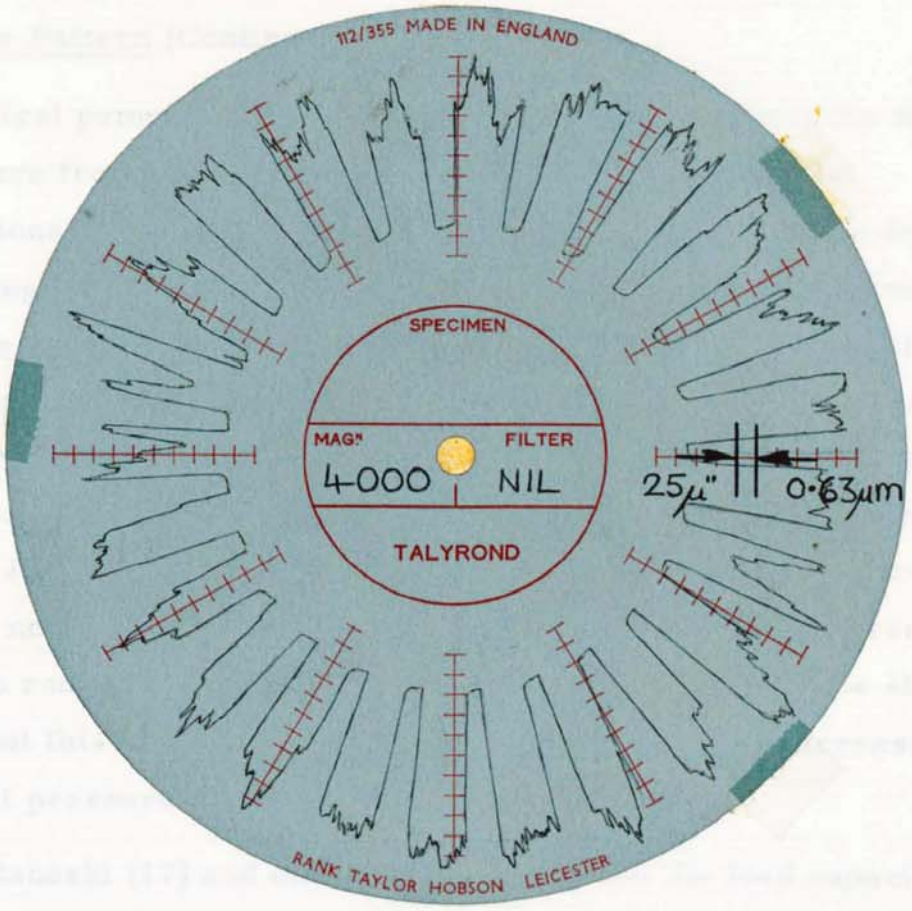

FIG. 69

PUMPING GROOVES FORMED BY ELECTROLYTIC ETCHING OF BORON CARBIDE

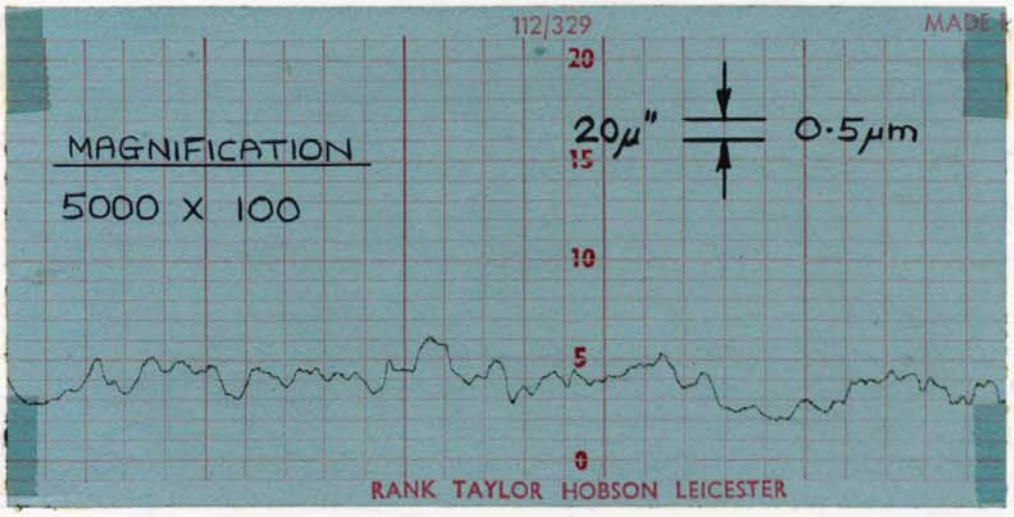

FIG. 70

BOTTOM OF PUMPING GROOVE FORMED BY AIR-ABRASIVE MACHINING

7.3.12 Groove Pattern (Continued)

Helical pumping grooves have been found to prevent the squeeze pressure from building up and under these rather special conditions, storage life will be reduced, especially where full grooving is specified. Squeeze support under shock loads must also be reduced when the rotor is airborne, but this loss will be counteracted by the increase in average journal pressure due to the grooves themselves. Appreciable squeeze film action will still occur between spiral grooved thrust surfaces where the entire land area can be utilised to generate squeeze pressure. Under normal conditions of storage, the presence of grooves will tend to reduce the mutual contact area and so improve the shelf life, but this may be cancelled by the corresponding increase in contact pressure.

Malanoski (17) and others have shown that the load capacity of a grooved journal bearing approaches an asymptotic maximum as the number of grooves approaches infinity. This has also been shown to be the case for a spiral grooved thrust element (31). In terms of operational life, it implies a minimum rubbing velocity during start/stop conditions and maximum resistance to overload. Manufacturing limitations make infinite grooving an impossible goal and components of this size rarely contain more than 50 grooves. With large numbers of grooves, the interposing land region can become very narrow, especially at the inner radius of a thrust plate, and leakage may then take place from local regions of high pressure across the lands. This suggests that infinite grooving would only be fully effective where the bearing clearances were also infinitely small.

In practice, the choice of groove number is found to be a compromise between performance and cost. Large numbers are costly to produce but give the closest approximation to ideal performance. Where the grooves are formed by some form of mechanical masking, lateral definition is difficult to maintain as the pattern becomes finer.

7.3.12 Groove Pattern (Continued)

Mask irregularities and distortion become important and mask life is limited. In particular, it has been shown (30) that a small reduction of the groove/land ratio can result in a marked decrease in support pressure, and this parameter is particularly vulnerable when fine groove patterns are formed.

Groove angle and length variations are usually small and will have no effect upon wear life. On thrust surfaces, a logarithmic spiral pattern can be shown to be slightly more effective than an equiangular spiral, but once again, the effect on wear life is considered here to be insignificant.

One of the most important practical features of a groove pattern is believed to be its ability to act as a safe haven for solid debris and contamination. This is clearly illustrated in Plate 37 where all the wear product has been deposited at the base of the grooves. Large abrasive particles which would otherwise continue to orbit the bearing clearance are frequently trapped in the groove region, and the extent of the corresponding damage is reduced. Provided crumbling or fracture of the groove edges does not occur (see section 7.3.11. and Appendix IV), cumulative damage will be greatly reduced and the operational life will be extended. In order to take maximum advantage of this effect, it is considered that the groove should extend over the entire wear surface in each case. This would involve the omission of a seal band on the thrust bearing and the use of a full herringbone groove pattern around the journal. Both configurations can result in a loss of load capacity and increased rubbing speeds during the start/stop phase.

7.4 Rotor Balance

Normal gyroscope practice requires the spinning rotor to be balanced within very fine limits (5×10^{-9} Kg.m) to eliminate vibration which might otherwise affect the instrument life and performance. Residual unbalance of this order will have no effect upon the operational life of the gas bearing in service, but during laboratory development there is a temptation to test bearings prior to balancing.

7.4 Rotor Balance (Continued)

Large out of balance forces will eventually promote a synchronous whirl condition in which the rotor axis will orbit its mean position at a speed equal to the rotational speed. This type of whirl is usually stable. On very large gyro rotors, previous workers have observed evidence of occasional contact during long periods of continuous running (107), but no further contact occurred after the rotors had been correctly balanced.

7.5 Rotor Mass

For given bearing dimensions, the specific loading will be proportional to rotor mass. As the specific loading is reduced, so take-off and touch-down will occur at a lower speed and wear damage will also be diminished. Under vibration, shock and acceleration loads, the specific loading will also decrease with rotor mass and high speed rubbing will be less likely to occur as a result of overload.

When starting from rest, the friction torque will, to a first approximation, be proportional to rotor mass. Any reduction in this mass will therefore improve the starting ability of the bearing where only a limited stall torque is available from the drive system.

Under storage conditions, wringing effects are less likely and molecular diffusion across the bearing interface will be retarded as the contact pressure between the bearing surfaces is reduced.

All aspects of wear and storage life are therefore improved as the rotor mass is reduced, and for maximum starting reliability, it is proposed that this mass should be reduced to the smallest possible value.

7.6 Rotor Inertia

In gyroscope applications, rotor inertia is only important in-so-far as it contributes to the product $I\omega$, the angular momentum. This product appears in equation 69 and determines the magnitude of the gyroscopic torque resulting from any given input rate.

7.6 Rotor Inertia (Continued)

During touch-down, the energy dissipation between the rubbing surfaces will be equal to the kinetic energy of rotation at the instant of contact.

$$\text{Energy Dissipation} = \tfrac{1}{2} I_R (\omega')^2 \qquad (78)$$

It seems reasonable to suppose that the surface damage as the wheel comes to rest will also be related to this energy loss, and it follows that damage will be reduced as I is reduced.

During take-off, the duration of the rubbing period, and hence the energy dissipation, will be governed by the angular acceleration of the rotor.

$$\frac{d\omega}{dt} = \frac{T_S}{I_R} \qquad (79)$$

Once again, it can be seen that a reduction in I will result in a more rapid take-off and the frictional energy dissipation will be minimised. Wildeman is reported (31) to have observed some correlation between wear damage and rotor acceleration during starting and it is shown here (section 6.2) that both the rate of energy dissipation and the total loss are reduced as the angular acceleration is increased.

Where a high angular momentum is due to predominance of the inertia term, the overall slew capacity of the assembly will probably be low, and angular overload may occur in service. Where any form of high speed rubbing occurs and the nett frictional torque exceeds the available motor torque, the rotor will drop out of synchronism. This loss of rotational speed will be more rapid for a low inertia rotor than for one having a high inertia. The reduction in speed will almost certainly help to minimise the surface damage, but it may not always be acceptable in terms of gyro performance.

It is therefore proposed that for minimum start/stop wear and maximum resistance to slew overload, the rotor inertia should be made as small as practicable.

7.7 Rotor Speed

In conventional gyroscopes, the attainment of a large angular momentum by using a high rotational speed is well known to be severely limited by the life of the rotor ball-bearings. This particular limitation does not occur in a gas bearing instrument. Where the ω term is predominant in the $I\omega$ product, a grooved journal bearing can be expected to have a relatively high slew capacity. This is because the radial force coefficient increases without limit with Λ (19), and hence with ω. In a smooth bearing the radial force coefficient approaches an asymptotic value as Λ increases, and at high rotational speeds, the resistance to slew inputs will progressively decrease. Thrust bearing performance will also be enhanced at speed.

Under overload conditions, the rate of surface damage will, for most unlubricated materials, increase with speed. Where the frictional energy dissipation is sufficient to cause either the material or its binder to approach their melting point, a massive increase in wear rate will occur (see section 7.2.2.2). Energy dissipation will be given by the relation:-

$$\text{Energy Dissipation} = T_F . \omega \qquad (80)$$

It follows that for any given bearing design, there will be an upper threshold speed, above which the rate of surface damage will increase sharply during overload. This limitation may not arise when using materials like boron carbide, where the wear process is predominantly due to thermo-chemical action. (See section 7.2.2.24.).

For all gyro applications, it is considered that the gas bearing rotor should therefore be driven at the highest rotational speed that practical and structural considerations will allow. On grooved journal bearings, stability requirements will impose an upper limit to rotational speed (17), but for very light rotors, this limit is usually acceptably high.

7.8 Compressibility Number, Λ

The operational life and reliability of a gas bearing will not be directly influenced by the compressibility number. Bearing performance will of course be closely related to this dimensionless group, and will ultimately decide the likelihood of overload in service.

7.9 Eccentricity Ratio, ε

For gyro applications, the design value of this parameter (under quiescent conditions) will usually be made as close to zero as possible, and typically <0.05. This implies the maximum possible stiffness and resistance to overload. The extent to which this ratio can safely increase in service as the bearing is loaded will be governed by the geometric accuracy of the bearing surfaces, but at $\varepsilon > 0.85$ there could be danger of sporadic contact between the asperity peaks, and also of loose debris momentarily jamming the position of minimum journal clearance. Plain journal bearings must often be run at high eccentricity for stability reasons but this does not apply to the grooved journal, which should therefore be operated at minimum eccentricity when life and reliability are important.

7.10 Attitude Angle, $\emptyset$

The attitude angle has not previously been considered in the context of operational life, and yet it can be shown to have considerable influence upon the nature of the wear process.

In both plain and grooved journal bearings, $\emptyset$ decreases with Λ, and hence with rotational speed (17). At the instant of touch-down where $\omega' \rightarrow 0$, $\emptyset \rightarrow 90°$ (1.57 radian) for a plain bearing, and approaches some lower angle on a grooved bearing. Rubbing therefore commences at a distance from the point on the journal shaft at which the rotor will eventually come to rest under the influence of gravity. The contact point thus moves backwards over the stationary surface as the rotor slides to rest, producing an extended wear scar over the circumference of the fixed member. A similar action will take place during the take-off period before the rotor becomes airborne.

7.10 Attitude Angle $\emptyset$ (Continued)

Such a wear scar can be seen in Plate 27 and extends over an angle of approximately 70° (1.22 radian) around the circumference of the shaft. This compares with a predicted attitude angle of 80° at touch-down (Section 6.7.3). The attitude angle effect therefore helps to distribute any start-stop wear over the surface of the stationary journal member, and prevents line-contact wear that might otherwise occur. Where bearing life is dependent upon controlled boundary lubrication, this distributed wear may be advantageous in reducing the likelihood of local rupture of the boundary film. On a very smooth wear surface, distribution of the wear region will also be beneficial, and gross local damage due to line-contact wear will be avoided. If however the stationary member has an appreciable level of surface roughness, many more surface asperities will be involved in the wear process, and the volume of wear product will increase. These asperities will not wear in an even manner (see Plate 27) and relatively large wear particles may occasionally be formed.

Under radial loading, the attitude angle will normally decrease as ε increases, (see CHAPTER 6) and will therefore determine the position on the stationary surface at which overload contact might first occur. When overload is severe and results in a marked decrease in rotor speed, the wear region will again move around the circumference of the journal shaft towards the load line.

The attitude angle is thus seen to play an important role in the wear process and its effect will depend upon both surface texture and the presence or otherwise of controlled boundary lubrication. A low value of $\emptyset$ is normally desirable from performance considerations and unlike a plain bearing, the grooved journal will permit some design flexibility where this parameter is concerned.

7.11 Orientation

When a gas bearing is employed in a free-gyro configuration, that is with the angular momentum generator gimballed about two intersecting axes, the rotor will generally be required to start and stop in any random orientation with respect to gravity.

7.11 Orientation (Continued)

Wear will therefore be spread evenly, subject to local geometry, over the entire journal and thrust surface. As previously discussed (Section 7.10), this wear distribution may be an advantage where the surfaces are very smooth or are boundary lubricated, but will certainly be a disadvantage when higher levels of surface roughness are involved. In this latter case, the volume of wear product may be such that stripping and cleaning is necessary after a preliminary running-in period (100).

On a triple rate gyro system, it is usually possible to arrange for the spin axes to remain horizontal during the start and stop period, while maintaining the input axes in three mutually perpendicular directions corresponding to roll, pitch and yaw. Start/stop wear is thus restricted to a known region of the fixed journal member (depending upon local geometry and attitude angle) and take-off or touch-down on the thrust bearing need not occur. During the run-down period, the rotor will be centralized between the thrust plates by the opposing thrust pressures. This centralizing action will exist as long as the rotor is in motion and it will tend to come to rest at a mid position between the fixed thrust members, provided the journal axis is approximately horizontal. Continuity measurements (116) have shown that this centralization occurs in practice and is unaffected by small deviations of the spin axis from its horizontal position.

If thrust contact can be eliminated in this manner during normal operation, considerable benefits are immediately available in terms of operational life and performance. Crowning of the thrust surface may no longer be essential and the thrust performance may be optimised for running conditions rather than for starting. Bearings are normally found to start more easily when supported on the journal as opposed to the thrust bearing, and this is reflected in a corresponding difference in touch-down speed and wear damage. Because the wear region is more closely defined, it becomes practicable to subject completed bearings to a series of start/stop cycles prior to shipping, without the need to strip and remove the consequent wear debris from those assemblies which successfully complete the test (100).

7.11 Orientation (Continued)

Where an H-form bearing operates for extended periods with the spin axis aligned vertically with respect to gravity, it is possible (80) that assymmetric positioning of the rotor within the total thrust clearance, will, in some circumstances, permit axial flow along the length of the journal and enhance the risk of external contamination entering the bearing. This effect will be discussed more fully in later sections of this Chapter.

7.12 Gas Properties

Operational life is not normally considered when the gaseous lubricant is selected and performance, thermal and cost considerations will normally dictate the final choice. For a given level of performance, an increase in viscosity will permit the bearing to operate at increased running clearances, where the effects of wear debris or ingested contamination may be less harmful. These increased clearances were at one time thought to offer advantages in manufacture and measurement (84), but this is no longer considered to be true when using modern production methods. A high thermal conductivity is also desirable in order to minimise temperature gradients throughout the bearing assembly. This will help to maintain the design clearances and will usually allow a more powerful spin motor to be utilised, with a consequent improvement in available starting torque.

Corrosion problems are avoided by the choice of an inert gas, but this advantage is lost if small amounts of oxygen and water vapour are added to promote boundary lubrication by fatty acids, since these materials do not function correctly in a truly inert atmosphere (39) (see also Section 7.2.2.20). The gas or gas mixture must be chosen so that liquefaction does not occur over the working temperature range of the bearing. When air is employed, solid CO_2 has been found (167) to form on the bearing surfaces at -80°C and may cause subsequent starting difficulties. Where the lubricating gas contains an appreciable quantity of water vapour, condensate may form within the bearing clearance under certain operating conditions, and has been reported by several previous workers (101) (102).

7.12 Gas Properties (Continued)

This water does not appear to interfere with normal running, but could easily prevent a small bearing from re-starting. It will be most likely to form in the sub-ambient region of a plain journal at low ambient temperatures. Condensation is shown here to be less likely to arise in a grooved journal bearing where sub-ambient pressures are rarely encountered due to the continuous pumping action of the grooves around its circumference. (See CHAPTER 6).

Helium is frequently chosen as a lubricant. It has a thermal conductivity five times greater than that of air and also offers a useful improvement in viscosity. Unfortunately, the attendent problems of hermetic sealing make it less suitable for rate gyro applications, where manufacturing and repair costs are important in comparison with more sophisticated inertial quality instruments.

7.13 Drive Characteristics

The characteristics of the rotor drive cannot be ignored when considering the operational life and reliability of the bearing.

Starting torque is considered here to be the most important single parameter, and above all else, will decide the ultimate life and reliability of a given bearing assembly. The ratio of motor starting torque to bearing friction torque must be as large as possible to allow for any change in friction coefficient during service. The torque margin will also ensure the maximum angular acceleration of the rotor under starting conditions (Figure 23), and will reduce the corresponding rubbing period to a minimum. This will in turn reduce the energy dissipation and wear rate as discussed in CHAPTER 6. Where the friction coefficient between the bearing surfaces does increase progressively in service, and the slope of the friction coefficient-time curve is shallow, a relatively small increase in motor stall torque will obviously result in a relatively large increase in start/stop life. This same situation will arise after a long period of storage, where the torque margin may be required to sever any molecular junctions that might have gradually formed across the bearing interface.

7.13 Drive Characteristics (Continued)

The level of synchronous torque available will be related to the bearing's viscous power dissipation at the design speed and hence to its ultimate load capacity and stiffness. High rotational speeds and small bearing clearances have previously been defined to be desirable, but viscous power dissipation will increase in a non-linear manner with each of these parameters and unless sufficient torque is available, the rotor will fail to reach synchronism. Figure 25 shows the variation of power dissipation with speed for a typical gas bearing assembly and Figure 30 illustrates the variation with bearing clearance. The synchronous power dissipation has been shown (CHAPTER 6) to increase as the bearing is loaded; rising sharply as the local running clearance approaches zero. This increase is shown in Figures 27 & 29 for a bearing assembly under torque loading. To maintain bearing speed and resistance to overload under these conditions, a reserve of motor torque must be available at synchronism.

Both starting and running torque are limited in practice by the power dissipation of the spin motor, in which as little as 30% of the total input power may be available as useful torque. This dissipation will in turn be restricted by the maximum safe working temperature of the assembly.

The electromagnetic braking effect exerted by the spin motor ironwork on a coasting rotor has been described in Section 5.5.7 and Figure 20 illustrates the considerable effect which this braking torque has upon both the run-down period and the angular deceleration prior to touch-down. In the absence of electro-magnetic braking, the rotor will spend a much longer period of time coasting at very high eccentricity ratios. Under these conditions, geometric imperfections and surface asperities could lead to intermittent 'bouncing' contact as recorded in Figures 14 & 15. Where a high degree of braking is available, the rotor will decelerate rapidly through the region and premature contact will be minimised.

7.13 Drive Characteristics (Continued)

In addition to rotational torque, any electrical drive system will exert both radial and axial forces on the gyro rotor. These result from magnetic and geometric misalignments of the fixed and moving motor components, and lead to an apparent increase in rotor mass (and hence in friction torque) during starting. On a hysteresis motor, axial forces have been found to be small in comparison with radial forces, which are primarily due to eccentricity of the motor air gap. Holmes (69) has investigated radial pull in a hysteresis motor and presents an expression derived by Bradford (70) for calculating the magnitude of the forces involved. Using this relation, it can be shown that the corresponding increase in friction torque is given by:-

$$\text{Torque increase} = \frac{\pi f D' L' B_p^2 \varepsilon'}{4} \qquad (81)$$

When applied to some of the experimental bearings described here, this expression indicated that the bearings would be unable to start on the available motor torque, when in practice, starting was found to be comparatively easy. A closer examination of Bradford's work shows that his original expression was derived for a multi-pole machine, and it may be quite inappropriate to apply this relation to a typical two-pole gyro spin motor*. This might account for the observed discrepancy between theory and practice, but practical difficulties prevented a closer investigation of the effect.

7.14 Cleanliness

Numerous references have already been made within this report to the generation of wear products and debris within the bearing. In this section, only contamination from external sources will be considered.

Contamination of the bearing surface can be broadly classified into three categories; hard particulate, soft particulate and fluidal. Each has its own characteristic effect upon bearing action.

* Badford concludes that a two-pole motor is a special case and will in theory have a unidirectional magnetic pull less than that of a multipole machine.

7.14 Cleanliness (Continued)

Hard particulate contamination can be due to residual machining abrasive and debris, and also to airborne mineral dusts such as quartz, calcium silicates and calcium aluminates. It is believed that all these particles can eventually result in damage to the bearing surface, regardless of its hardness, though machining abrasive and debris are usually considered to be the most harmful. Bearings contaminated in this manner often have a "gritty" feel when rotated slowly by hand. Once inside the bearing, individual particles tend to be relatively mobile, but can also lie dormant at the bottom of a groove or cavity for long periods until disturbed. Movement of an individual particle can cause a large and sudden rise in apparent friction coefficient, and this type of contamination has been associated with both intermittent and complete starting failures throughout this research.

Soft particulate material can arise from many sources, and includes skin particles, hairs, pollen and a variety of fiberous organics. Where the assembly area is close to a public or private highway, rubber dust from motor vehicle tyres will also be a contributing factor to the general level of contamination, as will carbon particles from incompletely burnt mineral fuels. From this rather incomplete list, human skin particles can be identified as the predominant form of contamination during bearing assembly. The entire human epidermis is shed approximately once every 28 days, and each individual is loosing skin particles at the rate of over 100 per minute throughout the working day. In one year the average operator will shed a sufficient quantity of skin scale to fill a large domestic bucket, and the majority of these particles are small enough to pass through the weave of protective nylon clothing. Plate 43 (b) shows a number of skin scales adhering to the surface of a bearing component, and many of these are comparable in size to the running clearance of the bearing.

7.14 Cleanliness (Continued)

Soft particulate material tends to be less mobile inside the bearing than harder material and can lead to a fairly large increase in friction over a short period. At low temperatures, some organics become very rigid and sudden starting failures can ensue. As with harder substances, intermittent increases in friction are possible, though less likely, as the particles move about the bearing surface.

Fluidal contamination is generally encountered in the form of a very thin film over some or all of the bearing surface. Finger grease, machining fluids and cleaning solvents are in this class, together with organic volatiles from other components within the gyro case. This latter group includes toluene, silicone oils, polyesters, methyl-isobutyl-ketone, n-butyl alcohol and phthalate esters. Finger grease is of particular concern because its properties will vary from one individual to another. A typical fingerprint has been found to consist of patches of grease and skin scale to approximately 200 to 300 micro inches (5 to 8 micro-metres) in depth. Its weight, found by weighing a large number of prints on a glass slide, is in the order of 10 micro grammes. Plate 43 (c) shows finger deposits on the corner of a bearing component due to careless handling. Fluidal contamination is complex if more than one substance is involved and its nett effect upon operational life difficult to predict. Low levels of contamination (below approximately 20 molecular layers) will often behave, for a short period, as a boundary lubricant, and bearing friction and wear will be reduced. Unfortunately, this lubricating action is both unpredictable and unreliable, and polymerisation and migration are known to occur (117). The combined effects of polymerisation and migration eventually result in high friction areas within the bearing assembly as local agglomeration of polymerisation products and residual contamination take place. Bearings contaminated in this manner have been found to be characterised by a relatively low level of friction coefficient immediately after assembly which rises progressively as the bearing is operated.

7.14 Cleanliness (Continued)

It has been observed here that this change in friction is accelerated as the operating temperature of the bearing is increased, supporting the view that chemical changes occur in the contaminant. High levels of fluidal contamination (corresponding to several hundred monolayers) result in an unsatisfactory performance on assembly and will immediately be apparent. The presence of fluidal contamination is also believed to reduce the mobility of particulate contamination and wear debris within the bearing clearance, causing individual particles to adhere to each other and to the wear surface. It has been noted (107) that self-acting gas bearings are comparatively resistant to either dirt particles or non-corrosive vapours alone, but are impaired by a combination of these two forms of contaminant. From this evidence it is clear that particle mobility is an important factor in minimising bearing friction and that this mobility cannot easily occur if appreciable amounts of fluidal material are present.

In order to ensure reliable starting over the operational life of the bearing, particulate and fluidal contamination must, in practice, be reduced to a minimum level during assembly. For airborne particulate contamination a statistical investigation has been carried out to determine the probability of suspended particles becoming trapped within the bearing clearance during assembly. It can be shown that for a linear distribution of 100 particles per cubic metre of up to 0.5 micrometres diameter (typical of a high quality clean room), there will be a probability of one particle becoming trapped in every 45,000 bearing assemblies. Even if one assumes a linear distribution of 400,000 particles per cubic metre (a heavily contaminated atmosphere), it is probable that only one suspended particle will be trapped in every 10 bearing assemblies. It is clear from these calculations that the danger from suspended particulate contamination is insignificant and that the majority of particles entering the bearing clearance during assembly are adhering to the bearing surfaces. This in turn highlights the importance of correctly chosen and applied cleaning techniques to remove attached particles immediately prior to assembly.

7.14 Cleanliness (Continued)

In addition to the direct effect upon operational life and reliability, there may also be an indirect reduction in wear life as a result of inadequate cleanliness or subsequent contamination. Reference has been made in CHAPTER 6 to the apparent relation between cleanliness and bearing pressure. If pumping efficiency is indeed impaired in this way, then load capacity and rubbing speed must also be degraded and these will ultimately be reflected in the overall operational life and reliability of the bearing. A variety of cleaning techniques are available. These include vacuum baking, pressure cooking, ultrasonic/vapour cleaning in a variety of solvents and glow-discharge cleaning in an Argon plasma. While the latter stage has been shown (86) to provide an almost perfect level of cleanliness, this is undesirable on the majority of materials unless a deliberate boundary lubricant is subsequently applied. In practice, many ceramic bearings are cleaned with a view to removing all particulate contamination and as much fluidal contamination as organic solvents will allow; the residual contamination providing an inevitable degree of boundary lubrication over the working life of the assembly. The success and consistency with which this residual level of contamination can be controlled is considered to be major factor in determining the long term frictional characteristics of the bearing. While nearly all stages of bearing manufacture have been either fully or partially automated, final assembly remains a manual operation and the degree of cleanliness achieved must rely to a great extent on the personal discipline of the personnel involved.

7.15 Surface Stress

All conventional machining techniques leave the machined surface in a state of mechanical stress. The magnitude of this stress will, in general, be related to both the energy dissipation at the surface and the amount of stock removal during machining.

7.15 Surface Stress (Continued)

Where the machining efficiency is high, low levels of surface stress may be expected, but where a relatively high energy dissipation is matched by a very low rate of stock removal (as during polishing) an appreciable level of stress may be involved. Thermo-chemical polishing of Boron Carbide is of particular concern because in this process, extreme levels of energy dissipation (high) and stock removal (low) are encountered.

The effects of surface stress in boron carbide were first observed here as a convex distortion of a polished thrust surface after the polished surface had been selectively broken under ion-bombardment. Similar distortion was later noted on a cylindrical surface when the procedure was repeated. A series of comparative experiments were then carried out to eliminate the source of stress and it was shown conclusively that distortion only occurred when a thermo-chemically polished surface was disturbed. Diamond ground or lapped surfaces showed no discernable movement after the surface had been broken and low energy ion-bombardment (72) was also eliminated as a source of stress. At this point it should be noted that high energy ion-bombardment at acceleration voltages approaching 100 k.v. is known to result in severe deformation of the crystal lattice. Distortion of semiconductor wafers due to this cause is apparently encountered in the electronics industry (107). No distortion occurred if the polished material was subjected to a high temperature stress relieving process prior to bombardment.

Because a flat polished surface always distorts into a convex profile, it may be concluded that the stress at the surface must be tensile. This tensile force acts in the stressed surface 'skin' only, in a direction parallel to the surface. Provided the stressed skin remains unbroken, equilibrium will be maintained. Penetration of the surface disturbs this equilibrium, which can only be re-established by a change in the overall geometry of the component.

7.15 Surface Stress (Continued)

Deflections from a true plane of up to 50 micro inches (1.15 micrometres) have been measured on discs of boron carbide approximately one inch (25 mm) diameter by 0.060 inches (1.5 mm) thick. From analysis developed in reference 105, it can be shown that the maximum tensile stress at the polished surface is given by the relation:-

$$\text{Maximum Stress} \quad \frac{2.d.m.E_m.t_w}{r^2} \frac{(3m + 1)}{(m - 1)} \frac{}{(5m + 1)} \qquad (82)$$

Substituting the appropriate values into equation 82 indicates surface stresses in the order of 3,000 p.s.i. ($20.7 \frac{MN}{m^2}$). Estimation of the depth of the stressed skin was difficult but most of the distortion appeared to have taken place after bombarding to a depth of 100 micro inches (2.5 micrometres). Stress levels appeared to be related to the duration of the thermo-chemical polishing process. Under laboratory conditions, polishing could be accomplished with a stock removal of less than 20 micro inches (0.5 micrometres) and this resulted in a fairly low level of stress. Under production polishing conditions, stock removals of 100 micro inches (2.5 micrometres) are more typical and the corresponding stress levels are found to increase by a factor of between two and three times.

The effect of surface stress on the wear properties of the surface is not easy to predict in advance. Long term distortion of the bearing surface under temperature or vibration conditions is theoretically possible but has not yet been observed. The average stress levels involved are very much lower than the rupture modulus of the material (50,000 p.s.i. ($342 \frac{MN}{m^2}$) for boron carbide) and are unlikely to impair the mechanical strength of the wear surface, though micro-defects in the surface might act as stress raisers and permit very much higher local stresses to exist. These stresses would in turn increase the likelihood of spontaneous debris generation as the defect region is subject to mechanical contact during rubbing conditions.

7.15 Surface Stress (Continued

In boron carbide, the effect of stress on the chemical properties of the surface is of even greater interest. It has long been known that mechanical stress increases the chemical reactivity of a surface; especially to oxidation. This increased chemical activity may be observed on thermo-chemically polished boron carbide, which looses its initial sheen over a period of weeks when exposed to air. The effect is slight, and was first noted when comparing a freshly polished surface with one polished previously. The original colour could be regained by heating to 1000°C in a reducing atmosphere, demonstrating that a minute amount of atmospheric oxidation had originally taken place. This is in sharp contrast to the normally inert qualities of this material (Section 7.2.2.20). Continuity measurements (Section 6.1) have occasionally suggested the presence of an oxide film on polished bearing surfaces. Surface stress may therefore enhance the ability of the bearing to thermo-chemically oxidise under rubbing conditions and it is possible that this effect may actually improve wear life of the assembly (See section 7.2.2.24). This same chemical activity at the stressed surface may also assist in retaining any potential boundary lubricant, for it is known that boundary lubricant molecules are difficult to attach to a corrosion resistant surface (100).

7.16 Floating Touchdown Characteristics

As a self acting rotor coasts to rest, the pressure generated within the bearing clearance will gradually leak away until the entire bearing reaches ambient pressure. If the leakage is slow and the speed decay rapid, sufficient pressure will remain to continue supporting the rotor for a brief period as its rotational speed reaches zero. The rotor therefore 'floats' momentarily on a cushion of gas before making contact with the stationary member. In this way, touchdown wear is virtually eliminated and low speed rubbing will only occur during the starting period.

7.16 Floating Touchdown Characteristics (Continued)

It appears that the floating touchdown effect was first encountered accidentally in the M.I.T. Draper Laboratories while examining gyro bearings of very low specific loading, and is reported by Sappupo (5).

It has been found that, to demonstrate the floating touchdown effect on one of the experimental bearing assemblies, the rotor is supported in a clamp and the normally stationary members spun by hand. The low mass of the boron carbide components was readily supported by the residual pressure for up to one second after they had ceased to rotate. In practice, the assembly was found to oscillate to and fro on the air cushion over an angle of approximately 2 degrees of arc (0.035 radian) immediately prior to contact. Stethoscopic examination did not reveal contact sounds that are normally heard as a bearing comes to rest.

The elimination of low speed rubbing during touchdown would seem to be highly desirable, and if floating touchdown characteristics could be incorporated as a deliberate design feature, an appreciable improvement in wear life should be possible. Unfortunately, the very desirable characteristics of floating touchdown cannot be entirely divorced from the reverse and less desirable feature of incomplete pressurisation of the bearing clearance as the rotor accelerates rapidly from rest. The experimental evidence supporting this latter hypothesis has been discussed in CHAPTER 6, where significant differences between touch-down and lift-off speed were noted. Many of the features which tend to delay de-pressurisation of the bearing clearance (for example a low inertia and a large trapped volume) are those which will also delay complete pressurisation throughout the take-off period. This reduction in take-off performance must therefore be taken into account where any deliberate optimisation to reduce or eliminate touch-down wear is attempted.

7.16 Floating Touchdown Characteristics (Continued)

On balance, optimisation to achieve floating touchdown characteristics is likely to result in an overall gain in wear life because the negative effect of increased rubbing speed at take-off will be more than offset by the reduction in contact period at high rates of angular acceleration (see Figs. 16 & 17 and Equation 72). The author became aware of the floating touchdown effect to date to carry out any comprehensive experimental or theoretical investigations, but a number of recommendations for future work in this area are made in Chapter 8.

7.17 Electrostatic Discharge within the Bearing.

In section 6.6, it was shown that evidence of electrical damage could occasionally be seen on the wear surfaces of certain experimental bearings. It is proposed that an elegant solution to the problem of rotor charge would be to insert a small alpha-radiation source in the gyro body, close to the outside of the rotor. This would create an ionised path to the outside of the spinning rotor through which any charge may leak away harmlessly. Such a solution would obviate the need for any form of rubbing brushgear, which would be totally unacceptable in most hydrodynamic bearing applications.

7.18 General Design Criteria

For cylindrical journal bearings, it is frequently desirable to make the bearing radius as small as possible, in order to reduce the friction torque arm to a minimum under starting conditions. Unfortunately, this also increases the specific loading by a proportional amount but in gyroscope applications, decreases the non-rotating gimbal mass in proportion to the square of the radius. In practice the choice of radius (if indeed any choice is available) is usually a compromise between these conflicting requirements. On flat thrust bearings, overall radius is less of a problem because crowning and other devices can be used to either minimise the contact radius or prevent contact altogether.

7.18 General Design Criteria (Continued)

The L/D ratio of the journal bearing influences not only the hydrodynamic performance but also flow rate between connected thrust bearings, and this flow can be a major contribution to the ingestion of external contamination. Trevorrow and Faddy (80) have shown that the journal flow parameter is also related to the cube of the clearance ratio:-

$$\text{Flow Parameter} = \frac{L}{D} \quad \frac{C^3_{(\text{THRUST})}}{C^3_{(\text{JOURNAL})}} \qquad (83)$$

For minimum flow along a connected bearing, this flow parameter should be maximised.

An additional method of reducing any flow through the bearing is to incorporate an annular seal band or ungrooved region towards the inner radius of the thrust bearing. On gyro bearings, where the overall annular width of the thrust face is often limited, this seal band uses valuable pumping area but still permits the thrust exhaust to enhance the pressure build-up in the journal. A further disadvantage is that the ungrooved region is less able to tolerate solid debris and contamination as previously discussed.

An alternative method of reducing journal flow is to vent the inner radius of each thrust bearing to atmosphere, thus making the thrust and journal elements independent of each other. From the point of view of ingestion, this situation is believed here to be worse than for the unvented case, with continuous flow now taking place through each thrust bearing under all operating conditions. The pressurising effect of thrust exhaust on the journal is also lost. Axial flow through a grooved journal would still be possible if the opposing journal grooves were of unequal depth.

The edges of all bearing surfaces should be smoothly radiused to minimise the danger of debris generation, and this becomes of special importance when using brittle ceramic materials. Smooth radii are known to be of particular importance at each end of the journal bore, where excessive angular misalignment will cause contact and a sharp corner would rapidly damage the stationary member.

7.18 General Design Criteria (Continued)

Last, but not least, is the need to ensure overall structural rigidity and minimum temperature gradients throughout the assembly.

7.19 Failure Mechanisms and their Effects

Very little published work is available concerning failure mechanisms in gas lubricated gyro bearings (4), (62). Exhaustive work has been carried out on the failure and deterioration of ball bearings but little of this is appropriate to gas lubrication.

Although overload life has been considered in detail throughout the preceding discussion, the operation of large numbers of bearings within their specified dynamic and environmental range has shown here (116) that a simple reluctance to start is by far the most predominant form of breakdown. In these circumstances, it is considered that failure due to overload can be safely neglected where a statistical distribution of failure life is to be investigated, though it should be noted that very short periods of overload are equivalent to very long periods of normal operation. A useful comparison is that of a boron carbide-tungsten carbide bearing combination, where 5 seconds of high speed rubbing at 400 revolutions/second has been found to generate mechanical damage comparable with that observed after some 40,000 start/stop cycles. (See Plate 27). The possible causes of failure have already been considered in detail, and in this section, only the measurable consequences of these events will be considered. Failure of the drive system or external fouling of the wheel assembly will be ignored.

Three basic forms of starting failure, as identified by the change in starting friction, can be observed, and are illustrated in Figure 71. Figure 71 (a) shows the gradual rise in bearing friction associated with ingestion of contaminating vapour, or with progressive deterioration of the boundary film. This form of curve would also be predicted from the theory of molecular diffusion across a stationary bearing interface. In Figure 71 (b) a more rapid rise in friction is shown prior to failure.

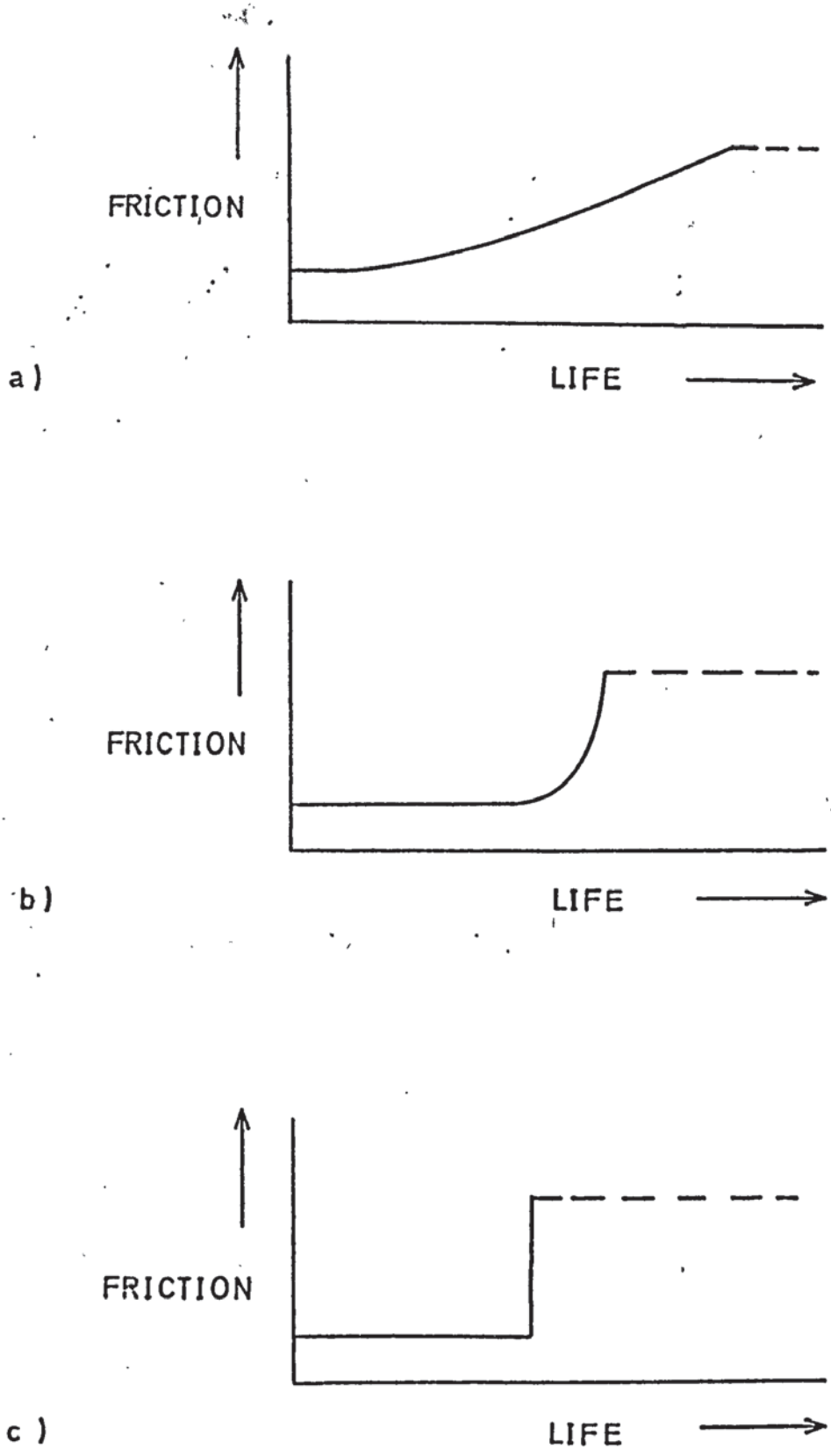

FIG. 71
FRICTIONAL FAILURE MODES.

7.19 Failure Mechanisms and their Effects (Continued)

This is characteristic of mechanical break-up of the wear surface and may be due to failure or disappearance of a boundary film. Figure 71 (c) represents the sudden frictional change caused by one or more hard particles between the bearing surfaces. The three curves correspond to somewhat idealised situations because in practice a series of fluctuations are often seen in friction coefficient over the working life of the bearing. A combination of any of the curves is also possible and interpretation then becomes difficult.

The anticipated distribution of failures with time over a large sample of bearings will now be considered, assuming that each bearing is subjected to a representative cycle of operating conditions. If failure were due to a simple mechanical 'wear-out' in each case, a classical distribution of failure as shown in Figure 72 (a) would be obtained. The initial failure rate rises rapidly to a small peak as early (manufacturing?) failures are identified, and then falls quickly to a hopefully low level which defines the M.T.B.F.* of the system. As the bearings leave this period of useful life and enter the 'wear-out' phase, a normal distribution of failure rate is obtained about the mean life of the assembly. Patterson has questioned this distribution (16) and suggests a ramp function as shown in Figure 72 (b); arguing that bearing life is limited by ingestion of external contamination and similar effects rather than by start/stop wear alone. Since this opinion is based upon a comparatively large sample of instruments in naval service, it cannot easily be ignored, and it is now suggested that the ramp function be superimposed upon the classical curve to yield the distribution shown in Figure 72 (c). The initial peak in this curve has been verified here but insufficient information is available to fully confirm the remainder of the plot.

* Mean Time Between Failures, as described in section 7.1.1.5.

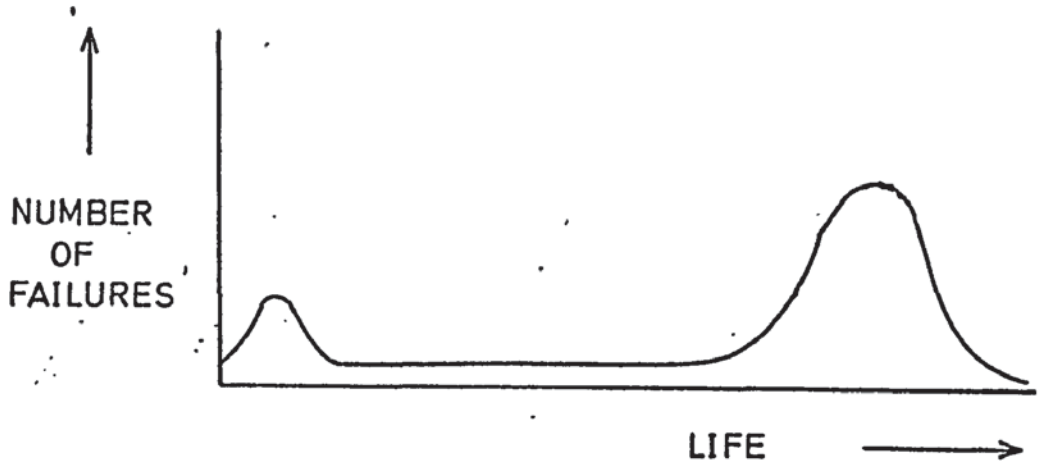

a) Mechanical wear-out

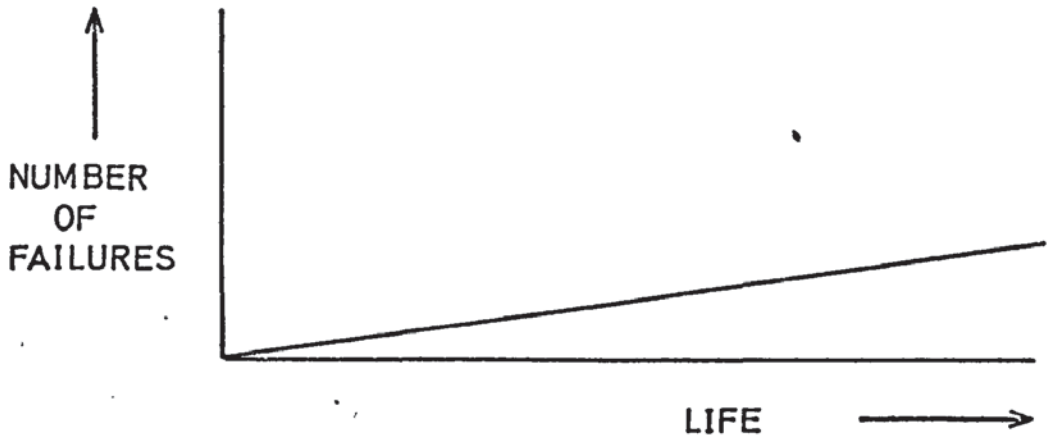

b) Ingestion failure

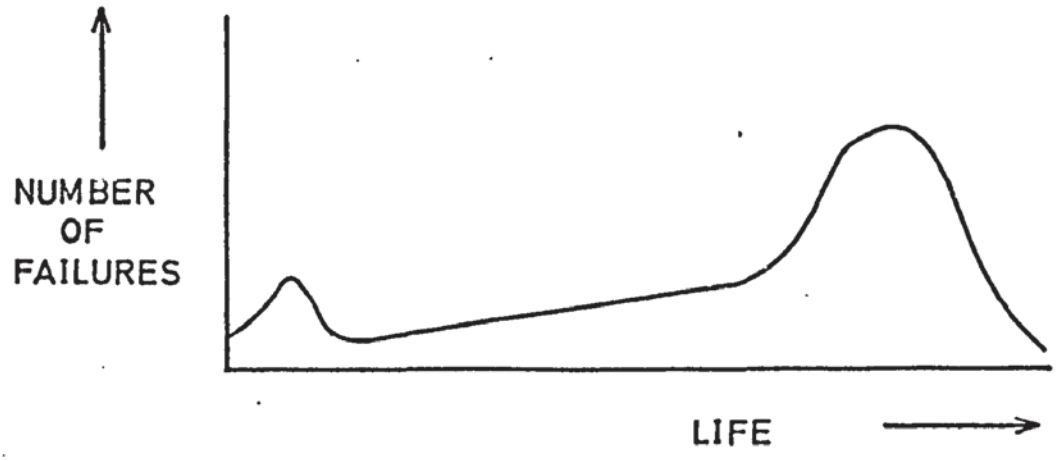

c) Mechanical wear-out plus ingestion

FIG. 72
ALTERNATIVE PATTERNS OF FAILURE DISTRIBUTION.

(NOT TO SCALE)

7.19 Failure Mechanisms and their Effects (Continued)

Most failure modes are known (4) to be closely associated with the local environment and can therefore be accelerated by temperature, vibration, thermal cycling, start/stop cycling and other changes in operating conditions. A similar sequence, referred to as a 'burn-in', can be used to reduce the width of the first peak on Figure 72 (c) and so identify premature failures prior to shipping. 'Burn-in' procedures are costly and time consuming and it is thus of some importance to ascertain the form of this peak so that their duration can be optimised. A 'burn-in' that is too short will result in early failures in service, while one that is too long may use up valuable operational life. Knowledge of failure rate over the central region is also required in order to establish reliability and warranty information, while the position and shape of the second peak will largely determine overhaul or replacement procedures (if any). The difficulties of obtaining accurate plots of failure distribution for a particular design are considerable and involve testing large numbers of bearings over a long period of time, for no accurate means are known by which the 'wear-out' process can be accelerated.

Problems are also involved in determining the precise cause of any individual failure, especially where no apparent damage to the wear surfaces has occurred. Contamination or debris weighing only a few micro-grammes may be involved and while many sophisticated analytical techniques are available (62), their widespread application to all failures would be a major undertaking.

The failure mode illustrated in Figure 71 (c) cannot be predicted in advance, but it should be possible to predict the failure pattern depicted in Figure 71 (a) by monitoring performance trends during 'burn-in' or service. For the intermediate case (Figure 71 (b)), advance warning is unlikely unless the small rise in friction prior to the rapid change can be detected at the appropriate time.

7.20 Optimisation to achieve maximum Operational Life

It is now possible to consider an "ideal" bearing in which the design is based solely on the requirement for maximum operational life. This bearing will then be compared with one optimised for performance alone, and its implications in terms of overall gyroscope design and cost will also be considered.

It will be convenient to divide the various design features into five groups in order of ranked importance. (See Fig. 73). The ranking will at times be a fairly arbitary one and is based upon the present understanding of operational life requirements for small gyro bearings, where storage, start/stop, running and overload life are all of approximately equal importance. Where certain operational features are considered to be of unusual significance, as for example storage life, then some minor changes to the ranking may be desirable as indicated in the main text.

Considering group one, which will be defined as features of exceptional importance, the ideal bearing would be constructed from material(s) having the maximum possible values of hardness, bond strength and melting point. Surface finish and texture would be as smooth as possible, preferably on a molecular level and particular care would be taken to ensure a high and consistent standard of cleanliness throughout the assembly. The specific loading of the bearing would be reduced to the minimum practicable value, implying a very low rotor mass, and the drive system optimised to provide the maximum torque under stall conditions.

Group two contains those design features which are judged to be only marginally less important than those in group one. Consequently, the bearing materials would be self lubricating with a low coefficient of friction at the specific loading and surface finish concerned. The mean running clearances would be as small as the availability of synchronous torque would allow and all wear surfaces would be fully grooved, with each groove completely free from machining damage and debris. The low inertia rotor would be driven at very high speed and would be specifically designed to achieve floating touchdown.

FACTORS CONSIDERED TO BE NECESSARY IN ORDER TO ACHIEVE MAXIMUM OPERATIONAL LIFE AND RELIABILITY

GROUP 1 (Exceptionally Significant)	B	G	C	GROUP 2 (Very Significant)	B	G	C	GROUP 3 (Fairly Significant)	B	G	C	GROUP 4 (Slightly Significant)	B	G	C	GROUP 5 (Insignificant)	B	G	C
High Motor Torque	√	√	X	Self Lubricating Matls	-	-	X	Low Porosity	√	-	X	High Specific Heat	-	-	-	Density	-	-	-
Good Surface Finish	-	-	X	Low Friction Coefficient	-	-	-	Low Solubility	-	-	-	High LH of Fusion	-	-	-	Electrical Conductivity	-	-	-
High Cleanliness	√	-	X	Low Rotor Inertia	√	X	-	High Dimensional Stability	√	√	X	High LH of Vapourisation	-	-	-	Young's Modulus	-	-	-
Low Rotor Mass	√	X	-	High Rotor Speed	√	√	-	High Chemical Stability	-	-	X	Journal Contact	-	-	-	Compressibility No.	-	-	-
High Hardness	-	-	X	Smooth Groove Profile	√	-	-	Fixed Orientation	-	-	-	Small Groove Depth	X	-	-	Dimensional Tolerance	-	-	-
High Melting Point	-	-	X	Full Groove Pattern	X	-	-	High Flow Parameter	√	-	-	Low Eccentricity	√	√	-				
High Bond Strength	-	-	X	Small Clearance	√	-	-	Unvented Thrust	X	-	-	Low Rotor Unbalance	√	√	-				
				Floating Touchdown	√	-	X	Low Attitude Angle	√	√	-	Selected Gas Properties	√	√	X				
				Discharge Elimination	-	√	X	Non-Magnetic Props	-	-	-								
								High Purity	-	-	X								
								Small Grain Size	-	-	X								
								High Boiling Point	-	-	X								
								High Thermal Conductivity	-	√	X								
								Low Expansion	√	-	X								
								Low Shear Modulus	-	-	-								
								High Rupture Modulus	-	-	X								
								High Compressive Modulus	√	-	X								
								Good Roundness	√	-	X								
								Good Straightness	√	-	X								
								Good Parallelism	√	-	X								
								Good Flatness	√	-	X								
								Good Squareness	√	-	X								
								Surface Stress	-	-	-								

FIG. 73

COMPARISON OF 'IDEAL' BEARING PARAMETERS WITH THOSE REQUIRED FROM PERFORMANCE & COST CONSIDERATIONS

B - Effect on bearing performance
G - Effect on gyro performance
C - Influence on manufacturing costs.

X = Known conflict.
√ = Known benefit.

7.20 Optimisation to achieve maximum Operational Life (Continued)

Finally, the dissipation of electric charge would be considered at an early stage and provision for external earthing incorporated if required.

The majority of features are ascribed to the third group and are classified as important in order to ensure maximum bearing life. Each non-magnetic bearing material would be of high mechanical and chemical stability and the mutual solubility of any rubbing pair would be low. Small grain size, low porosity and high purity would be combined with high boiling point and thermal conductivity, while thermal expansion and shear modulus would be low. To ensure adequate mechanical strength at the wear surface, high values of Rupture and Compressive moduli are also required. Surface geometry in terms of roundness, parallelism, straightness, squareness and flatness would be controlled as closely as available manufacturing techniques would allow and where surface roughness cannot be reduced to a molecular level, the attitude angle at touch-down should be minimised. The bearing will be operated in a fixed orientation with respect to gravity during the start or stop period and all start/stop wear confined to the journal. Minimal ingestion will be ensured by maximising the flow parameter and selecting an unvented thrust design with no seal band. Sharp corners to the wear surfaces are highly undesirable and are replaced by polished radii. Consideration of surface stress will also be included in this group but as discussed in the appropriate section, this may be advantageous to thermo-chemical lubrication and no general recommendation can be made.

In group four are those features which have by comparison a lesser influence upon operational life. These include the specific heat, latent heat of fusion and latent heat of vapourisation, which should all be high and the gas properties, of which high thermal conductivity and viscosity are the most significant. The residual unbalance of the rotating member would be small and under all specified operating conditions, this rotating member would operate at a low eccentricity ratio.

7.20 Optimisation to achieve maximum Operational Life (Continued)

In the event of excessive misalignment the relative geometry would be such that only journal contact could occur and shallow pumping grooves are used to increase rotor support at low speed.

Finally, in the fifth group, are placed those features which are considered to have no significant effect upon operational life. These include material densities, overall dimensional tolerances, elastic moduli, the compressibility number and the electrical conductivity of the bearing materials. Some qualification may be required with regard to the latter parameter when the electrical effects within the bearing are more fully understood (see section 7.17).

This, then, is an 'ideal' bearing, which if all the listed requirements could be satisfied simultaneously, could be expected to provide optimum operational life and reliability. Unfortunately, materials combining all the desired physical and chemical properties are as yet unknown and manufacturing and hydrodynamic limitations will impose a finite limit to many of the other desirable features.

Having established the broad concept of an 'ideal' bearing of optimum life, it is now possible to contrast this imaginary bearing with similar bearings optimised for performance alone (9), (10), (13), (19), (67), (91). On considering each parameter in turn in groups one to five, (see the comparative table illustrated in Fig.73) it is seen that very few conflicts occur between these two requirements, with the majority of features necessary for maximum life being either complimentary to or independant of those required for optimum performance. In only three cases does conflict arise, vis; the extent and nature of the groove pattern, the use of shallow pumping grooves and the choice of unvented thrust bearings without seal belts. The conflicts are not serious in practice and are discussed more fully in the appropriate sub-sections (7.3.10 & 7.3.12).

7.20 Optimisation to achieve maximum Operational Life (Continued)

The interaction between the 'ideal' bearing requirements and the overall gyroscope and system demand is now considered. Here, the conflicts are still few in number, but are of an altogether more serious nature. For most gyroscopes a high angular momentum is required in order that the precessional torque can overcome the gimbal bearing friction and any imposed spring restraint. In a simple rate gyro (Appendix I), decreasing the spring constant will result in an undesirable reduction in the natural frequency of the instrument. Synchronous rotor speed will normally be limited by the available power supply frequency, i.e. 400 revolutions/second for a 2-pole motor at 400 c/s. Under these circumstances, rotor inertia must often be high rather than low, and this in turn is inevitably reflected in an increase in rotor mass and a corresponding rise in specific loading. All these factors are unfavourable to both life and performance. Starting torque from the drive system will be limited from volume and thermal considerations and system or installation restrictions may prevent the bearing from being operated in its preferred orientation.

Optimisation for maximum life will also incur a penalty in terms of cost. Bearing materials whose properties approach the desired extremes are usually the result of lengthy development and are expensive. The attainment of close geometric tolerances is also costly, but some qualification of these two statements is required. In both cases, heavy investment can be expected during the design/development stages as specialised materials and manufacturing arrangements are acquired and as the additional design parameters are either optimised or investigated (e.g. floating touchdown and electrostatic effects). Once these preliminary requisites have been established, the additional cost per bearing as a result of optimising for maximum operational life and reliability will not necessarily be very high. This implies that the 'ideal' bearing would be financially attractive when large numbers of bearings are to be made and the extra investment can be amortised over a greater number of units.

7.20 Optimisation to achieve maximum Operational Life (Continued)

The proposed bearing is seen (Fig. 73) to agree well with hydrodynamic performance requirements, less well with the demands of the gyroscope as a whole, and to incur additional costs during both design and manufacture. In practice, some compromise will be necessary and complete optimisation for either life and reliability or performance is unlikely to be achieved.

Events have already overtaken this work and since commencing the investigation, evidence of a trend to many of the features proposed here has emerged in some U.S.A. designs (5), (59). These include the extensive use of thermo-chemically polished boron carbide and ion-machined grooves in each bearing surface. The use of high speed, low inertia wheels of very low specific loading is especially interesting, though it appears that these particular features were chosen primarily from unusual performance considerations rather than solely to achieve optimum life. Confirmatory evidence of their nett effect upon operational life and reliability may not be available for several years, but a study of prior publications (106) suggests that an overall M.T.B.F. of at least 100,000 hours is anticipated from this generation of bearings.

CHAPTER 8

RECOMMENDATIONS FOR FUTURE WORK

In the light of the experimental and theoretical work carried out, and the survey of relevant literature, a number of recommendations can now be made for future work relating directly to hydrodynamic gyro bearings and the improvement or prediction of their operational life.

8.1 Extension of Theoretical Work

8.1.1 Further Development of the Numerical Programme

This development should include the addition of a corresponding segment in which the pressure distribution and load parameters are evaluated for a finite grooved thrust element, and the entire programme should be extended to consider a greater number of grooves. Consideration should be given to improving both the accuracy and the numerical stability at higher compressibility numbers along the lines suggested in the text. In addition, it is proposed that it should be possible to vary the dependent variable throughout the course of the solution, in order to ensure optimum convergence over a greater range of solutions than has been practicable to date.

8.1.2 Analysis of Floating Touchdown Effect

This effect (rotor support due to residual film pressure) was discovered too late to consider in this report, and as far as is known, no detailed hydrodynamic analysis of it has been published. The proposed analysis should consider the design criteria necessary to achieve deliberate floating touchdown on a given bearing configuration and also the effect of this optimisation on the full speed load and stiffness characteristics of the assembly. It is proposed that the use of closed 'pockets' or gas reservoirs to enhance the effect should be considered as a means of extending floating touchdown characteristics to bearings whose specific loading would otherwise be too high to permit zero speed support. In particular, a theoretical study of rotor oscillation prior to contact could be used in conjunction with traces of the back e.m.f. referred to in section 5.5.5, as a useful diagnostic check on touchdown performance. The effects of partial support in reducing

8.1.2 Analysis of Floating Touchdown Effect (Continued)

touchdown speed should also be considered, together with the reverse effects of incomplete pressurisation of the clearance volume during take-off.

At first inspection, the problems is of a time dependant dynamic nature and may well be quite complex.

8.2 Extension of Experimental Work

8.2.1 Experimental Investigation of the Electrostatic Discharge Phenomena

The mechanism(s) by which electric charge is gained and lost by a spinning gas bearing rotor should be investigated in greater detail and the practical conditions established for discharge damage to occur on a typical bearing assembly. It is proposed that larger model bearings could be used which would permit the insertion of electrostatic sensing probes into the bearing clearance and also allow the gas properties, pressure, humidity and minimum film thickness to be controlled at will.

8.2.2 Development of Test Methods to Yield Basic Bearing Data from Production Instruments

A vast amount of design and performance data is, in theory, available to the bearing engineer from even the most modest manufacturing programme. Much of this data will be of a statistical nature and from a much larger sample than would have been available at the bearing development stage. Performance data will be of particular value because production bearings are invariably more representative of the designer's intentions than early hand made experimental models. The major obstacle is in extracting this data in a rapid and simple manner without prejudice to the manufacturing programme itself. Testing must of course be non-destructive and for both practical and economic reasons it is preferable to extract all data once the bearing has been assembled into a finished instrument.

8.2.2 Development of Test Methods to Yield Basic Bearing Data from Production Instruments (Continued)

It is proposed that experimental methods should be devised which are suitable for incorporating into production testing and which will yield such basic information as load capacities, stiffnesses, attitude angles, eccentricity ratios, viscous torque and dynamic characteristics over a range of operating conditions. In this way, test results previously requiring lengthy laboratory work could be obtained from each bearing produced, and in conjunction with the known dimensional and geometric variations, would add greatly to existing knowledge. These tests are distinct from comparative tests used to assess the integrity of the bearing, though where possible the two should be combined.

The methods envisaged include the deduction of attitude angle and eccentricity ratio from the change in mass centre of the complete instrument, derivation of bearing stiffness from the dynamic response of the assembly to an external impact, and bearing load capacity from the sharp change in power consumption prior to overload.

CHAPTER 9

CONCLUSIONS

9.1 Theoretical Analysis

A straightforward numerical iterative solution is the most suitable approach if random defects and manufacturing limitations are to be examined and a rectangular mesh pattern of variable aspect ratio will allow finite difference methods to be conveniently employed on helically grooved journal bearings (See CHAPTER 4 sections 4.3 & 4.6).

Replacing the dependent variable $\bar{P}$ with $\bar{P}^2$ results in a considerable improvement in the numerical stability of a grooved journal solution and will ensure convergence up to compressibility values of 6 in this case (See CHAPTER 6 section 6.7). In addition to the well known 'rapid' numerical instability, characteristic of this method of solution, a comparatively 'slow' instability was also observed. (See CHAPTER 4 section 4.12). This instability is more difficult to detect but may be identified by comparing the magnitude of the computed pressure profiles obtained using different values of relaxation factor.

Agreement between the numerical and experimental results is generally poor, with experimental pressure values up to 40% less than those predicted by the computer programme. The majority of this discrepancy is considered to be due to the influence of the large pressure ripple over the groove region and its effect on the local stability and accuracy of the solution. (See CHAPTER 6 section 6.7). The theoretical analysis does however predict the overall shape of the pressure profile very closely (See Figures 33,35,36,40 and CHAPTER 6 section 6.7.1); agreeing well with both prior solutions and with experimental curves plotted from actual gyro bearings. Agreement between the predicted and experimental attitude angles is reasonably good (See Figure 47 and CHAPTER 6 section 6.7.3).

9.1 Theoretical Analysis (Continued)

Provided the rotational speed of the bearing is sufficiently high, helical grooving of the journal will maintain super-ambient pressures throughout the bearing under any eccentricity conditions (See Figures 37 & 39 and CHAPTER 6 Section 6.7.1) and this additional pressure component will assist in preventing the formation of condensate within the bearing clearance under extreme environmental conditions (See CHAPTER 7 Section 7.12). The pressure at any point within an 'H'-form bearing assembly is found to be equal to the algebraic sum of the components due to thrust exhaust, journal groove pumping and journal eccentricity or misalignment (See CHAPTER 6, Section 6.7.1.).

9.2 Experimental Work

For measurements on actual gyro bearings of small dimensions, great care is necessary in the design of the test rigs and experimental procedures (See CHAPTER 5). Even where these precautions are taken, accurate measurement of rotor deflection and attitude angle is still very difficult at eccentricity ratios below 0.1 (See CHAPTER 6 Section 6.7.3.).

Very small amounts of contamination are found to significantly reduce the measured bearing pressures (See CHAPTER 6 Section 6.7.1.) and no prior reference to this effect can be found. Take-off speed is higher than touch-down speed for the grooved bearing considered and this is due to the delay in pressurising the bearing clearance as the rotor accelerates rapidly from rest (See CHAPTER 6 Section 6.1). Electrical continuity measurements (See CHAPTER 6 Section 6.1) show three distinct phases of bearing contact during touch-down and continuity records made during take-off indicate the presence of very thin oxide films between the ceramic bearing surfaces.

Electrostatic discharge may occur between a spinning rotor and the stationary bearing surface, and this will occasionally form a series of small craters in one of the wear surfaces (See CHAPTER 6 Section 6.6).

9.2 Experimental Work (Continued)

Discharge experiments using a fine tungsten wire lead to the conclusion that the spinning rotor acquires a positive charge, and that ceramic surfaces such as boron carbide are less likely to be damaged than ferrous surfaces. Electrostatic discharge also provides a satisfactory explanation to the well known continuous running wear-out phenomena reported elsewhere (See CHAPTER 6 Page 141 .

Fleming's (1) prediction of laminar eddies within the groove is partly confirmed on a bearing model, and the possibility of both stagnant and length-wise flow within a pumping groove is also demonstrated (See CHAPTER 6 Section 6.4). The experiments suggest that the aspect ratio of the groove is the predominant factor in deciding which type of flow pattern is obtained, but that no single aspect ratio can support the four flow patterns that have been proposed.

9.3 Operational Life

Optimisation for maximum life and reliability can now be considered at an early design stage (See CHAPTER 7 Section 7.20) and high motor torque, good surface finish, high cleanliness, low rotor mass, high surface hardness, high surface melting point and high material bond strength are found to be the most important factors for achieving a long operational life. No significant conflicts are found between the requirements for maximum life and those required for maximum performance (See Figure 73/.). The selection of bearing materials and combinations by examining their physical and chemical properties can now replace the tedious wear-testing hitherto employed (See CHAPTER 7 Section 7.2).

Operational life and reliability is influenced by many factors not previously considered, including the attitude angle (CHAPTER 7 Section 7.10), surface stress (CHAPTER 7 Section 7.15), vented or unvented thrust bearings (CHAPTER 7 Section 7.18), pumping groove parameters (CHAPTER 7 Sections 7.3.10 to 7.3.12) and rotor roundness (CHAPTER 7 Section 7.3.2).

9.3 Operational Life (Continued)

When optimising a bearing design for operational life and reliability, it is useful to consider the concept of an 'Ideal' bearing (CHAPTER 7 Section 7.20) in which a long operational life is the sole requirement.

9.4 Statistical Investigation

No significant correlation is found between geometric tolerances, test performance and bearing failure over the range of samples investigated (See CHAPTER 6 Section 6.5). A wide range of geometric variation is difficult to obtain from the specialised manufacturing equipment employed to produce this type of bearing and an accurate correlation between bearing failure and the remaining parameters will only possible when a higher proportion of the test sample have failed. Present indications suggest that this position may not be reached for many years.

9.5 Additional Work

Additional work is required in a number of areas.

Further development of the numerical programme is desirable in order to further improve the stability and also to include a greater number of pumping grooves. (See CHAPTER 8, Section 8.1.1).

Theoretical analysis of the floating touchdown effect is required, and this analysis should also consider the reverse effect of incomplete pressurisation during take-off which was noted here (See CHAPTER 8, Section 8.1.2).

Further work is also important into the mechanism and effects of electrostatic discharge in self-acting gyro bearings (See CHAPTER 8, Section 8.2.1).

In addition, test methods should be devised which will allow basic bearing data to be extracted from production gyros (See CHAPTER 8, Section 8.2.2). This will in turn allow the statistical investigation commenced here (CHAPTER 5, Section 5.12) to be greatly extended and improved.

APPENDIX I

THE SINGLE AXIS RATE GYROSCOPE

All gyroscopes utilise the fundamental property of a spinning inertial mass; that its axis of rotation attempts to remain fixed in space and will exert an orthogonal couple when any applied torque acts to deflect this axis. The sense of this generated or gyroscopic couple will tend to align the spin axis vector with the torque input vector.

In a free-gyro configuration, normally used to provide a vertical or azimuth reference, the spinning mass is gimballed about two or more axes and gimbal freedom is largely unrestrained. For a rate gyro, gimbal motion is normally, though not necessarily, restricted to one axis, and some form of electrical or mechanical spring restraint applied to the gimbal movement. In the former case, the electrically generated torque is servo controlled to maintain zero spin axis deflection over a defined range of input rates, and such an instrument is referred to as a 'closed-loop' or feedback gyroscope. The latter arrangement may be termed an 'open-loop' gyro. Both forms of rate gyroscope are attached directly to the frame of the 'vehicle', and are used to sense and measure its rotation about one or more chosen axes. The Series 700 gyro is a single axis instrument in that it is designed to respond to motion about a single input axis.

Figure 74 illustrates a typical single axis open loop rate gyroscope. Rotation of the complete instrument about its input axis will produce a gyroscopic torque about the output axis. The torque, generated by motion of the rotating mass, must be transmitted to the gimbal frame through the gas bearing film. This torque is proportional to the rate of rotation about the input axis (see equation 69).

Under the action of this torque, the gimbal assembly will rotate about the output axis until the gyroscopic torque is balanced by the restoring torque of the torsional spring. The higher the input rate, the greater the gyroscopic torque and thus the further the torsional spring must deflect to reach equilibrium.

The angular deflection of the gimbal is sensed by a pick-off, whose electrical output signal is therefore proportional to the applied angular input rate at any instant.

NOT TO SCALE

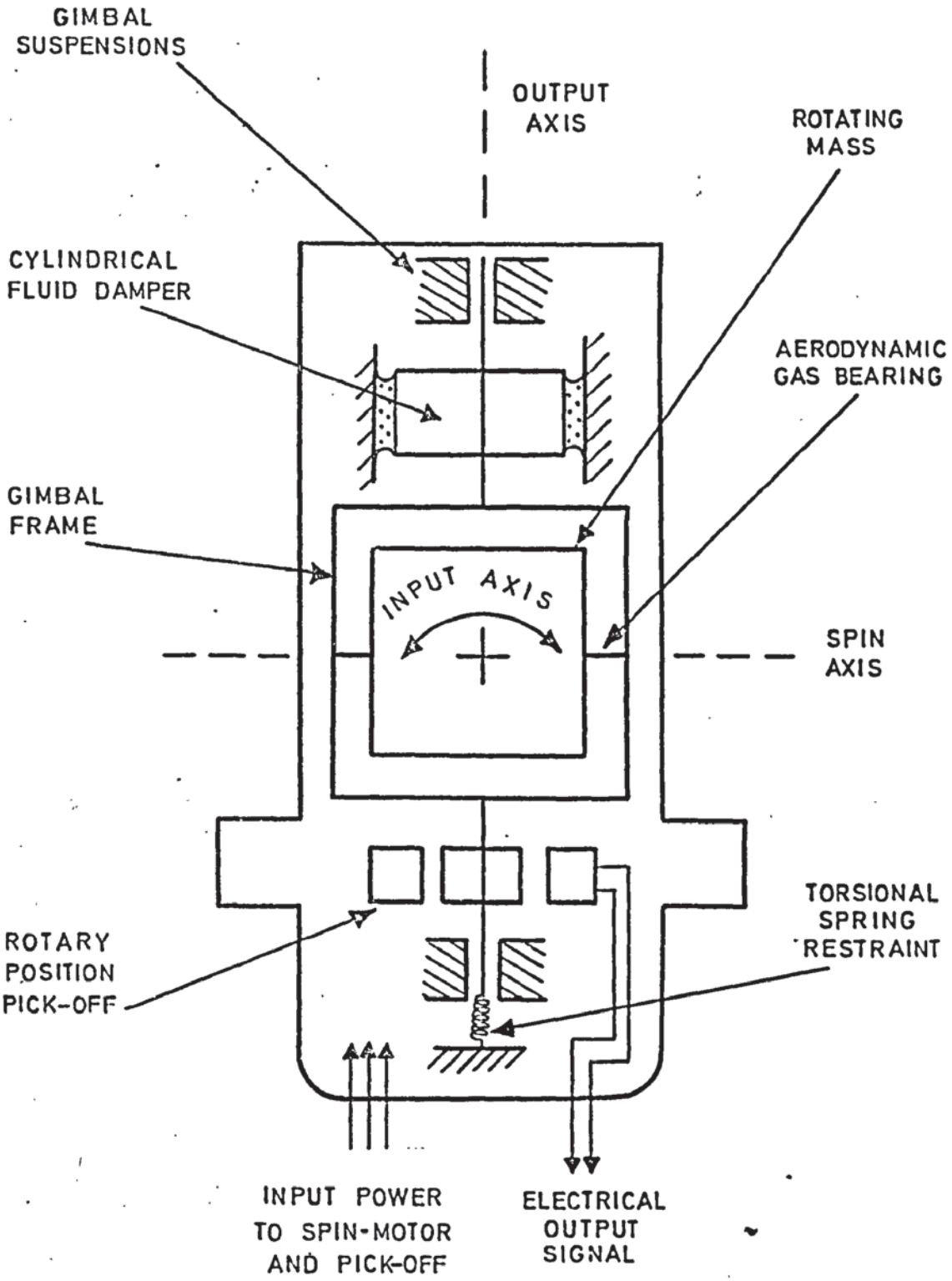

FIG. 74
A SINGLE AXIS
RATE GYROSCOPE

A choice of torsional spring rates will allow instruments of differing scale factors to be constructed, and in a typical aviation control application, an input rate of ±20°/sec may give an output of ±3.3 volts.

The rotary pick-off is constructed as a variable reluctance transformer and is energised from an a.c. voltage source applied across the primary terminals. The modulated output signal from the secondary winding may be processed by additional circuitry within the gyro case to compensate for the effect of external temperature variations. Viscous damping about the output axis is obtained from a cylindrical fluid damper attached between the gimbal and outer case. The mechanical design of this concentric cylindrical damper allows for partial compensation of the damping characteristics as the viscosity of the interposing fluid changes with temperature. Rotation of the gimbal takes place between two conventional ball bearings, and the torsional spring restraint is obtained from a torsion bar attached at one end to the gimbal and anchored to the gyro case at the other. Alternatively, the gimbal may be mounted on a flexure-suspension system. This combines high radial and axial stiffness with relatively low torsional stiffness, and replaces both the torsion bar and the gimbal ball bearings. Gimbal deflection is limited in each case to about ±2 degrees of arc by mechanical stops, and this allows the rotor spin motor to be energised via flexible electrical ligaments which are strung between the moving gimbal frame and the stationary outer case.

The rate gyroscope is therefore used to measure the rate and sense of rotation about a predetermined axis. In an aviation control application, three such instruments are frequently used to achieve short-term stabilisation about the aircraft's roll, pitch and yaw axes. Other applications include the stabilisation of guns, aerials, radar dishes, marine steering systems, helicopters, missiles and missile launchers.

APPENDIX II

TEST BEARING SUMMARY

BEARING NUMBER	MAIN BEARING CLEARANCE		GROOVE DEPTH	
	JOURNAL	THRUST	JOURNAL	THRUST
4	80μ"(2.04μm)	90μ"(2.29μm)	90μ"(2.29μm)	235μ"(5.97μm)
5	150μ"(3.80μm)	85μ"(2.16μm)	150μ"(3.80μm)	240μ"(6.10μm)
28	85μ"(2.16μm)	82μ"(2.10μm)	100μ"(2.54μm)	200μ"(5.08μm)
30	55μ"(1.40μm)	110μ"(2.80μm)	70μ"(1.78μm)	230μ"(5.84μm)
37	87μ"(2.20μm)	105μ"(2.68μm)	90μ"(2.29μm)	230μ"(5.84μm)
101	62μ"(1.58μm)	90μ"(2.29μm)	112μ"(2.85μm)	210μ"(5.33μm)
122	100μ"(2.54μm)	95μ"(2.42μm)	90μ"(2.29μm)	220μ"(5.60μm)
131	90μ"(2.29μm)	100μ"(2.54μm)	90μ"(2.29μm)	230μ"(5.84μm)
218	88μ"(2.24μm)	100μ"(2.54μm)	112μ"(2.85μm)	230μ"(5.84μm)
225c	93μ"(2.36μm)	80μ"(2.04μm)	90μ"(2.29μm)	250μ"(6.35μm)

Thrust Bearing

Number of grooves	=	24/plate
Groove pattern	=	Logarithmic spiral
Groove/Land ratio	=	1.5
Seal Band	=	Nil
Groove Angle	=	72°

Journal Bearing

Number of grooves	=	36 each end
Groove pattern	=	Equiangular partial helix
Groove/Land ratio	=	1.0
Helix angle	=	27°
Groove length	=	$\frac{1}{3} \times L$

APPENDIX III

ACCURACY OF EXPERIMENTAL RESULTS

In experimental measurements of this kind, especially those involving dimensions and movements in the order of micro-inches, the accuracy of the final results must inevitably be questioned. To answer these queries in a satisfactory manner, it is necessary to consider in turn both the measurements themselves and other possible sources of random and systematic error, and to establish what influence they are likely to have upon the final results.

All conventional test equipment is calibrated periodically by the laboratory calibration department and it is assumed that no gross errors were introduced from this source.

1. Basic bearing dimensions

Even using conventional measuring equipment, bearing diameters and lengths can be determined to better than one part in 4000, and as performance is directly proportional to their magnitude, the nominal bearing size does not present a problem.

On the other hand, bearing clearances normally appear in the describing equations to the second or third power, and their errors therefore hold a greater degree of significance. They are measured using special techniques and equipment that cannot be described here for commercial reasons. The mean radial and axial clearances are related directly to calibration grade slip gauges (B.S.S.888) that have been verified at the National Physical Laboratory. Allowing for wringing errors (0.25 micro inch or 0.006 micrometres per junction) and gauge non-linearity, it is probable that the true mean clearances are known to within ±4 micro inches (±0.1 micrometres).

From a practical standpoint, repeatability and consistency are considered more important that a knowledge of the absolute clearance. Individual clearance measurements normally repeat within an indicated one micro inch (0.025 micrometres) when taken within a short period on the same equipment, and within an indicated 2.5 micro inches (0.06 micrometres) over a period of some eighteen months.

1. Basic bearing dimensions (Continued)

When experimental bearings were double-checked by an independent metrology unit some distance from the manufacturing area, the nominal clearance values differed from those recorded during manufacture by only 2 micro inches (0.05 micrometres).

2. Bearing geometry & groove dimensions

These features are normally recorded on Taylor Hobson 'Talyrond', 'Talysurf' and 'Talylin' equipment, and the manufacturers do not guarantee geometric readings below two micro inches (0.05 micrometres). With care, geometric variations can be resolved down to these limits but interpretation of the resulting charts has proved a frequent source of error and, for consistency, is best carried out by one person.

To the geometric tolerances such as roundness, straightness, parallelism etc., may be attached a probable measurement error of ± 1 micro inch (±0.025 micrometres) and a corresponding error of about ±3 micro inches (±0.075 micrometres) to the measurement of groove depth.

Lateral groove dimensions are far less critical and can be measured to one part in 200 by conventional optical methods if required.

As an additional precaution, each experimental bearing was re-measured on duplicate metrology equipment before assembly.

3. Differential expansion

Change in bearing clearance with temperature was minimised by operating the bearings within a temperature controlled area. Air temperature close to the test rig normally lay within a 2°C band and self heating was estimated from a thermocouple junction attached to the bearing.

Accuracy of the experimental value for the differential temperature coefficient was believed to be ±0.02 micro inches/inch/°C.

3. Differential expansion (Continued)

Variations in ambient temperature will give a maximum clearance change of just under one micro inch (0.025 micrometres) and the temperature coefficient errors of 0.1 micro inch (0.0025 micrometres) are therefore negligible by comparison.

The above estimates assume no significant temperature gradients throughout the bearing structure. Proof of this is difficult, but it is well known that good thermal conductivity exists across the air film and both gimbal and test cradle structures are designed to minimise such gradients.

4. Elastohydrodynamic effects

The high elastic modulii and relatively thick section of the bearing components allow negligible distortion of the bearing surfaces by the generated pressure profile. Though not known a priori, it can be shown in retrospect to be negligible by assuming, for ease of calculation, that the maximum recorded pressure acts over the entire bearing surface.

The elastic modulus of boron carbide was verified by load/deflection measurements on a typical thrust plate.

5. Centrifugal growth

The bore diameter of the rotor increases with speed under the action of centrifugal force, and the corresponding increase in journal bearing clearance is given by the relation:-

$$\Delta C = \frac{\ell \omega^2 R}{4.Go.E_m} \left(\frac{3m-2}{m-1} R_1^2 + \frac{m-2}{m-1} R^2 \right) \qquad (105) \qquad 84$$

The high elastic modulus of the rotor material helps to minimise this effect, which is found to be negligible at all but the very highest rotational speeds.

Where appropriate, the final clearance values have been corrected for this change.

6. Stability of bearing materials

A sample of tungsten carbide, identical to that forming the rotating portion of the bearing, has been deposited at the National Physical Laboratory and periodically measured over a duration of fifteen years by interferometric methods. No significant dimensional change was reported.

Comparable work on the stability of boron carbide is not known, but a knowledge of its manufacturing process suggests that it should be no less stable than tungsten carbide.

7. Accuracy of pressure measurements

Comparison against a U-tube manometer showed that gauge pressures could be obtained within ±0.05 p.s.i. (345 N/m^2) up to about 20 p.s.i.g., (0.138 MN/m^2) increasing to ±0.25 p.s.i. (1724 N/m^2) at 50 p.s.i.g. (0.345 MN/m^2).

Barometric pressure variations were found to be negligible over the period of measurement, but could otherwise have been used to correct the nominal value of ambient pressure, P_A.

Nominal ambient pressure was measured on a recording barometer and is known to within ±0.1%. For those measurements performed at reduced ambient pressure, the gauge accuracy is estimated to be ±2%.

8. Accuracy of angular measurements

When using the O.M.T. table, the error between any pair of angular positions can readily be kept within ±0.25° and within ±0.5° when using a metal protractor on the centrifuge.

Initial alignment of (say) the first pressure tapping with the O.M.T. table datum is more difficult and errors of up to ±2° could be involved.

9. Rotational speed

In a true synchronous motor, the speed of rotation is proportional to the supply frequency and this may be continuously monitored and controlled within ±0.25% without much difficulty.

The accuracy of the photo-tachometer is limited primarily by the accuracy of the output meter, which in this case was ±1% of full scale reading.

During the course of the experimental work, it was noted that under certain circumstances, a steady slip could occur between the rotor and stator of a hysteresis motor when running at 'synchronism'. This slip error has not previously been reported and was found to be in the order of 0.02%. It is believed to be due to creepage of the induced magnetic poles around the circumference of the hysteresis ring. The error is too small to be of concern here, and, as might be expected, can be cured by over-volting the motor winding and hence increasing the magnetising field strength. In a larger machine, the slip may not be insignificant and over-volting may lead to temperature problems where precise measurements are required. To overcome such a problem, it is proposed that some form of geometric discontinuity could be machined across the diameter of the ring, to allow the induced poles to lock into position at synchronism.

10. Accuracy of time measurements

Time intervals were normally recorded on a laboratory stop watch marked in increments of 0.01 seconds. After checking the stop watch against an electronic timer, simple experiments were carried out to determine operator error for anticipated and unanticipated events. For anticipated events (found by repeatedly attempting to stop the watch pointer against a given mark), operator error was ±0.1 seconds, while for unanticipated events (found by masking the watch face and attempting to stop the pointer as soon as it appeared in a 'window'), the error rose to between +0.2 and +0.4 seconds. Most of the events involved here could be anticipated. Wherever practicable, a large number of readings were taken and the average time interval calculated.

10. Accuracy of time measurements (Continued)

For those events measured on a U.V. recorder, time intervals could be established within ±0.01 seconds by making use of the recorder's time-marker.

11. Accuracy of slew rate

Angular input rates used to torque load the bearing are applied by a precision Gyro Calibration Table, incorporating an electronic speed control system and calibrated to an accuracy of 0.25% full scale. This was normally verified prior to each series of tests by timing complete revolutions against a stop watch.

12. Friction measurements

The accuracy of starting friction measurement is influenced by the spread of the spin motor characteristics, and also by the rotor weight.

Over the range of torque levels involved, the spread of motor characteristics lay within $\pm 2\frac{1}{2}\%$, while rotor weight was known to within ±0.002%.

The supply voltage to each spin motor was measured on a sub-standard voltmeter whose maximum error of indication lay within ±1%.

13. Lubricant viscosity

The numerical value of absolute viscosity for a gaseous lubricant is directly related to its temperature. Established values for air are quoted in several references, (31) (84) and have been used throughout this analysis. The accuracy of determination is not stated, but in practice, the major source of error is likely to be due to an inaccurate knowledge of the air film temperature within the bearing. It was discovered that a value for this temperature could be derived by working backwards from a knowledge of the change in bearing clearance when 'hot'. The change in clearance between room and running temperature was given by the capacitor probe, and gave better results than direct thermocouple temperature measurements.

13. Lubricant viscosity (Continued)

Viscosity variation with ambient pressure is well documented. At very low pressures the viscosity tends towards a constant value and this non-linear relation must be taken into account when investigating bearing performance at high altitude.

Variation in composition of the lubricant will modify its viscous and compressibility characteristics and care is required to prevent cleaning solvent vapours from entering or remaining in the bearing. Precautions are also required when using certain types of temperature cabinet which use liquid CO_2 to achieve rapid cooling, the viscosity of this gas is significantly lower than that of air and some loss in bearing performance will occur if the bearing lubricant is displaced. Ambient humidity was maintained at approximately 45% throughout the test period.

14. Accuracy of applied loads

14.1 Torque loads

These are related to rotor speed, slew rate and rotor inertia. The two former quantities have already been considered, and inertia is calculated from the rotor dimensions and mass.

Rotor mass is known to within ±0.002%, on a laboratory balance, while all rotor dimensions are known to better than one Part in 4000. Density variations throughout the rotor material are closely controlled during manufacture and do not exceed 0.5%. Mass variation between rotors was ±0.13%, and it is reasonable to assume that inertia variations were also of this order.

14.2 Centrifugal loads

These are a function of the rotor mass, its distance from the centrifuge axis and the centrifuge speed.

Mass has been discussed previously, the radius arm is known to one part in 1000 and the rotational speed of the centrifuge arm is servo-controlled to within ±0.5%.

14.2 Centrifugal loads (Continued)

A simple centrifuge has the inherent disadvantage that a 'G'-gradient exists along the radius of the centrifuge arm. For small, symmetric bearings, this gradient is of little consequence, but for larger or more complex structures, the provision of a uniform 'G' field would be a distinct advantage.

It can be shown that if a separate platform is mounted at the end of the centrifuge arm and this platform rotated at an angular velocity equal and opposite to that of the arm, a uniform 'G'-vector will exist over the entire contra-rotating surface.

For investigating anisoelastic effects in large asymmetric bearing structures, it would be necessary to adopt this modified technique.

14.3 Gravitational loads

These are determined by the weight of the rotor, as measured on a laboratory balance to within 0.002%. The local gravitational constant has been measured close to the laboratory and is known to seven significant figures.

15. Accuracy of deflection measurements

Measurement of rotor deflection under load will be influenced by calibration errors, linearity errors and resolution errors in the probe and its associated equipment.

Since final calibration is carried out in situ against a known bearing clearance, calibration errors will be proportional to the clearance error (approximately ±4%). Eccentricity ratio and attitude angle are calculated from relative movements and are not affected by calibration errors.

Over the range of deflections considered, linearity error was found to be negligible, and as far as could be judged, the probe was capable of resolving the smallest deflection that could be generated.

15. Accuracy of deflection measurements (Continued)

By far the major sources of error are the combined effects of thermal/electrical drift and electrical noise. The special procedures adopted to overcome these errors have already been described, but it is clear that for movements below about 2 micro inches (0.05 micrometres), measurements are close to the threshold of the equipment.

Self generated noise in the probe system appears to be a result of non-homogeneous electrical properties in the rotor material, rotor run-out effects due to roundness and concentricity errors in the rotor assembly, and local defects (e.g. balancing and machining marks) at the rotor surface. With foresight, many of the above sources can be minimised and residual noise reduced to tolerable limits by careful use of electronic filters on the D.V.M.

Errors due to changes in probe area and dielectric gas constant with temperature can be shown to be negligible over the range of ambient temperatures involved.

Advise was sought from the manufacturers of the gauge unit to establish the minimum guard ring dimensions that could be used, and the usual corrections for rotor curvature applied where appropriate.

16. Dynamic rotor balance

Excessive rotor unbalance will have an indirect effect upon the accuracy of some of the measurements previously described, and is also undesirable from performance considerations.

For these reasons, each rotor was dynamically balanced to within 0.5 milligramme-cm of residual unbalance, prior to assembly of the test bearings.

17. Position of pressure tappings

The true position of each pressure tapping is known to within ±0.005" (±0.13mm). The accuracy is limited by the ultrasonic drilling technique eventually used on boron carbide components and can be improved considerably on softer materials.

18. Error analysis

The combination of random and systematic errors previously discussed are considered and an attempt made to summarise their nett effect upon those parameters which are of special interest.

Since almost all of the known errors are independent of each other, it would be unrealistic to perform a simple summation in each case. The appropriate errors are therefore compounded by accepted statistical techniques (71), to achieve a numerical estimate of the resultant standard error in each case. Any contributing error which is less than one quarter of the dominant error will be ignored, since experience shows that its contribution to the resultant error would be negligible.

(a) Dimensionless bearing pressure $\overline{P}$

For measured values of $\overline{P}$ up to 2.4, under normal ambient pressure conditions, an error of ±0.0079 is expected. Above this value of $\overline{P}$ the error may rise to ±0.025.

At reduced ambient pressures, an overall error of ±0.04 may be assigned to values of $\overline{P}$ below 2.4.

(b) Positional errors in the dimensionless pressure profile

The true angular-position error of a point on the circumferential pressure profile will be within ±2 degrees of arc and the corresponding error in the dimensionless axial co-ordinate $\overline{Y}$, of any point on the axial co-ordinate $\overline{Y}$, of any point on the axial pressure profile, will be ±0.0055.

(c) Eccentricity ratio and attitude angle

Estimation of measurement error in the above quantities is less easy than for the parameters already considered; both being associated with unpredictable drift, noise and other effects within the measuring system.

(c) Eccentricity ratio and attitude angle (Continued)

An indication of the random error component may be made by computing the standard error on the mean for a typical set of orthogonal deflection readings. The standard error is also computed for a typical set of calibration readings and the appropriate errors combined statistically as before to obtain the resultant standard error.

It is found that the resultant standard error on an eccentricity ratio of 0.0225 is ±0.0003. On an attitude angle of 16.96 degrees of arc, the corresponding error is ±0.3 degrees.

These errors are very small, due to the large number of deflection readings obtained at each rotor position, and decrease further as larger values of ε and ψ are measured. However, they relate only to errors of a random nature, and tell nothing about any systematic errors which may have been present in the measuring system.

(d) Compressibility number Λ

Uncertainties concerning the true value of bearing clearance represent the dominant error in the calculation of Λ, with viscosity variations due to temperature contributing to a lesser degree.

For $\Lambda = 15$, a resultant error of ±2.3 (±15%) is suggested, and this error will vary approximately pro rata over the range of Λ considered. This is because, in general, the parameters used to vary Λ (speed and ambient pressure) do not contribute significantly to the resultant standard error. Had significant variations in bearing clearance been used instead of speed and pressure variations, a disproportionate increase in resultant error would have occurred at higher values of compressibility number because the percentage clearance error increases as the nominal clearance is reduced.

(e) Time base error

The duration of events recorded on the bearing contact traces (Fig.12,13,14, etc.) are known to within ±0.01 seconds.

(f) Power dissipation

Calculations indicate a resultant standard error of about ±0.1 watts, originating from individual errors in decay, timing and rotor speed determination.

ACCURACY OF NUMERICAL RESULTS

Numerical solutions in general are limited by the truncation error involved in approximating the differential equations by difference schemes. In comparison with the truncation error, that due to the allowable residual EPSI can normally be ignored providing EPSI is small enough (EPSI is 0.001 for these solutions and therefore negligible in comparison with the pressure distributions obtained).

As discussedin CHAPTER 9.,it is believed that the predominant source of error here is due to the pressure ripple effect over the grooved region and it is therefore considered that in comparison, the overall truncation error can also be ignored at this stage.

APPENDIX IV

REVIEW OF MANUFACTURING METHODS

It is not within the scope of this paper to consider the specialised manufacturing methods in great depth; nor would this be possible, since many current techniques are the subject of varying degrees of commercial reticence. This is especially true of those techniques which have recently led to significant reductions in overall manufacturing cost.

Throughout this discussion, there will merely be considered the general principles of manufacture that are common knowledge, in-so-far as these influence the operational life and performance of the bearing. The techniques discussed may be applied to any bearing configuration, but this review will consider their application to the H-form bearing in particular. Comments and conclusions apply only to the manufacture of hydrodynamic bearings of small dimensions. Larger bearings (and therefore, one assumes, larger tolerances) may well be more accommodating, and many of the disadvantages referred to need no longer apply.

The final choice of manufacturing methods will usually be influenced by financial and 'local' factors, rather than by technical considerations alone. Local factors will include not only the availability of existing plant and facilities, but also the particular expertise and prior accomplishments of the manufacturer.

The final section of this Appendix will outline the manufacturing methods adopted in this instance.

1. Formation of the bearing surface

Three basic methods of construction are normally used to provide a wear resistant surface at those points within the bearing structure that are exposed to rubbing contact. Many variations on these three approaches are possible and any particular bearing design may utilise more than one method of construction.

1.1 Method One, Solid construction

Each bearing component is machined from a solid piece of material which has the desired physical and chemical properties.

1.1. Solid construction (Continued)

This method of construction is particularly suitable for ceramic and cermet materials, which may be either hot pressed or sintered to the desired form prior to machining. It has the prime advantage that mechanical stability and strength exist throughout the bulk of the component, and that interface problems encountered in fabricated structures are avoided. The rigidity and dimensional stability of ceramics and cermets in particular, allow geometric tolerances and surface finishes to be attained that would be almost impossible on softer or hard faced materials. In practice, these advantages more than compensate for the more obvious difficulties of rapid stock removal on hard materials in general. Unfortunately, only certain bearing configurations lend themselves to this form of construction, and in gyroscope applications, the multiple and conflicting requirements of rotor inertia, specific bearing loading, gimbal mass and electrical properties, often impose too great a compromise on the choice of the bearing materials.

A sleeved form of construction can be used to overcome some of these difficulties, but usually at the expense of increased manufacturing costs and decreased mechanical stability. Early difficulties in the bulk machining of hard materials have been largely overcome in recent years, and as a result, this form of construction can now be considered on equal terms with surface treatment methods.

1.2 Method Two, Surface treatment

Here, the bearing components are machined from a material not normally suited to bearing applications and the wear resistant surface formed at a later stage by physical or chemical treatment. The base material may be chosen either for its ease of fabrication (e.g. aluminium alloy or steel), or for special properties relating to other design features (e.g. beryllium or magnetic iron).

1.2 Surface treatment (Continued)

Surface treatment may include those cases where a wear resistant layer is built up on the base surface, as for example in flame spraying, vacuum deposition, electroplating, and ion-plating, or where chemical conversion of the original surface has taken place during case hardening or ion-implantation. A clear distinction cannot easily be made because some of the coating techniques (88) may be modified to produce a diffused alloy layer between the wear resistant coating and its base material. This improves the adhesion and eliminates a sudden change in properties throughout the bearing hintersurface.

Surface treatment has the advantage of preserving the original magnetic, electrical or mechanical properties of the base material and retaining (if necessary) the bulk differential expansion coefficient where dissimilar wear surfaces are specified. It has the added advantage that pumping grooves and other features may be formed by masking the bearing surface during the application of a wear resistant layer.

Unfortunately, a number of disadvantages are inherent in the use of surface treatments to form wear resistant surfaces.

Commercial flame spraying often results in a porous structure that is only suitable for the largest gas bearing applications and problems of adhesion, cracking and distortion are not unknown. Internal diameters are difficult to treat and the degree of difficulty increases rapidly with the $\frac{L}{D}$ ratio; becoming uneconomic when $\frac{L}{D} > 3$. Specialist spraying of certain materials, for example detonation plating of chrome oxide, can yield excellent results, but are very costly and only available in the U.S.A. With the exception of vacuum deposition and ion-plating, other coatings require subsequent machining in order to obtain the required bearing dimensions and surface finish. Since the original 'datum' surface has been lost, it is often necessary to provide an additional datum surface which can be protected during the coating process, and which can be used as a reference location during final machining.

1.2 Surface treatment (Continued)

If this reference is not provided there is a danger of breaking through the thin coating during final machining, and uniformity of depth cannot be guaranteed if any pre-formed pumping grooves are present.

This requirement to provide a highly accurate reference surface, together with the inevitable masking problems and the need for further machining tends to cancel many of the advantages of a coated construction. Vacuum techniques for the deposition of very thin homogeneous films can overcome these disadvantages, but only at the expense of high capital cost.

1.3 Method Three, Moulded bearings

In this form of construction a plastic or composite material is applied to the surface of an accurately formed master. After solidification or curing, a replica of the original surface is produced without the need for further machining. Pumping grooves and other features may be moulded directly in certain cases and the moulding matrix may incorporate solid lubricants and fibre reinforcements as desired.

Despite its potential for producing hydrodynamic bearings at very low cost, and recent development in at least two government research laboratories*, this method of manufacture has not yet emerged as one suitable for widespread application to precision gyroscopes. Dimensional stability over the operational temperature range is one major drawback and the wear properties of the bearing surface are not suitable for bearings of high specific loading. Bearing clearance will be influenced by shrinkage after moulding and it is unlikely that this can be controlled to within the required dimensional limits. This latter restriction does not necessarily apply to conical or hemispherical bearing designs, where selected spacers can be used to achieve the correct degree of clearance, but would represent a major obstacle in the large scale manufacture of H-form configurations.

* The Royal Aeronautical Establishment Farnborough and the National Tribology Centre, Risley.

1.3 Moulded bearings (Continued)

Of the three basic construction methods considered, fabrication of each bearing component from solid material would appear to represent the designer's first choice, provided that the properties required of the bearing material or materials are compatible with those demanded by the assembly as a whole. The success with which this compatibility may be achieved will depend upon the initial choice of bearing configuration and designer's ingenuity. Surface treatments are only to be recommended where a solid construction has been discounted for other technical reasons. Moulded bearings do not appear suited to current gyroscope requirements and will not be considered further.

2. Grinding

The hardness of the bearing surface and the dimensional accuracies involved normally rule out turning, and leave grinding as the basic machining method used on most current bearing designs. Diamond wheels are required on the harder materials.

Grinding is used to provide the basic size and geometry of the bearing surface, but surface finish and texture normally require further attention. The grinding techniques used are an extension (though sometimes a considerable extension) of normal high precision grinding practice. For experimental quantities, grinding can be used for stock removal only; geometry and size being obtained later by corrective hand or machine lapping. This approach can be shown to be uneconomic for production batches and the grinding technique must be refined to produce the closest possible approximation to the final bearing contour.

Few commercially available grinding machines are capable of machining to the required limits on actual bearing components, though their performance on artificially rigid 'test mandrels' may be deceptively acceptable. Those machines meeting the required specification invariably utilise hydrodynamic oil-fed bearings on the wheelhead and radial stiffness is maintained by automatically closing the running clearances as the wheel speed is reduced.

2. Grinding (Continued)

Hydrostatic air bearings have been applied to some grinding machines and the resulting improvement in true running of the spindle axis has allowed sub-micro inch surface finishes to be obtained from grinding wheels that would normally be used for rapid stock removal. This is due to the fact that each protruding grit on the wheels periphery cuts to almost exactly the same depth at each rotation of the grinding wheel. Surface finish therefore tends to be independent of the grit size and is more closely related to the radial 'run-out' of the spindle axis. In contrast, the more conventional grinding machine must use very fine abrasive wheels if sub-micro inch finishes are required and significant running errors are present in the wheel spindle bearings. The two types of finish are contrasted in Figures 59 & 60.

In the writer's experience, radial stiffness of the workhead and wheelhead bearings represents the most important single factor in the consistent attainment of the tolerances under discussion, and this requirement is still not fully appreciated by all manufacturers of grinding equipment. A minimum radial stiffness of 1×10^6 lb per inch (7×10^8 Kg/m^2) appears to be advisable, and while this is readily achieved on hydrodynamic oil bearings, hydrostatic air bearings are generally limited to approximately 5×10^5 lb per inch (3.5×10^8 Kg/m^2) when operating from a normal workshop air supply.

The above remarks refer specifically to cylindrical grinding but apply equally well to the production of thrust surfaces by surface grinding.

3. Honing

Contrary to popular belief, the honing process does not always correct the geometric errors introduced by conventional machining methods. While the classical three-point lobing can normally be corrected to within conventional engineering tolerances, it is possible for honing to exaggerate roundness errors on components whose geometry is approaching the limits referred to in CHAPTER 3

3. Honing (Continued)

This is particularly true of diamond honing on small diameter ceramic components and may be related to the rapid rate of stone and shoe wear in this case. Parallelism and straightness are also difficult to control on small $\frac{L}{D}$ ratios and for these and other reasons, honing does not appear to be widely used for producing hydrodynamic gas bearings.

Many of the techniques of honing have been extended into the field of thermo-chemical polishing (Appendix IV Section 5.2) with considerable success.

4. Lapping

Lapping ranks as one of the oldest and most basic machining methods, and, given time and expertise is capable of meeting almost any geometric or surface finish requirement. Capital equipment costs are very low and lapping has been used, in one form or another, for machining gas bearings since their inception. It can be used to produce final geometry and finish, and subject to economic considerations, can be considered as an effective means of adjusting the basic dimensions of the mating components. Recent development has concentrated on removing some of the traditional mystique surrounding its application to gas bearing components and it can now be regarded as a viable production technique.

Two basic forms of lapping process may be distinguished in relation to gas bearing work. Both rely upon the generation of either a random or complex motion between the lap and workpiece. In Free Abrasive Lapping, relative motion occurs between both the lap and the abrasive particles and between the workpiece and the abrasive particles throughout the lapping cycle.

This combined rolling and skidding action of the abrasive across the workpiece results in rapid stock removal and in metals and cermets, the lapped surface will have a matt appearance and will consist of large numbers of intersecting scratches - comparable in depth to the abrasive dimensions.

4. Lapping (Continued)

Ceramic materials will generally exhibit a broken granular structure and may also show occasional scratch tracks as in Plate 42 & Fig. 58.

In Contained Abrasive Lapping, relative motion only occurs between the abrasive and the workpiece; each abrasive particle being firmly embedded into the surface of the lap. The rate of stock removal is considerably lower than for the previous case and very fine surface finishes can be obtained on some materials (see Plate 40). Magnification of metallic workpieces reveals an infrastructure of fine random scratches whose depth is proportional to the protruding portion of a typical abrasive grain from the lap surface. These fine scratches are illustrated in Fig. 57.

A third form of lapping action is possible in which a bonded abrasive structure is substituted for the conventional lap. Operation is a mixture of free and contained abrasive action and surface finish is therefore limited by the strength of the abrasive bond. Bonded abrasive lapping has not been widely used for gas bearing manufacture.

In practice, most lapping operations involve a combination of free and contained abrasive action and the success of finish lapping depends largely upon how well the free abrasive component can be suppressed. Diamond grit is the most commonly used abrasive for gas bearing lapping. Breakdown of individual diamond particles throughout the lapping cycle occurs less readily than with softer abrasives and initial preparation of the lap surface will therefore have a decisive influence upon the quality and texture of the finish ultimately obtained.

Finish lapping of gas bearing surfaces will normally show two major defects which, while they are not unknown in normal commercial lapping, assume a far greater degree of significance in relation to gas bearing components. Once an otherwise acceptable lapping sequence has been established, these defects tend to lie outside the operator's control and can result in an unacceptable number of rejects at the inspection stage.

4. Lapping (Continued)

The first type of defect is known as 'surface pull-out' and occurs predominantly in ceramic and cermet structures. Here, as shown in Plate 40.(c), the lapping action plucks some of the looser surface grains from the workpiece matrix and the surface texture is progressively degraded. Surface finish measurements alone will not reveal this effect and optical inspection must be used. In extreme cases, the workpiece assumes a granular appearance and the required surface finish will not be attained. The second defect is characterised by occasional 'comet tails' and ragged scratches across the lapped surface. This is due to contained abrasive grains pulling out or shearing at the lap surface and subsequently rolling between lap and workpiece. It can also be caused by rolling 'pull-out' grains from ceramic and cermet components. The two effects are closely related in ceramics and cumulative damage to the lapped surface may occur in loosely bonded materials.

Recently published work from M.I.T. Draper Laboratories (77) has shown that pull-out can be almost totally eliminated by high pressure lapping. In this technique, the lap and workpiece are apparently forced together under hydraulic pressure during lapping. Contact pressures up to 20,000 p.s.i. (140 MN/m^2) are used and considerable improvements in surface finish over conventional lapping are reported.

The mechanism responsible for the success of high-pressure lapping has not, as far as the writer is aware, been widely discussed, but from lapping experiments here it appears that the very high pressure forces both workpiece and lap into intimate contact over the entire area of the workpiece, leaving literally no space for loose surface grains to enter. There also appears to be a secondary effect in which the contained abrasive particles are pressed deeper into the lap, with the now smaller protruding portion producing shallower cuts and hence a finer overall surface finish.

4. Lapping (Continued)

Though technically successful, high pressure lapping does require costly and elaborate equipment, especially if applied to other than flat surfaces, and its widespread use is likely to be retarded on this account.

Suitably shaped laps and appropriate lapping motions can be used to form accurate bores, journals and hemispheres in addition to flat thrust faces.

5. Polishing

Polishing, in one form or another, is normally required to improve the surface finish and texture of gas bearing wear surfaces. The reasons for this are related to life and reliability rather than performance and have been discussed in detail in previous Chapters. Polishing may be conveniently sub-divided into conventional polishing and the relatively new thermo-chemical polishing. In both cases, polishing must be carefully controlled and severely limited in its extent if deterioration of basic geometry and size are to be avoided.

All forms of polishing are regarded with justified concern within an industrial environment because they are difficult to perform by fully automatic equipment and tend to rely heavily upon operator skill and experience. Unless a high level of supervision is provided, this reliance upon hand-finishing or semi-hand finishing methods will result in problems of consistency and quality control. On gas bearing surfaces, these problems are exaggerated further by the measurement difficulties involved when investigating sub-micro inch finishes. Measurements, especially of surface texture, tend to become subjective unless very sophisticated equipment is employed and it may be unrealistic to expect this equipment to be available on the shop floor.

5.1 Conventional Polishing

Improvement of gas bearing surfaces by conventional polishing is a fairly well known, if not well understood technique.

5.1 Conventional Polishing (Continued)

Modern gas bearing work normally involves the use of fine diamond abrasives and is directed at materials of 1000 V.P.N. hardness or greater. Unfortunately, most polishing research has been carried out using soft metals and may not be entirely relevant to hard ceramic and cermet materials. On the basis of this work, two rival theories have been proposed; the melting hypothesis and the fine abrasion hypothesis.

The melting hypothesis suggests that material is smeared from the high spots to form a thin smooth skin over the polished surface. This skin is called a Beilby layer after its discoverer Sir George Beilby, who demonstrated the re-appearance of scratches when the layer was dissolved by etchant. An alternative explanation of the effect was proposed by Samuals in 1956, who observed that an etchant could preferentially attack the damaged material beneath the visible scratch after the scratch itself had been removed by other means.

While the presence of a Beilby layer can be convincingly demonstrated on softer metals, it does not explain the action of polishing on ceramic and cermet materials. The soft cobalt matrix in (say) sintered tungsten carbide, may allow a partial smearing action between the carbide grains but 'Steroscan' photographs indicate straightforward abrasion on the sectioned surface of individual grains. This can be seen in Plate 31. Aluminium oxide crystals within a dense compact also show a fine criss-cross pattern of scratch marks under "Steroscan" examination after fine polishing on contained diamond abrasive. Bowden and Hughes (39) showed an apparent relation between polishing ability and melting point of the materials involved, but more recent work has shown that this does not hold for materials with a high melting point. Since most current bearing materials tend to have a high melting point, it is found in practice that the corresponding polishing abrasives are chosen for their relative hardness to the material being polished.

5.1 Conventional Polishing (Continued)

The fine abrasion hypothesis first proposed by Newton suggests that polishing merely covers the surface in question with very fine scratches. If one accepts the wave theory of light, it can be shown that scratches which are closer together than the wavelength of light, or shallower than half the wavelength of light will not influence reflection from the polished surface. Light will therefore be reflected from the surface as if it were perfectly smooth and the scratches themselves would be invisible under any optical magnification. It would still, however, be possible to see many of these scratches under a scanning electron microscope, which thus becomes a powerful tool for the study of polished bearing surfaces.

Rabinowiez (27) has recently proposed that neither of these two old and rival hypotheses is entirely correct. His tests have shown that polishing is akin to burnishing, in which molecules are ripped from the high spots at loads below a certain critical load. This produces a surface which is smooth on a molecular scale. For loading above the critical level, large clusters of molecules are torn from the surface and a relatively rough finish is produced. The critical load is directly related to the molecular bonding forces involved. Polishing and burnishing are distinguished in practice by the relative magnitudes of the critical loads. In each case, soft matrix polishing allows a very much higher load to be applied and is considerably faster.

Rabinowiez's analogy with burnishing suggests that firm matrix polishing on a molecular scale should not occur above a relatively modest critical load. If this conclusion is referred to the very fine surface finishes obtainable from high pressure lapping (77), an apparent conflict is seen. Unfortunately Rabinowiez's work was carried out on soft metals (e.g. Copper, Silver, Aluminium etc.) and did not consider materials of extreme hardness that are now successfully polished by high pressure lapping.

5.1 Conventional Polishing (Continued)

The most likely explanation appears to be that high pressure lapping will deform both surfaces in question until their contact area approaches 100%, compared with contact areas of less than 0.1% in a typical burnishing situation when using a radiused tool. This results in a considerable decrease in true specific load and, when combined with the high molecular bond forces in ceramic and cermet materials, allows proportionately higher values of critical load to be achieved.

Experience here, based upon the examination of many hundreds of polished bearing samples by optical, profilometer and 'Steroscan' methods tends to confirm for hard materials Rabinowiez's general conclusion on soft materials; i.e. that polishing is a form of micro-machining on a molecular scale. Smearing or melting of the surface has not been observed and exceptionally fine finishes can normally be obtained over a wide range of surface speeds and pressures, provided 'pull-out' and grain dislodgement can be avoided.

In practice, conventional polishing of gas bearing surfaces is usually carried out dry, using a contained abrasive. Polishing in general is normally associated with the use of a soft matrix or mop to contain the abrasive grit, but in gas bearing work, such an approach is of limited value. Uncontrolled rounding of corners and an overall degredation in geometry invariably results as the soft matrix distorts under polishing pressure and polishing is prolonged. On fine ground metal bearing surfaces, a useful improvement in surface finish can be obtained by correctly chosen techniques, but it is seldom possible to remove all machining marks without distorting the basic bearing shape.

To overcome the problem of geometric distortion, gas bearing polishing is often carried out on a firm matrix, for example cast iron, which has previously been prepared to a geometric accuracy approaching that ultimately required on the final component.

5.1 Conventional Polishing (Continued)

Very careful and lengthy preparation is required before polishing to ensure that all the abrasive grains are held firmly in the matrix, for if a single grain becomes detached, a free abrasive situation will result and the ensuing scratches will only be removed by resort to lapping on a coarser grade of abrasive. Here lies the weakness of polishing on a firm matrix, for grain dislodgement will occur more easily under the relatively high friction conditions of dry lapping. This can be clearly seen in Plate 41.

A number of ingenious methods have been evolved to overcome the problem of grain dislodgement during polishing. One, attributed to the Royal Aeronautical Establishment, Farnborough, uses a layer of 0.0008" (0.02mm) thick aluminium cooking foil over the surface of a conventional lapping plate. The soft aluminium surface allows the abrasive to embed easily and subsequently deforms around each grain under lapping pressure, effectively locking it in place. The rigid under-surface maintains the necessary geometric accuracy. Although excellent results are obtained on a laboratory scale (see Plate 39 and Figure 56), the method is not entirely suitable for production use.

From the previous discussions it can be seen that the distinction between polishing and lapping on gas bearing surfaces is small and is often one of degree only. Polishing as such will normally imply contained abrasive on a dry surface, but much will depend upon the nature of the bearing material and the ultimate finish and geometry required.

5.2 Thermo-Chemical Polishing*

This effect was discovered by chance in this laboratory, when it was noted that synchronous overload of a boron carbide bearing resulted in a very highly polished patch, superior in surface finish to the original polish that was being achieved at that time.

* (In the absence of any recognised nomenclature, the writer will refer to this technique as 'Thermo-Chemical Polishing'. For the example discussed, heat and subsequent chemical action appear to be the principal distinguishing features.

* The term 'dry-lapping' has been used elsewhere but since conventional lapping may also be performed without lubrication, an alternative name is appropriate.

(It was later learnt that the effect had previously been observed by various other workers when attempting to grind boron carbide sand-blast nozzles with high speed aluminium oxide wheels). Boron carbide is the only material known here that will respond to this form of polishing and may be unique in this respect. However, it is possible, in principle, that other materials could be polished in an analogous manner and in boron carbide bearings, thermo-chemical polishing can play an important part in the wear process. For these reasons the mechanism of this form of polishing will be considered in some detail.

Thermo-chemical polishing of boron carbide may occur when the material surface is subjected to frictional heating and high local pressure in the presence of oxygen. The surface layer is progressively oxidised and a rich black polish is produced on the carbide surface. Surface finishes down to 0.1 micro inches C.L.A. are rapidly achieved and the original geometry either maintained or improved.

Chemical changes at the ceramic surface are summarised by the following reaction.

$$B_4C + 3O_2 = 2B_2O_3 + C \qquad (85)$$

Local temperatures of between 600°C and 1000°C appear to be necessary for chemical conversion of the surface layers to occur at an appreciable rate. The reaction given in equation 85 may not be strictly accurate because the stoichiometric composition B_4C is only an approximation. A variety of boron-carbon 'compounds' are said to exist and Podszus (38) has identified BC_1, B_2C, B_3C, B_4C and B_6C. Commercial 'boron carbide' referred to in this report is almost certainly a mixture of several crystaline forms, and the formula $B_{3.8}C$ has been suggested as stoichiometrically correct.

5.2 Thermo-Chemical Polishing (Continued)

The reaction is further complicated by the fact that the nascent carbon in equation 85 may react further with an excess of oxygen and yield either CO_2 or CO at higher temperatures. Carbon dioxide may in turn allow further oxidation of the carbide according to the relation

$$B_4C + 3CO_2 = 2B_2O_3 + 4C. \qquad (86)$$

In a straightforward chemical oxidation of boron carbide, Glasson and Jones (37) suggest that at low temperatures, the initial diboron trioxide layer protects any remaining boron carbide and newly-formed carbon; oxidation then relying mainly on diffusion of oxygen through the trioxide surface. It is unlikely that such a diffusion process could occur during thermo-chemical polishing, since any oxidation products are immediately removed from the surface by mechanical action, and at temperatures around 1000°C, the volatility of diboron trioxide allows little protection. This rapid removal of the softer oxidation product provides the most satisfactory explanation for the rapidity of the polishing process once suitable conditions have been established.

Originally, it was believed here that thermo-chemical polishing of B_4C in air could lead to the formation of small quantities of hexagonal boron nitride and graphite and that these lamellar materials subsequently behaved as solid lubricants during the polishing process. It now appears improbable that the high temperatures (1800 to 1900°C) required for nitridation are obtained and that any lubrication is a direct result of the continuous formation of a relatively soft oxide of low melting point (450°C). Some additional lubrication may be provided by the free carbon by product of the oxidation reaction and lamellar graphite inclusions have been observed in 'Steroscan' photographs of B_4C fracture faces. The latter source of lubricant is not substantiated in practice, where low quality (commercial grade) carbide containing significant amounts of graphite second phase is found to be no easier to polish than high quality (instrument grade) material in which lamellar graphite is not evident.

5.2 Thermo-Chemical Polishing (Continued)

In practice, thermo-chemical polishing is carried out by rubbing the bearing surface at high speed against a second surface. This second surface is normally, but not necessarily, composed of boron carbide. Polishing is carried out dry, without application of any external lubricant or abrasive and is initially accompanied by a harsh shrieking noise and considerable heat generation. Careful control of contact pressure will allow the process to go through a number of audible changes, culminating in a relatively noiseless condition which has been found to correspond to the optimum polishing state. Thin white powdery filaments are generated and appear as a 'candy-floss' structure around the component. This material has been analysed in the company's laboratory and was found to contain diboron trioxide.

A prime requirement for the second surface is that it should have a high melting point, in order to survive the high local temperatures involved. Its hardness and wear resistance should also be sufficient to allow its geometry to remain essentially unaltered throughout the polishing cycle, otherwise distortion of the bearing surface may occur. Diamond cannot be used because rapid oxidation and eventual combustion will occur in air at temperatures of around 800°C.

The use of boron carbide against itself is a particular case in which simultaneous polishing of both surfaces occurs.

'Steroscan' examination of a polished boron carbide surface indicates that level plateaux are first formed across the protruding peak of each material grain. As polishing progresses, each plateau increases in area until a level surface showing only intergranular porosity is produced. The exceptional grain boundary strength of hot pressed boron carbide prevents pull-out of individual grains during thermo-chemical polishing and each grain is individually sectioned by the oxidation process. As polishing proceeds, the reactive area increases rapidly at first before slowly approaching an asymptotic value determined by the residual porosity of the material.

5.2 Thermo-Chemical Polishing (Continued)

Thus while the rate of stock removal tends to remain fairly constant, the rate of dimensional change falls off rapidly as a satisfactory surface polish is approached. This is a considerable advantage when considering the very real problems of polishing actual components as opposed to unimportant test pieces.

'Steroscan' investigations of individual crystal grains (Plate 38) show hardly any scratches across the polished area, in sharp contrast to even the very finest form of conventional polishing. Polishing debris is absent under the highest magnifications involved. It is this elimination of fine scratches and debris, coupled with the relatively large proportion of the surface that can be levelled (due to lack of pull-out) which gives thermo-chemically polished boron carbide its characteristic colour and sheen (See Fig.55).

Stokes (36) has reported plastic flow in boron carbide after polishing but despite examination of many dozens of 'Steroscan' photographs, the writer has observed no evidence of this occurring.

6. Groove Formation

Hydrodynamic gyro bearings invariably utilise grooving, pockets or similar features at the bearing surface. These discontinuities are used to generate or modify the load capacity and stiffness of the bearing, and also to suppress certain hydrodynamic instabilities which might otherwise occur. Renewed activity in grooved bearings has made the manufacturing methods concerned of particular interest, and it is shown in CHAPTER 7. that their choice is a decisive factor when considering the operational life and reliability of a completed bearing assembly.

The methods are listed in approximate order of current usage and have been employed to form steps, pockets and grooves in a variety of bearing materials. Gyro bearings normally employ helical or spiral groove patterns and the conclusions will therefore refer specifically to features of this form.

6.1 Air-Abrasive Methods

A fine stream of abrasive grit is directed against the masked bearing surface and the cutting action of the abrasive allowed to erode the exposed bearing material until the desired groove depth has been obtained. Wet or dry abrasive may be used and aluminium oxide, silicon carbide or boron carbide are commonly chosen.

The abrasive impact results in a very granular finish at the base of the groove and lateral penetration under the edge of the mask produces very ragged side walls and damage to the bearing wear surface. Mask wear can also be a problem and groove depth and consistency are very difficult to control on small bearings. Air-abrasive machining's major disadvantage is that large amounts of loosely attached debris remain at the floor and walls of the grooves. In softer materials the abrasive grit becomes partially embedded in the groove while on harder multi-phase ceramics and cermets, large grains of bearing material stand proud of the mean groove surface. For materials in the hardness range 600 to 2000 V.P.N., air-abrasive machining is relatively effective, but outside this range the cutting efficiency decreases. On materials of extreme hardness, impact of the abrasive can cause fracture of individual crystal grains and increase the likelihood of spontaneous debris generation in service.

Despite the above disadvantages, continued development has allowed air-abrasive techniques to assume a major role in bearing manufacture. They require inexpensive equipment and are widely used on both experimental and production bearing programmes. Figure 70 illustrates the irregular texture of a typical air-abraded groove.

6.2 Ion-Machining

Ion-machining is similar in many ways to air abrasive machining, with the exception that atomic particles, for example argon ions, replace the abrasive grit and electrostatic forces are used to accelerate the 'abrasive' particles instead of air.

6.2 Ion-Machining (Continued)

A full description of the process is given by the author in reference 72, and will not be repeated here.

In sharp contrast to abrasive machining in particular and to other forms of machining in general, ion-machining leaves the bearing surface totally free of debris and loose material. An excellent surface finish is possible at the groove base and virtually no undercutting occurs at the groove edge. 'Steroscan' examination reveals a smooth radiused contour that is typical of ion bombardement. (See Plate 43 & Figs. 67 & 68).

Ion-machining is effective on any material regardless of its mechanical hardness, and very accurate control of machining rate is possible. Capital equipment costs were originally high but recent refinements have reduced these by a factor of three or more.

6.3 Spray Masking

Where the wear resistant surface is applied by metal spraying or detonation plating, suitable metal masks may be used to form the groove pattern directly. Groove depth may then be reduced to design limits by subsequent machining on the hard surface. Surface finish at the base of each groove will be determined by the initial machining but the nature of the spraying technique leaves the groove edge badly defined and liable to crumble during final machining. The use of photoetched metal masks may give rise to various edge effects during spraying and sharp walled grooves may be difficult to obtain. Where large numbers of pumping grooves are required on small bearing components, the masks themselves are both fragile and costly, and further practical complications arise when the bearing surface has either single or double curvature.

At its best, flame spray masking can produce an acceptable groove pattern on flat thrust bearings above one inch in diameter, but it is an expensive process and the resultant groove edges are often a source of debris. Many of the disadvantages of spray masking relate to the use of flame spraying in general, and these are discussed in section 1.2. of this Appendix.

6.4 Electrical Discharge Machining

Electrical discharge or spark-machining can be used in those cases where the bearing material is electrically conductive. Its application to ceramic bearings is therefore limited to semi-conducting materials like silicon and boron carbide. Conventional EDM equipment is used and the required groove pattern formed on the electrode surface by chemical photo-etching or die-sinking methods.

When used to machine pumping grooves in silicon or boron carbides, the electrical input power is limited and this results in a low machining rate. For boron carbide in particular, any attempt to increase the input power can result in the component 'exploding' under the combined effects of thermal and electrical stress. Because very shallow grooves are usually required, this does not usually represent a practical limitation and with suitable equipment a number of components may be machined simultaneously.

Electrical discharge machining will yield grooves of good lateral definition and consistent depth, but under high magnification, the machined surface is found to be very rough and littered with solidified machining debris. The electrical energy of each spark discharge is sufficient to locally melt the bearing surface and this material is immediately quenched by the surrounding oil. On the ceramic materials described, this sudden quenching causes a network of fine cracks to form in the fused surface layer. These surface cracks are comparable in depth to the pumping grooves themselves and are highly undesirable from the bearing point of view.

Groove formation in single or double curvature surfaces is theoretically possible but electrode wear and other practical difficulties have limited its general application to flat thrust surfaces. Capital equipment costs are fairly high but since most large manufacturers use EDM equipment for other purposes, this does not normally preclude its use.

6.5 Diamond Scribing

In this manufacturing method, a diamond tool is traversed over the bearing surface a number of times to form each groove. Hemispherical bearings have been grooved in this manner* using a three-dimensional pantograph arrangement and indexing the bearing after each cut. Brittle ceramic materials like chrome oxide have been machined in this way and groove profile and depth control are determined by the accuracy of the equipment. For gyro bearings, an exceptionally high order of precision is implied.

The process is slow and laborious where large numbers of grooves are involved and the cost per instrument is likely to be very high. Commercial equipment is not, as far as the writer is aware, available, and its development and manufacture must be regarded as a major undertaking.

Lateral groove definition is good but a finite number of traverses along each groove will result in a ragged finish to the groove base, together with the possibility of loosely attached machining debris. Definition at the blocked end of a groove is poor.

6.6 Ultrasonic Machining

Conventional ultrasonic machining equipment may be used to produce groove patterns in hard bearing surfaces and either boron carbide or diamond dust abrasive are commonly used. With care, rapid stock removal can be achieved but the process is not readily applied to large scale production and continuous supervision and adjustment are required.

Lateral groove definition is limited by excess slurry around the edges of the tool and brittle ceramic materials are prone to chipping under resonance conditions between the tool and workpiece. Surface finish will be related to the size of abrasive grit, but even with sub-micron diamond, the machined surface is rough and irregular with evidence of loose debris and ingrained abrasive.

* M.I.T. Draper Laboratories (87).

6.6 Ultrasonic Machining (Continued)

Ultrasonic machining of curved surfaces presents many problems and like spark-machining it is generally confined to grooving flat thrust plates.

6.7 Chemical Etching

Chemical etching is one of the more obvious methods of forming shallow depressions but it pre-supposes that a suitable etchant for the material in question can be found and that a corresponding resist* is available. Most metals will respond to correctly chosen or blended etchants but ceramics and cermets are attacked less readily.

Masking is normally carried out by applying a commercial photo-resist lacquer to the bearing surface and exposing to U.V. light through a photographic negative of the groove pattern. After processing the remaining resist protects the bearing land area and etching may proceed in the groove region. Photo-etch masking on single or double curvature surfaces has presented formidable problems but a successful method has been developed at the Royal Aeronautical Establishment for conical surfaces. In this method a projection system is used to form an image of the groove pattern over the sensitised bearing surface. The pattern is projected down the axis of the cone and the optical characteristics allow a sufficient depth of field to ensure an acceptably sharp groove pattern over the cone surface (68).

Groove definition is limited by lateral etching of the groove walls and eventual undercutting of the resist pattern. Physical and chemical modifications to the etching arrangements are possible which reduce the tendency for lateral erosion and promote vertical attack, but undercutting still remains a major limitation where fine groove patterns are desired.

Chemical etching in general will preferentially attack the grain boundaries of the bearing material. As a result, etch rate is often unpredictable and very poor surface finishes can be obtained.

* A chemical substance applied to the surface of the material to protect it from the action of the etchant.

6.7 Chemical Etching (Continued)

Loosened grains present a debris hazard and intensive cleaning techniques are necessary to ensure complete removal of the etchant from within the pores of the material. This preferential etching of grain boundaries has been put to good use by at least one research group (87) who have chemically deposited nickel plating in such a manner that all the grain boundaries are normal to the substrate surface. Vertically etched walls with minimal undercutting are therefore possible. Though developed for the production of ion-machining masks, this arrangement may eventually lead to a useful extension of direct chemical etching on plated bearing surfaces.

Control of groove depth is frequently difficult when using chemical etching methods. Where wear resistant coatings can be applied to the bearing surface, it is often possible to select an etchant which will attack the coating but not the base material. In this way, grooves of accurate depth can be produced but excessive etching can preferentially attack the interface between coating and substrate and lateral groove profile is rapidly destroyed.

Rapid expansion of the semi-conductor industry has seen the development of many sophisticated photo-etch systems* and it is probable that many of these could be adapted to gas bearing manufacture. Unfortunately, many of these multi-stage processes are very complex and require an exceptionally high degree of control to ensure optimum results. This in turn implies a high order of expenditure which may not be justified on small manufacturing programmes.

6.8 Electro-chemical Etching

This method of groove formation is very similar to chemical etching. It is particularly useful on semi-conducting ceramics and cermets which are either resistant to normal chemical attack or would require etchants for which no photo-resist is known.

* For example the 'RISTON' photopolymer film resist system developed by the Du Pont company.

6.8 Electro-chemical Etching (Continued)

Boron carbide for example is unaffected by acids and alkalies at any temperature, whereas electro-chemical etching can be carried out using potassium hydroxide electrolyte at a potential of a few volts.

In a simple etching system, the workpiece forms the cathode of an electrical cell containing a suitable liquid electrolyte. An electric potential between the electrodes will then cause erosion to occur over the unmasked surface of the conducting workpiece.

Disadvantages are common with those for ordinary etching, but in practice, the grain boundaries are attacked to an even higher degree and surface finish and depth control are very poor. (As a consequence, electro-chemical etching is frequently used to examine the grain structure of bearing materials prior to machining). A typical groove is illustrated in Plate 45 and Fig.69.

6.9 Vacuum Deposition Masking

Pumping grooves may be formed by vacuum deposition of wear resistant material through a suitable masking arrangement. One such technique is described in detail by the author in reference 88, but many variations on this theme are possible. Very clean and accurate grooves can be obtained. Edge effects and errors introduced by the masking system have a tendency to produce rounded corners at the working surface of the deposit, but defects of this nature are free from debris and are normally acceptable. Unlike spray masking methods, no further machining is required and potential damage to the groove edges eliminated.

Groove formation by acid etching of vacuum deposited films may not be practicable since many films are more homogeneous than their parent materials and therefore less susceptible to chemical attack.

6.10 Lapping

Various lapping methods are available for forming groove patterns, but these are little used on current gyro bearings.

6.10 Lapping (Continued)

Accurate depth control and sub-micro inch finishes are obtainable but lateral groove definition is difficult to maintain. Groove lapping to gyro bearing standards is a slow process, especially on hard materials, and less suitable for large scale production than some of the techniques previously described.

Individual lapping of each thrust plate groove is required and in this case, uniformity of depth between adjacent grooves may be difficult to obtain. Simplification of tooling is often obtained by using a circular arc groove profile instead of the optimum logarithmic spiral pattern, but special purpose equipment is still required. Helical grooves on cylindrical journals present a more difficult problem, but the use of existing automatic gear hobbing machines has been suggested as one possible solution. In this method the gear hob would be replaced by a suitable 'lapping hob' and progressive generation of all grooves obtained as relative motion occurs between the rotating hob and shaft at their point of contact.

Groove lapping increases in difficulty as the bearing size decreases and as the number of grooves becomes larger. Lap wear then becomes a major problem and lap replacement is both time consuming and costly.

6.11 Grinding

Circular arc and helical grooves may be generated by selective grinding of the bearing surface but in practice, this method of groove formation is not economically viable for small bearings containing large numbers of grooves. Ground grooves are generally free from attached debris but grinding burrs are thrown up on the groove corners and must be removed before use. Larger hydrodynamic bearings are sometimes produced in this manner, but the technique has little to commend it when compared with, for example, air-abrasive methods of groove formation.

6.12 Milling

Milling is not suitable for groove formation on precision hydrodynamic gyro bearings. It has been used successfully on larger hydrostatic gyro bearings, and also on large scale hydrodynamic models where relatively soft bearing materials can be employed.

6.13 Coining

Coining of ductile bearing components (12) will produce an accurate and debris free groove pattern but like milling, is not suitable for precision hydrodynamic bearings.

6.14 Moulding

Where a moulded of cast bearing structure can be tolerated, a groove pattern can be formed directly as a replica of an accurately machined master component. Excellent debris-free grooves can be produced in this way but as already explained, moulded forms of construction have found little application to modern gyro requirements.

6.15 Foil Bonding

By photo-etching or stamping a suitable pattern out of thin metal foil and then bonding this foil to a machined bearing surface, a grooved bearing may be formed in which the groove depth is determined by the foil thickness and in which the wear surface is composed of foil material. The manufacturing technique for flat thrust bearings is described by Muyderman (67).

Though suitable for some larger bearings it is doubtful if this method of manufacture could be used on gyro bearings.

6.16 Laser Machining

Laser machining of bearing grooves has been proposed for a number of years but the writer is not aware of this having been carried out on anything more than an experimental scale. Masking or pattern generation methods may be used but a study of current laser technology suggests the application of laser machining to gas bearing manufacture may be costly and that machining time per component may be high.

6.16 Laser Machining (Continued)

Power densities of 10^{12} Watts/mm^2 are more than sufficient to vapourise all known bearing materials and the use of pulsed lasers to trim thin film electronic circuits has demonstrated that precisely controlled amounts of metal can be removed from selected areas without producing appreciable debris. (122).

Application to brittle ceramic materials may produce a fine crack pattern similar to that observed after Electric Discharge Machining, as the molten material remaining under the vapourised layer cools rapidly at the end of each laser pulse. For this reason, laser machining may be less useful than had originally been thought.

7. Selection of Manufacturing Methods

On reviewing the available methods of manufacture, it was decided to adopt the following manufacturing methods to prepare the majority of the experimental bearings described in this report (Plate 3). The bearing components were diamond ground from hot-pressed or sintered ceramic blanks as described in Method One, Section 1.1. of this Appendix, it being considered that the mechanical rigidity and dimensional stability of this arrangement outweighed all its known disadvantages. Diamond lapping (Section 4) was used to prepare the bearing surface prior to final polishing. Thermo-Chemical polishing was employed where possible (Section 5.2), but conventional diamond polishing (Section 5.1) was used for materials that would not respond to the former technique. It was considered that these methods would allow the finest possible surface finish to be achieved and it is shown in Chapter 9. that surface finish and texture are a major influence on the life and reliability of the bearing. Ion-machining (Section 6.2) was selected as the most suitable method for forming the pumping grooves in the polished bearing surface. It was considered that the outstanding precision and cleanliness of this particular groove-forming technique left no alternative choice if life and reliability were important, and this aspect is discussed more fully in Chapter 9.

A smaller number of bearings (Plates 1 & 2) were manufactured by alternative means (Sections 1.2 & 6.9) for evaluation purposes.

APPENDIX V

COMPUTER PRINT-OUT

This Print-Out shows the programme arrangement for evaluating bearing performance under angular misalignment.

```
                      PA=14.7+0.3*2**(KON-1)                                    GRO 6230
                      P=1.000+0.07*2**(KON-1)                                   GRO 6240
   60                 DO 173I=1,IMAX,1                                          GRO 6250
                      DO 173 J=2,JMOD,1                                         GRO 6260
                  173 Z(I,J)=P*P                                                GRO 6270
                      KOP=0                                                     GRO 6275
                  179 KOP=KOP+1                                                 GRO 6282
   65                 IF (KOP.EQ.1) GO TO 185                                   GRO 6284
                      IF (KOP.EQ.2) GO TO 171                                   GRO 6286
                      IF (KOP.EQ.3) GO TO 172                                   GRO 6288
                      IF (KOP.EQ.4) GO TO 176                                   GRO 6290
                      IF (KOP.EQ.5) GO TO 177                                   GRO 6292
   70                 IF (KOP.EQ.6) GO TO 178                                   GRO 6294
                      GO TO 167                                                 GRO 6296
                  178 DEL=0.0000793                                             GRO 6298
                      GO TO 170                                                 GRO 6300
                  177 DEL=0.0000595                                             GRO 6302
   75                 GO TO 170                                                 GRO 6304
                  176 DEL=0.0000397                                             GRO 6306
                      GO TO 170                                                 GRO 6308
                  172 DEL=0.0000198                                             GRO 6310
                      GO TO 170                                                 GRO 6312
   80             171 DEL=0.0000099                                             GRO 6314
                      GOTO 170
                  185 CONTINUE                                                  GRO 6325
                      DEL=0.0000000                                             GRO 6330
                  170 CONTINUE                                                  GRO 6340
   85                 S=(3.14159*MU*W*R*R)/(5*PA*C*C)                           GRO 6400
                  175 CONTINUE                                                  GRO 6420
                      DO 41=1,IMAX,1                                            GRO 6425
                      DO 4J=1,JMAX,1                                            GRO 6450
                    4 H(I,J)=1+E*COS((I-1)*X)+DEL/C*((L/2-(J-1)*L+Y)*COS((I-1)*X+TH)  GRO 6475
   90             174 CONTINUE                                                  GRO 6480
                      WRITE (2,63)W                                             GRO 6500
                   63 FORMAT (4H W =,1F10.2,2X,3HRPM)                           GRO 6525
                      WRITE (2,64)E                                             GRO 6550
                   64 FORMAT (4H E =,1F6.3)                                     GRO 6575
   95                 WRITE (2,75)S                                             GRO 6600
                   75 FORMAT (22H COMPRESSIBILITY NO. =,1F7.2)                  GRO 6625
                      RAT=DEL*L/(2*C)
                      WRITE(2,186)RAT
                  186 FORMAT(21H MISALIGNMENT RATIO =,1F7.3)
  100             168 CONTINUE                                                  GRO 6825
                      Q=1                                                       GRO 7100
                      N=0                                                       GRO 7200
                      KIP=0                                                     GRO 7220
                      ALSTOR=769                                                GRO 7240
  105                 KAP=0                                                     GRO 7260
                      F=1.870                                                   GRO 7280
                      NAP=0                                                     GRO 7290
                    5 ALPHA=0                                                   GRO 7300
                      DO 28I=1,IMAX,1                                           GRO 7500
  110                 DO 28J=2,JMOD,1                                           GRO 7600
                      T=K(Q)                                                    GRO 7700
                      IF (I-1)6,14,6                                            GRO 7800
                    6 IF (I-IMAX)7,20,7                                         GRO 7900
                    7 IF (T-8)8,37,8                                            GRO 8000
```

```
                    8 IF (T-7)9,54,9                                                    GRO 8100
                    9 IF (T-1)10,43,10                                                  GRO 8200
                   10 IF (T-2)11,42,11                                                  GRO 8300
                   11 IF (T-3)12,45,12                                                  GRO 8400
                   12 IF (T-4)13,44,13                                                  GRO 8500
               120 13 IF (T-5)88,40,88                                                  GRO 8600
                   88 IF (T-6)89,41,89                                                  GRO 8605
                   89 IF (T-9)90,125,90                                                 GRO 8610
                   90 IF (T-10)91,126,91                                                GRO 8615
                   91 IF (T-11)92,127,92                                                GRO 8620
               125 92 IF (T-12)93,128,93                                                GRO 8625
                   93 IF (T-13)94,129,94                                                GRO 8630
                   94 IF (T-14)95,130,95                                                GRO 8635
                   95 IF (T-15)96,131,96                                                GRO 8640
                   96 IF (T-16)133,132,133                                              GRO 8645
               130 14 IF (T-1)15,51,15                                                  GRO 8700
                   15 IF (T-2)16,53,16                                                  GRO 8800
                   16 IF (T-3)17,50,17                                                  GRO 8900
                   17 IF (T-4)18,52,18                                                  GRO 9000
                   18 IF (T-5)19,40,19                                                  GRO 9100
               135 19 IF (T-6)101,41,101                                                GRO 9200
                  101 IF (T-7)102,134,102                                               GRO 9205
                  102 IF (T-8)103,39,103                                                GRO 9210
                  103 IF (T-9)104,135,104                                               GRO 9215
                  104 IF (T-10)105,136,105                                              GRO 9220
               140 105 IF (T-11)106,137,106                                             GRO 9225
                  106 IF (T-12)107,138,107                                              GRO 9230
                  107 IF (T-13)108,139,108                                              GRO 9235
                  108 IF (T-14)109,140,109                                              GRO 9240
                  109 IF (T-15)110,141,110                                              GRO 9245
               145 110 IF (T-16)143,142,143                                             GRO 9250
                   20 IF (T-1)21,47,21                                                  GRO 9300
                   21 IF (T-2)22,49,22                                                  GRO 9400
                   22 IF (T-3)23,46,23                                                  GRO 9500
                   23 IF (T-4)24,48,24                                                  GRO 9600
               150 24 IF (T-5)25,40,25                                                  GRO 9700
                   25 IF (T-6)115,41,115                                                GRO 9800
                  115 IF (T-7)116,144,116                                               GRO 9805
                  116 IF (T-8)117,38,117                                                GRO 9810
                  117 IF (T-9)118,145,118                                               GRO 9815
               155 118 IF (T-10)119,146,119                                             GRO 9820
                  119 IF (T-11)120,147,120                                              GRO 9825
                  120 IF (T-12)121,148,121                                              GRO 9830
                  121 IF (T-13)122,149,122                                              GRO 9835
                  122 IF (T-14)123,150,123                                              GRO 9840
               160 123 IF (T-15)124,151,124                                             GRO 9845
                  124 IF (T-16)153,152,153                                              GRO 9850
                   35 Q=Q+1                                                             GRO 9900
                      IF (Q-QMAX)26,26,36                                               GRO10000
                   36 Q=1                                                               GRO10100
               165 26 PRESS=SQRT(ABS(VAR))                                              GRO10140
                      IF (VAR.GT.0.000.AND.PRESS.LT.0.999) GO TO 183                    GRO10142
                      IF(KAP .GT. NAP) NAP=KAP
                      NAP=NAP+1                                                         GRO10144
                      IF (NAP.EQ.1) F=1.80                                              GRO10146
               170    IF (NAP.EQ.2) F=1.70                                              GRO10147
                      IF (NAP.EQ.3) F=1.60                                              GRO10148
```

```
                IF (NAP.EQ.4) F=1.50                                    GR010149
                IF (NAP.EQ.5) F=1.40                                    GR010150
                IF (NAP.EQ.6) F=1.30                                    GR010151
  175           IF (NAP.EQ.7) F=1.20                                    GR010151
                IF (NAP.EQ.8) F=1.00                                    GR010153
                IF (NAP.EQ.9) F=0.90                                    GR010154
                IF (NAP.EQ.10) F=0.60                                   GR010155
                IF (NAP.EQ.11) F=0.30                                   GR010156
  180           IF (NAP.EQ.12) F=0.10                                   GR010157
                WRITE(2,70)F
            184 FORMAT(3X,9H=UNSTABLE)                                  GR010160
                WRITE(2,184)                                            GR010161
            183 CONTINUE                                                GR010162
  185           PREV=SORT(ABS(Z(I,J)))                                  GR010180
                DIFF=PRESS-PREV                                         GR010200
                IF (ABS(DIFF)-EPSI)28,28,27                             GR010300
             27 ALPHA=ALPHA+1                                           GR010400
             28 Z(I,J)=ABS(VAR)                                         GR010500
  190           N=N+1                                                   GR010600
                KIP=KIP+1                                               GR010605
                IF (KIP.NE.3) GO TO 180                                 GR010610
                KIP=0                                                   GR010615
                IF (ALPHA-ALSTOR)182,181,181                            GP010620
  195       181 IF(NAP .GT. KAP) KAP=NAP
                KAP=KAP+1                                               GR010625
                IF (KAP.EQ.1) F=1.80                                    GR010630
                IF (KAP.EQ.2) F=1.70                                    GR010631
                IF (KAP.EQ.3) F=1.60                                    GR010632
  200           IF (KAP.EQ.4) F=1.50                                    GR010633
                IF (KAP.EQ.5) F=1.40                                    GR010634
                IF (KAP.EQ.6) F=1.30                                    GR010635
                IF (KAP.EQ.7) F=1.20                                    GR010636
                IF (KAP.EQ.8) F=1.00                                    GR010637
  205           IF (KAP.EQ.9) F=0.90                                    GR010638
                IF (KAP.EQ.10) F=0.60                                   GR010639
                IF (KAP.EQ.11) F=0.30                                   GR010640
                IF (KAP.EQ.12) F=0.10                                   GR010641
                IF(KAP .GT. 12)GOTO 182
  210           WRITE (2,70)F                                           GR010660
            182 ALSTOR=ALPHA                                            GR010665
            180 CONTINUE                                                GR010670
                IF (N-NMAX)29,32,32                                     GR010700
             29 IF (ALPHA)30,32,30                                      GR010800
  215        30 WRITE(2,31)N,ALPHA                                      GR010900
             31 FORMAT (1H ,I14,1I6)                                    GR011000
                GO TO 5                                                 GR011100
             32 WRITE(2,31)N,ALPHA                                      GR011200
                DO 169M=1,IMAX,1                                        GR011300
  220           DO 33J=1,JMAX,1                                         GR011350
                I=IMAX+1-M                                              GR011400
             33 PGRID(J)=SORT(ABS(Z(I,J)))                              GR011450
                WRITE(2,34)(PGRID(IARL),IARL=1,18)                      GR011500
             34 FORMAT (18F6.3)                                         GR011600
  225       169 CONTINUE                                                GR011605
                IF (F.EQ.00.000) GO TO 160                              GR011610
                W1=W2=UT=PHI=0                                          GR011620
                DO 155I=1,IMAX,1                                        GR011630
```

```
                      DO 155J=1,JMAX,1                                                  GR011640
      230             P=SQRT(ABS(Z(I,J)))                                               GR011645
                      W1=W1+(-P*X*Y*COS((I-1)*X))                                       GR011650
                  155 W2=W2+P*X*Y*SIN((I-1)*X)                                          GR011660
                      WT=SQRT(W1*W1+W2*W2)                                              GR011670
                      PHI=ATAN(W1/W2)*57.296                                            GR011680
      235             PHI=90.00-PHI                                                     GR011685
                      WRITE (2,156)W1                                                   GR011690
                  156 FORMAT (6H W1 = ,1F6.3)                                           GR011700
                      WRITE (2,157)W2                                                   GR011710
                  157 FORMAT (6H W2 = ,1F6.3)                                           GR011720
      240             WRITE (2,158)WT                                                   GR011730
                  158 FORMAT (6H WT = ,1F6.3)                                           GR011740
                      WRITE (2,159)PHI                                                  GR011750
                  159 FORMAT (7H PHI = ,1F6.2,4H DEG)                                   GR011760
                  160 IF (DEL.EQ.0.00000) GO TO 166                                     GR011770
      245             M1=M2=MT=PSI=0                                                    GR011780
                      DO 161I=1,IMAX,1                                                  GR011790
                      DO 161J=1,JMAX,1                                                  GR011800
                      P=SQRT(ABS(Z(I,J)))                                               GR011805
                      M1=M1+(-P*X*Y*(0.5-(J-1)*Y)*COS((I-1)*X+TH))                      GR011810
      250         161 M2=M2+P*X*Y*(0.5-(J-1)*Y)*SIN((I-1)*X+TH)                         GR011820
                      MT=SQRT(M1*M1+M2*M2)                                              GR011830
                      PSI=ATAN(M1/M2)*57.296                                            GR011840
                      WRITE (2,162)M1                                                   GR011850
                  162 FORMAT (6H M1 = ,1F6.3)                                           GR011860
      255             WRITE (2,163)M2                                                   GR011870
                  163 FORMAT (6H M2 = ,1F6.3)                                           GR011880
                      WRITE (2,164)MT                                                   GR011890
                  164 FORMAT (6H MT = ,1F6.3)                                           GR011900
                      WRITE (2,165)PSI                                                  GR011910
      260         165 FORMAT (7H PSI = ,1F6.2,4H DEG)                                   GR011920
                  166 CONTINUE                                                          GR011930
                      N=0                                                               GR012100
                      GO TO 179                                                         GR012200
                  167 CONTINUE                                                          GR012500
      265             GO TO 79                                                          GR012550
                   37 M1=(M(I,J+1)+M(I,J))/2                                            GR012600
                      M2=(M(I+1,J)+M(I,J))/2                                            GR012700
                      M3=(M(I,J-1)+M(I,J))/2                                            GR012800
                      M4=(M(I-1,J)+M(I,J))/2                                            GR012900
      270             GO TO 81                                                          GR012950
                   54 M1=(M(I,J+1)+M(I,J))/2+G                                          GR013000
                      M2=(M(I+1,J)+M(I,J))/2+G                                          GR013100
                      M3=(M(I,J-1)+M(I,J))/2+G                                          GR013200
                      M4=(M(I-1,J)+M(I,J))/2+G                                          GR013300
      275             Z1=(Z(I,J+1)+Z(I,J))/2                                            GR013400
                      Z2=(Z(I+1,J)+Z(I,J))/2                                            GR013500
                      Z3=(Z(I,J-1)+Z(I,J))/2                                            GR013600
                      Z4=(Z(I-1,J)+Z(I,J))/2                                            GR013700
                  C   EQUATION  1                                                       GR013710
      280             OVAR=((S*M(I,J)+Z2)/(4*Z(I,J)**0.5*X)-(S*M(I,J)+Z4)/(4*Z(I,J)**0.5*GR013800
                     1X)+(S*M(I,J)+Z2)/(2*Z(I,J)**0.5*X)-(S*M(I,J)+Z4)/(2*Z(I,J)**0.5*X)GR013900
                     2+(S*Z(I,J)**0.5*W2)/(2*X)-(S*Z(I,J)**0.5*W4)/(2*X)-(M2*M2*M2*Z(I+1GR014000
                     3,J))/(2*X*X)-(M4*M4*M4*Z(I-1,J))/(2*X*X)-(M1*M1*M1*Z(I,J+1))/(8*B*GR014100
                     4B*Y*Y)-(M3*M3*M3*Z(I,J-1))/(8*B*B*Y*Y))/(-(M2*M2*M2)/(2*X*X)-(M4*MGR014200
      285            54*M4)/(2*X*X)-(M1*M1*M1)/(8*B*B*Y*Y)-(M3*M3*M3)/(8*B*B*Y*Y)+(S*M(IGR014210
```

```
PROGRAM GROV      76/76   OPT=1   TRACE                UMRCC FTN 4.1.170A   18/05/74  03.45.23

     6,J)+Z2)/(4+Z(I,J)**1.5+X)-(S+H(I,J)+Z4)/(4+Z(I,J)**1.5+X)-(S+H2)/(GR014220
     72+Z(I,J)**0.5+X)+(S+H4)/(2+Z(I,J)**0.5+X))                          GR014230
      VAR=F+VAR+(1-F)+Z(I,J)                                              GR014240
      GO TO 35                                                            GR014300
 290  38 H1=(H(I,J+1)+H(I,J))/2                                           GR014400
      H2=(H(I+1-IMAX,J)+H(I,J))/2                                         GR014500
      H3=(H(I,J-1)+H(I,J))/2                                              GR014600
      H4=(H(I-1,J)+H(I,J))/2                                              GR014700
     86 Z1=(Z(I,J+1)+Z(I,J))/2                                            GR014800
 295  Z2=(Z(I+1-IMAX,J)+Z(I,J))/2                                         GR014900
      Z3=(Z(I,J-1)+Z(I,J))/2                                              GR015000
      Z4=(Z(I-1,J)+Z(I,J))/2                                              GR015100
C  EQUATION  2                                                           GR015150
      OVAR=((S+H(I,J)+Z2)/(4+Z(I,J)**0.5+X)-(S+H(I,J)+Z4)/(4+Z(I,J)**0.5+GR015200
 300  1X)+(S+H(I,J)+Z2)/(2+Z(I,J)**0.5+X)-(S+H(I,J)+Z4)/(2+Z(I,J)**0.5+X)GR015300
      2+(S+Z(I,J)**0.5+H2)/(2+X)-(S+Z(I,J)**0.5+H4)/(2+X)-(H2+H2+H2+Z(I+1GR015400
      3-IMAX,J))/(2+X+X1-(H4+H4+H4+Z(I-1,J))/(2+X+X)-(H1+H1+H1+Z(I,J+1))/GR015500
      4(A+B+B+Y+Y)-(H3+H3+H3+Z(I,J-1))/(B+B+B+Y+Y))/(-(H2+H2+H2)/(2+X+X)-GR015510
      5(H4+H4+H4)/(2+X+X)-(H1+H1+H1)/(B+B+B+Y+Y)-(H3+H3+H3)/(B+B+B+Y+Y)+(GR015520
 305  6S+H(I,J)+Z2)/(4+Z(I,J)**1.5+X)-(S+H(I,J)+Z4)/(4+Z(I,J)**1.5+X)-(S+GR015530
      7H2)/(2+Z(I,J)**0.5+X)+(S+H4)/(2+Z(I,J)**0.5+X))                     GR015540
      VAR=F+VAR+(1-F)+Z(I,J)                                              GR015550
      GO TO 35                                                            GR015650
     39 H1=(H(I,J+1)+H(I,J))/2                                            GR015700
 310  H2=(H(I+1,J)+H(I,J))/2                                              GR015800
      H3=(H(I,J-1)+H(I,J))/2                                              GR015900
      H4=(H(I-1+IMAX,J)+H(I,J))/2                                         GR016000
     87 Z1=(Z(I,J+1)+Z(I,J))/2                                            GR016100
      Z2=(Z(I+1,J)+Z(I,J))/2                                              GR016200
 315  Z3=(Z(I,J-1)+Z(I,J))/2                                              GR016300
      Z4=(Z(I-1+IMAX,J)+Z(I,J))/2                                         GR016400
C  EQUATION  3                                                           GR016410
      OVAR=((S+H(I,J)+Z2)/(4+Z(I,J)**0.5+X)-(S+H(I,J)+Z4)/(4+Z(I,J)**0.5+GR016500
      1X)+(S+H(I,J)+Z2)/(2+Z(I,J)**0.5+X)-(S+H(I,J)+Z4)/(2+Z(I,J)**0.5+X)GR016600
 320  2+(S+Z(I,J)**0.5+H2)/(2+X)-(S+Z(I,J)**0.5+H4)/(2+X)-(H2+H2+H2+Z(I+1GR016700
      3,J))/(2+X+X)-(H4+H4+H4+Z(I-1+IMAX,J))/(2+X+X)-(H1+H1+H1+Z(I,J+1))/GR016800
      4(A+B+B+Y+Y)-(H3+H3+H3+Z(I,J-1))/(B+B+B+Y+Y))/(-(H2+H2+H2)/(2+X+X)-GR016810
      5(H4+H4+H4)/(2+X+X)-(H1+H1+H1)/(B+B+B+Y+Y)-(H3+H3+H3)/(B+B+B+Y+Y)+(GR016820
      6S+H(I,J)+Z2)/(4+Z(I,J)**1.5+X)-(S+H(I,J)+Z4)/(4+Z(I,J)**1.5+X)-(S+GR016830
 325  7H2)/(2+Z(I,J)**0.5+X)+(S+H4)/(2+Z(I,J)**0.5+X))                    GR016840
      VAR=F+VAR+(1-F)+Z(I,J)                                              GR016850
      GO TO 35                                                            GR016950
     40 CALL GPORO                                                        GR017000
C  EQUATION  4                                                           GR017010
 330  OVAR=(-(Z3+HG+HG+HG)/Y+(Z(I,J-1)+HG+HG+HG)/(4+Y)-(Z1+H(I,J)+H(I,J)+GR017100
      1H(I,J))/Y+(Z(I,J+1)+H(I,J)+H(I,J)+H(I,J))/(4+Y))/(-(3+H(I,J)+H(I,JGR017200
      2)+H(I,J))/(4+Y)-(3+HG+HG+HG)/(4+Y))                                GR017300
      VAR=F+VAR+(1-F)+Z(I,J)                                              GR017350
      GO TO 35                                                            GR017400
 335  41 CALL GRORO                                                        GR017500
C  EQUATION  5                                                           GR017525
      OVAR=((Z1+HG+HG+HG)/Y-(Z(I,J+1)+HG+HG+HG)/(4+Y)+(Z3+H(I,J)+H(I,J)+HGR017600
      1(I,J))/Y-(Z(I,J-1)+H(I,J)+H(I,J)+H(I,J))/(4+Y))/((3+H(I,J)+H(I,J)+GR017700
      2H(I,J))/(4+Y)+(3+HG+HG+HG)/(4+Y))                                  GR017800
 340  VAR=F+VAR+(1-F)+Z(I,J)                                              GR017850
      GO TO 35                                                            GR017900
     42 CALL GRORO                                                        GR018000
```

```
                C  EQUATION  6                                                                  GR018010
                     0VAR=(-(X*HG*HG*HG*Z3)/(4*B*B*S*Y)+(X*HG*HG*HG*Z(I,J-1))/(16*B*B*S*GR018100
                     1Y)+(Z(I,J)**0.5*HG*Y)/2+(Y*HG*HG*HG*Z2)/(S*X)-(Y*HG*HG*HG*Z(I+1,J)GR018200
                     2)/(4*S*X)-(X*H(I,J)**3*Z1)/(4*B*B*S*Y)+(X*H(I,J)**3*Z(I,J+1))/(16*GR018300
                     3B*B*S*Y)-(Z(I,J)**0.5*H(I,J)*Y)/2+(Y*H(I,J)**3*Z4)/(S*X)-(Y*H(I,J)GR018400
                     4**3*Z(I-1,J))/(4*S*X))/(-(3*X*H(I,J)**3)/(16*B*B*S*Y)+(H(I,J)*Y)/(GR018500
                     52*Z(I,J)**0.5)+(3*Y*H(I,J)**3)/(4*S*X)-(3*X*HG*HG*HG)/(16*B*B*S*Y)GR018600
                     6-(HG*Y)/(2*Z(I,J)**0.5)+(3*Y*HG*HG*HG)/(4*S*X))                            GR018700
                      VAR=F*VAR+(1-F)*Z(I,J)                                                     GR018750
                      GO TO 35                                                                   GR018800
                   43 CALL GROBO                                                                 GR018900
                C  EQUATION  7                                                                   GR018910
                     0VAR=((X*HG*HG*HG*Z1)/(4*B*B*S*Y)-(X*HG*HG*HG*Z(I,J+1))/(16*B*B*S*YGR019000
                     1)+(Z(I,J)**0.5*HG*Y)/2-(Y*HG*HG*HG*Z4)/(S*X)+(Y*HG*HG*HG*Z(I-1,J))GR019100
                     2/(4*S*X)+(X*H(I,J)**3*Z3)/(4*B*B*S*Y)-(X*H(I,J)**3*Z(I,J-1))/(16*BGR019200
                     3*B*S*Y)-(Z(I,J)**0.5*H(I,J)*Y)/2-(Y*H(I,J)**3*Z2)/(S*X)+(Y*H(I,J)*GR019300
                     4**3*Z(I+1,J))/(4*S*X))/((3*X*H(I,J)**3)/(16*B*B*S*Y)+(H(I,J)*Y)/(2*GR019400
                     5Z(I,J)**0.5)-(3*Y*H(I,J)**3)/(4*S*X)+(3*X*HG*HG*HG)/(16*B*B*S*Y)-(GR019500
                     6HG*Y)/(2*Z(I,J)**0.5)-(3*Y*HG*HG*HG)/(4*S*X))                             GR019600
                      VAR=F*VAR+(1-F)*Z(I,J)                                                     GR019650
                      GO TO 35                                                                   GR019700
                   44 CALL GROBO                                                                 GR019800
                C  EQUATION  8                                                                   GR019810
                     0VAR=((X*HG*HG*HG*Z1)/(4*B*B*S*Y)-(X*HG*HG*HG*Z(I,J+1))/(16*B*B*S*YGR019900
                     1)+(Z(I,J)**0.5*HG*Y)/2+(Y*HG*HG*HG*Z2)/(S*X)-(Y*HG*HG*HG*Z(I+1,J))GR020000
                     2/(4*S*X)+(X*H(I,J)**3*Z3)/(4*B*B*S*Y)-(X*H(I,J)**3*Z(I,J-1))/(16*BGR020100
                     3*B*S*Y)-(Z(I,J)**0.5*H(I,J)*Y)/2+(Y*H(I,J)**3*Z4)/(S*X)-(Y*H(I,J)*GR020200
                     4**3*Z(I-1,J))/(4*S*X))/((3*X*H(I,J)**3)/(16*B*B*S*Y)+(H(I,J)*Y)/(2*GR020300
                     57(I,J)**0.5)+(3*Y*H(I,J)**3)/(4*S*X)+(3*X*HG*HG*HG)/(16*B*B*S*Y)-(GR020400
                     6HG*Y)/(2*Z(I,J)**0.5)+(3*Y*HG*HG*HG)/(4*S*X))                             GR020500
                      VAR=F*VAR+(1-F)*Z(I,J)                                                     GR020550
                      GO TO 35                                                                   GR020600
                   45 CALL GPORO                                                                 GR020700
                C  EQUATION  9                                                                   GR020710
                     0VAR=(-(X*HG*HG*HG*Z3)/(4*B*B*S*Y)+(X*HG*HG*HG*Z(I,J-1))/(16*B*B*S*GR020800
                     1Y)+(Z(I,J)**0.5*HG*Y)/2-(Y*HG*HG*HG*Z4)/(S*X)+(Y*HG*HG*HG*Z(I-1,J)GR020900
                     2)/(4*S*X)-(X*H(I,J)**3*Z1)/(4*B*B*S*Y)+(X*H(I,J)**3*Z(I,J+1))/(16*GR021000
                     3B*B*S*Y)-(Z(I,J)**0.5*H(I,J)*Y)/2-(Y*H(I,J)**3*Z2)/(S*X)+(Y*H(I,J)GR021100
                     4**3*Z(I+1,J))/(4*S*X))/(-(3*X*H(I,J)**3)/(16*B*B*S*Y)+(H(I,J)*Y)/(GR021200
                     52*Z(I,J)**0.5)-(3*Y*H(I,J)**3)/(4*S*X)-(3*X*HG*HG*HG)/(16*B*B*S*Y)GR021300
                     6-(HG*Y)/(2*Z(I,J)**0.5)-(3*Y*HG*HG*HG)/(4*S*X))                            GR021400
                      VAR=F*VAR+(1-F)*Z(I,J)                                                     GR021450
                      GO TO 35                                                                   GR021500
                   46 CALL GROCY                                                                 GR021600
                C  EQUATION 10                                                                   GR021610
                     0VAR=(-(X*HG*HG*HG*Z3)/(4*B*B*S*Y)+(X*HG*HG*HG*Z(I,J-1))/(16*B*B*S*GR021700
                     1Y)+(Z(I,J)**0.5*HG*Y)/2-(Y*HG*HG*HG*Z4)/(S*X)+(Y*HG*HG*HG*Z(I-1,J)GR021800
                     2)/(4*S*X)-(X*H(I,J)**3*Z1)/(4*B*B*S*Y)+(X*H(I,J)**3*Z(I,J+1))/(16*GR021900
                     3B*B*S*Y)-(Z(I,J)**0.5*H(I,J)*Y)/2-(Y*H(I,J)**3*Z2)/(S*X)+(Y*H(I,J)GR022000
                     4**3*Z(I+1-IMAX,J))/(4*S*X))/(-(3*X*H(I,J)**3)/(16*B*B*S*Y)+(H(I,J)GR022100
                     5*Y)/(2*Z(I,J)**0.5)-(3*Y*H(I,J)**3)/(4*S*X)-(3*X*HG*HG*HG)/(16*B*BGR022200
                     6*S*Y)-(HG*Y)/(2*Z(I,J)**0.5)-(3*Y*HG*HG*HG)/(4*S*X))                       GR022300
                      VAR=F*VAR+(1-F)*Z(I,J)                                                     GR022350
                      GO TO 35                                                                   GR022400
                   47 CALL GROCY                                                                 GR022500
                C  EQUATION 11                                                                   GR022510
                     0VAR=((X*HG*HG*HG*Z1)/(4*B*B*S*Y)-(X*HG*HG*HG*Z(I,J+1))/(16*B*B*S*YGR022600
```

```
                1)+(Z(I,J)**0.5*HG*Y)/2-(Y*HG*HG*HG*Z4)/(S*X)+(Y*HG*HG*HG*Z(I-1,J))GR022700
                2/(4*S*X)+(X*H(I,J)**3*Z3)/(4*B*B*S*Y)-(X*H(I,J)**3*Z(I,J-1))/(16*BGR022800
                3*B*S*Y)-(Z(I,J)**0.5*H(I,J)*Y)/2-(Y*H(I,J)**3*Z2)/(S*X)+(Y*H(I,J)*GR022900
                4*3*Z(I+1-IMAX,J))/(4*S*X))/((3*X*H(I,J)**3)/(16*B*B*S*Y)+(H(I,J)*YGR023000
                5)/(2*Z(I,J)**0.5)-(3*Y*H(I,J)**3)/(4*S*X)+(3*X*HG*HG*HG)/(16*B*B*SGR023100
      405       6*Y)-(HG*Y)/(2*Z(I,J)**0.5)-(3*Y*HG*HG*HG)/(4*S*X))                GR023200
                 VAR=F*VAR+(1-F)*Z(I,J)                                            GR023250
                 GO TO 35                                                          GR023300
               48 CALL GROCY                                                       GR023400
              C  EQUATION 12                                                       GR023410
                OVAR=((X*HG*HG*HG*Z1)/(4*B*B*S*Y)-(X*HG*HG*HG*Z(I,J+1))/(16*B*B*S*YGR023500
      410       1)+(Z(I,J)**0.5*HG*Y)/2+(Y*HG*HG*HG*Z2)/(S*X)-(Y*HG*HG*HG*Z(I+1-IMAGR023600
                2X,J))/(4*S*X)+(X*H(I,J)**3*Z3)/(4*B*B*S*Y)-(X*H(I,J)**3*Z(I,J-1))/GR023700
                3(16*B*B*S*Y)-(Z(I,J)**0.5*H(I,J)*Y)/2+(Y*H(I,J)**3*Z4)/(S*X)-(Y*H(GR023800
                4I,J)**3*Z(I-1,J))/(4*S*X))/((3*X*H(I,J)**3)/(16*B*B*S*Y)+(H(I,J)*YGR023900
      415       5)/(2*Z(I,J)**0.5)+(3*Y*H(I,J)**3)/(4*S*X)+(3*X*HG*HG*HG)/(16*B*B*SGR024000
                6*Y)-(HG*Y)/(2*Z(I,J)**0.5)+(3*Y*HG*HG*HG)/(4*S*X))                GR024100
                 VAR=F*VAR+(1-F)*Z(I,J)                                            GR024150
                 GO TO 35                                                          GR024200
               49 CALL GROCY                                                       GR024300
      420      C  EQUATION 13                                                       GR024310
                OVAR=(-(X*HG*HG*HG*Z3)/(4*B*B*S*Y)+(X*HG*HG*HG*Z(I,J-1))/(16*B*B*S*GR024400
                1Y)+(Z(I,J)**0.5*HG*Y)/2+(Y*HG*HG*HG*Z2)/(S*X)-(Y*HG*HG*HG*Z(I+1-IMGR024500
                2AX,J))/(4*S*X)-(X*H(I,J)**3*Z1)/(4*B*B*S*Y)+(X*H(I,J)**3*Z(I,J+1))GR024600
                3/(16*B*B*S*Y)-(Z(I,J)**0.5*H(I,J)*Y)/2+(Y*H(I,J)**3*Z4)/(S*X)-(Y*HGR024700
      425       4(I,J)**3*Z(I-1,J))/(4*S*X))/(-(3*X*H(I,J)**3)/(16*B*B*S*Y)+(H(I,J)GR024800
                5*Y)/(2*Z(I,J)**0.5)+(3*Y*H(I,J)**3)/(4*S*X)-(3*X*HG*HG*HG)/(16*B*BGR024900
                6*S*Y)-(HG*Y)/(2*Z(I,J)**0.5)+(3*Y*HG*HG*HG)/(4*S*X))              GR025000
                 VAR=F*VAR+(1-F)*Z(I,J)                                            GR025050
                 GO TO 35                                                          GR025100
      430       50 CALL GROAD                                                      GR025200
              C  EQUATION 14                                                       GR025210
                OVAR=(-(X*HG*HG*HG*Z3)/(4*B*B*S*Y)+(X*HG*HG*HG*Z(I,J-1))/(16*B*B*S*GR025300
                1Y)+(Z(I,J)**0.5*HG*Y)/2-(Y*HG*HG*HG*Z4)/(S*X)+(Y*HG*HG*HG*Z(I-1*IMGR025400
                2AX,J))/(4*S*X)-(Y*H(I,J)**3*Z1)/(4*B*B*S*Y)+(X*H(I,J)**3*Z(I,J+1))GR025500
      435       3/(16*B*B*S*Y)-(Z(I,J)**0.5*H(I,J)*Y)/2-(Y*H(I,J)**3*Z2)/(S*X)+(Y*HGR025600
                4(I,J)**3*Z(I+1,J))/(4*S*X))/(-(3*X*H(I,J)**3)/(16*B*B*S*Y)+(H(I,J)GR025700
                5*Y)/(2*Z(I,J)**0.5)-(3*Y*H(I,J)**3)/(4*S*X)-(3*X*HG*HG*HG)/(16*B*BGR025800
                6*S*Y)-(HG*Y)/(2*Z(I,J)**0.5)-(3*Y*HG*HG*HG)/(4*S*X))              GR025900
                 VAR=F*VAR+(1-F)*Z(I,J)                                            GR025950
      440        GO TO 35                                                          GR026000
               51 CALL GROAD                                                       GR026100
              C  EQUATION 15                                                       GR026110
                OVAR=((X*HG*HG*HG*Z1)/(4*B*B*S*Y)-(X*HG*HG*HG*Z(I,J+1))/(16*B*B*S*YGR026200
                1)+(Z(I,J)**0.5*HG*Y)/2-(Y*HG*HG*HG*Z4)/(S*X)+(Y*HG*HG*HG*Z(I-1*I*AGR026300
      445       2X,J))/(4*S*X)+(X*H(I,J)**3*Z3)/(4*B*B*S*Y)-(X*H(I,J)**3*Z(I,J-1))/GR026400
                3(16*B*B*S*Y)-(Z(I,J)**0.5*H(I,J)*Y)/2-(Y*H(I,J)**3*Z2)/(S*X)+(Y*H(GR026500
                4I,J)**3*Z(I+1,J))/(4*S*X))/((3*X*H(I,J)**3)/(16*B*B*S*Y)+(H(I,J)*YGR026600
                5)/(2*Z(I,J)**0.5)-(3*Y*H(I,J)**3)/(4*S*X)+(3*X*HG*HG*HG)/(16*B*B*SGR026700
                6*Y)-(HG*Y)/(2*Z(I,J)**0.5)-(3*Y*HG*HG*HG)/(4*S*X))                GR026800
      450        VAR=F*VAR+(1-F)*Z(I,J)                                            GR026850
                 GO TO 35                                                          GR026900
               52 CALL GROAD                                                       GR027000
              C  EQUATION 16                                                       GR027010
                OVAR=((X*HG*HG*HG*Z1)/(4*B*B*S*Y)-(X*HG*HG*HG*Z(I,J+1))/(16*B*B*S*YGR027100
      455       1)+(Z(I,J)**0.5*HG*Y)/2+(Y*HG*HG*HG*Z2)/(S*X)-(Y*HG*HG*HG*Z(I+1,J))GR027200
                2/(4*S*X)+(X*H(I,J)**3*Z3)/(4*B*B*S*Y)-(X*H(I,J)**3*Z(I,J-1))/(16*BGR027300
```

```
                3*B*S*Y)-(Z(I,J)**0.5*H(I,J)*Y)/2+(Y*H(I,J)**3*Z4)/(S*X)-(Y*H(I,J)+GR027400
                4*3+Z(I-1+IMAX,J))/(4*S*X))/((3*X*H(I,J)**3)/(16*B*B*S*Y)+(H(I,J)*YGR027500
                5)/(2*Z(I,J)**0.5)+(3*Y*H(I,J)**3)/(4*S*X)+(3*X*HG*HG*HG)/(16*B*B*SGR027600
   460          6*Y)-(HG*Y)/(2*Z(I,J)**0.5)+(3*Y*HG*HG*HG)/(4*S*X))                    GR027700
                 VAR=F*VAR+(1-F)*Z(I,J)                                                GR027750
                 GO TO 35                                                              GR027800
              53 CALL GROAD                                                            GR027900
              C  EQUATION 17                                                           GR027910
   465          0VAR=(-(X*HG*HG*HG*Z3)/(4*B*B*S*Y)+(X*HG*HG*HG*Z(I,J-1))/(16*B*B*S*GR028000
                1Y)+(Z(I,J)**0.5*HG*Y)/2*(Y*HG*HG*HG*Z2)/(S*X)-(Y*HG*HG*HG*Z(I+1,J)GR028100
                2)/(4*S*X)-(X*H(I,J)**3*Z1)/(4*B*B*S*Y)+(X*H(I,J)**3*Z(I,J+1))/(16*GR028200
                3B*B*S*Y)-(Z(I,J)**0.5*H(I,J)*Y)/2+(Y*H(I,J)**3*Z4)/(S*X)-(Y*H(I,J)GR028300
                4**3*Z(I-1+IMAX,J))/(4*S*X))/(-(3*X*H(I,J)**3)/(16*B*B*S*Y)+(H(I,J)GR028400
   470          5*Y)/(2*Z(I,J)**0.5)+(3*Y*H(I,J)**3)/(4*S*X)-(3*X*HG*HG*HG)/(16*B*BGR028500
                6*S*Y)-(HG*Y)/(2*Z(I,J)**0.5)+(3*Y*HG*HG*HG)/(4*S*X))                  GR028600
                 VAR=F*VAR+(1-F)*Z(I,J)                                                GR028650
                 GO TO 35                                                              GR028700
              C  MODO9                                                                 GR028800
   475          125 M1=(H(I,J+1)+H(I,J))/2                                            GR028900
                    M2=(H(I+1,J)+G*H(I,J))/2                                         GR029000
                    M3=(H(I,J-1)+G*H(I,J))/2                                         GR029100
                    M4=(H(I-1,J)+H(I,J))/2                                           GR029200
                    GO TO A1                                                         GR029300
   480          C  MOD10                                                             GR029400
                  126 M1=(H(I,J+1)+G*H(I,J))/2                                       GR029500
                    M2=(H(I+1,J)+H(I,J))/2                                           GR029600
                    M3=(H(I,J-1)+H(I,J))/2                                           GR029700
                    M4=(H(I-1,J)+G*H(I,J))/2                                         GR029800
   485              GO TO A1                                                         GR029900
                C  MOD11                                                           GR030000
                  127 M1=(H(I,J+1)+H(I,J))/2                                       GR030100
                    M2=(H(I+1,J)+H(I,J))/2                                         GR030200
                    M3=(H(I,J-1)+H(I,J))/2                                         GR030300
   490              M4=(H(I-1,J)+G*H(I,J))/2                                       GR030400
                    GO TO A1                                                       GR030500
                C  MOD12                                                           GR030600
                  128 M1=(H(I,J+1)+H(I,J))/2                                       GR030700
                    M2=(H(I+1,J)+H(I,J))/2                                         GR030800
   495              M3=(H(I,J-1)+G*H(I,J))/2                                       GR030900
                    M4=(H(I-1,J)+H(I,J))/2                                         GR031000
                    GO TO A1                                                       GR031100
                C  MOD13                                                           GR031200
                  129 M1=(H(I,J+1)+G*H(I,J))/2                                     GR031300
   500              M2=(H(I+1,J)+H(I,J))/2                                         GR031400
                    M3=(H(I,J-1)+H(I,J))/2                                         GR031500
                    M4=(H(I-1,J)+H(I,J))/2                                         GR031600
                    GO TO A1                                                       GR031700
                C  MOD14                                                           GR031800
   505            130 M1=(H(I,J+1)+H(I,J))/2                                      GR031900
                    M2=(H(I+1,J)+H(I,J))/2                                         GR032000
                    M3=(H(I,J-1)+G*H(I,J))/2                                       GR032100
                    M4=(H(I-1,J)+G*H(I,J))/2                                       GR032200
                    GO TO A1                                                       GR032300
   510          C  MOD15                                                           GR032400
                  131 M1=(H(I,J+1)+G*H(I,J))/2                                     GR032500
                    M2=(H(I+1,J)+G*H(I,J))/2                                       GR032600
                    M3=(H(I,J-1)+H(I,J))/2                                         GR032700
```

```
                  H4=(H(I-1,J)+H(I,J))/2                                    GR032800
      515         GO TO 81                                                  GR032900
                C  MOD16                                                    GR033000
                  132 H1=(H(I,J+1)+H(I,J))/2                                GR033100
                      H2=(H(I+1,J)+G+H(I,J))/2                              GR033200
                      H3=(H(I,J-1)+G+H(I,J))/2                              GR033300
      520             H4=(H(I-1,J)+G+H(I,J))/2                              GR033400
                      GO TO 81                                              GR033500
                C  MOD17                                                    GR033600
                  133 H1=(H(I,J+1)+G+H(I,J))/2                              GR033700
                      H2=(H(I+1,J)+G+H(I,J))/2                              GR033800
      525             H3=(H(I,J-1)+H(I,J))/2                                GR033900
                      H4=(H(I-1,J)+G+H(I,J))/2                              GR034000
                      GO TO 81                                              GR034100
                C  MOD07J                                                   GR034200
                  134 H1=(H(I,J+1)+H(I,J))/2+G                              GR034300
      530             H2=(H(I+1,J)+H(I,J))/2+G                              GR034400
                      H3=(H(I,J-1)+H(I,J))/2+G                              GR034500
                      H4=(H(I-1+IMAX,J)+H(I,J))/2+G                         GR034600
                      GO TO 87                                              GR034700
                C  MOD09J                                                   GR034800
      535           135 H1=(H(I,J+1)+H(I,J))/2                              GR034900
                      H2=(H(I+1,J)+G+H(I,J))/2                              GR035000
                      H3=(H(I,J-1)+G+H(I,J))/2                              GR035100
                      H4=(H(I-1+IMAX,J)+H(I,J))/2                           GR035200
                      GO TO 87                                              GR035300
      540         C  MOD10J                                                 GR035400
                  136 H1=(H(I,J+1)+G+H(I,J))/2                              GR035500
                      H2=(H(I+1,J)+H(I,J))/2                                GR035600
                      H3=(H(I,J-1)+H(I,J))/2                                GR035700
                      H4=(H(I-1+IMAX,J)+G+H(I,J))/2                         GR035800
      545             GO TO 87                                              GR035900
                C  MOD11J                                                   GR036000
                  137 H1=(H(I,J+1)+H(I,J))/2                                GR036100
                      H2=(H(I+1,J)+H(I,J))/2                                GR036200
                      H3=(H(I,J-1)+H(I,J))/2                                GR036300
      550             H4=(H(I-1+IMAX,J)+G+H(I,J))/2                         GR036400
                      GO TO 87                                              GR036500
                C  MOD12J                                                   GR036600
                  138 H1=(H(I,J+1)+H(I,J))/2                                GR036700
                      H2=(H(I+1,J)+H(I,J))/2                                GR036800
      555             H3=(H(I,J-1)+G+H(I,J))/2                              GR036900
                      H4=(H(I-1+IMAX,J)+H(I,J))/2                           GR037000
                      GO TO 87                                              GR037100
                C  MOD13J                                                   GR037200
                  139 H1=(H(I,J+1)+G+H(I,J))/2                              GR037300
      560             H2=(H(I+1,J)+H(I,J))/2                                GR037400
                      H3=(H(I,J-1)+H(I,J))/2                                GR037500
                      H4=(H(I-1+IMAX,J)+H(I,J))/2                           GR037600
                      GO TO 87                                              GR037700
                C  MOD14J                                                   GR037800
      565           140 H1=(H(I,J+1)+H(I,J))/2                              GR037900
                      H2=(H(I+1,J)+H(I,J))/2                                GR038000
                      H3=(H(I,J-1)+G+H(I,J))/2                              GR038100
                      H4=(H(I-1+IMAX,J)+G+H(I,J))/2                         GR038200
                      GO TO 87                                              GR038300
      570         C  MOD15J                                                 GR038400
```

```
PROGRAM GROV      76/76   OPT=1   TRACE                    UMRCC FTN 4.1.170A   10/05/74  03.45.23

      141 H1=(H(I,J+1)+G+H(I,J))/2                                          GR038500
          H2=(H(I+1,J)+G+H(I,J))/2                                          GR038600
          H3=(H(I,J-1)+H(I,J))/2                                            GR038700
          H4=(H(I-1+IMAX,J)+H(I,J))/2                                       GR038800
          GO TO 87                                                          GR038900
C  MOD16J                                                                  GR039000
      142 H1=(H(I,J+1)+H(I,J))/2                                            GR039100
          H2=(H(I+1,J)+G+H(I,J))/2                                          GR039200
          H3=(H(I,J-1)+G+H(I,J))/2                                          GR039300
          H4=(H(I-1+IMAX,J)+G+H(I,J))/2                                     GR039400
          GO TO 87                                                          GR039500
C  MOD17J                                                                  GR039600
      143 H1=(H(I,J+1)+G+H(I,J))/2                                          GR039700
          H2=(H(I+1,J)+G+H(I,J))/2                                          GR039800
          H3=(H(I,J-1)+H(I,J))/2                                            GR039900
          H4=(H(I-1+IMAX,J)+G+H(I,J))/2                                     GR040000
          GO TO 87                                                          GR040100
C  MOD07B                                                                  GR040200
      144 H1=(H(I,J+1)+H(I,J))/2+G                                          GR040300
          H2=(H(I+1-IMAX,J)+H(I,J))/2+G                                     GR040400
          H3=(H(I,J-1)+H(I,J))/2+G                                          GR040500
          H4=(H(I-1,J)+H(I,J))/2+G                                          GR040600
          GO TO 86                                                          GR040700
C  MOD09B                                                                  GR040800
      145 H1=(H(I,J+1)+H(I,J))/2                                            GR040900
          H2=(H(I+1-IMAX,J)+G+H(I,J))/2                                     GR041000
          H3=(H(I,J-1)+G+H(I,J))/2                                          GR041100
          H4=(H(I-1,J)+H(I,J))/2                                            GR041200
          GO TO 86                                                          GR041300
C  MOD10B                                                                  GR041400
      146 H1=(H(I,J+1)+G+H(I,J))/2                                          GR041500
          H2=(H(I+1-IMAX,J)+H(I,J))/2                                       GR041600
          H3=(H(I,J-1)+H(I,J))/2                                            GR041700
          H4=(H(I-1,J)+G+H(I,J))/2                                          GR041800
          GO TO 86                                                          GR041900
C  MOD11B                                                                  GR042000
      147 H1=(H(I,J+1)+H(I,J))/2                                            GR042100
          H2=(H(I+1-IMAX,J)+H(I,J))/2                                       GR042200
          H3=(H(I,J-1)+H(I,J))/2                                            GR042300
          H4=(H(I-1,J)+G+H(I,J))/2                                          GR042400
          GO TO 86                                                          GR042500
C  MOD12B                                                                  GR042600
      148 H1=(H(I,J+1)+H(I,J))/2                                            GR042700
          H2=(H(I+1-IMAX,J)+H(I,J))/2                                       GR042800
          H3=(H(I,J-1)+G+H(I,J))/2                                          GR042900
          H4=(H(I-1,J)+H(I,J))/2                                            GR043000
          GO TO 86                                                          GR043100
C  MOD13B                                                                  GR043200
      149 H1=(H(I,J+1)+G+H(I,J))/2                                          GR043300
          H2=(H(I+1-IMAX,J)+H(I,J))/2                                       GR043400
          H3=(H(I,J-1)+H(I,J))/2                                            GR043500
          H4=(H(I-1,J)+H(I,J))/2                                            GR043600
          GO TO 86                                                          GR043700
C  MOD14B                                                                  GR043800
      150 H1=(H(I,J+1)+H(I,J))/2                                            GR043900
          H2=(H(I+1-IMAX,J)+H(I,J))/2                                       GR044000
          H3=(H(I,J-1)+G+H(I,J))/2                                          GR044100
```

```
                  H4=(H(I-1,J)+G+H(I,J))/2                                GR044200
                  GO TO 86                                                GR044300
  630         C  MOD158                                                  GR044400
              151 H1=(H(I,J+1)+G+H(I,J))/2                                GR044500
                  H2=(H(I+1-IMAX,J)+G+H(I,J))/2                           GR044600
                  H3=(H(I,J-1)+H(I,J))/2                                  GR044700
                  H4=(H(I-1,J)+H(I,J))/2                                  GR044800
  635             GO TO 86                                                GR044900
                C  MOD168                                                 GR045000
                152 H1=(H(I,J+1)+H(I,J))/2                                GR045100
                  H2=(H(I+1-IMAX,J)+G+H(I,J))/2                           GR045200
                  H3=(H(I,J-1)+G+H(I,J))/2                                GR045300
  640             H4=(H(I-1,J)+G+H(I,J))/2                                GR045400
                  GO TO 86                                                GR045500
                C  MOD178                                                 GR045600
                153 H1=(H(I,J+1)+G+H(I,J))/2                              GR045700
                  H2=(H(I+1-IMAX,J)+G+H(I,J))/2                           GR045800
  645             H3=(H(I,J-1)+H(I,J))/2                                  GR045900
                  H4=(H(I-1,J)+G+H(I,J))/2                                GR046000
                  GO TO 86                                                GR046100
                 79 STOP                                                  GR046200
                  END                                                     GR046300
```

SUBROUTINE GROBO 76/76 OPT=1 TRACE UMRCC FTN 4.1.170A 18/05/74 03.45.50

```
      SUBROUTINE GROBO                                                  GR046400
      REAL Z(48,18),H(48,18)                                            GR046500
      COMMON /FRED/Z,H,I,J,HG,G,Z1,Z2,Z3,Z4,IMAX                        GR046600
      Z1=(Z(I,J+1)+Z(I,J))/2                                            GR046700
    5 Z2=(Z(I+1,J)+Z(I,J))/2                                            GR046800
      Z3=(Z(I,J-1)+Z(I,J))/2                                            GR046900
      Z4=(Z(I-1,J)+Z(I,J))/2                                            GR047000
      HG=H(I,J)+G                                                       GR047100
      RETURN                                                            GR047200
   10 END                                                               GR047300
```

```
      SUBROUTINE GROCY                                                  GR047400
      REAL Z(4R,1R),H(4R,1R)                                            GR047500
      COMMON /FRED/Z,H,I,J,HG,G,Z1,Z2,Z3,Z4,IMAX                        GR047600
      Z1=(Z(I,J+1)+Z(I,J))/2                                            GR047700
      Z2=(Z(I+1-IMAX,J)+Z(I,J))/2                                       GR047800
      Z3=(Z(I,J-1)+Z(I,J))/2                                            GR047900
      Z4=(Z(I-1,J)+Z(I,J))/2                                            GR048000
      HG=H(I,J)+G                                                       GR048100
      RETURN                                                            GR048200
      END                                                               GR048300
```

```
      SUBROUTINE GROAD                                                  GR048400
      REAL Z(48,18),H(48,18)                                            GR048500
      COMMON /FRED/Z,H,I,J,HG,G,Z1,Z2,Z3,Z4,IMAX                        GR048600
      Z1=(Z(I,J+1)+Z(I,J))/2                                            GR048700
      Z2=(Z(I+1,J)+Z(I,J))/2                                            GR048800
      Z3=(Z(I,J-1)+Z(I,J))/2                                            GR048900
      Z4=(Z(I-1+IMAX,J)+Z(I,J))/2                                       GR049000
      HG=H(I,J)+G                                                       GR049100
      RETURN                                                            GR049200
      END                                                               GR049300
```

REFERENCES

1. FLEMING D.P. (et Al), Experiments on Power Loss in Herringbone-Grooved Gas-Lubricated Journal Bearings, NASA TN-D-5224, 1969.

2. CUNNINGHAM R.E. (et Al), Experiments on Stability of Herringbone-Grooved Gas-Lubricated Journal Bearings to High Comp. Nos. NASA TN D-4440, 1967.

3. AUSMAN J.S., Theory & Design of Self-Acting Gas-Lubricated Journal Bearings including Misalignment Effects, 1st Internat. Symp. on Gas Brgs. ACR-49, pp.161-192, Washington 1959.

4. FREEMAN A.P., Inertial-Gyro Testing for Reliability, AGARD I/N Proceedings, No.116/3-A, 3-1, 1972.

5. SAPUPPO M.S., Strapdown Inertial Gyroscope, AGARD I/N Proceedings No.116, 3-A, 2-1, 1972.

6. THOMPSON R., Borides : Their Chemistry and Applications, R.Inst.Chem. Lect. Ser.5., 1965.

7. THOMPSON R., The Chemistry of Borides and Related Compounds, Borax Consolidated Ltd. (Reprint).

8. WHIPPLE R.T.P., The Inclined Groove Bearing, AERE Report T/R 622, Harwell, 1958.

9. HIRS G.G., The Load Capacity and Stability Characteristics of Hydrodynamic Grooved Jnl. Bearings, Trans. ASLE 8, 296-305, 1965.

10. HAMROCK B.J., Designing the Brawny Gas Bearing, Machine Design, Dec.23, 1971.

11. CASTELLI V. & PIRVICS J., Equilibrium Characteristics of Axial Groove Gas Lubricated Bearings, Trans. ASME, Inl. Lub. Tech., April 1967.

12. ROOD L., Investigation of the Spherical Hydrostatic Gas Bearing for Two Axis Gyros, Trans. ASME, Jnl. Lub. Tech., Jan.1971.

13. HAMROCK B.J., & FLEMING D.P., Optimisation of Self Acting Herringbone Grooved Journal Bearings for Max. Radial Load Capacity, Proc. Southampton G.B. Symposium, 1971.

14. WOOD M.D., Slip Flow in Spiral-Grooved Thrust Bearings, Proc. Southampton G.B. Symposium, 1969.

15. TREVORROW E.U., The Effect of Groove Edge Sharpness in Rayleigh Step Bearings, Proc. Southampton G.B. Symposium, 7. 1969.

16. BEARDMORE G., Development of the Series 700 Gas Bearing Gyro, Proc. 5th Internat. Gas Brg. Symp., Southampton Univ. Paper 7, 1971.

17. MALANOSKI S.B., Experiments on an Ultrastable Gas Journal Bearing, Trans. ASME, Paper 66 - Lub 6. 1966.

18. NAHAVANDI A. & OSTERLE F., A novel form of Self-Acting Gas Lubricated Thrust Bearing, Trans. ASLE 4, 124-130, 1961.

19. VOHR J.H., & CHOW C.Y., Characteristics of Herringbone Grooved Gas Lubricated Journal Bearings. Trans ASME, Jnl. Basic Eng., D, Vol 87, No.3., 1965.

20. GNANADOSS A.A. & OSBORNE M.R., The Numerical Solution of Reynold's Equation for a Journal Bearing, Quart. Jnl. Mech & App. Math; Vol, XVII Pt.2., 1964.

21. STERNLICHT B. & ELWELL R.C.? Theoretical and Experimental Analysis of Hydrodynamic Gas-Lubricated Journal Bearings, Trans ASME, 57-F-18. 1957.

22. GROSS W.A., Numerical Analysis of Gas Lubricated Films, 1st Gas Brg. Symp. Washington, 1959.

23. RAIMONDI A.A., A Numerical Solution for the Gas Lubricated Full Journal Bearing of Finite Length, ASLE Trans.4, 131-155, 1961.

24. RAIMONDI A.A., & BOYD J., A Solution for the Finite Journal Bearing and its application to Analysis and Design. Pt.I, II, III Trans. ASLE Lube. Conf., 1956.

25. PINKUS O., Solution of Reynold's Equation for Finite Journal Bearings, ASME Paper 57-F-12, 1956.

26. ELROD H.G. & BURGDORFER A., Refinements of the theory of the infinitely-long self-acting Gas Lub. Jnl. Bearing, 1st Inter. Gas Brg. Symp. Washington D.C., 1959.

27. RABINOWIEZ E., 'Polishing', Scientific American, Vol.218 No.9 June, 1968.

28. AUSMAN J.S., The Fluid Dynamic Theory of Gas Lubricated Bearings, ASME-ASLE Lube. Conf., Paper 56-LUB-6, 1956.

29. AUSMAN J.S., Torque Produced by Misalignment of Hydrodynamic Gas Lubricated Journal Bearings, ASME-ASLE Paper 59-Lub 3, 1959.

30. WHITLEY S. & WILLIAMS L.G., The Gas Lubricated Spiral Groove Thrust Bearing, U.K.A.E. I.G. Report 28, (R.D/CA), 1959.

31. R.P.I. - M.T.I., Gas Bearing Design Manual, Rensselaer Polytechnic Institute, N.Y., U.S.A., 1967.

32. CAMERON, Principles of Lubrication, Longman, 1966.

33. FADDY, D., The theoretical performance of statically loaded pairs of conical gas bearings, R.A.E. Tech. Report 69174, 1969.

34. WACHMANN C. & MALANOSKI S.B., Thermal distortion of Spiral grooved Gas Lubricated Thrust Bearings, Trans. ASME, Paper 70-Lube 5-14, 1971.

35. GROUEFF S., The Manhatten Project, Collins, 1967.

36. STOKES, R., ONR/ACO Gas Lub. Brg. Research Meeting, Philadelphia, U.S.A., 1971.

37. GLASSON D.R., & JONES J.A., Production and Applications of Boron Carbide, John Graymore Chem. Labs., Plymouth Polytechnic.

38. PODZUS E., Z. Anorg. Chem., 1933, 211, 41. 1933.

39. BOWDEN F.P. & TABOR D., Friction and Lubrication in Solids, Clarendon Press, Oxford, 1964.

40. BOTO, A., Ball Bearing J., 153, 1968, 13.

41. KITAMURA S., Elec. Eng. Jap. 86 (6), 1966, 95.

42. GRUNDBERG L., Brit J. App. Phys. 9, 1958, 85.

43. T-W-FIENNES W.G., A Study of the Electrical Conductivity of Lubricating Oil Films, Lond. Univ. Ph.D. Thesis, 1971.

44. HOLM R., Electrical Contacts Handbook, Third Ed., Springer Verlag, Berlin, 1958.

45. PEARSON G.L., Phys. Rev. 56, 1939, 471.

46. CANTRIL J.M. & POHL H.A., Conf. on Electrical Insulation & Dielectric Phenomena, 1969, N.A.S., N.R.C. Publ. 1964, 105.

47. CANTRIL J.M. & POHL H.A., J.Electro Chem. Soc. 115 (7), 1968, 700.

48. MACALPINE J.M.K. & COOKSON A.H., Proc. IEE 187 (3), 1970, 646.

49. MIRZA J.S., SMITH C.W. & CALDERWOOD J.H., J. Phys.(D) 3 (4), 1970, 580.

50. Van OSENBRUGG C., Phil. Tech. Rev.30 (6/7), 1969, 195.

51. KOK J.A., Electrical Breakdown of Liquids, Phillips Tech. Lib. 1961.

52. WILSON R.W., Proc. Phys. Soc. (B) 68 (9), 1955, 625.

53. FUREY M.J., Trans ASLE 4 1961, 1.

54. CAMERON A., J. Inst. Pet. 40, 1954, 191.

55. BEARDMORE G., Electrostatic Charging of Rotors, Mins. 9th U.K. Gas Brg. Pnl. Meeting, Paper 3, 1971.

56. KILMISTER G.T.F., MUNDAY A.J., Design Manufacture & Performance of an Externally Pressurised Boring Head, Southampton Univ. Rept. SR/MT 2662, 1971.

57. DENHARD W.G., The Conflict of Computer and Hardware in Gas Bearing Applications, Mins. 5th ONR/UK Gas Brg. Pnl. Meeting, Paper 1., 1972.

58. HALL E., The Application of Beryllia to an Integral Gimbal Gas Bearing Gyro Design, Mins. 5th ONR/UK Gas Brg. Pnl. Meeting, Paper 2., 1972.

59. NELSON J.L., Boron Carbide for Gas Bearing Applications, Mins. 5th ONR/UK Gas Brg. Pnl. Meeting, Paper 3, 1972.

60. LANSDOWN A.R., Some Techniques for Studying Surfaces, Mins, 5th ONR/UK Gas Brg. Pnl. Meeting, Paper 5, 1972.

61. ELROD H.G., Fluid dynamic effects of surface roughness in Gas Bearings, Mins. 5th ONR/UK Gas Brg. Pnl. Meeting, Paper 6, 1972.

62. PUBLICOVER J., Recent work re failure mechanisms in Ceramic Gas Bearing Gyros. Mins 5th ONR/UK Gas Brg. Pnl. Meeting, Paper 13, 1972.

63. GIELISSE P.J., Ceramic Machining, Mins ONR/UK Gas Lub. Brg. Research Meeting, Philadelphia, USA, 1971.

64. TAYLOR K., Sputter Etching of Grooves, Mins. ONR/UK Gas Lub. Brg. Research Meeting, Philadelphia, USA, 1971.

65. PATTERSON A.G., Manufacture of Spiral Groove Bearings, Mins. ONR/UK Gas Lub. Brg. Research Meeting, Philadelphia, USA, 1971.

66. GEILING D.W., Mean Free Path effects in Gyro Gas Bearings, Mins. ONR/UK Gas Lub. Brg. Research Meeting, Philadelphia, USA, 1971.

67. MUYDERMAN, E.A., Spiral Groove Bearings, Thesis. Tech. University, Delft, Netherlands, 1964.

68. FADDY D. & ELLIS T.L., Conical Gas Bearings for Gyroscope Spin Axis Support, R.A.E. Tech. Memo IEE 202, 1968.

69. HOLMES J., Radial magnetic Pull in Gyro Motors, Mins. 7th UK Gas Brg. Pnl. Meeting, Paper 1, 1970.

70. BRADFORD, Procs. IEE Vol.115, No.11, 1968.

71. MORONEY, M.J., Facts from Figures, Penguin Books, 1960.

72. BEARDMORE G., Ion-machining, a technique for cutting pumping grooves in gas bearing components, Proc. 5th Internat. Gas Brg. Symp. Southampton Univ. Paper 8, 1971.

73. BERBEN T.J. & BERGHOUT C.W., Lubrication with Gases, Philips Tech. Rev. Vol.28, No.6, 1968.

74. PATTERSON A.G., Gas Lubrication applied to Gyros, Instrument Practice, April 1962, p.p. 426-432.

75. HARRISON W., The Hydrodynamic Theory of Lubrication with special reference to air as a lubricant. Trans. Camb. Phil. Soc.22, p.p. 267-292, 1913.

76. GLASSON D.R. & JONES J.A., *Formation and reactivity of* Borides, Carbides and Silicides, Pt I & II Jnl. App. Chem., May, 1969.

77. DENHARD W., Work at M.I.T. on Gas Brg. applications, Mins. 3rd ONR/UK Gas Brg. Pnl. Meeting, Paper 13, 1970.

78. YOUNG D.G., Gas Bearing Materials, Mins 5th UK Gas Brg. Pnl. Meeting, Paper 4, 1969.

79. GALVIN D., Lubrication of Tungsten Carbide, Mins 5th UK Gas Brg. Pnl. Meeting, Paper 5, 1969.

80. TREVORROW E.U. & FADDY D, The effect of axial flow along the journal on connected thrust bearings, Proc. Southampton G.B. Symp. Paper 14, 1969.

81. YOUNG D.G., Gas Bearing work at Sperry Gyroscope Div., Mins 1st ONR/UK Gas Brg. Pnl. Meeting, Paper 12, 1968.

82. FADDY D., Gas Bearing work for Aircraft Gyros, Mins. 1st ONR/UK Gas Brg. Pnl. Meeting, Paper 13, 1968.

83. PATTERSON A.G., Review of Gas Bearing Gyro Development in the United Kingdom, Trans. ASME, 68-LubS-29, 1968.

84. GRASSAM N.S. & POWELL J.W., Gas Lubricated Bearings, Butterworth, London, 1964.

85. SMITH G.D., Numerical Solution of Partial Differential Equations, Oxford University Press, 1969.

86. POPOVIC N. & BUTLER A.L., Ion bombardment cleaning of Gyro wheels, 5th Internat. Gas Brg. Symp. Southampton, Paper 19, 1971.

87. SCHIESSER, R.J., Advanced Fabrication techniques for opposed hemispherical self acting Gas Bearings, 5th Internat. Gas Brg. Symp. Southampton, Paper 23, 1971.

88. BEARDMORE, G., The vacuum deposition of wear and corrosion resistant surfaces on gas bearing components, 4th Gas Brg. Symp. Southampton, Paper 15, 1969.

89. BUTLER A.L., Vibration Data on Spool Type Gas Bearing, 4th Gas Brg. Symp. Southampton, Paper 13, 1969.

90. WHITLEY S., The design of the spiral groove thrust bearing, 3rd Gas Brg. Symp. Southampton, Paper 13, 1967.

91. CASTELLI V. & VOHR J.H., Performance characteristics of Herringbone groove Journal Brgs operating at high eccentricity ratios with misalignment, 3rd Gas Brg. Symp. Southampton, Paper 14, 1967.

92. HINKLE J.G. & FULLER D.D., Evaluation of friction and characteristics of materials for gas lubricated bearings under conditions of start-stop and whirl induced rubbing, 3rd Gas Brg. Symp. Southampton, Paper 24, 1967.

93. KINGSBURY A., Experiments with an Air Lubricated Journal, Inl. pf American Soc. of Naval Engineers, Vol. 9, p.p. 267-292, 1897.

94. DuBOIS, G.B. (et al), Properties of Misaligned Journal Bearings, ASME Trans, Paper 56 - LUB-7, 1956.

95. MARSH H. The Stability of Aerodynamic Gas Bearings, Ph.D. Thesis, Cambridge University, 1963.

96. PAN C.H.T., A Universally valid compressible theory for gas lubricated narrow, spiral grooved thrust bearings, 4th Gas Brg. Symp. Southampton, Paper 31, 1969.

97. CASTELLI V. & PIRVICS J., A review of numerical methods in gas bearing film analysis, ASME Paper No. 68, LUB-11, 1968.

98. GALVIN G.D., Lubrication of Tungsten Carbide, 5th UK Gas Brg. Panel Meeting, A.C.O. 1969.

99. YOUNG D.G., Review of experience with Gas Bearing Materials, Mins. ONR-ACO Gas Brg. Research Meeting, Philadelphia U.S.A., 1971.

100. PRICE N., Non-Corrodable Shafts for the G.I.V. -6 Gyroscope, U.K. Gas Brg. Pnl. Meeting, A.C.O. 1973.

101. POWELL J.W., 'Gas behaviour and load capacity of hydrodynamic gas journal bearings', I.Mech.E. Lub. & Wear Conf. Paper 11, 1963.

102. COLE J. & KERR J., 'Observations on performance of air lubricated bearings' Proc. of Conf. on Lub. & Wear, I.Mech.E., Oct. 1957, 164.

103. YOUNG D.G., 'Development of friction in gyroscope bearings' ONR/UK Gas Brg. Research Meeting, Columbia U.S.A., 1969.

104. WALDRON W., 'Evaluation of Bearing Materials for Advanced Aircraft Engines on Air Bearings', Mins. ONR/UK Gas Bearing Meeting, Philadelphia, 1971.

105. MORLEY A., Strength of Materials, Longmans, 1948.

106. DRAPER C.S., 'Background for Specification, Engineering and Operational Realisation of inertial sensors, etc.' M.I.T/I.L Report R-623, 1968.

107. Private verbal communications to the author.

108. CONSTANTINESCU V.N., 'Lubrication in Turbulent Regime', AEC-TR-6959, U.S. Atomic Energy Commission, 1968.

109. WILDMANN M., 'Grooved plate gas lubricated thrust bearings with special reference to the spiral groove bearing'. ASME Trans. LUB-25, Paper 64, 1964.

110. WILDMANN M., 'On the Behaviour of a Grooved Plate Thrust Bearing with compressible lubricant', Jnl. Lub. Tech., Trans. ASME, Series F, Vol 90, No.1, 1968.

111. FORSYTHE G.E. & WASOW W.R., 'Finite diff. methods for partial differential equations', Wiley, New York, 1960.

112. PINK, E., 'Evaluation of design methods for externally pressurised bearings' Mins. 10th U.K. Gas Brg. Pnl. Meeting, Paper 8, 1973.

113. I.C.L. COMPUTERS L.T.D., 'Statistical Analysis Mark 2 - 1900 Series' Technical Publication No.4301, I.C.L. Tech.Pubs. Dept., Ed.3/., 1971.

114. SPRINGBORN, R.K., 'Non-traditional machining processes' A.S.T.M.E. Publications, 1967.

115. I.C.L. COMPUTERS L.T.D., 'Fortran 1900 Series' Technical Publication No. TL1167, I.C.L. Publications Dept., 1968.

116. SMITHS INDUSTRIES LIMITED, TR.345, 'The Series 700 Gas Bearing Gyroscope, 1974.

117. GALVIN, G.D. (et Al), 'Developments in supercleaning and boundary lubrication for gas bearing gyros related to surface phenomena', Journal of Lub. Tech., Trans. A.S.M.E., Oct. 1968.

118. PATTERSON, A.G., 'The evaluation and design of an aerodynamic gas bearing', Southampton Gas Bearing Symposium, Paper 1/., 1965.

119. DENHARD, W.G. & PAN, C.H.T., 'Application of Gas-Lubricated bearings to instruments', A.S.M.E. Trans., Journal of Lub. Tech. 1968.

120 ALLEN, D.N. de G. 'Relaxation Methods' McGraw Hill Inc. 1st Ed. 1954.

121. DIGGLE, J.W. & DAMJANOVIC, A. 'The inhibition of the dendritic electrocrystallization of zinc from doped alkaline zincate solutions' J. Electrochem. Soc. (USA) Vol.119, No.12, P.1649-58, DEC 1972.

122. BADER, R.F. 'Automatic laser resistor trimming', Solid State Technol. (USA), Vol.15, No.9, P.44-6, SEPT. 1972.